AAAS

Science

15 MAY 2025

Can brain waves betray a suspect's guilt?
p. 694

Melting a Wigner solid
pp. 702 & 736

One genome, multiple nuclei
pp. 703 & 784

ON THE MOVE

Connectivity of Pleistocene horse populations across Beringia and beyond **p. 748**

ASU Science

PRIZE FOR TRANSFORMATIONAL IMPACT

Apply now to the Arizona State University and *Science* Prize for Transformational Impact!

Arizona State University and *Science* have partnered to create the **ASU–*Science* Prize for Transformational Impact**. This prize recognizes transformational research that uses innovative methods and approaches to identify problems and develop solutions with impacts on policy and decision-making.

The grand prize winner will receive a prize of **US$30,000** and their prize-winning essay will be published in *Science* online and print. A runner-up will receive **US$10,000** and have their essay published in *Science* online.

APPLY BY **AUGUST 15, 2025**

www. Science.org/ASU

CONTENTS

15 MAY 2025 | VOLUME 388 | ISSUE 6748

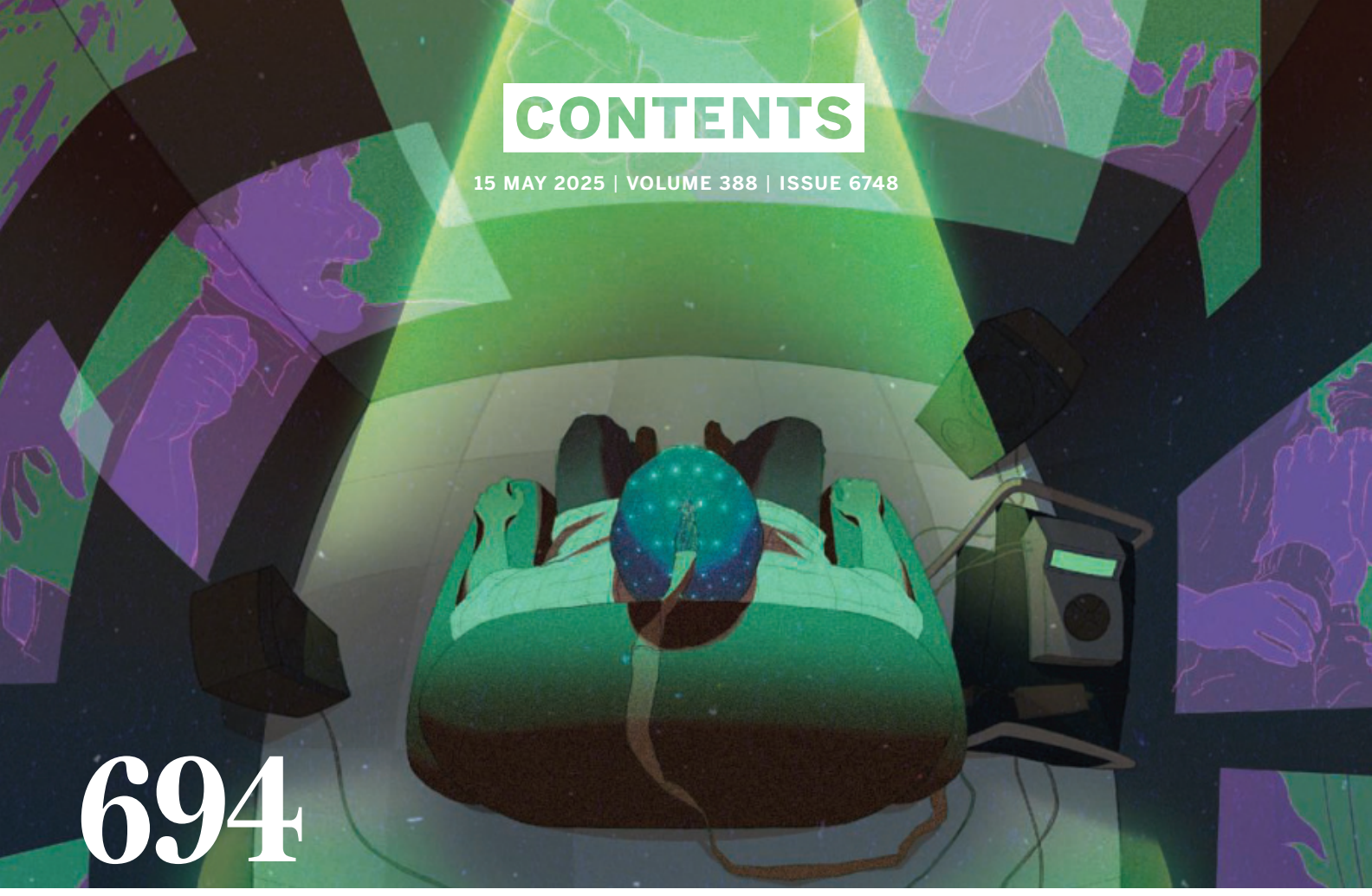

694

EDITORIAL

NEWS

FEATURES

COMMENTARY

PERSPECTIVES

POLICY FORUM

BOOKS ET AL.

ILLUSTRATION: DION MBD

New from Princeton University Press

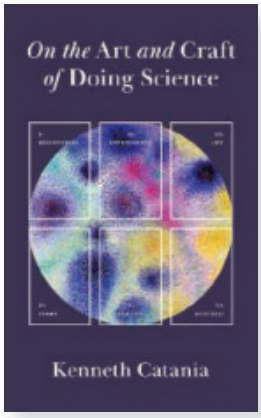

A scientist's personal reflections on how to harness creativity and curiosity to generate new ideas and discover the unexpected

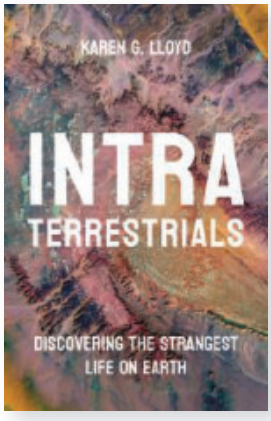

A biologist's firsthand account of the hunt for life beneath earth's surface—and how new discoveries are challenging our most basic assumptions about the nature of life on Earth

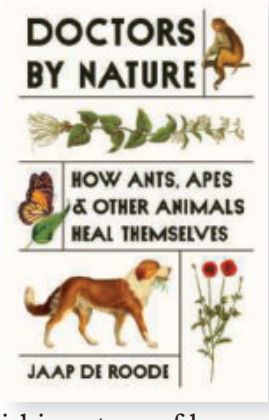

The astonishing story of how animals use medicine and what it can teach us about healing ourselves

Where Science Gets Social.

AAAS.ORG/COMMUNITY

AAAS' Member Community is a one-stop destination for scientists and STEM enthusiasts alike. It's "Where Science Gets Social": a community where facts matter, ideas are big and there's always a reason to come hang out, share, discuss and explore.

Member COMMUNITY
AAAS

ON THE COVER

Two semiwild Camargue horses gallop through the wetlands and marshes of southern France. Research traces horse movements across Eurasia and the Americas during the Late Pleistocene. By moving together with interrelated life forms, horses bring balance and sustainability to their ecosystems. See page 748. Photo: Art Wolfe

PHOTO: F. DESCHANDOL AND P. SABINE/BIOSPHOTO/MINDEN PICTURES

***Science* serves as a forum for discussion of important issues related to the advancement of science by publishing material on which a consensus has been reached as well as including the presentation of minority or conflicting points of view. Accordingly, all articles published in *Science*—including editorials, news, commentary, and book reviews—are signed and reflect the individual views of the authors and not official points of view adopted by AAAS or the institutions with which the authors are affiliated.** *Science* (ISSN 0036-8075) is published weekly on Thursday, except last week in December, by the American Association for the Advancement of Science, 1200 New York Avenue, NW, Washington, DC 20005. Periodicals mail postage (publication No. 484460) paid at Washington, DC, and additional mailing offices. Copyright © 2025 by the American Association for the Advancement of Science. The title *Science* is a registered trademark of the AAAS. Domestic individual membership, including subscription (12 months): $165 ($74 allocated to subscription). Domestic institutional subscription (51 issues): $2865; Foreign postage extra: Air assist delivery: $135. First class, airmail, student, and emeritus rates on request. Canadian rates with GST available upon request, GST #125488122. Publications Mail Agreement Number 1069624. **Printed in the U.S.A. Change of address:** Allow 4 weeks, giving old and new addresses and 8-digit account number. **Postmaster:** Send change of address to AAAS, P.O. Box 96178, Washington, DC 20090–6178. **Single-copy sales:** $15 each plus shipping and handling available from backissues.science.org; bulk rate on request. **Authorization to reproduce** material for internal or personal use under circumstances not falling within the fair use provisions of the Copyright Act can be obtained through the Copyright Clearance Center (CCC), www.copyright.com. The identification code for *Science* is 0036-8075. *Science* is indexed in the *Reader's Guide to Periodical Literature* and in several specialized indexes.

Science AAAS

EDITOR-IN-CHIEF Holden Thorp, hthorp@aaas.org

EXECUTIVE EDITOR Valda Vinson

EDITORS, RESEARCH Sacha Vignieri, Jake S. Yeston **EDITOR, COMMENTARY** Lisa D. Chong

DEPUTY EXECUTIVE EDITOR Lauren Kmec

DEPUTY EDITORS Stella M. Hurtley (UK), Phillip D. Szuromi **SENIOR EDITORS** Caroline Ash (UK), Michael A. Funk, Angela Hessler, Di Jiang, Priscilla N. Kelly, Marc S. Lavine (Canada), Sarah Lempriere (UK), Mattia Maroso, Yevgeniya Nusinovich, Ian S. Osborne (UK), L. Bryan Ray, H. Jesse Smith, Keith T. Smith (UK), Jelena Stajic, Peter Stern (UK), Yury V. Suleymanov, Valerie B. Thompson, Brad Wible **ASSOCIATE EDITORS** Jack Huang, Sumin Jin, Bianca Lopez, Sarah Ross (UK), Madeleine Seale (UK), Corinne Simonti, Ekeoma Uzogara **SENIOR LETTERS EDITOR** Jennifer Sills **NEWSLETTER EDITOR** Christie Wilcox **RESEARCH & DATA ANALYST** Jessica L. Slater **LEAD CONTENT PRODUCTION EDITORS** Chris Filiatreau, Harry Jach Sr. **CONTENT PRODUCTION EDITOR** Amelia Beyna **CONTENT PRODUCTION EDITORS** Anne Abraham, Robert French, Julia Haber-Katris, Nida Masiulis, Abigail Shashikanth, Suzanne M. White **EDITORIAL MANAGER** Joi S. Granger **SENIOR PROGRAM ASSOCIATE** Maryrose Madrid **EDITORIAL ASSOCIATES** Aneera Dobbins, Lisa Johnson, Jerry Richardson, Anita Wynn **SENIOR EDITORIAL COORDINATORS** Alexander Kief, Ronmel Navas, Isabel Schnaidt, Alice Whaley (UK), Brian White **EDITORIAL COORDINATORS** Clair Goodhead (UK), Kat Kirkman, Samantha Price **ADMINISTRATIVE COORDINATOR** Karalee P. Rogers **ASI DIRECTOR, OPERATIONS** Janet Clements (UK) **ASI OFFICE MANAGER** Carly Hayward (UK) **ASI SR. OFFICE ADMINISTRATORS** Simon Brignell (UK), Jessica Waldock (UK) **COMMUNICATIONS DIRECTOR** Meagan Phelan **DEPUTY DIRECTOR** Matthew Wright **SENIOR WRITERS** Walter Beckwith, Joseph Cariz, Abigail Eisenstadt **WRITER** Mahathi Ramaswamy **SENIOR COMMUNICATIONS ASSOCIATES** Zachary Graber, Sarah Woods **COMMUNICATIONS ASSOCIATES** Kiara Brooks, Haley Riley, Mackenzie Williams

NEWS EDITOR Tim Appenzeller

NEWS MANAGING EDITOR John Travis **INTERNATIONAL EDITOR** David Malakoff **DEPUTY NEWS EDITORS** Rachel Bernstein, Shraddha Chakradhar, Martin Enserink, David Grimm, Eric Hand, Michael Price, Kelly Servick, Matt Warren (Europe) **SENIOR CORRESPONDENTS** Daniel Clery (UK), Jon Cohen, Jeffrey Mervis **ASSOCIATE EDITORS** Jeffrey Brainard, Michael Greshko, Katie Langin **NEWS REPORTERS** Adrian Cho, Jennifer Couzin-Frankel, Phie Jacobs, Jocelyn Kaiser, Rodrigo Pérez Ortega (Mexico City), Robert F. Service, Erik Stokstad, Paul Voosen, Meredith Wadman **CONSULTING EDITOR** Elizabeth Culotta **CONTRIBUTING CORRESPONDENTS** Vaishnavi Chandrashekhar, Dan Charles, Warren Cornwall, Andrew Curry (Berlin), Ann Gibbons, Sam Kean, Kai Kupferschmidt (Berlin), Andrew Lawler, Mitch Leslie, Virginia Morell, Dennis Normile (Tokyo), Cathleen O'Grady, Elisabeth Pain (Careers), Charles Piller, Sara Reardon, Richard Stone (Senior Asia Correspondent), Gretchen Vogel (Berlin), Lizzie Wade (Mexico City) **INTERN** Alexa Robles-Gil **COPY EDITORS** Julia Cole (Senior Copy Editor), Hannah Knighton, Cyra Master (Copy Chief) **ADMINISTRATIVE SUPPORT** Meagan Weiland

CREATIVE DIRECTOR Beth Rakouskas

DESIGN MANAGING EDITOR Chrystal Smith **GRAPHICS MANAGING EDITOR** Chris Bickel **PHOTOGRAPHY MANAGING EDITOR** Emily Petersen **MULTIMEDIA MANAGING PRODUCER** Kevin McLean **DIGITAL DIRECTOR** Kara Estelle-Powers **DESIGN EDITOR** Marcy Atarod **DESIGNER** Noelle Jessup **SENIOR SCIENTIFIC ILLUSTRATOR** Noelle Burgess **SCIENTIFIC ILLUSTRATORS** Austin Fisher, Kellie Holoski, Ashley Mastin **SENIOR GRAPHICS EDITOR** Monica Hersher **GRAPHICS EDITOR** Veronica Penney **SENIOR PHOTO EDITOR** Charles Borst **PHOTO EDITOR** Elizabeth Billman **SENIOR PODCAST PRODUCER** Sarah Crespi **SENIOR VIDEO PRODUCER** Meagan Cantwell **SOCIAL MEDIA STRATEGIST** Jessica Hubbard **SOCIAL MEDIA PRODUCER** Sabrina Jenkins **WEB DESIGNER** Jennie Pajerowski

CHIEF EXECUTIVE OFFICER AND EXECUTIVE PUBLISHER

Sudip Parikh

PUBLISHER, SCIENCE FAMILY OF JOURNALS Bill Moran

DIRECTOR, BUSINESS OPERATIONS & ANALYSIS Eric Knott **MANAGER, BUSINESS OPERATIONS** Jessica Tierney **MANAGER, BUSINESS ANALYSIS** Cory Lipman **BUSINESS ANALYSTS** Kurt Ennis, Maggie Clark, Isacco Fusi **BUSINESS OPERATIONS ADMINISTRATOR** Taylor Fisher **DIGITAL SPECIALIST** Marissa Zuckerman **SENIOR PRODUCTION MANAGER** Jason Hillman **SENIOR MANAGER, PUBLISHING AND CONTENT SYSTEMS** Marcus Spiegler **CONTENT OPERATIONS MANAGER** Rebecca Doshi **PUBLISHING PLATFORM MANAGER** Jessica Loayza **PUBLISHING SYSTEMS SPECIALIST, PROJECT COORDINATOR** Jacob Hedrick **SENIOR PRODUCTION SPECIALIST** Kristin Wowk **PRODUCTION SPECIALISTS** Kelsey Cartelli, Audrey Diggs **SPECIAL PROJECTS ASSOCIATE** Shantel Agnew

MARKETING DIRECTOR Sharice Collins **ASSOCIATE DIRECTOR, MARKETING** Justin Sawyers **GLOBAL MARKETING MANAGER** Allison Pritchard **ASSOCIATE DIRECTOR, MARKETING SYSTEMS & STRATEGY** Aimee Aponte **SENIOR MARKETING MANAGER** Shawana Arnold **MARKETING MANAGER** Ashley Evans **MARKETING ASSOCIATES** Hugues Beaulieu, Ashley Hylton, Lorena Chirinos Rodriguez, Jenna Voris **MARKETING ASSISTANT** Courtney Ford **SENIOR DESIGNER** Kim Huynh

DIRECTOR AND SENIOR EDITOR, CUSTOM PUBLISHING Erika Gebel Berg **ADVERTISING PRODUCTION OPERATIONS MANAGER** Deborah Tompkins **DESIGNER, CUSTOM PUBLISHING** Jeremy Huntsinger **SENIOR TRAFFIC ASSOCIATE** Christine Hall

DIRECTOR, PRODUCT MANAGEMENT Kris Bishop **PRODUCT DEVELOPMENT MANAGER** Scott Chernoff **ASSOCIATE DIRECTOR, PUBLISHING INTELLIGENCE** Rasmus Andersen **SR. PRODUCT ASSOCIATE** Robert Koepke **PRODUCT ASSOCIATES** Caroline Breul, Anne Mason

ASSOCIATE DIRECTOR, INSTITUTIONAL LICENSING MARKETING Kess Knight **ASSOCIATE DIRECTOR, INSTITUTIONAL LICENSING SALES** Ryan Rexroth **INSTITUTIONAL LICENSING MANAGER** Nazim Mohammedi, Claudia Paulsen-Young **SENIOR MANAGER, INSTITUTIONAL LICENSING OPERATIONS** Judy Lillibridge **MANAGER, RENEWAL & RETENTION** Lana Guz **SYSTEMS & OPERATIONS ANALYST** Ben Teincuff **FULFILLMENT ANALYST** Aminta Reyes

ASSOCIATE DIRECTOR, INTERNATIONAL Roger Goncalves **ASSOCIATE DIRECTOR, US ADVERTISING** Stephanie O'Connor **US MID WEST, MID ATLANTIC AND SOUTH EAST SALES MANAGER** Chris Hoag **DIRECTOR, OUTREACH AND STRATEGIC PARTNERSHIPS, ASIA** Shoupeng Liu **SALES REP, ROW** Sarah Lelarge **SALES ADMIN ASSISTANT, ROW** Victoria Glasbey **DIRECTOR OF GLOBAL COLLABORATION AND ACADEMIC PUBLISHING RELATIONS, ASIA** Xiaoying Chu **ASSOCIATE DIRECTOR, INTERNATIONAL COLLABORATION** Grace Yao **SALES MANAGER** Danny Zhao **MARKETING MANAGER** Kilo Lan **ASCA CORPORATION, JAPAN** Rie Rambelli (Tokyo), Miyuki Tani (Osaka)

DIRECTOR, COPYRIGHT, LICENSING AND SPECIAL PROJECTS Emilie David **RIGHTS AND PERMISSIONS ASSOCIATE** Elizabeth Sandler **LICENSING ASSOCIATE** Virginia Warren **RIGHTS AND LICENSING COORDINATOR** Dana James **CONTRACT SUPPORT SPECIALIST** Michael Wheeler

EDITORIAL
science_editors@aaas.org

NEWS
science_news@aaas.org

INFORMATION FOR AUTHORS
science.org/authors/science-information-authors

REPRINTS AND PERMISSIONS
science.org/help/reprints-and-permissions

MULTIMEDIA CONTACTS
SciencePodcast@aaas.org
ScienceVideo@aaas.org

MEDIA CONTACTS
scipak@aaas.org

PRODUCT ADVERTISING & CUSTOM PUBLISHING
advertising.science.org
science_advertising@aaas.org

CLASSIFIED ADVERTISING
advertising.science.org/science-careers
advertise@sciencecareers.org

JOB POSTING CUSTOMER SERVICE
employers.sciencecareers.org
support@sciencecareers.org

MEMBERSHIP AND INDIVIDUAL SUBSCRIPTIONS
science.org/subscriptions

MEMBER BENEFITS
aaas.org/membership/benefits

INSTITUTIONAL SALES AND SITE LICENSES
science.org/librarian

AAAS BOARD OF DIRECTORS
CHAIR Gilda A. Barabino
PRESIDENT Keith R. Yamamoto
PRESIDENT-ELECT Willie E. May
TREASURER Carolyn N. Ainslie

CHIEF EXECUTIVE OFFICER
Sudip Parikh

BOARD
Cynthia M. Beall
Janine Austin Clayton
Kaye Husbands Fealing
Kathleen Hall Jamieson
Jane Maienschein
Robert B. Millard
Babak Parviz
William D. Provine
Juan S. Ramírez Lugo
Susan M. Rosenberg
Vassiliki Betty Smocovitis

BOARD OF REVIEWING EDITORS (Statistics board members indicated with **(S)**)

Erin Adams, *U. of Chicago*
Takuzo Aida, *U. of Tokyo*
Leslie Aiello, *Wenner-Gren Fdn.*
Anastassia Alexandrova, *UCLA*
Mohammed AlQuraishi, *Columbia U.*
James Analytis, *UC Berkeley*
Paola Arlotta, *Harvard U.*
Jennifer Balch, *U. of Colorado*
Nenad Ban, *ETH Zürich*
Carolina Barillas-Mury, *NIH, NIAID*
Christopher Barratt, *U. of Dundee*
Franz Bauer, *Pontificia U. Católica de Chile*
Ray H. Baughman, *UT Dallas*
Carlo Beenakker, *Leiden U.*
Sarah Bergbreiter, *Carnegie Mellon U.*
Kiros T. Berhane, *Columbia U.*
Aude Bernheim, *Inst. Pasteur*
Joseph J. Berry, *NREL*
Dominique Bonnet, *Francis Crick Inst.*
Chris Bowler, *École Normale Supérieure*
Ian Boyd, *U. of St. Andrews*
Malcolm Brenner, *Baylor Coll. of Med.*
Emily Brodsky, *UC Santa Cruz*
Ron Brookmeyer, *UCLA* **(S)**
Christian Büchel, *UKE Hamburg*
Johannes Buchner, *TUM*
Dennis Burton, *Scripps Res.*
Carter Tribley Butts, *UC Irvine*
György Buzsáki, *NYU School of Med.*
Annmarie Carlton, *UC Irvine*
Jane Carlton, *John Hopkins U.*
Simon Cauchemez, *Inst. Pasteur*
Ling-Ling Chen, *SIBCB, CAS*
Hilde Cheroutre, *La Jolla Inst.*
Wendy Cho, *UIUC*
Ib Chorkendorff, *Denmark TU*
Chunaram Choudhary, *København Fdn.*
Karlene Cimprich, *Stanford U.*
Laura Colgin, *UT Austin*
James J. Collins, *MIT*
Robert Cook-Deegan, *Arizona State U.*
Carolyn Coyne, *Duke U.*
Roberta Croce, *VU Amsterdam*
Ismaila Dabo, *Penn State U.*
Jeff L. Dangl, *UNC*
Nicolas Dauphas, *U. of Chicago*
Claude Desplan, *NYU*
Sandra Díaz, *U. Nacional de Córdoba*
Samuel Díaz-Muñoz, *UC Davis*
Ulrike Diebold, *TU Wien*
Stefanie Dimmeler, *Goethe-U. Frankfurt*
Hong Ding, *Inst. of Physics, CAS*
Dennis Discher, *UPenn*
Jennifer A. Doudna, *UC Berkeley*
Ruth Drdla-Schutting, *Med. U. Vienna*
Raissa M. D'Souza, *UC Davis*
Bruce Dunn, *UCLA*
William Dunphy, *Caltech*
Scott Edwards, *Harvard U.*
Todd A. Ehlers, *U. of Glasgow*
Tobias Erb, *MPS, MPI Terrestrial Microbiology*
Beate Escher, *UFZ & U. of Tübingen*
Barry Everitt, *U. of Cambridge*
Vanessa Ezenwa, *U. of Georgia*
Toren Finkel, *U. of Pitt. Med. Ctr.*
Natascha Förster Schreiber, *MPI Extraterrestrial Phys.*
Elaine Fuchs, *Rockefeller U.*
Caixia Gao, *Inst. of Genetics and Developmental Bio., CAS*
Daniel Geschwind, *UCLA*
Lindsey Gillson, *U. of Cape Town*
Alemu Gonsamo Gosa, *McMaster U.*
Simon Greenhill, *U. of Auckland*
Gillian Griffiths, *U. of Cambridge*
Nicolas Gruber, *ETH Zürich*
Hua Guo, *U. of New Mexico*
Taekjip Ha, *Johns Hopkins U.*
Daniel Haber, *Mass. General Hos..*
Hamida Hammad, *VIB IRC*
Wolf-Dietrich Hardt, *ETH Zürich*
Kelley Harris, *U. of Wash*
Carl-Philipp Heisenberg, *IST Austria*
Christoph Hess, *U. of Basel & U. of Cambridge*
Heather Hickman, *NIAID, NIH*
Hans Hilgenkamp, *U. of Twente*
Janneke Hille Ris Lambers, *ETH Zürich*
Kai-Uwe Hinrichs, *U. of Bremen*
Deirdre Hollingsworth, *U. of Oxford*
Pinshane Huang, *UIUC*
Christina Hulbe, *U. of Otago, New Zealand*
Randall Hulet, *Rice U.*
Auke Ijspeert, *EPFL*
Gwyneth Ingram, *ENS Lyon*
Darrell Irvine, *Scripps Res.*
Erich Jarvis, *Rockefeller U.*
Peter Jonas, *IST Austria*
Sheena Josselyn, *U. of Toronto*
Matt Kaeberlein, *U. of Wash.*
Daniel Kammen, *UC Berkeley*
Kisuk Kang, *Seoul Nat. U.*
Vedika Khemani, *Stanford U.*
V. Narry Kim, *Seoul Nat. U.*
Nancy Knowlton, *Smithsonian*
Etienne Koechlin, *École Normale Supérieure*
Alex L. Kolodkin, *Johns Hopkins U.*
LaShanda Korley, *U. of Delaware*
Paul Kubes, *U. of Calgary*
Laura Lackner, *Northwestern U.*
Gabriel Lander, *Scripps Res.* **(S)**
Mitchell A. Lazar, *UPenn*
Hedwig Lee, *Duke U.*
Fei Li, *Xi'an Jiaotong U.*
Jianyu Li, *McGill U.*
Ryan Lively, *Georgia Tech*
Luis Liz-Marzán, *CIC biomaGUNE*
Omar Lizardo, *UCLA*
Jonathan Losos, *WUSTL*
Ke Lu, *Inst. of Metal Res., CAS*
Christian Lüscher, *U. of Geneva*
Jean Lynch-Stieglitz, *Georgia Tech*
David Lyons, *U. of Edinburgh*
Fabienne Mackay, *QIMR Berghofer*
Zeynep Madak-Erdogan, *UIUC*
Vidya Madhavan, *UIUC*
Anne Magurran, *U. of St. Andrews*
Ari Pekka Mähönen, *U. of Helsinki*
Asifa Majid, *U. of Oxford*
Oscar Marín, *King's Coll. London*
Matthew Marinella, *Arizona State U.*
Charles Marshall, *UC Berkeley*
Christopher Marx, *U. of Idaho*
Geraldine Masson, *CNRS*
Jennifer McElwain, *Trinity College Dublin*
Scott McIntosh, *NCAR*
Rodrigo Medellín, *U. Nacional Autónoma de México*
Mayank Mehta, *UCLA*
C. Jessica Metcalf, *Princeton U.*
Tom Misteli, *NCI, NIH*
Jeffery Molkentin, *Cincinnati Children's Hospital Medical Center*
Alison Motsinger-Reif, *NIEHS, NIH* **(S)**
Rosa Moysés, *U. of São Paulo School of Medicine*
Daniel Neumark, *UC Berkeley*
Thi Hoang Duong Nguyen, *MRC LMB*
Helga Nowotny, *Vienna Sci. & Tech. Fund*
Pilar Ossorio, *U. of Wisconsin*
Andrew Oswald, *U. of Warwick*
Isabella Pagano, *Istituto Nazionale di Astrofisica*
Giovanni Parmigiani, *Dana-Farber* **(S)**
Zak Page, *UT Austin*
Sergiu Pasca, *Standford U.*
Julie Pfeiffer, *UT Southwestern Med. Ctr.*
Philip Phillips, *UIUC*
Matthieu Piel, *Inst. Curie*
Kathrin Plath, *UCLA*
Martin Plenio, *Ulm U.*
Katherine Pollard, *UCSF*
Elvira Poloczanska, *Alfred-Wegener-Inst.*
Julia Pongratz, *Ludwig Maximilians U.*
Philippe Poulin, *CNRS*
Suzie Pun, *U. of Wash*
Lei Stanley Qi, *Stanford U.*
Simona Radutoiu, *Aarhus U.*
Maanasa Raghavan, *U. of Chicago*
Trevor Robbins, *U. of Cambridge*
Adrienne Roeder, *Cornell U.*
Joeri Rogelj, *Imperial Coll. London*
John Rubenstein, *SickKids*
Yvette Running Horse Collin, *Toulouse U.*
Mike Ryan, *UT Austin*
Alberto Salleo, *Stanford U.*
Miquel Salmeron, *Lawrence Berkeley Nat. Lab*
Nitin Samarth, *Penn State U.*
Erica Ollmann Saphire, *La Jolla Inst.*
Joachim Saur, *U. zu Köln*
Alexander Schier, *Harvard U.*
Wolfram Schlenker, *Columbia U.*
Susannah Scott, *UC Santa Barbara*
Anuj Shah, *U. of Chicago*
Vladimir Shalaev, *Purdue U.*
Jie Shan, *Cornell U.*
Jay Shendure, *U. of Wash.*
Steve Sherwood, *U. of New South Wales*
Ken Shirasu, *RIKEN CSRS*
Brian Shoichet, *UCSF*
Robert Siliciano, *JHU School of Med.*
Emma Slack, *ETH Zürich & U. of Oxford*
Richard Smith, *UNC* **(S)**
Ivan Soltesz, *Stanford U.*
John Speakman, *U. of Aberdeen*
Allan C. Spradling, *Carnegie Institution for Sci.*
V. S. Subrahmanian, *Northwestern U.*
Sandip Sukhtankar, *U. of Virginia*
Naomi Tague, *UC Santa Barbara*
A. Alec Talin, *Sandia Natl. Labs*
Patrick Tan, *Duke-NUS Med. School*
Sarah Teichmann, *Wellcome Sanger Inst.*
Dörthe Tetzlaff, *Leibniz Institute of Freshwater Ecology and Inland Fisheries*
Amanda Thomas, *U. of Oregon*
Rocio Titiunik, *Princeton U.*
Shubha Tole, *Tata Inst. of Fundamental Res.*
Maria-Elena Torres Padilla, *Helmholtz Zentrum München*
Kimani Toussaint, *Brown U.*
Barbara Treutlein, *ETH Zürich*
Li-Huei Tsai, *MIT*
Jason Tylianakis, *U. of Canterbury*
Matthew Vander Heiden, *MIT*
Wim van der Putten, *Netherlands Inst. of Ecology*
Jo Van Ginderachter, *VIB, U. of Ghent*
Ivo Vankelecom, *KU Leuven*
Henrique Veiga-Fernandes, *Champalimaud Fdn.*
Reinhilde Veugelers, *KU Leuven*
Elizabeth Villa, *UC San Diego*
Bert Vogelstein, *Johns Hopkins U.*
Julia Von Blume, *Yale School of Med.*
David Wallach, *Weizmann Inst.*
Jane-Ling Wang, *UC Davis* **(S)**
Jessica Ware, *Amer. Mus. of Natural Hist.*
David Waxman, *Fudan U.*
Alex Webb, *U. of Cambridge*
Chris Wikle, *U. of Missouri* **(S)**
Terrie Williams, *UC Santa Cruz*
Ian A. Wilson, *Scripps Res.* **(S)**
Sylvia Wirth, *ISC Marc Jeannerod*
Hao Wu, *Harvard U.*
Amir Yacoby, *Harvard U.*
Benjamin Youngblood, *St. Jude*
Yu Xie, *Princeton U.*
Kenneth Zaret, *UPenn School of Med.*
Lidong Zhao, *Beihang U.*
Bing Zhu, *Inst. of Biophysics, CAS*
Xiaowei Zhuang, *Harvard U.*
Maria Zuber, *MIT*

Institutionalizing politicized science

Donald Moynihan *and* **Pamela Herd**

The opening months of the Trump administration represent a historic disruption to America's scientific agencies. Staff have been fired or reassigned in the name of efficiency, resulting in chaos. Grants have been canceled mid-project for featuring the wrong words. "Pauses" and "reviews" are designed to block spending, in the hope that Congress will make the current impoundment of funds a baseline for permanent disinvestment. While the scientific community waits to see what the new normal will be, the Trump administration has a plan to institutionalize a much more politicized structure of control over government broadly, including both public scientific investments and the use of scientific knowledge in policy actions.

"Schedule F" (now renamed Schedule Policy/Career) is shorthand for an executive order that is a sharp break with civil service merit principles, which assume that career employees should be retained on the basis of performance and protected against political coercion. The US is already unusual in the degree to which it reserves the top layers of organizational leadership for short-term political appointees. Schedule F will vastly expand the number of appointees, adding a proposed 50,000 from the current 4000. It does so by involuntarily reclassifying career civil servants as appointees, removing job protections, the basic constraint against political interference.

The administration says that the purpose of Schedule F is to increase accountability for civil servants involved in policy-making. Set aside the fact that civil servants are accountable in multiple ways, Trump's own justifications strike a more conspiratorial tone, including "the deep state can and must be brought to heel." But what better way to actually institutionalize a deep state than by expanding political influence over what constitutes good science?

Studies show that politicization of public services generally worsens public-sector outcomes. Public employees invest less in developing their expertise and become more likely to exit. Instability and lack of experience reduce organizational performance. Politicization increases the influence of more ideologically radical appointees relative to more moderate civil servants. Politicization also reduces accountability. Bureaucrats worried about being fired fail to share uncongenial information with their political bosses and become less likely to respond to congressional oversight. As politicization begets lower transparency and administrative capacity, it increases waste and inefficiency.

What might this mean for scientific agencies? Agencies like the National Science Foundation (NSF) and the National Institutes for Health (NIH) cannot meet their statutorily mandated scientific missions if politics, rather than scientific expertise, drive decision-making. Federally supported science has been so successful, in no small part, because agency staff are typically expert scientists beholden to ensuring that the agencies deliver world-class science. Now, many could be turned into political appointees. The proposed policy defines grantmaking positions as "policy-making," which includes "drafting of funding opportunity announcements, evaluation of grant applications, or recommending or selecting grant recipients." This definition, which neatly matches agencies' own definitions for certain career staff, would include most NIH program officers and NSF program directors.

The past few months at NIH and NSF preview how politicized scientific agencies would operate. Funding choices that reflected the consensus of some of the best scientists in the world were reversed by nonscientists. Program officers have, at points, been told not to communicate with the scientific community or have had their engagement limited. Scientific agencies have been directed to effectively reduce the flow of funds to a trickle by adding new layers of redundant review and red tape and even violating court orders to reinstate canceled grants.

Career officials in scientific agencies are unwilling hostages...

Other agencies, including regulatory agencies, apply rather than fund basic science, but the risks of politicization are no less. How confident can Americans be that federal employees will not have to choose between their job and scientific values in areas such as climate change, food safety, extreme weather forecasting, or public health?

Career officials in scientific agencies are unwilling hostages in Trump's politicization of science, wondering if they will lose their jobs for trying to defend the congressionally mandated missions of their organizations. Although the current era of layoffs will hopefully soon be over, the purpose of Schedule F is to permanently instill the degree of political control over science fueling the sense of fear that pervades those agencies now.

The federal rulemaking process allows public comment on the proposed policy until 23 May. Those with first-hand experience and knowledge of the scientific process will have particular credibility to weigh in. Such comments matter: They must be read and responded to by federal officials and can provide the basis for courts overturning new rules from the executive branch. Vannevar Bush's 1945 blueprint for America's scientific infrastructure emphasized the centrality of protecting scientific organizations from politicization. That vision has been extraordinarily successful. Schedule F assumes the opposite: It treats scientific independence as a threat to be minimized. □

Donald Moynihan is the J. Ira and Nicki Harris Family Professor of Public Policy, Gerald R. Ford School of Public Policy, University of Michigan, Ann Arbor, MI, USA. dmoyn@umich.edu **Pamela Herd** is the Carol Kakalec Kohn Professor of Social Policy, Gerald R. Ford School of Public Policy, University of Michigan, Ann Arbor, MI, USA. pherd@umich.edu

Published online 8 May 2025; 10.1126/science.ady6128

Kate Starbird has weathered right-wing attacks on her digital misinformation research for years.

PHOTO: JOVELLE TAMAYO/*THE WASHINGTON POST* VIA GETTY IMAGES

U.S. SCIENCE

With Trump's cuts escalating, 'fear factor' silences researchers

Many worry about retribution. But for others, speaking out is worth the risk

WARREN CORNWALL

In February, shortly after U.S. President Donald Trump was inaugurated, Rebekah Tromble launched a program to advise scientists and journalists targeted for intimidation and harassment. But she announced it quietly, fearing the very kind of attacks the initiative was meant to counter. "We were truly concerned that trying to draw too much attention to our work would jeopardize our funding," says the George Washington University social scientist. "It's a bit counterintuitive for a program that is actually trying to reach and help people."

Tromble's paradoxical situation is emblematic of the fear and self-censorship coursing through the nation's scientific establishment today. As the Trump administration fires swaths of government researchers, cancels scientific grants, and targets leading universities with punishing funding freezes, scientists who might once have welcomed public attention for their work or spoken up on issues affecting their field are instead opting for silence.

"The lived experience of a scientist right now is terrifying," said one prominent health researcher who asked not to be named out of concern their funding would be targeted. "We love getting our research in *The New York Times* and *Science*. You can imagine how much fear is involved if we are saying 'no.'"

Interviews with science advocacy groups and scientists working in a range of disciplines confirm that what Jen Jones, director of the Center for Science and Democracy at the Union of Concerned Scientists, calls "the fear factor" is rampant. Scientists "have been made to feel like they cannot open their mouth for fear of losing whatever they have left," she says.

Jones sees it as an escalation of tactics already on display before Trump returned to the White House. She points to billionaire Elon Musk, enlisted by Trump to lead a campaign to shrink federal spending, who used his massive following on his social media platform, X, to target midlevel government officials, including scientists who would normally go unnoticed. "Trump and Musk have spent years perfecting their campaign of fear and intimidation," Jones says. Well before the election, Tromble conceived her program in response to that mounting threat.

Now, the rhetoric is coupled with control of the vast levers of government, which the new administration has swiftly used to cut funding for specific research projects and institutions. Since Trump's inauguration, the two premier federal science funding agencies, the National Science Foundation (NSF) and the National Institutes of Health (NIH), have together canceled more than 2000 grants totaling more than $1.5 billion.

White House spokesperson Kush Desai told *Science* in a statement that "the Trump administration is spending its first few months reviewing the previous administration's projects, identifying waste, and realigning our research spending to match the American people's priorities and continue our innovative dominance." NSF declined to answer questions about whether agency officials have heard from scientists afraid of retribution, or whether they were concerned such fears might affect open discussions about research. NIH did not respond to a request for comment.

Although fields such as climate science and public health faced political attacks before this year, U.S. scientists of many stripes now feel at heightened risk, says Janice Lachance, CEO of the American Geophysical Union (AGU), which has nearly 60,000 members working in earth and space science. Some researchers have asked the organization to scrub their names from its public list of committee volunteers because of concern that being identified for their work might make them vulnerable to retribution. Others have demurred when AGU officials asked to share their stories of funding cuts with congressional staff trying to document impacts on active research projects.

Even scientists accustomed to controversy and the public spotlight acknowledge the fear factor. The threats are "so vast and capricious," says Gregg Gonsalves, a Yale University epidemiologist and veteran of political struggles around AIDS research going back to the 1980s. "As I'm sitting here talking to you, I realize it's not without its risks."

Gonsalves was one of nearly 900 Yale faculty who signed an April letter calling on the university to resist any threats to academic freedom. He says many scientists worry their institutions won't support them if they speak out. "They are very worried about whether their colleagues, universities, institutions have their back." Lachance agrees, noting, "Scientists are seeing some major institutions—some very powerful private sector entities—proceeding with caution."

Several senior scientists who asked not to be named said that even if they could weather any damage, they keep quiet because they worry about the impact of a lost grant on Ph.D. students, laboratory staff, and others. "It's all the people who depend on you," said a health science professor who asked not to be named.

There are signs that scientists are starting to feel emboldened. Gonsalves points to Harvard University's resistance to demands from the Trump administration as a watershed moment. In April, Harvard President Alan Garber sent a letter to administration officials vigorously rejecting a list of demands for federal oversight of university operations. Harvard has since sued to overturn a federal funding freeze on more than $2.2 billion in research grants imposed by the administration—which has now cut off all future grant funding to the university.

At 62, Gonsalves says he has concluded that any price he pays for speaking out is outweighed by the toll the current administration is taking on the future of scientists and research in the United States. "It's the next generation we have to protect and care about," he says. "That's what keeps me going."

Scientists might also be realizing that there's little safety in silence, says Kate Starbird, a University of Washington computer scientist who for years has been targeted by right-wing activists and some Republican members of Congress for her work on digital misinformation. At a recent conference on computer-human interaction hosted by the Association for Computing Machinery, she met scientists whose NSF grants had been canceled even though their research had no obvious connection to conservative hot-button issues. "I just don't know [that] there's a lot of wisdom in keeping our heads down anymore," says Starbird, who has been outspoken for years. "I never had the option of keeping my head down."

Tromble decided to be more vocal as well after NSF canceled funding for the final year of a 3-year, $5 million grant to study online harassment of experts and design a system to help people who are targeted. "The big risk for us was losing the funding, and now we've lost the funding," Tromble says of her earlier decision to keep a low profile. She is now discussing her research more openly and working to raise philanthropic money to help maintain Expert Voices Together, the program launched in February.

Starbird hopes others will feel emboldened. She fears the scientific community is in danger of missing the chance to shape public perceptions about what the new administration is doing to U.S. research—and she's taking lessons from her own experience. After the 2020 presidential election, she and fellow researchers were accused of conspiring to censor right-wing claims that the election was stolen from Trump. At first, they decided to ignore the false charges—a missed chance to push back against them before they metastasized, she says. Four years later, she says, "I think we are at risk of missing the golden window." □

TRUMP TRACKER

DISASTER DATABASE SUSPENDED The National Oceanic and Atmospheric Administration (NOAA) will no longer update its influential database of billion-dollar weather and climate disasters in the United States, the agency announced last week, citing "evolving priorities, statutory mandates, and staffing changes." The database has been a frequent target of Republicans, who have claimed it has scientific and methodological flaws. It shows a rise in disasters since 1980, likely driven largely by population growth and migration; it has not attributed disasters to climate change. Adam Smith, the NOAA researcher who led the work, recently left the agency, saying in a LinkedIn post last week that he soon hopes to "revisit and refresh the analysis with new data, tools, and context" at a new organization.

TALLYING NIH CUTS President Donald Trump's administration has so far canceled at least $1.8 billion in National Institutes of Health (NIH) grants, $544 million of which had not already been spent, according to an analysis published last week in *JAMA*. The authors used records from the Department of Health and Human Services's (HHS's) Tracking Accountability in Government Grants System. Between 28 February and 8 April, 694 NIH grants were canceled, including 400 research project grants, they found. Among NIH's 27 institutes and centers, the National Institute on Minority Health and Health Disparities saw the greatest cut (29.6%) as a proportion of its previous grant funding.

SURGEON GENERAL PICK Trump last week nominated a new surgeon general candidate: Stanford University–educated ear, nose, and throat surgeon Casey Means, who left her residency to become a health influencer and wellness entrepreneur. Means replaces Trump's earlier pick, Janette Nesheiwat, whose nomination foundered on evidence of résumé fabrications. Trump praised Means's "impeccable MAHA [Make America Healthy Again] credentials," referring to HHS Secretary Robert F. Kennedy Jr.'s focus on chronic disease treatment and prevention. But Kennedy has already been forced to defend Means against a wave of criticism from the conservative camp: Influential right-wing voice Laura Loomer called Means "a total crackpot" and other opponents have argued she hasn't sufficiently come out against vaccines. The Senate must confirm the nominee.

U.S. SCIENCE POLICY

Trump takes steps toward a radically different NSF

Democrats question latest changes in how the research agency makes grants **JEFFREY MERVIS**

Smaller. Cheaper. More constrained. That appears to be the vision for the National Science Foundation (NSF) that is emerging from an unprecedented series of changes by President Donald Trump's administration, including moves last week to restructure the organization and transform how it awards grants.

The changes would result in a shrunken NSF that focuses on a handful of fields seen as economic drivers rather than supporting basic research across all disciplines. Its process of choosing what to fund would no longer rely heavily on scientists on leave from their universities, bringing with them fresh ideas on how to invest in cutting-edge science. And NSF would care less about finding the "missing millions," NSF's phrase for increasing the diversity of the country's scientific workforce.

Trump is a long way from achieving that vision for the country's second largest funder of science. But last week's restructuring comes on top of previous steps that have halted new awards, terminated existing grants, and reduced the agency's 1700-person staff. The administration has also called for slashing NSF's overhead payments to universities, and shrinking its $9 billion budget by more than half.

NSF officials have been largely silent about the larger significance of the changes. And its presidentially appointed oversight body, the National Science Board, so far has not commented on any of them, although one member, Alondra Nelson, resigned this week. And though individual scientists have expressed alarm about the turmoil at the agency, the sharpest public criticism to date has come from a handful of Democrats in Congress, who think the changes are misguided and will harm NSF and the U.S. research enterprise.

"Mere months ago, each of these individual decisions would have been an unprecedented shock," a dozen members of the science committee in the House of Representatives that oversees NSF wrote in an 8 May letter to Brian Stone. He has been NSF's acting director since the abrupt resignation last month of Sethuraman "Panch" Panchanathan, a Trump appointee. "President Trump has made this chaos and destruction commonplace. However, we refuse to accept this as our new reality."

A 9 May memo obtained by *Science* from NSF's chief management officer, Micah Cheatham, describes some of the changes. *Science* has learned about others from sources inside and outside the agency who requested anonymity because they feared reprisal.

> "So, who is in charge here? ... How far does DOGE's influence reach?"
>
> **Democratic lawmakers**
> U.S. House of Representatives

The United States's second largest research funder is facing strong political winds.

One major change would abolish NSF's current 37 divisions, spread across eight directorates, which distribute funding to researchers in a wide range of fields, from the social sciences to physics. Those divisions would be replaced by clusters that would focus on five areas: artificial intelligence, quantum information science, biotechnology, nuclear energy, and translational science.

Last week, NSF preemptively eliminated one of those divisions within the education directorate, on equity for excellence in science, technology, engineering, and math, and fired its entire staff, believed to number between 15 and 20. However, on 12 May NSF rescinded both moves after a federal judge temporarily blocked the White House from laying off workers at several agencies in a suit brought by a labor union representing federal employees.

"The focus on a few areas is gravely concerning," says Suzanne Ortega, who leads the Council of Graduate Schools. "The basic, curiosity-driven science that has paid off so handsomely for the country over the decades doesn't necessarily start in one of those fields. And the idea that the insights of social scientists aren't important in understanding today's world and our political adversaries is just ridiculous."

A second change dramatically reduces NSF's roster of employees on loan from universities for stints of 1 to 4 years. The number of such positions, called rotators, would drop by 81%, from 368 to 70. The surviving positions would be distributed across the five priority areas and filled by existing rotators "to the maximum extent possible," Cheatham said in his memo.

A third major disruption to the status quo is the termination of existing grants. In the past month, NSF has pulled the plug on more than 1400 awards, amounting to a loss of more than $1 billion in promised funding.

The education directorate has been hit hardest. The terminations include grants from several programs mandated by Congress, notably the 34-year-old Louis Stokes Alliances for Minority Participation and the Eddie Bernice Johnson INCLUDES Initiative to broaden participation in science and engineering, which began in 2011. The Trump administration apparently saw both programs as violating a presidential directive on diversity, equity, and inclusion (DEI) that bans funding for any research that favors one demographic group or excludes participation by some groups.

The grant terminations have disproportionately affected principal investigators (PIs) from groups traditionally underrepresented in science—notably women, racial and ethnic minorities, and those with disabilities—according to data collected by NSF. Women are PIs on 58% of the canceled grants, although they are PIs on only 34% of all active NSF grants.

PHOTO: E. BILLMAN/*SCIENCE*

Similarly, Blacks are PIs on 17% of the terminated grants, although they make only 4% of the total pool. Hispanic PIs and those with disabilities were twice as likely to lose a grant.

All the recent moves are consistent with Trump's request to Congress this month to shrink the agency's budget by 55%, to $4 billion, for the 2026 fiscal year that starts on 1 October. So is NSF's plan to reduce by 60% the number of administrators classified as senior executive service (SES) employees, who earn salaries much higher than the regular federal pay scale. NSF's current roster of 143 SES positions will plunge to 59, according to Cheatham's memo, a number it says is commensurate with NSF's "new organizational structure and proposed future budgets."

NSF's decision to abolish its divisions also appears to be part of a larger restructuring of the agency's grantmaking process that would add a new layer of review. Currently, for all but the biggest grants, the final step in the award process is for a division director to concur with a recommendation made by a program officer, based in part on input from review panels. (The NSF system differs from the one used by the National Institutes of Health, where advisory councils for each institute have the final say and proposals are typically funded based on scores assigned by a review panel.)

Last week, NSF staff were briefed on the new process for vetting proposals. Those that are highly recommended, but modestly out of step with the DEI directive, could gain final approval after tweaks, according to a slide presentation obtained by *Science*. But proposals seen as having more serious flaws would be declined without additional comment. And even proposals that get a green light from a division director would be screened by a new body, whose membership has not been determined.

Science advocates fear the additional review could be a mechanism to force NSF to fund only research that suits the ideological bent of the Trump administration. And Democrats on the House science committee suspect NSF is already feeling that pressure.

"So, who is in charge here?" they wrote to Stone. "How much is [the White House budget office] dictating decisions based on hard-right political ideology and not scientific or research expertise?" And in a reference to billionaire Elon Musk and his team at the Department of Government Efficiency, the legislators ask pointedly: "How far does DOGE's influence reach?"

The legislators could soon get a chance to ask those questions in person if, as has long been the tradition, House and Senate panels summon NSF officials to testify on the administration's budget request. □

IN FOCUS

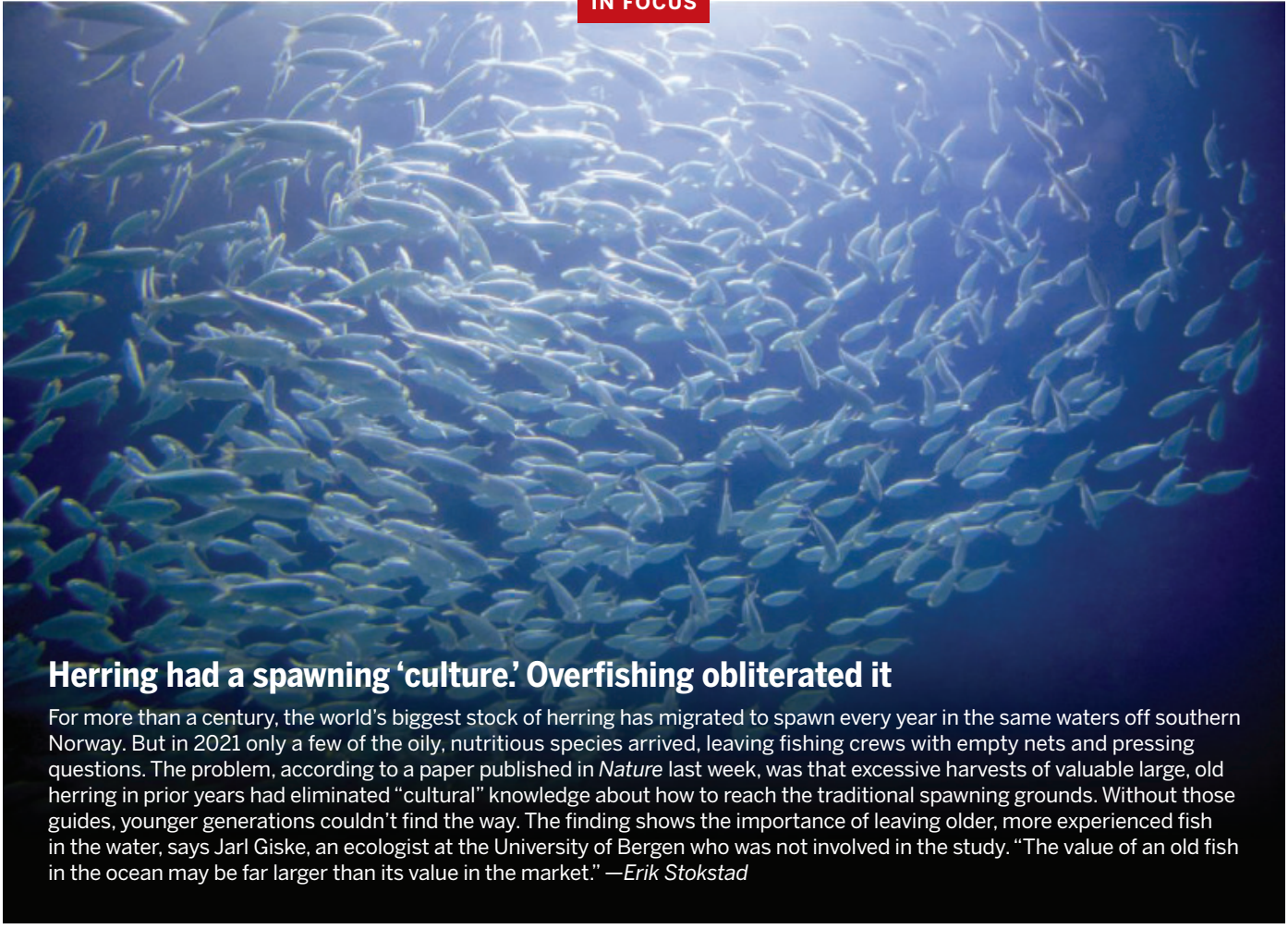

PHOTO: PICTURE PARTNERS/SCIENCE SOURCE

Herring had a spawning 'culture.' Overfishing obliterated it

For more than a century, the world's biggest stock of herring has migrated to spawn every year in the same waters off southern Norway. But in 2021 only a few of the oily, nutritious species arrived, leaving fishing crews with empty nets and pressing questions. The problem, according to a paper published in *Nature* last week, was that excessive harvests of valuable large, old herring in prior years had eliminated "cultural" knowledge about how to reach the traditional spawning grounds. Without those guides, younger generations couldn't find the way. The finding shows the importance of leaving older, more experienced fish in the water, says Jarl Giske, an ecologist at the University of Bergen who was not involved in the study. "The value of an old fish in the ocean may be far larger than its value in the market." —*Erik Stokstad*

ENVIRONMENT

Project to revive Louisiana coastline runs aground

Politics and lawsuits imperil plans to divert the Mississippi River to build new land

WARREN CORNWALL

On a steamy August morning in 2023, Louisiana officials gathered near swampy Barataria Bay to break ground on what was meant to be the $3 billion centerpiece of the campaign to save the state's shrinking coastline.

Then-Governor John Bel Edwards, a Democrat, hefted a symbolic shovel full of dirt to mark the beginning of a 3.5-kilometer-long canal designed to siphon precious land-building mud from the Mississippi River to the sediment-starved bay. "Today will be remembered as a critical turning point for Louisiana's coast," Edwards declared.

Yet nearly 2 years later, one of the nation's most ambitious ecological restoration projects, hailed as a model of how to reverse coastal land loss, is at a standstill. It is embroiled in lawsuits and political wrangling, fueled in part by the complex environmental impacts of diverting much of the Mississippi's flow. The most recent blow came in late April, when the U.S. Army Corps of Engineers suspended a critical construction permit after the current governor claimed Edwards had covered up a report on those impacts.

"The project is as close to being dead as it's ever been," says Charles Sutcliffe, a Louisiana-based policy adviser to the National Wildlife Federation who, as a state official, helped shepherd the project through the administrations of Edwards and his predecessor, Republican Bobby Jindal.

Many national and state environmental groups had hailed the project, known as the Mid-Barataria Sediment Diversion, as a way to revive the state's ailing coast, which loses the equivalent of 10 city blocks of coastal wetlands every day as they erode and sink under their own weight. A major reason is that dams and levees have straitjacketed the Mississippi, trapping sand and mud that would have replenished watery coastal land.

The diversion was predicted to reverse that trend in Barataria Bay, a maze of marshland and open water some 40 kilometers south of New Orleans that teems with wildlife. By 2070, the Army Corps estimated it would build roughly 54 square kilometers of land.

From the start, however, local officials and commercial fishers objected that the diversion would exacerbate flooding in communities along the river's final kilometers and that the flush of river water would lower salinity levels in the bay, destroying valuable shrimp and oyster fisheries. Those concerns gained a sympathetic ear when Jeff Landry, a Republican, moved into the governor's office in 2024. At a state legislative hearing in November 2024, Landry warned the project's side effects would "break our culture." In early April, his administration ordered a 90-day pause on construction work.

Then, in late April, Landry announced in social media posts that Edwards "hid reports" from the Army Corps that showed the diversion could require $50 million a year in dredging, starve fish of oxygen, and impact drinking water. "This project is like a John Grisham novel, a real-life 'Pelican Brief,'" Landry wrote, likening it to the best-selling thriller featuring assassinations and a Louisiana oil project that threatens wildlife. Edwards responded on Facebook that Landry's claims were "flat out wrong."

The disputed study is a 500-page technical document prepared in 2022 by a private environmental consulting firm for the Coastal Protection and Restoration Authority

No exit

In 2023, Louisiana began construction on a diversion that was set to channel part of the Mississippi River's flow into Barataria Bay. The project, which estimates suggest would have built 54 square kilometers of land by 2070 in an area with shrinking wetlands, is now at a standstill.

CREDITS: (GRAPHIC) M. HERSHER/*SCIENCE*; (DATA) NATIONAL LEVEE DATABASE; (IMAGE) © PLANET LABS PBC

(CPRA), the state agency overseeing construction of the diversion. Later versions of the report were sent to the Army Corps, but did not pass on some information in the earlier draft, according to a letter to CPRA from Col. Cullen Jones, commander of the Army Corps office in New Orleans.

Plaquemines Parish, the local government for the area, had already sued to block the project, and Landry's claims deepen its concerns, says parish attorney Rennie Buras. "The Parish now has additional concerns that CPRA withheld crucial data from the US Corps of Engineers and the public as well," Buras wrote in an email to *Science*.

Edwards, meanwhile, has said the report's findings were shared with the Army Corps in 2022, but the agency "determined that the information and data were not relevant" for the diversion approval process. The report looked at what might happen under "worst-case" scenarios, such as long periods of low river flows and buildup of sediment in the diversion channel, Edwards noted in a 6 May letter to the Army Corps. Because of that, it didn't give a complete picture of how the project would perform.

Jones had earlier agreed with Edwards's assessment of the report. In a letter to a state official at the end of March, he wrote that although the document should have been given to the agency earlier, its contents would not have affected the permit.

But Jones reversed course in late April, following a meeting with two Landry appointees. In a 25 April letter, Jones said the Army Corps was suspending the main federal permit for the construction, citing the report and other factors, such as claims by the state that it might not be able to afford the necessary dredging.

Although the latest twist imperils the diversion project, it's not clear whether the blow will be fatal, or what might take the project's place. The main source of its funding was to be compensation from energy giant BP for the 2010 *Deepwater Horizon* oil spill, which coated parts of Barataria Bay in oil. In October 2024, federal officials overseeing much of that money warned that if the diversion project is canceled, the state might need to pay back $500 million already spent. "No other single restoration project has been planned and studied as extensively over the past decades," the officials wrote in a letter to CPRA.

Other options, such as proposals to build a smaller diversion or dredge sediment from elsewhere and dump it in the bay, have been floated, notes Ehab Meselhe, a Tulane University water resource engineer and an expert on modeling coastal Louisiana water dynamics. "Probably there are options that have the least objections from people and maybe that's what they should do," Meselhe says. "Because waiting is not good either. As we discuss, as we continue to deliberate, the coast is vanishing." □

IMAGE: KARENA YAN/NABLA BIO

DRUG DEVELOPMENT

AI-designed antibody candidates hit a crucial target

Companies find enticing drug leads that bind to tricky cell membrane proteins

An engineered antibody (orange) binds to the outer portion of a cell membrane protein (green).

ROBERT F. SERVICE

Roughly one-third of all U.S. Food and Drug Administration–approved medicines, with collective annual sales of nearly $200 billion, target a single family of cell membrane proteins, called the G protein–coupled receptors (GPCRs), which deliver chemical messages in and out of cells. A growing number of the drugs are antibodies, which can lock tightly to specific proteins. But GPCRs are a tough target to hit, even for antibodies, because they barely protrude beyond the cell membrane.

Increasingly, antibody designers are using artificial intelligence (AI) to take aim. Researchers at Nabla Bio, a Massachusetts-based biotech company, report this week that their new AI has, in a matter of months, conjured up dozens of GPCR-targeting antibody candidates, which promise to work as well as drugs that have spent years in the traditional pipeline. One marks a first for an AI-designed protein: It can turn on cell membrane signaling rather than blocking it.

"If the results are solid, it's a breakthrough," says Wei Wang, a biochemist at the University of California San Diego. David Baker, a protein design expert at the University of Washington and co-founder of Xaira Therapeutics, a California-based antibody design startup, says it's an example of how quickly the field is accelerating. "It's a very exciting time," Baker says.

Antibodies, like all proteins, consist of chains of amino acids that fold up into fantastically complex 3D shapes, which govern what they bind to. In the body they block pathogens from entering cells or tag diseased cells for the immune system. But they can also be used to block disease-related proteins or deliver drugs that are attached as payloads. More than 160 engineered antibodies are approved for treating cancer, infections, and immune-related diseases. And with thousands of new versions in development, the market is expected to balloon to $455 billion a year by 2028, according to a 2022 analysis in *Antibody Therapeutics*. As Baker puts it, "Antibodies are the coin of the realm for the pharmaceutical industry."

But designing antibodies is laborious. Candidates typically go through multiple rounds of improvements to ensure they have all the properties of good drugs, such as the ability to dissolve in bodily fluids and a specificity that prevents them from binding to unwanted sites and causing side effects. AI represents a way to speed up the discovery process. "Now, you can build all those [properties] in from the beginning," Baker says.

An early example of the promise came in November 2024, when researchers led by Surge Biswas, Nabla Bio's CEO, reported that their AI discovered antibodies that bind to CXCR7, one in the family of some 800 GPCR membrane proteins. That was an accomplishment, Biswas says, but the AI's creations were "not that competitive with traditional antibodies."

To improve its designs, the Nabla team tweaked its AI approach, borrowing an idea known as "test-time scaling," a process of reasoning and iteration that OpenAI developed for its large language model ChatGPT. The AI begins by generating multiple proposed solutions to

a problem, then sifts them through multiple reasoning steps until a final answer is produced. Now, Biswas says, "We're bringing this idea to biology for the first time."

Better results followed quickly. In a preprint posted on 12 May on the company's website and expected soon on the bioRxiv server, the Nabla Bio team reports its AI designed tens of thousands of GPCR-binding antibodies. Lab studies showed dozens of them had "affinities"—a measure of their binding strength—as high or higher than existing antibody drugs that took years to develop. For example, some could target CXCR7 while not affecting a closely related membrane protein called CXCR4, a level of discrimination most GPCR drugs struggle with.

But perhaps most impressive among the leads was one that didn't block its target, but instead turned it on. "If you have the ability to turn [GPCRs] on or off, you basically can control cellular biology and the disease state," Biswas says. The AI was able to learn from that single surprise success to create hundreds more candidates that flick switches on.

"That's impressive if it's validated," says Andrew Bradbury, chief scientist at Specifica, a biotech company that designs antibody libraries for pharma companies. When it comes to AI antibody drug design, he says, "there is a lot of froth and a lot of money."

But AI is proving adept at designing antibodies aimed at other targets. In February, Baker and his colleagues reported the AI-aided discovery of antibodies that bind to an influenza protein common to all strains, an achievement that could open the way to a universal flu drug. The team also reported antibodies that block a potent toxin produced by the bacteria *Clostridium difficile*, a common and deadly hospital-acquired infection.

Last fall, researchers at Absci, a biotech firm based in Washington state, reported designing the first antibody capable of binding to a protein target on HIV known as the caldera region. The region exists in all HIV strains, meaning it could lead to an all-purpose antibody drug against HIV. The company is also designing antibodies to treat endometriosis, inflammatory bowel disease, and even hair loss, says company co-founder Sean McClain.

The progress "is incredible," McClain says. With so many possible antibody targets and therapies, there's room for all of the companies now jumping in, McClain says. "It takes a village." □

THEY SAID IT

For me, the answer now lies in refusal, the withdrawal of participation from systems that require dishonesty as the price of belonging.

Alondra Nelson, sociologist at the Institute for Advanced Study, in *Time*, on why she is resigning from government bodies including the National Science Board, which oversees the National Science Foundation.

INFECTIOUS DISEASE

Mosquito-borne viral disease sweeps Indian Ocean islands

Safety issues with the only available vaccine are complicating the response to chikungunya **MEREDITH WADMAN**

Twenty years ago, when the painful viral disease chikungunya exploded on the Indian Ocean island of Réunion and sickened hundreds of thousands, doctors longed for a vaccine. Now, the virus is surging again, causing nearly 50,000 confirmed cases and 12 deaths on the island, a French department, and spreading on neighboring islands including Mauritius. This time a vaccine called Ixchiq, made by Valneva, is available. But safety problems have cropped up, and on 7 May, the European Medicines Agency (EMA) suspended the vaccine's use in people 65 years and older after two deaths and multiple serious adverse events. On 9 May, U.S. regulators followed, recommending a pause in the vaccine's use in people 60 and older.

The outbreak on Réunion may be showing signs of ebbing. But need for the vaccine will persist, as the virus is expected to spread beyond the Indian Ocean, imported with travelers returning from that region. Tulio de Oliveira, director of the Centre for Epidemic Response and Innovation (CERI) at Stellenbosch University, notes, "There's a special concern when summer is starting in Europe and there is higher susceptibility for chikungunya transmission." Authorities in France have identified 766 imported cases since January, when the epidemic began, 97% of them in travelers returning from Réunion.

Caused by a virus transmitted by *Aedes aegypti* and *A. albopictus* mosquitoes, chikungunya causes fever, excruciating joint pain, headache, joint swelling, and rash. People usually recover within a week, but some develop heart and brain inflammation, and severe pain can last for months and even years. (The word means "disease that bends up the joints" in Kimakonde, an East African language.) It is endemic in parts of Latin America and Asia, and across central Africa in a belt that extends to the Indian Ocean islands, where warm, wet conditions are especially hospitable to the mosquitoes that transmit the virus.

The disease exploded on Réunion in 2005–06 after the virus acquired a mutation in its envelope gene that is thought to make it more readily transmitted by *A. albopictus*, also known as the

The viral disease chikungunya has led to hundreds of hospitalizations on the island of Réunion.

PHOTO: RICHARD BOUHET/AFP VIA GETTY IMAGES

Asian tiger mosquito, which predominates on Réunion. The virus causing the new outbreak "evolved a bit [since 2005–06], but the circulating lineage now still carries [that mutation]," Muriel Vincent, an epidemiologist on Réunion with Public Health France, said at a World Health Organization (WHO) webinar on 7 May. "We assume that's why we saw such an explosive circulation."

Houriiyah Tegally, a bioinformatician who is head of data science at CERI, believes there is another factor. "It's been a really long time now, 20 years" since the last big outbreak, enough time for an entire generation of young people to be born without immunity to the virus, Tegally says. She adds that French people and other Europeans often retire to Réunion, providing another population of immunologically naïve people.

The new vaccine promised to help stem the spread. Made of a live, weakened version of the virus, Ixchiq was approved for those ages 18 and older in 2023 by the U.S. Food and Drug Administration (FDA). Since then, regulators in the European Union, Canada, and the United Kingdom have followed suit. Last month, it was approved for those ages 12 to 17 in the EU.

But six reports of serious adverse events to a U.S. vaccine monitoring system led a U.S. Centers for Disease Control and Prevention (CDC) advisory committee to recommend on 16 April that the vaccine be used with caution in people 65 years and older. The problems became clearer in recent weeks as Réunion launched an emergency vaccination campaign with a priority, according to a Valneva press release, on older, more at risk adults. But a global total of 17 serious adverse events, including two deaths, have alarmed EMA. "Ixchiq must not be used in adults aged 65 years and above" or in people with weakened immune systems, EMA wrote, saying the halt is a temporary measure while it conducts an in-depth review. The recommendation followed a similar one made by the French vaccine regulatory agency on 25 April, which stopped the administration of vaccines to those in that age group on Réunion. FDA also said it would conduct a new risk-benefit analysis for people 60 and older.

The adverse events in the elderly are "pretty big news [but] not so surprising," says David Hamer, an infectious disease physician at Boston University who is surveillance lead for GeoSentinel, an infectious disease surveillance network. In people with weak immune systems because of age or immunosuppression for other reasons, a live weakened virus vaccination "may not be … safe," he says.

In a press release last week, Valneva asserted that all those affected by adverse events had "significant underlying medical conditions and/or co-medications." EMA noted that the two deaths, both on Réunion, occurred in an 84-year-old man who developed brain inflammation and a 77-year-old man with Parkinson's disease.

But the vaccine's limitations worry public health experts. "The age range for which it's approved and the safety concerns are limiting the ability to use the vaccine in people at highest risk of severe disease," says Philip Krause, a physician and former vaccine regulator with FDA who participated in a recent WHO consultation on chikungunya vaccines. Very young children and the elderly are most vulnerable to the disease. For instance, of about 70 patients hospitalized with severe disease on Réunion, 23 were infants less than 3 months old.

Meanwhile, the virus remains a threat beyond Réunion. The last Réunion outbreak also traveled to India, where it infected an estimated 1.4 million people. Hamer says his surveillance network is now picking up cases in travelers returning from Sri Lanka.

With the arrival of cooler weather in the Southern Hemisphere, the number of cases on Réunion may be on the decline, Vincent said during the 7 May webinar. The average of 20,000 weekly cases reported by family medicine clinics (though not necessarily confirmed with genetic testing) in recent weeks fell to 14,000 in the week that ended on 4 May, she said. Since the epidemic was declared in January, there have been about 174,000 such cases.

Hamer says a tailing off wouldn't be surprising. "The natural history of these outbreaks, especially on an island, is they blast through in a very short period of time and fade away." □

IN OTHER NEWS

Base editing helps baby

In what may be a world first, researchers helped a sick baby boy with an ultrarare, life-threatening disease by developing a gene editor tailored to his mutation. The boy has severe carbamoyl phosphate synthetase 1 (CPS1) deficiency; he lacks an enzyme the liver needs to create harmless urea from ammonia, produced by the breakdown of proteins. Without treatment and a special diet, ammonia would accumulate in his blood and damage organs. Soon after he was born with mutations in both CPS1 genes, researchers at the Children's Hospital of Philadelphia and Penn Medicine raced to tailor and test a form of CRISPR known as a base editor in cells and lab animals. It targets the one-letter typo in one of the boy's CPS1 copies. The team then infused fat particles carrying RNA encoding the editing tools into the 7-month-old. After three doses, he can consume more protein and needs less medication, the researchers reported this week at the annual meeting of the American Society of Gene & Cell Therapy in New Orleans and in *The New England Journal of Medicine*. The team hopes to use such bespoke base editors to treat more babies with rare metabolic disorders. —*Jocelyn Kaiser*

TRUMP ADMINISTRATION

Executive order on risky research brings confusion

Directive aims to restrict gain-of-function studies on microbes and more, but no one knows what's affected

KAI KUPFERSCHMIDT

On 6 May, new rules governing risky research on certain human toxins and pathogens such as viruses and bacteria were supposed to go into effect in the United States, 1 year after they had been announced. The regulations were specifically meant to clarify federal oversight over experiments in which scientists may deliberately or unintentionally give pathogens new capabilities, so-called gain-of-function (GOF) research.

But instead, the evening before the policy would have begun, President Donald Trump signed an executive order instructing the Office of Science and Technology Policy (OSTP) at the White House to draw up new, stricter rules for the controversial studies within 120 days. The order, accompanied by a fact sheet citing Trump's belief that GOF research led to COVID-19 and could produce future pandemics, promises more transparency on such work, stiffer penalties for scientists who violate the rules, and a ban on federal funding for such studies in countries of concern, such as China. But the immediate impact of the new order was confusion.

> "Everyone is trying to figure out what this means."
>
> **Gigi Gronvall**, Johns Hopkins University

"Everyone is trying to work out what exactly this means," says Gigi Gronvall, an immunologist and biosecurity expert at Johns Hopkins University who, like others, was unclear whether the order meant an immediate pause on all GOF research funded by the National Institutes of Health (NIH) or other federal entities, including the military.

Researchers who fear a lot of GOF research carries more risks than benefits welcomed Trump's order. But many others worry the administration's definition of GOF is vague and overly broad, meaning it could ensnare pathogen or toxin studies that have low risk but high potential benefits. (Very few U.S.-funded studies need extra federal review under the current, narrower GOF criteria.)

Given Trump's willingness to threaten or cut federal research funding to reshape U.S. science, the policy outlined in the new executive order could create a chill on legitimate research into viruses, bacteria, and other microbes, says Gregory Koblentz, a biodefense expert at George Mason University. "There is a high likelihood that research institutions will simply curtail such research for fear of running afoul of poorly worded policies and regulations that would impose draconian penalties on the institution," he says.

GOF research has long been a difficult issue for policymakers. Since 2020, it has become a hot button political issue as Trump and other politicians have claimed U.S.-funded GOF research at a Chinese lab led to the leak of the virus that causes COVID-19.

U.S. efforts to regulate risky pathogen research started after envelopes containing anthrax powder were sent to U.S. politicians and media in 2001, killing five people. The U.S. government adopted a policy on "dual-use research of concern" that listed seven types of experiments on certain high-risk pathogens that needed additional oversight, such as work that increases a pathogen's virulence or shows how to make vaccines against it ineffective.

In 2017, an additional framework was adopted for GOF research on the most dangerous class of microorganisms, those deemed most likely to lead to a pandemic. Experiments that could be "reasonably anticipated" to make such "potential pandemic pathogens" more transmissible or more virulent needed to undergo an extra layer of federal review under the framework. That has only been done for four projects, two of which went ahead. (Both have since ended.)

In May 2024, the Biden administration released a new set of tighter rules expanding the range of pathogen and toxin experiments that needed additional review. Universities had been preparing for those rules to go into effect ever since, developing institutional policies, creating guidance documents, and training staff to implement the new policy, says David Gillum, a biosafety expert at the University of Nevada, Reno. But in his executive order, Trump said Biden "allowed dangerous gain-of-function research within the United States with insufficient levels of oversight."

Trump's order lays out the broad outlines of the new GOF policy due within 120 days. They include requiring institutions that receive federal funding to publicly disclose all GOF research—including even, "to the maximum extent permitted by law," privately funded work—and punishing researchers who violate the rules with immediate revocation of their federal funding and a ban on additional funding for up to 5 years. The order also says the policy must better regulate companies or others selling synthetic nucleic acids, so their orders, for example, can't help create deadly pathogens from scratch.

One question is whether any U.S. research needs to be halted right away. The White House fact sheet stated it "pauses research using infectious pathogens and toxins in the United States that may pose a danger to American citizens." And in a notice published on 7 May, the NIH Office of Science Policy wrote that until the new guidance is in place "research meeting the definition of dangerous gain-of-function research is to be paused." The executive order itself, however, only instructs OSTP to "establish guidance ... with respect to suspension of federally funded dangerous gain-of-function research."

"We need to get more clarity from the administration about what they're saying and what the order actually does," says Allen Segal, chief strategy and public affairs officer for the American Society for Microbiology.

In a 9 May email, the Association of American Universities cited "conversations with DC-based stakeholders" and vaguely advised its members "to immediately pause all federally funded domestic or international research" covered by the executive order. It said NIH estimated

that "about 1000 projects need to be paused," a tally the agency has not confirmed to *Science*.

Given recent funding cuts and staff losses at NIH, the agency is unlikely to have the personnel and resources to do go through hundreds or thousands of infectious disease studies and determine which should be halted, terminated, or resumed, Koblentz says. "So, any 'pause' may be quite lengthy and obviously very disruptive."

Still, Trump's announcement is an improvement on the Biden rules, says Marc Lipsitch, an epidemiologist at the Harvard T.H. Chan School of Public Health who has advocated for greater GOF research oversight. "If this had been written by the Bush administration or the Biden administration, I would be 95% supportive," he adds. Given the Trump administration's track record in science, however, Lipsitch worries about the policy's implementation.

The Biden policy scheduled to take effect listed the pathogens it covered and which rules applied to them, depending on how dangerous they were deemed; the new executive order does no such thing. "The two next to each other are just night and day in terms of clarity," says Johns Hopkins virologist Andrew Pekosz. In fact, the new order could be read to ban huge swaths of infectious disease research, cautions Angela Rasmussen, a virologist at the University of Saskatchewan.

Gronvall says the focus on possible lab leaks could detract from other measures to prevent pandemics. The government is doing little to curb the spread of the H5N1 influenza virus, a pathogen widely believed to have pandemic potential, in birds and cattle, she notes. "In this administration's outlook, diseases come from labs, not nature, so they aren't doing anything about it."

Segal points out that the U.S. has led the way on regulating GOF research globally—but thinks that if it takes matters too far, that could actually make the world a more dangerous place. "Frankly, we should be looking to export the way that we [regulate] this to other places, rather than making it more difficult," he says. "Otherwise, what we're going to wind up doing is encouraging researchers to go places where there's less stringent regulation." □

BY THE NUMBERS

The Gates Foundation surprised global health experts last week by announcing it would spend Bill Gates's remaining fortune much more quickly than originally planned.

2045

Year the foundation now plans to close

$200 BILLION

Amount Gates says he expects the foundation to spend by then, on top of $100 billion spent in its 25 years so far

5,000,000

Children under age 5 who died globally in 2019. The foundation hopes to halve that number.

IN FOCUS

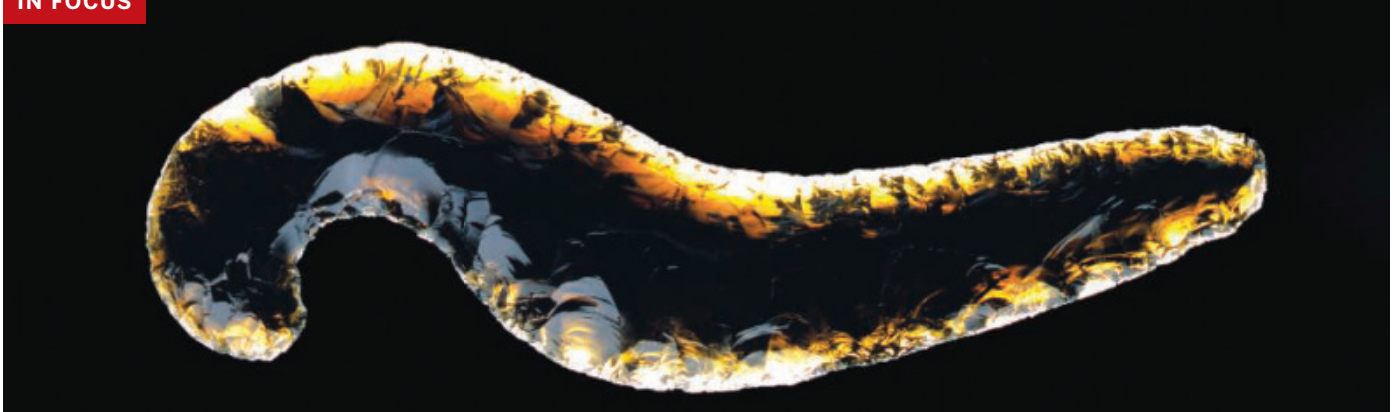

PHOTO: MICHEL ZABÉ/PROYECTO TEMPLO MAYOR/INAH

Aztec Empire sought obsidian from far and wide

Obsidian, a volcanic glass valued by the Mexica (also called Aztec) people for its sharpness and dark, glossy look, fueled a massive and complex trade network with other cultures across Mesoamerica, according to the largest analysis to date of obsidian artifacts from Tenochtitlan, the capital of the Mexica Empire. The study, published this week in the *Proceedings of the National Academy of Sciences*, involved 788 artifacts, including weapons, earrings, and decorated skulls. Researchers used a technique called x-ray fluorescence to measure trace elements that point to an item's geological source. Nearly 90% of the obsidian came from the Sierra de Pachuca some 94 kilometers northeast of Tenochtitlan, known for the distinctive green and golden obsidian used in ritual objects such as the scepter, or *ehecatopilli* (pictured), associated with the wind god Ehecatl-Quetzalcoatl. When the Mexica consolidated their empire around 1430 C.E., the sources of more prosaic tools such as blades expanded to far-flung sites, some linked to the rival P'urhepecha culture—an indication that the Mexica's increasing political reach reshaped their access to key resources. —*Rodrigo Pérez Ortega*

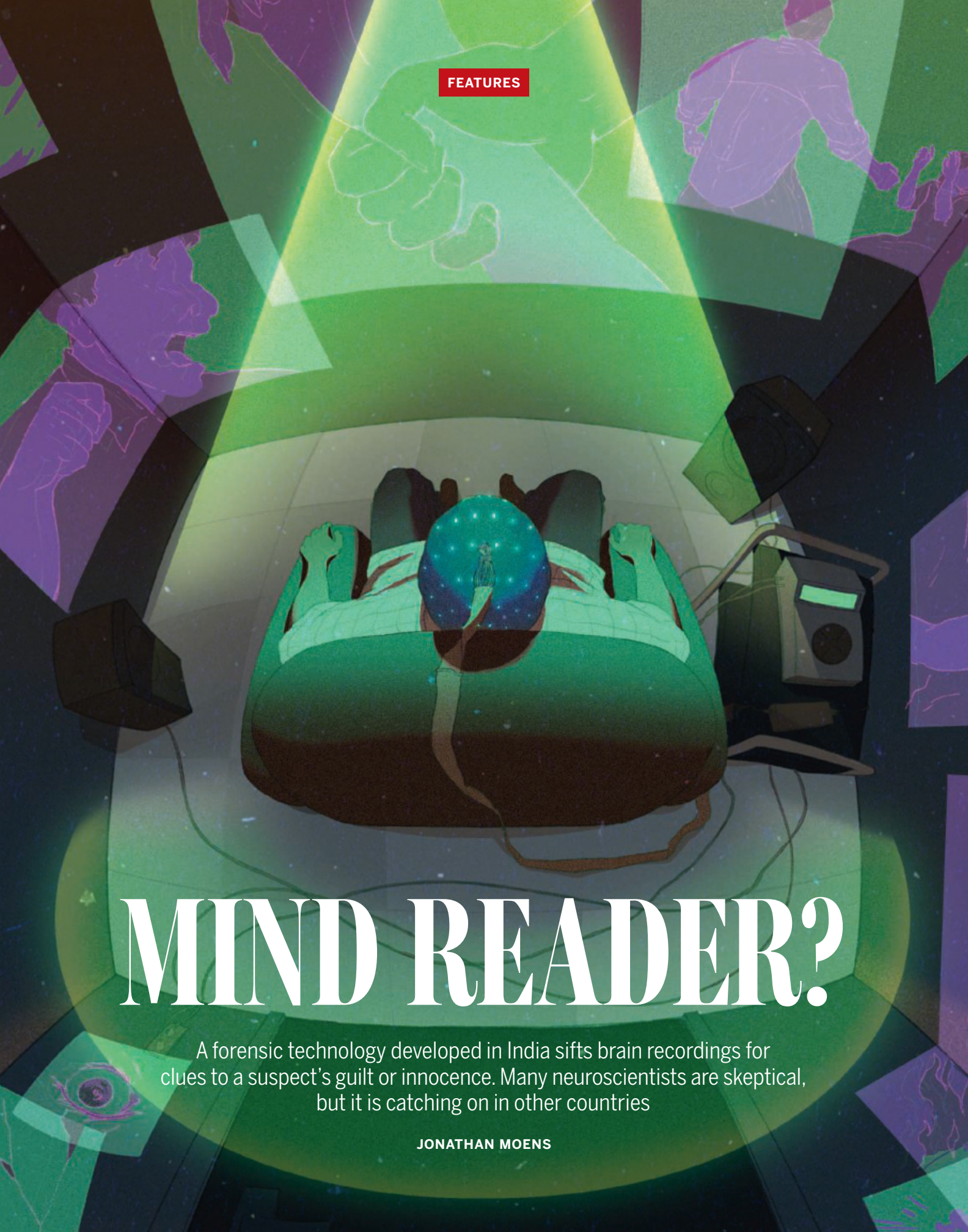

MIND READER?

A forensic technology developed in India sifts brain recordings for clues to a suspect's guilt or innocence. Many neuroscientists are skeptical, but it is catching on in other countries

JONATHAN MOENS

One day in 2021, an Indian student in her early teens came to her family with some distressing news: At school, a man in his 20s had called her into an empty classroom and raped her at knifepoint. Later, after the student found out she was pregnant and decided to abort, she filed a statement with the police.

The man accused of the crime, Surjaram, denied everything and sought to be released on bail. To prove his innocence, he asked to undergo three forensic science tests, including one called brain electrical oscillation signature profiling (BEOS).

During the test, he would likely have sat quietly in an empty room, listening to a series of short, first-person phrases recounting the crime scene—perhaps "I called the girl into the room," "I closed the door," and "I pulled a knife"—while a headset recorded his brain's electrical activity. Meanwhile, a computer monitored how his brain responded to each phrase, looking for telltale signs that he had participated in the crime. In Surjaram's case, the results were what he hoped for: His brain signals suggested he had no experience of these events, and was therefore innocent.

Based largely on BEOS and the other two tests—lie detection and narcoanalysis, which involves injecting suspects with a "truth serum"—the judge released Surjaram from police custody. The case was sent to another court, but the judgments aren't publicly available.

That case is one of at least 700 police investigations in India since the early 2000s in which suspects accused of serious crimes such as murder, rape, and terrorism have undergone BEOS tests. Proponents of the technology claim it is near-infallible. "It's very helpful," says Asha Srivastava, dean of the National Forensic Sciences University (NFSU), who says she has conducted BEOS tests on thousands of suspects herself. She sees it as an objective and more humane way to obtain information than torture, a practice Indian police are notorious for. "We are on a mission to make police friendly."

But multiple scientific and legal experts say BEOS rests on scant evidence. The method hasn't properly been vetted by the scientific community, they say, and the Bengaluru-based company that developed the technology, Axxonet, has only published a few studies on its effectiveness, which experts say are flawed. "Definitely I would not be in favor of this being used in an actual case," says Narayanan Srinivasan, a cognitive scientist at the Indian Institute of Technology (IIT) Kanpur.

Despite this, the use of BEOS shows no sign of stopping. Although BEOS evidence has not been admissible in Indian courts since 2010, *Science* has found multiple recent court judgments in which BEOS tests appear to have influenced judges' decisions about whether suspected rapists and others should be released on bail. Police and investigative agencies continue to use the systems, which can cost upward of $100,000, to generate leads, corroborate findings, and screen suspects—sometimes years after the original crime. And although Axxonet says they're not in the business of actively selling their technology, *Science* has learned that in the past few years, forensic scientists affiliated with NFSU have been promoting the technology abroad, giving lectures about its merits to officials in several countries in South America, Africa, and Asia. Some overseas groups have already bought BEOS-related equipment, or are negotiating its purchase.

"BEOS has been validated and proved itself to be a useful tool during complex investigations," says Chetan Mukundan, a director of Axxonet and son of the technology's inventor. BEOS reports are not primary evidence, he adds, but are always corroborated with other investigative tools. India's Ministry of Home Affairs did not respond to multiple requests for comment.

"The stakes are very high," says Owen Jones, a professor of law and biological sciences at Vanderbilt University. "Reliably discovering from brain activities whether a suspect or witness has personal knowledge of an event could transform justice, internationally, in a positive way. But admitting unreliable evidence that may carry the veneer of science would do the opposite."

THE GENESIS OF BEOS can be traced back to the United States, where, in the mid-1980s, neuroscientist Lawrence Farwell developed a technology called brain fingerprinting, which he claims has had a 100% success rate in filtering criminals from innocents. The technology is based on a pattern of electrical activity in the brain called the P300, which shows up as a spike in an electroencephalogram (EEG) recording about 300 milliseconds after something unexpected or meaningful appears—for example a "boop" sound after a string of "beep" noises.

Farwell's idea was to leverage this signal for counterterrorism or crime fighting by exposing suspects to images and words, some of which are related to a crime. If a suspect shows a P300 peak (particularly if it is followed by a subsequent dip in the signal) when they read or see crime details that only the perpetrator would know, that suggests they might have been involved, he says.

Multiple experts consulted by *Science* say there's little evidence it works, but Farwell cites publications in journals including *Psychophysiology*, the *Journal of Forensic Sciences*,

ILLUSTRATION: (OPPOSITE PAGE) DION MBD

and *Cognitive Neurodynamics*. "The objective fact is that the scientific community has found my research to be worthy of publication in the top scientific journals," he told *Science*.

A 2001 review by the U.S. Government Accountability Office concluded that government agencies such as CIA and FBI "do not foresee using the brain fingerprinting technique," mainly because of its "limited use." But Farwell says the agencies did not try to evaluate the validity of his technology and that brain fingerprinting had since been sold to the government of Pakistan, where he conducted "extensive training and guidance in real-world applications."

In India, Champadi Raman Mukundan, a well-known clinical psychologist, was intrigued by the concept and signed an agreement with the Directorate of Forensic Science (DFS) in Gandhinagar—a state government lab—to develop the technology. Rather than focusing on the P300 signal, Mukundan set out to incorporate multiple other brain signals to reveal not only whether someone knows about a crime, but also whether they have what he called "experiential knowledge" of the crime—meaning they actively participated in it.

Mukundan set up a company, Axxonet, and around 2005, the team created a BEOS prototype. The technology is based on the idea that the emotions and physical sensations associated with an experience leave imprints in the brain, says Priyanka Kacker, who researches behavioral forensics at NFSU and worked with Mukundan. Recalling an experience involves reactivating those imprints—and the brain areas responsible for encoding them. Mukundan claims the BEOS system can assess whether a person has firsthand experience of an event by tracking changes in these regions.

In practice, the first step is for forensic scientists to interview both the police and the suspect to get their versions of events. These are then broken up into two scripts consisting of short phrases, or "probes," which are played to the suspect, who wears an EEG headset to measure electrical brain activity. For each phrase, software monitors the activity for signs that the suspect has experiential knowledge of that event.

A forensic scientist then evaluates the system's findings, looking for sequential instances of experiential knowledge during phrases that describe key aspects of the crime. "If you get experiential knowledge on a probe, like, 'I took a knife,' that obviously cannot be interpreted as that person has killed him," says Deepti Puranik, a forensic scientist at the Narsee Monjee Institute of Management Studies who says she has done 200 to 300 BEOS tests over the past 2 decades. A response to a second phrase like, "I held it to his neck," however, would raise the chances that the person had taken part. "You have to look at the sequence."

Axxonet's website says BEOS was "adapted and developed" based on a flurry of EEG studies dating back to the 1980s, most of which investigate brain function in patients with conditions such as schizophrenia, alcoholism, and obsessive compulsive disorder. More recent studies allegedly supported the efficacy of BEOS. But researchers say those studies were poorly conducted and many were published in little-known journals. "I have not heard of a single one of these journals," said Sridhar Devarajan, a neuroscientist at IIT Bengaluru. "The hypotheses and the methods are, to put it mildly, frivolous and sloppy."

The study Axxonet cites most often was conducted by DFS between 2006 and 2008, after BEOS had already been applied in hundreds of real-world cases, and hasn't been published in a peer-reviewed journal. It included 110 participants, about half of whom were told to conduct a mock crime in which they break into a room and steal from a piggy bank. The other half were told about the facts of the crime but did not actually perform it. The researchers then performed BEOS tests on all participants.

The results suggest the technology could correctly identify people who had committed the crime about 90% of the time and misclassified about 5% of those who didn't. The study concludes that "BEOS profiling can be used as a valid scientific test for forensic purposes."

That evidence isn't enough to support the real-world use of a device that could have a major impact on a person's life, skeptics say. For a start, the sample size is far too small, Devarajan says, adding that such research should include "tens of thousands" of participants. Others point out that the results haven't been validated elsewhere. "With anything like this, I would be doubly sure, triply sure, before I would say anything about [a suspect]," Srinivasan says.

> **"I would not be in favor of this being used in an actual case."** **Narayanan Srinivasan**, Indian Institute of Technology Kanpur

Chetan Mukundan says further research has been conducted in the field, including one "robust independent field trial" by a non-Indian law enforcement agency that yielded excellent results. "Unfortunately for us the report is confidential."

Others say so little is known about the algorithms, methods, and data analyses underlying BEOS that it is impossible to scrutinize it in any kind of meaningful way. "They wouldn't reveal it to me. It was totally proprietary," says Emily Murphy, associate professor at the University of California College of the Law, San Francisco, who met with the elder Mukundan in 2009 to study BEOS and its application in law.

Meghana Srivatsav, a psychologist at Flame University, interned at DFS in 2011 before working for a year at Axxonet. She recalls that BEOS was a work in progress, constantly being tweaked and tested, even while it was used in high-stakes, real-world

cases. "That's not how it should work," she says. "When there's uncertainty in the lab, and we are testing and retesting and that is put into practice, as a scientist, I see that as a bit of a problem."

Though the workings of BEOS are proprietary, "the experts in the system who need to know about the internals of the technology have tested and validated it," says Chetan Mukundan. The technology relies on advances in neural processing, he adds, and is constantly being updated to "accommodate new releases and security patches" and user feedback.

Yet the science underpinning BEOS doesn't square with what we know about how the brain works, neuroscientists say. "I'm very critical of the approach and the results," says Rafael Yuste, a neuroscientist at Columbia University and chair of the Neurorights Foundation, which works on protecting people's brain data. Our memories are highly malleable, and it's not easy to disentangle their neurobiological underpinnings from those of similar phenomena, such as false memories or imagination, adds Anthony Wagner, a psychologist at Stanford University and director of the Stanford Memory Lab. A neural signal detected by BEOS could in fact reflect a memory generated when a suspect was interviewed, rather than a real memory of the crime, he suggests.

If BEOS were able to reliably tease out truly experienced memories, that would constitute a major scientific development. "It'd be great to see the evidence that they've had this breakthrough," Wagner says. "I would be very skeptical."

DESPITE THESE concerns, BEOS has become an important component of the arsenal of forensic tests used by the Indian police. Initially, tests were only conducted at DFS in Gandhinagar, but at least five other state forensic laboratories in the country have either carried out BEOS tests or purchased the system. NFSU, set up in 2008 by India's prime minister, Narendra Modi, while he was still chief minister of Gujarat, also carries out tests.

As in Surjaram's case, BEOS is often used in concert with two other questionable techniques: lie detection—also known as polygraph—and narco-analysis, in which a "truth serum" injected into suspects puts them into a stupor and supposedly renders them more apt to speak. "These technologies have a history which has been discredited," says Jinee Lokaneeta, a political scientist at Drew University whose 2020 book *The Truth Machines: Policing, Violence, and Scientific Interrogations in India* explores the use of these technologies. "And yet they sort of remain."

One rationale for adopting those technologies has been to modernize the Indian criminal justice system and ease the rampant use of physical torture by police, Lokaneeta says. But in some cases, they have simply led to new forms of harm. In 2006, Abdul Wahid Shaikh and 12 other suspects were accused of being involved in the Mumbai train bombings, a series of seven blasts on a suburban railway that killed more than 200 people. Shaikh and the others were incarcerated and, during interrogation, underwent multiple rounds of narcoanalysis, BEOS, and polygraph tests. Some were conducted with the permission of courts and in controlled settings, such as in a hospital. But Shaikh says he was also sometimes brought into police custody where authorities "forcefully conducted these tests." In 2015, 9 years after he was first arrested, the courts ruled there wasn't enough evidence to incriminate Shaikh and acquitted him.

BEOS also drew criticism after a high-profile 2008 case, in which a woman called Aditi Sharma and her lover Pravin were accused of poisoning Sharma's former fiancé with a prasad—a traditional Indian sweet—laced with arsenic. Sharma underwent a series of tests, including BEOS, which suggested she was guilty. She and Pravin were initially sentenced to life imprisonment, only to be released on bail months later because of a lack of direct incriminating evidence. U.S. scientists quoted in a story in *The New York Times* condemned the use of BEOS, which they said was not credible.

Meanwhile the Indian government had assembled a small team of leading neuroscientists to independently review the research behind the technology and visit forensic science laboratories where BEOS was being used. The committee identified a number of concerns, particularly regarding "experiential knowledge": Among other things, it found that there was no supporting peer-reviewed research validating the concept and that irrelevant probes were just as likely to elicit a telltale signal as relevant ones.

BY THE NUMBERS

700+

Police investigations since the early 2000s in which brain electrical oscillation signature profiling (BEOS) has been used

150,000

Forensic experts the Indian government aims to employ by 2028

$118,000

Recent sales price of a BEOS system

Their 2008 report concluded that the scientific basis for BEOS was "suboptimal" and recommended it not be used as evidence in court. The government disagreed. Four months after the committee finished its review, DFS disbanded it, arguing that not all members had visited the laboratories, which were "doing good work."

Two years later, however, India's Supreme Court stepped in with a judgment that restricted the technology, although because of legal rather than scientific concerns. Its ruling stated that forced use of BEOS and other forensic technologies such as lie detection and narcoanalysis violate a person's right against self-incrimination. Among other safeguards, investigators must first obtain a person's consent and grant them access to a lawyer, the court said. The judgment also ruled that the test results themselves cannot be brought into courtrooms but that any other evidence investigators obtain through such tests can be.

THE SUPREME COURT'S DECISION has had an impact. Several courts have reversed earlier decisions in cases where police didn't get proper consent to conduct BEOS and other forensic tests, for instance. In some cases, suspects who were initially sentenced to life imprisonment were later deemed innocent.

DATA: JINEE LOKANEETA, *THE TRUTH MACHINES: POLICING, VIOLENCE, AND SCIENTIFIC INTERROGATIONS IN INDIA*; NATIONAL FORENSIC SCIENCES UNIVERSITY; STATE FORENSIC SCIENCE LABORATORY CHHATTISGARGH; AMIT SHAH

However, *Science* has found that BEOS still shapes high-stakes court decisions, particularly on bail applications. The Supreme Court ruling might seem to ban courts from considering BEOS results in those hearings. But the rules for bail applications are generally less stringent than for other court procedures, in part because final judgments are made later during the trial. "You're not bound by the rules of evidence very strictly when you're looking at bail," says Chinmay Kanojia, a criminal defense lawyer in India.

In one judgment from 2021, a man accused of raping and murdering a girl underwent a BEOS test 7 years after the crime during a court-ordered reinvestigation—a delay that compounds skepticism about the technique. "It's very likely that there is no empirical evidence that would support claims that the BEOS method is capable of accurate memory detection at long delays," Wagner says. The BEOS evidence suggested the man was guilty, and the court rejected his bail application.

In another case from 2018, a headmaster from a school in Ahmedabad was accused of raping one of his students, a 7-year-old girl. The judge initially leaned toward believing the girl's story, but changed his mind when he saw that BEOS, lie detection, and narcoanalysis test results pointed toward the man's innocence. "It is only with the aid of the results of the three scientific tests that I am in a position to reach an appropriate conclusion," said Jamshed Burjor Pardiwala, the high court judge on the case.

Pardiwala's decision to release the man on bail was later overturned by the Supreme Court, citing procedural violations. But he has since become a Supreme Court judge and in May 2028 is slated to become chief justice of India, the highest ranking position in the Indian judiciary.

Science contacted the Supreme Court of India with questions for Pardiwala but did not get a response after multiple attempts.

More recently, even the Supreme Court itself has deferred to evidence from BEOS and the other forensic technologies it had sought to regulate. In 2023, the court intervened in a case where murder suspects had been discharged, saying the order had "failed to consider" that these technologies pointed toward their guilt. It ordered the trial to go forward.

AS INDIA'S CRIMINAL JUSTICE system grapples with how to use BEOS, the government has made forensic sciences a top national priority. "In the next 10 years, India's criminal justice system will be the most modern, scientific, and speedy in the world," according to a November 2024 press release from the Ministry of Home Affairs. To do this, the country aims to have at least 150,000 forensic experts by 2028.

The institution spearheading this effort is NFSU, which trains students in the use of BEOS and emphasizes its value. The tool is "99.99% accurate and reliable," says Pravesh Charan, who is doing a doctoral degree at the university. Professors at the university teach that any lapses during tests are attributable to the experimenter themselves, rather than the technology. "If that person is not trained in using the BEOS system, especially how to prepare probes, then that could be a major limitation," Kacker says. "Otherwise, systemwise, there is no such limitation."

> "We will get to a point where there will be an unbeatable lie detector test."
>
> **Jared Genser**
> Neurorights Foundation

NFSU did not respond to multiple requests for comment.

Meanwhile police and forensic science laboratories around India have continued to acquire the technology. In 2022, police in the state of Karnataka added BEOS to their investigative toolkit. And last year, a forensic science laboratory in Raipur, a city in central India, bought a BEOS system for the equivalent of about $118,000.

Axxonet says they "do not actively pursue the sale of BEOS-based tools." But forensic scientists at NFSU have been promoting the technology abroad. Last year Charan conducted a training session on forensic science techniques, including BEOS, for police officials in Guyana, and says they are in the process of buying the technology.

In September 2024, Charan also conducted a training session for the Bangladesh Institute of Forensic Psychology and Sciences, a company that says it consults for various organizations, including Bangladesh's military and intelligence and law enforcement agencies. In October 2022, Kacker showcased various forensic techniques, including BEOS, to delegates from Rwanda, according to her university's annual report. A few months ago, she gave a lecture on these technologies to Tanzanian police. Trade data also show that a private security company in Singapore called PCS Security purchased BEOS-related equipment in 2018.

In April 2023, NFSU inaugurated its first-ever campus abroad in Jinja, Uganda, where it will likely teach students the same forensic science techniques they learn in India.

BEOS' EXPANDING SPHERE of influence "doesn't surprise me, but it does concern me," says Marcello Ienca, professor of ethics of artificial intelligence (AI) and neuroscience at the Technical University of Munich. To him, the quick proliferation of unvalidated brain-reading technologies underscores the importance of developing international regulations.

Ironically, those concerns may sharpen if BEOS or some other neurotechnology ultimately does live up to its billing. "I think there is every reason to believe that we will get to a point where there will be an unbeatable lie detector test," says Jared Genser, general counsel of the Neurorights Foundation, citing advancements in AI and recent breakthroughs in neurotechnologies. That, he and others say, could pose a serious threat to privacy and autonomy. "We do need to be thinking now about the guardrails for that kind of technology." □

Jonathan Moens is a science and investigative journalist in Rome. This story was supported by the *Science* Fund for Investigative Reporting and an Investigative Reporters and Editors Freelance Investigative Fellowship Award.

eppendorf & Science

PRIZE FOR NEURO BIOLOGY

2024 Winner
Laura Seeholzer, Ph.D.
University of California San Francisco, School of Medicine, USA

For research on airway neuroendocrine cells responding to external threats

Application Deadline
June 15, 2025

Call for Entries 2025

Eppendorf & Science Prize for Neurobiology
The annual Eppendorf & Science Prize for Neurobiology is an international prize which honors young scientists for outstanding neurobiological research based on methods of molecular, cellular, systems, or organismic biology. If you are 35 years of age or younger and doing great research, now is the time to submit an entry for this prize.
It's easy to apply! Write a 1,000-word essay and tell the world about your work.

eppendorf.com/prize

As the winner, you could be next to receive
> Prize money of US$25,000
> Publication of your work in *Science*
> Full support to attend the Prize Ceremony held in conjunction with the Annual Meeting of the Society for Neuroscience in the USA
> 10-year AAAS membership and online subscription to *Science*
> Complimentary products worth US$1,000 from Eppendorf
> An invitation to visit Eppendorf in Hamburg, Germany

eppendorf

Science AAAS

AAAS® and Science® are registered trademarks of the American Association for the Advancement of Science, USA. Eppendorf® and the Eppendorf Brand Design are registered trademarks of Eppendorf SE, Germany.
All rights reserved, including graphics and images. Copyright © 2025 by Eppendorf SE. Photography: Brian Carey, figMedia

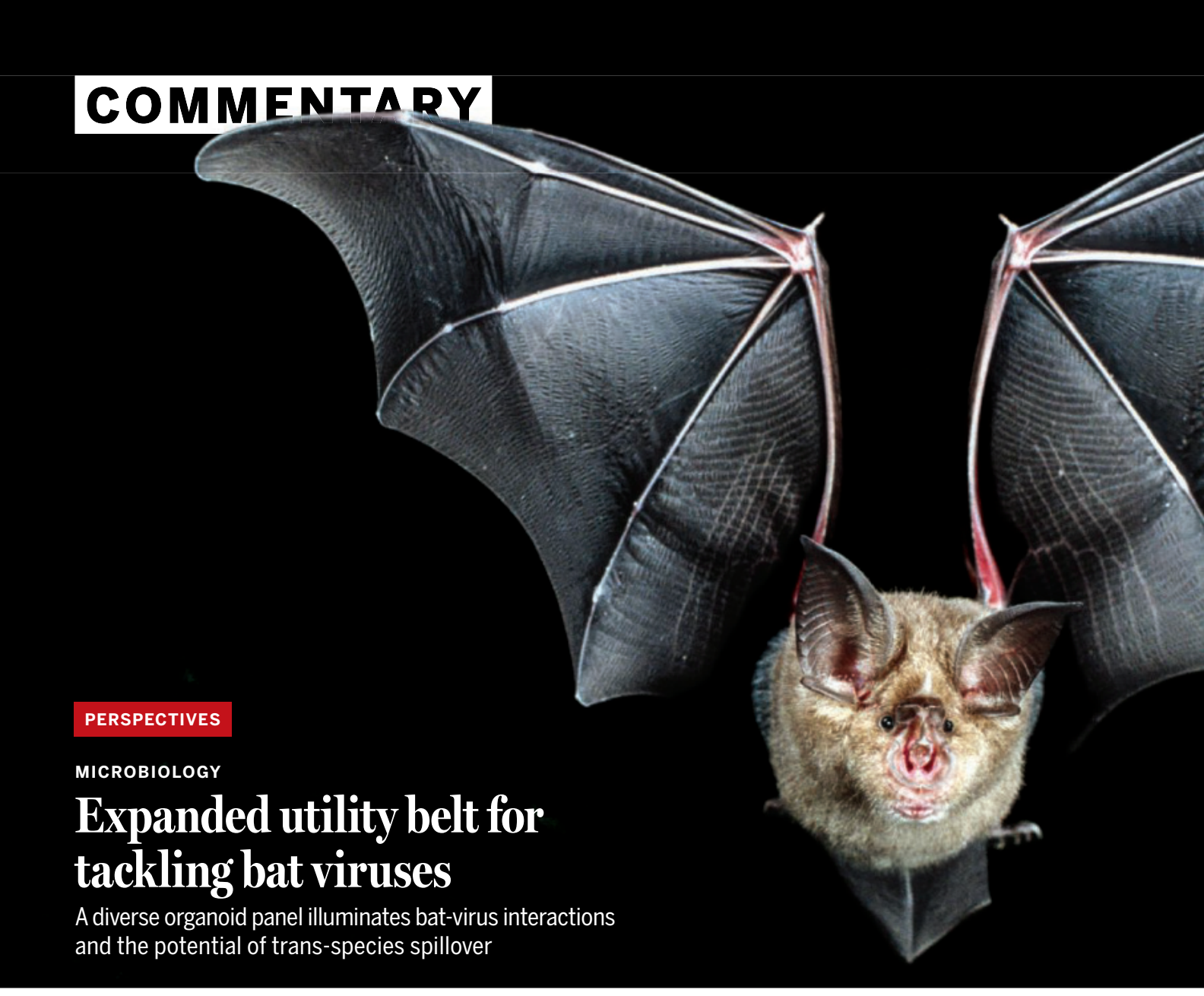

PERSPECTIVES

MICROBIOLOGY

Expanded utility belt for tackling bat viruses

A diverse organoid panel illuminates bat-virus interactions and the potential of trans-species spillover

Jie Zhou[1,2,3] *and* **Kwok Yung Yuen**[1,2,3]

Bats harbor a large and diverse array of viruses, including relatives of the viruses that caused human outbreaks of severe acute respiratory syndrome (SARS) (*1*), Middle East respiratory syndrome (MERS), and the COVID-19 pandemic. Yet the bats carrying these viruses show minimal signs of disease. This puzzling coexistence has made bats a focus for studying viral spillover—when a virus is transmitted to another species—and host pathogenesis. However, most bat viruses have not been isolated and propagated in laboratories, owing to the lack of biologically relevant experimental models that mimic native bat cells. On page 756 of this issue, Kim *et al.* (*2*) report the establishment of bat organoids—laboratory-grown bat tissue models—derived from five bat species that support the growth of several different bat viruses. This should improve the ability to isolate bat viruses, test antivirals, and undertake surveillance for trans-species viral spillovers.

The past decade has witnessed rapid advances in organoid biology and their applications. Sometimes referred to as "mini organs," these three-dimensional tissue-like structures derived from stem cells display complex tissue organization and function. Organoids enable the study of complex biological processes in culture plates, providing more biologically relevant settings than conventional two-dimensional cell culture models.

The mammalian gastrointestinal and respiratory tracts are among the most common routes of microbial invasion. In bats and other mammals, including humans, epithelial cells lining the respiratory and intestinal mucosa are the primary targets of virus entry. The susceptibility of these epithelial cells to particular viruses dictates which host species, and which tissues within them, can be infected (viral tropism). Mucosal epithelial cells elicit a cascade of responses upon infection to contain virus invasion and maintain homeostasis. As a result, the interaction between viruses and mucosal epithelial cells governs viral tropism, viral pathogenesis, and disease manifestation in hosts. The recurrent spillovers of bat-borne viruses and increasing prevalence of human viral infections have fueled growing attention on the trans-species potential of animal viruses and human susceptibility to existing and emerging viruses. Organoids provide a promising means to address these challenges, especially where conventional in vitro and in vivo models have proven limited.

PHOTO: F DESCHANDOL AND P SABINE/BIOSPHOTO/MINDEN PICTURES

Several viruses that infect humans, including coronaviruses and influenza viruses, have originated in bats.

Adult stem cell (ASC)–derived epithelial organoids have become popular tools for studying respiratory and intestinal microbial infections. They are more phenotypically mature than pluripotent stem cell (PSC)–derived organoids, which are optimal for research in developmental biology (*3*). The first ASC-derived human organoids, human intestinal organoids, have become a vital and powerful tool for virus research (*4*, *5*). Human noroviruses are the most common causes of acute gastroenteritis worldwide. Enormous effort has been invested in establishing in vitro cultivation methods for these viruses over the past four decades, with few successes. However, the demonstration of active norovirus replication in human intestinal organoids (*6*) has enabled unprecedented in vitro studies of these previously unculturable viruses. Similarly, on the basis of productive MERS coronavirus (MERS-CoV) infection in human intestinal organoids, with corroborating results from mouse experiments, it was shown that the human intestinal tract serves as an alternative route of MERS-CoV infection (the primary route is the respiratory tract) (*7*). Severe acute respiratory syndrome coronavirus 2 (SARS-CoV-2), the causative virus of COVID-19, also has been reported to have an enteric tropism (*8*).

Respiratory organoids have been successfully established by using human primary lung tissues and nasal epithelial cells (*9*–*11*). Upon induction of maturation, biologically active nasal organoids, airway organoids, and alveolar organoids can be readily generated, enabling the entire human respiratory epithelium to be reconstructed and expanded in culture plates with excellent efficiency and stability. This enabled, for example, serial propagation of human rhinovirus C, which is responsible for the common cold (*12*). This large family of human Rhinoviruses has long been recalcitrant to in vitro cultivation and investigation.

In early 2020, the first bat organoid model, the intestinal organoid of the Chinese horseshoe bat (*Rhinolophus sinicus*), was established (*8*). This model system supported productive SARS-CoV-2, and infection in these organoids provided initial wet lab evidence, lending support to the bat origin of SARS-CoV-2. A comparative study of bat and human intestinal organoids revealed that rapid and robust induction of innate immune responses enabled bat cells to constrain viral propagation in the early phase of infection (*13*), which might be the biological basis for how bats are able to host viruses asymptomatically. Bat airway epithelium organoids now have been generated from different bat species (*14*) and used to reconstruct bat antiviral responses (*15*).

Kim *et al.* have substantially expanded the range of bat organoids by deriving them from four types of tissue—including respiratory, intestinal, and renal—and taken from five diverse wild bat species. Demonstrating the applications of the expanded panel, the authors used this panel of organoids to isolate and characterize bat-borne orthoreoviruses and paramyxoviruses and to test the efficacy of different antiviral drugs. The study nicely showcases the benefits of collaborative research, integrating organoid biology and virology. As inherently interdisciplinary research, organoid-based virus research requires scientists from each discipline to form a strong partnership.

There are an estimated 1400 bat species in the world that vary in their habitats and behaviors. The expanded panel of bat-derived organoids of Kim *et al.* offers a potential means for isolating pathogens, testing therapeutics, and predicting spillover risks. By bridging the gap between metagenomic discovery and experimental virology, this approach should illuminate long-standing mysteries of bat biology and viral ecology that were previously inaccessible to laboratory investigation. □

REFERENCES AND NOTES

1. S. K. Lau *et al.*, *Proc. Natl. Acad. Sci. U.S.A.* **102**, 14040 (2005).
2. H. Kim *et al.*, *Science* **388**, 756 (2025).
3. J. Kim, B.-K. Koo, J. A. Knoblich, *Nat. Rev. Mol. Cell Biol.* **21**, 571 (2020).
4. T. Sato *et al.*, *Gastroenterology* **141**, 1762 (2011).
5. H. Clevers, *Nat. Rev. Mol. Cell Biol.* **21**, 355 (2020).
6. K. Ettayebi *et al.*, *Science* **353**, 1387 (2016).
7. J. Zhou *et al.*, *Science Adv.* **3**, eaao4966 (2017).
8. J. Zhou *et al.*, *Nat. Med.* **26**, 1077 (2020).
9. J. Zhou *et al.*, *Proc. Natl. Acad. Sci. U.S.A.* **115**, 6822 (2018).
10. M. C. Chiu *et al.*, *mBio* **13**, e0194422 (2022).
11. M. C. Chiu *et al.*, *Cell Discov.* **8**, 57 (2022).
12. C. Li *et al.*, *Nat. Commun.* **15**, 10772 (2024).
13. X. Liu *et al.*, *Signal Transduct. Target Ther.* **7**, 392 (2022).
14. L. L. Y. Chan *et al.*, *Emerg. Microb. Infect.* **12**, e2148561 (2023).
15. M. J. Kellner *et al.*, bioRxiv 588241 [Preprint] (2024); https://doi.org/10.1101/2024.04.05.588241.

ACKNOWLEDGMENTS

J.Z. and K.Y.Y. acknowledge support from the University Grant Committee and Innovation and Technology Commission, the Government of the Hong Kong Special Administrative Region of the People's Republic of China.

10.1126/science.adx9000

[1]Department of Microbiology, School of Clinical Medicine, Li Ka Shing Faculty of Medicine, The University of Hong Kong, Hong Kong, China. [2]State Key Laboratory of Emerging Infectious Diseases, The University of Hong Kong, Hong Kong, China. [3]Centre for Virology, Vaccinology and Therapeutics, Hong Kong Science and Technology Park, Hong Kong, China. Email: jiezhou@hku.hk

CONDENSED MATTER PHYSICS

Watching electronic ice melt

An experiment captures images of the transition between liquid and solid states of an electron system

Sandeep Joy[1,2] *and* **Brian Skinner**[3]

One of the most familiar phase transitions on Earth is the freezing and melting of water. Underlying this transition is the competition between the kinetic energy of water molecules and the potential energy arising from their mutual interactions. When the temperature falls below the freezing point, the interaction energy wins this competition and water freezes. A two-dimensional (2D) system of electrons exhibits a similar competition between kinetic and potential energies that also gives rise to a freezing–melting transition. However, the nature of this transition in an electron system has remained mysterious for decades. On page 736 of this issue, Xiang *et al.* (*1*) report direct imaging of the melting and freezing of a Wigner crystal—a periodic 2D lattice of strongly interacting electrons. The observed intricate spatial patterns raise fascinating questions about the nature of this fundamental phase transition in the quantum realm.

As in water, the liquid and solid phases of the 2D electron system are unusual in that the solid phase has a lower density than the liquid phase. Unlike water, however, transitions between liquid and solid phases in an electron system can occur at absolute zero temperature. The electrons' kinetic energy arises from quantum mechanical fluctuations—jittering of the electron positions due to quantum mechanical uncertainty. This quantum kinetic energy drops more quickly with decreasing electron density than does the strength of the electrons' interactions, causing the electron system to freeze below a critical density. Such a transition, called Wigner crystallization, was predicted theoretically in 1934 (*2*), but it has been notoriously difficult to realize experimentally. The magnitudes of both the interaction and kinetic energies are small at the transition, and the delicate interplay of these energies is easily interrupted by finite-temperature effects or disorder. Previous studies that imaged Wigner crystals relied on the use of an additional stabilizing force such as a periodic structural modulation (*3*) or a strong magnetic field (*4*) that modified the nature of the phase transition.

There is also a more fundamental difficulty associated with observing the Wigner crystallization transition. When water freezes, large chunks of ice can be seen floating in water. But such macroscopic phase separation is effectively prohibited in an electron system by the long-range Coulomb interactions between electrons. Solid and liquid phases of the electron system have different densities of electrons, whereas the positive background charge that neutralizes these negative charges has a uniform density. Thus, a macroscopic domain of either phase would have a large total charge that is proportional to the area of the domain, and consequently enormous electrostatic forces would act to rip these domains apart, making macroscopic phase separation impossible. An important question, then, is how the electron system can change from one phase to another. One proposed answer is that electrons freeze by passing through a series of microemulsions (*5*–*8*) in which solid and liquid phases are tightly mixed or marbled together. Alternatively, the freezing transition could be dominated by disorder that smoothly modulates the spatial density of electrons. In this scenario, regions with low electron density become solid, whereas other regions with high electron density remain liquid (*9, 10*).

Quantum melting and freezing of electrons

A two-dimensional (2D) system of electrons solidifies at low electron densities in a process known as Wigner crystallization. The electron solid melts into liquid through an intermediate stage in which islands of solid domains are surrounded by liquid phase.

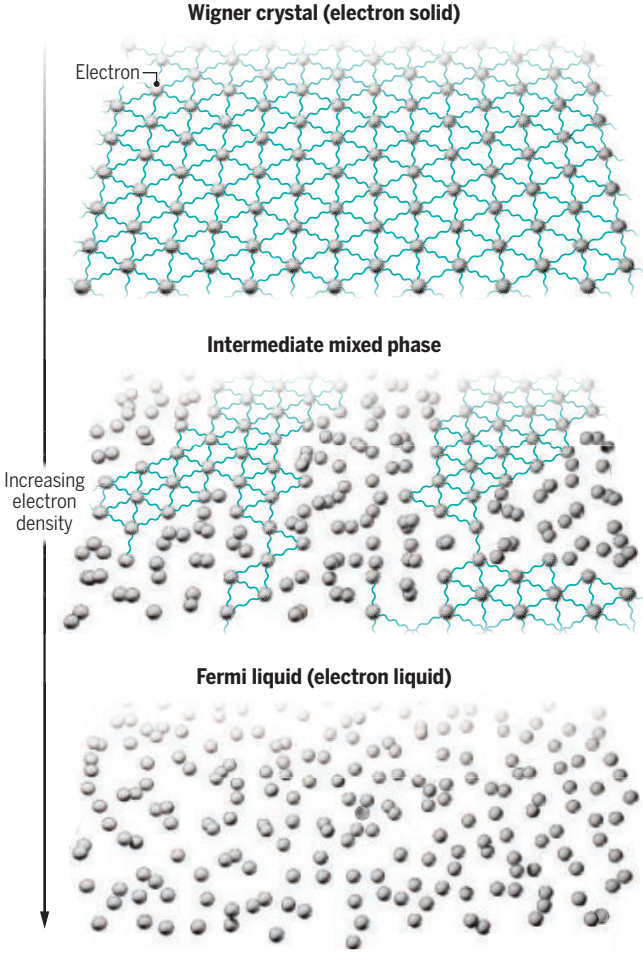

GRAPHIC: N. BURGESS/*SCIENCE*

Xiang *et al.* used noninvasive scanning tunneling microscopy to directly image freezing and melting of a 2D system with a low density of electron holes (a vacancy in an electronic orbital that behaves as a positive counterpart to the electron) in bilayer molybdenum diselenide. The observations showed that near the critical hole density associated with the melting and freezing transitions (analogous to the critical electron density), the system separated into a random pattern of alternating solid and liquid regions that are typically tens of nanometers in diameter (see the figure). The solid regions exhibited a crystalline lattice pattern of holes, whereas the liquid regions displayed a nearly uniform hole density. Varying the overall hole density of the system caused these regions to grow and shrink, with the system becoming either a uniform solid phase or uniform liquid phase far from the critical density. However, the range of hole density over which a phase mixture was observed was larger than the nominal upper bound for the microemulsion scenario by more than an order of magnitude (*11*). This indicates that the disorder-free microemulsion theory does not describe the ex-

periment. At the same time, a key prediction of the disorder-driven scenario was also not borne out because both liquid and solid regions always had essentially identical hole densities.

The study of Xiang *et al*. presents a challenge to existing theories about the Wigner crystallization transition but also provides important clues to resolve this puzzle, particularly through watching the "quantum densification" and "quantum melting" processes. In quantum densification, the hole density of the solid phase changed when additional holes were injected into the sample. Xiang *et al*. noticed that, rather than producing a smooth reduction in the lattice spacing between holes, densification occurs through an abrupt reconfiguration of a small local region (just a few holes wide), similar to when a new person enters a crowded elevator. In quantum melting, the solid phase transforms to liquid when the hole density is brought above the critical value. Xiang *et al*. show that this melting occurs by a process in which solid islands shrink and are gradually inundated by surrounding liquid regions as the hole density increases. These findings suggest that certain hole positions are pinned in place, presumably by impurities in the sample, which play a crucial role in the freezing and melting processes.

At present, there is no established theory that can explain the spatial patterns imaged by Xiang *et al*. The process by which a 2D crystal of electrons (or holes) melts or freezes may involve an intricate interplay between disorder and interactions. Perhaps the experimentally observed patterns are best described as a disorder-precipitated microemulsion, similar to how certain molecules in air can seed the formation of clouds. Indeed, Xiang *et al*. showed that the samples have a noticeable concentration of isovalent defects (extraneous atoms in the material that substitute for others with the same charge), which could be playing this role. Further investigation is essential to fully grasp the mechanisms behind quantum freezing and melting. □

REFERENCES AND NOTES

1. Z. Xiang *et al*., *Science* **388**, 736 (2025).
2. E. Wigner, *Phys. Rev.* **46**, 1002 (1934).
3. H. Li *et al*., *Nature* **597**, 650 (2021).
4. Y.-C. Tsui *et al*., *Nature* **628**, 287 (2024).
5. B. Spivak, *Phys. Rev. B Condens. Matter* **67**, 125205 (2003).
6. B. Spivak, S. A. Kivelson, *Phys. Rev. B Condens. Matter Mater. Phys.* **70**, 155114 (2004).
7. J. Lorenzana, C. Castellani, C. Di Castro, *Phys. Rev. B Condens. Matter* **64**, 235127 (2001).
8. C. Ortix, J. Lorenzana, C. Di Castro, *Phys. Rev. B Condens. Matter Mater. Phys.* **73**, 245117 (2006).
9. T. Ando, A. B. Fowler, F. Stern, *Rev. Mod. Phys.* **54**, 437 (1982).
10. J. Falson *et al*., *Nat. Mater.* **21**, 311 (2022).
11. S. Joy, B. Skinner, *Phys. Rev. B* **108**, L241110 (2023).

ACKNOWLEDGMENTS

B.S. acknowledges support from the US National Science Foundation under grant no. DMR-2045742. S.J. acknowledges support from Florida State University through the Quantum Postdoctoral Fellowship, and from the National High Magnetic Field Laboratory supported by the US National Science Foundation (grant no. DMR-2128556) and the State of Florida.

10.1126/science.adx5775

[1]National High Magnetic Field Laboratory, Tallahassee, FL, USA.
[2]Department of Physics, Florida State University, Tallahassee, FL, USA.
[3]Department of Physics, Ohio State University, Columbus, OH, USA.
Email: sj24u@fsu.edu; skinner.352@osu.edu

CELL BIOLOGY

A nuclear house divided

Certain fungal plant pathogens maintain varying chromosome distributions across multiple nuclei

Timothy J. Mitchison[1] *and* **William T. Sullivan**[2]

Students learn that a eukaryotic cell contains a single nucleus that encapsulates the genome. Most eukaryotes are diploid, which means that each nucleus contains two sets of chromosomes (2N), one from each parent, before DNA replication occurs, and then twice that amount after this duplication (4N). The nuclei of gametes contain a haploid (1N) genome after segregation and separation of parental chromosomes during meiosis. In fungi, the second meiotic division (meiosis II), which generates haploid gametes, is often followed by a round of ordinary cell division (mitosis) to generate eight haploid ascospores in each fruiting body (an ascus). Nuclei containing fewer than a haploid set of chromosomes likely lack many genes necessary for cell or organism viability. On page 784 of this issue, Xu *et al*. (*1*) report that in two species of fungi, the haploid genome is spread across multiple nuclei, providing striking exceptions to these previously universal concepts.

The functional importance and adaptive benefits of syncytial cells growing with their genome split between different nuclei are not obvious.

Sclerotinia sclerotiorum is an important crop pathogen whose genetics and cell biology are little explored (*2*). *S. sclerotiorum* ascospores contain two nuclei, which is unusual, but not unprecedented, for a eukaryotic cell. For example, human heart muscle cells often contain two diploid nuclei (*3*). However, Xu *et al*. found that each nucleus in an *S. sclerotiorum* ascospore does not contain a whole haploid genome as expected. Rather, the 16 chromosomes are distributed between the two nuclei so that each contains approximately half the genome, with different spores exhibiting distinct, apparently random chromosome combinations in each nucleus (see the figure). This unusual observation is difficult to reconcile with classical genetics and cell biology, yet Xu *et al*. show that *S. sclerotiorum* is not alone in its quirkiness by demonstrating that the genome of *Botrytis cinerea*, another plant fungal pathogen, is also distributed across multiple nuclei. The data of Xu *et al*. prove that the genome is distributed between nuclei in an apparently haphazard way; however, showing that this distribution is truly random would require additional statistics.

Strong evidence is required to invalidate the generality of the "one whole genome per nucleus" rule, and Xu *et al*. accordingly provide documentation and results from rigorous testing. Using fluorescence microscopy and electron microscopy, they demonstrated that each *S. sclerotiorum* ascospore contains two distinct nuclei. Chromosome-specific fluorescent hybridization probes revealed that the entire haploid complement of 16 chromosomes is distributed across the two nuclei in each ascospore. Surprisingly, polymerase chain reaction analysis using chromosome-specific primers revealed that the distribution of chromosomes between the two nuclei is erratic and varies substantially between nuclear pairs in different asco-

spores. Xu *et al.* followed this by providing evidence that in *B. cinerea,* 18 chromosomes are distributed across four or five nuclei in each of its ascospores.

Nuclei containing less than a full genome could not support life if present at one nucleus per cell. However, filamentous fungi grow as syncytial mycelia, which are characterized by large, elongated cells containing tens to hundreds of nuclei (*2*, *4*). When *S. sclerotiorum* ascospores germinate and grow into syncytia (multinucleate cells), the complete genome is likely divided between nuclei pairs that contain complementary sets of chromosomes. Nuclei in fungal syncytia divide by a process called karyokinesis. This nuclear division occurs without separation of other cellular material and allows the syncytial mycelium to accumulate hundreds of nuclei per cell (*5*). Although syncytial growth with a population of different nuclei is possible in principle, it presents challenges. For example, nuclei with fewer chromosomes might have a proliferation advantage and outcompete others during DNA replication and karyokinesis. Xu *et al.* speculate that this is prevented by the coordination of replication and division between nuclei, as observed in syncytia of some other fungal species with standard diploid nuclei (*4*, *6*).

Maintaining a genome distributed across multiple nuclei also presents a major challenge for sexual reproduction that requires substantial changes to the canonical events of meiosis and mitosis. Although Xu *et al.* did not elucidate the mechanism by which haploid chromosomes are separated to generate spore nuclei containing approximately half the genome, two possibilities can be envisaged. After meiosis II, haploid nuclei might undergo fission without mitosis. Perhaps a more appealing idea is that replication is suppressed during the extra round of mitosis that occurs after meiosis II, generating the eight haploid spores in *S. sclerotiorum*. This would result in mitosis with unreplicated chromosomes attaching to one of the two spindle pole bodies and segregating to each pole of a future daughter cell in a quasi-random way.

More perplexing is the question of how nuclei with different sets of chromosomes reassemble the full genome before meiosis and ascospore formation. Sexual reproduction in fungi usually involves the fusion of mycelia of different mating types followed by congression of nuclei and then nuclear fusion (karyogamy). This generates diploid nuclei that undergo meiosis to produce haploid spores. Different mating types are thought to exist in *S. sclerotiorum*, but the sexual cycle is poorly understood. Assuming karyogamy occurs in *S. sclerotiorum*, it must include an unknown process that allows pairs of nuclei with complementary sets of chromosomes to recognize each other and fuse to regenerate a full genome before meiosis. Perhaps sister nuclei formed during the ascospore reduction event remain physically linked by a yet unknown structure that persists through multiple rounds of mitosis. Careful tracking of marked nuclei during syncytial growth might reveal such physical connections. How karyogamy could be accomplished in *B. cinerea* with the genome distributed across four to five nuclei is truly puzzling.

The functional importance and adaptive benefits of syncytial cells growing with their genome split between different nuclei are not obvious. Xu *et al.* speculate that syncytial cells might cope with stressful local environments by using nuclei with different chromosomes to generate unbalanced but adaptive gene expression. This would be consistent with observations showing that unbalanced gene expression resulting from abnormal karyotypes can promote survival under stress in yeast (*7*). Dividing the genome among several smaller nuclei might also provide physical benefits to a growing syncytium; the nuclear surface area–to–volume ratio would be larger, which could speed up nuclear transport and perhaps make karyogamy easier.

The discoveries of Xu *et al.* raise many unsolved questions concerning the mechanisms of karyokinesis and karyogamy as well as the biology of nuclei more generally, which will stimulate much interest and may also lead to new ways to combat these destructive crop pathogens. Furthermore, numerous tissues in higher eukaryotes are syncytial (*8*). It will be interesting to investigate whether the adaptive benefit of fungal syncytia, and even the possibility of splitting the genome between different nuclei, apply beyond fungi. □

Newfound nucleus biology

The genome is divided between two nuclei in the ascospores of the fungus *Sclerotinia sclerotiorum* (only three out of 16 chromosomes are shown for clarity). After ascospore germination, chromosomes are divided among nuclei in a growing syncytial cell. Genome separation after meiosis II could occur by nuclear fission (not shown) or by mitosis without a preceding S phase. The events that bring together the separated genome before meiosis are unknown.

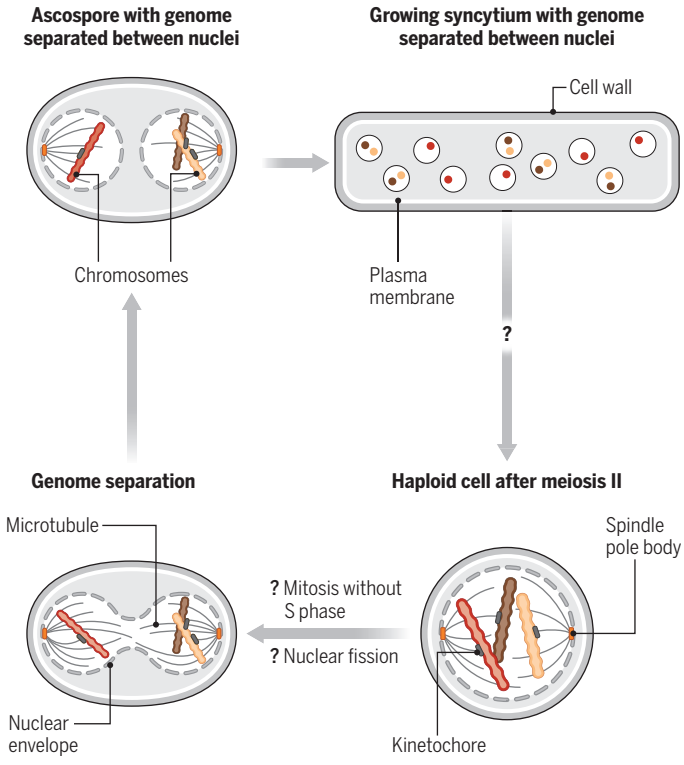

GRAPHIC: A. FISHER/*SCIENCE*

REFERENCES AND NOTES

1. Y. Xu *et al.*, *Science* **388**, 784 (2025).
2. Q. Shang, D. Jiang, J. Xie, J. Cheng, X. Xiao, *Mol. Plant Pathol.* **25**, e13423 (2024).
3. A. N. Paradis, M. S. Gay, L. Zhang, *Drug Discov. Today* **19**, 602 (2014).
4. A. P. Mela, A. M. Rico-Ramírez, N. L. Glass, *Cells* **9**, 2255 (2020).
5. J. C. García Cortés, M. Ramos, M. Osumi, P. Pérez, J. C. Ribas, *Microbiol. Mol. Biol. Rev.* **80**, 779 (2016).
6. A. S. Gladfelter, *Curr. Opin. Microbiol.* **9**, 547 (2006).
7. N. Pavelka *et al.*, *Nature* **468**, 321 (2010).
8. N. G. Peterson, D. T. Fox, *Chromosome Res.* **29**, 245 (2021).

ACKNOWLEDGMENTS

T.J.M. and W.T.S. acknowledge support from the National Institute of General Medical Sciences (grants 131753 and 139595, respectively).

10.1126/science.adx8689

[1]Department of Systems Biology, Harvard Medical School, Boston, MA, USA. [2]Department of Molecular, Cellular and Developmental Biology, University of California Santa Cruz, Santa Cruz, CA, USA. Email: timothy_mitchison@hms.harvard.edu

CELLULAR NEUROSCIENCE

Astrocytes, hidden puppet masters of the brain

Astrocyte signaling pathways influence neuronal networks and behavioral responses to neuromodulators

Cagla Eroglu[1,2]

It is accepted that neuromodulators such as norepinephrine and dopamine bind to and activate receptors on neurons to influence the activity of neuronal circuits and plasticity (changes in strength or wiring patterns) of synaptic connections, thus shaping the behavior of the organism. Unlike classical neurotransmitters (e.g., glutamate), which typically mediate fast, point-to-point synaptic communication, neuromodulators diffuse broadly through neural tissue to regulate the strength, duration, and plasticity of neuronal signaling. Emerging evidence now implicates astrocytes—traditionally seen as passive support cells—as active players in neuromodulation (*1*–*3*). However, whether astrocytes are necessary intermediaries in neuromodulation or represent regulatory adjuncts to neuronal actions is unclear. On pages 763, 769, and 776 of this issue, Guttenplan *et al.* (*4*), Chen *et al.* (*5*), and Lefton *et al.* (*6*), respectively, address these gaps in knowledge by reporting that astrocytes are indispensable for neuromodulatory signaling across diverse neural circuits, behavioral contexts, and species.

Astrocytes tightly ensheathe neuronal processes in the brain, particularly synapses, and can sense neuromodulators through G protein–coupled receptors (GPCRs), a family of cell-surface receptors that relay external signals into cells by modulating levels of secondary messengers such as calcium or cyclic adenosine monophosphate (cAMP). Astrocytes then respond by releasing gliotransmitters such as adenosine triphosphate (ATP) or adenosine, which influence neuronal activity and thus behavior. Previous work in fruit fly (*Drosophila melanogaster*) larvae indicated that astrocytic GPCR signaling by the neuromodulators octopamine and tyramine, which are functional analogs of mammalian norepinephrine, modulates olfactory-driven movement and touch-induced startle responses (*1*). Guttenplan *et al.* built on this finding by investigating how astrocytes use GPCR signaling to modulate neuronal circuit activity and behavior in flies and in astrocytes isolated from rat brains. They report that tyramine activation of astrocytic octopamine-tyramine receptors (a type of GPCR) induced intracellular calcium elevations in *Drosophila* and made astrocytes more responsive to neurotransmitters such as dopamine and glutamate.

Guttenplan *et al.* found that this gating of astrocytic responses to dopamine was mediated by a GPCR-driven reduction in cAMP levels, occurring independently and in parallel to calcium signaling, which then regulated the localization of dopamine receptors to the astrocyte surface. Using genetic approaches, the authors went on to investigate the role of astrocytic cAMP signaling in *Drosophila*. To do this, they reduced cAMP in astrocytes by blocking the expression of specific proteins (called $G_{\alpha i}$ proteins) that normally control its levels. This manipulation changed the activity of dopamine-releasing neurons, measured by imaging their calcium signals. Fly larvae with disrupted astrocytic cAMP signaling showed disrupted larval righting reflex, an innate behavior used to measure motor coordination. Astrocytic manipulations delayed the ability of larvae to quickly turn themselves upright, demonstrating that astrocytic cAMP signaling contributes directly to neuromodulation of motor behavior.

Guttenplan *et al.* also identified a similar GPCR-cAMP signaling cascade in response to dopamine and norepinephrine in astrocytes isolated from rat brains and grown in culture, indicating an evolutionarily conserved mechanism. The authors used genetic (RNA interference) and pharmacological (adenylate cyclase inhibitors) approaches to image astrocytic calcium responses to various neurotransmitters. They found that lowering cAMP signaling—either directly or by using an α2 adrenergic receptor agonist to mimic norepinephrine—enabled astrocytes to respond robustly to dopamine, supporting the existence of a conserved astrocytic neuromodulatory signaling mechanism in mammals. The authors acknowledge that the potential altered responsiveness of rat astrocytes grown outside their natural brain environment and the incomplete validation of adrenergic receptor expression and specificity in mammalian astrocytes in vivo represent limitations of the study. Nevertheless, these findings lay important groundwork for future studies to further explore and confirm this astrocytic gating mechanism within intact mammalian brains and to understand its broader role in modulating neuronal circuits and behaviors in vivo.

Previous work in zebrafish (*Danio rerio*) showed that astrocytes respond to norepinephrine with calcium signals that trigger ATP release, influencing the transition between behaviors in an active-passive behavioral assay (*2*). In this assay, zebrafish larvae are exposed to repeated visual or tactile stimuli, which prompt vigorous swimming responses (active state). Over repeated unsuccessful attempts to swim forward in response to these stimuli, larvae gradually transition to a passive, disengaged state characterized by diminished swimming efforts. This previous work firmly established a role for astrocytes in

Astrocytes take center stage in neuromodulation

Neuromodulators (specifically norepinephrine in mammals and fish, and tyramine in fruit flies) bind to G protein–coupled receptors (GPCRs) on the surface of astrocytes, initiating an increase in intracellular calcium (Ca^{2+}) concentrations and a decrease in cyclic adenosine monophosphate (cAMP) signaling. Increased calcium triggers the release of adenosine triphosphate (ATP), which is converted to adenosine in the extracellular space. Adenosine binds to receptors on the presynaptic terminal to inhibit the release of neurotransmitter from synaptic vesicles, thus modulating neuronal circuit activity. The decrease in cAMP signaling results in increased trafficking of dopamine receptors to the surface of the astrocyte, thus gating astrocytic responsivenes to dopamine.

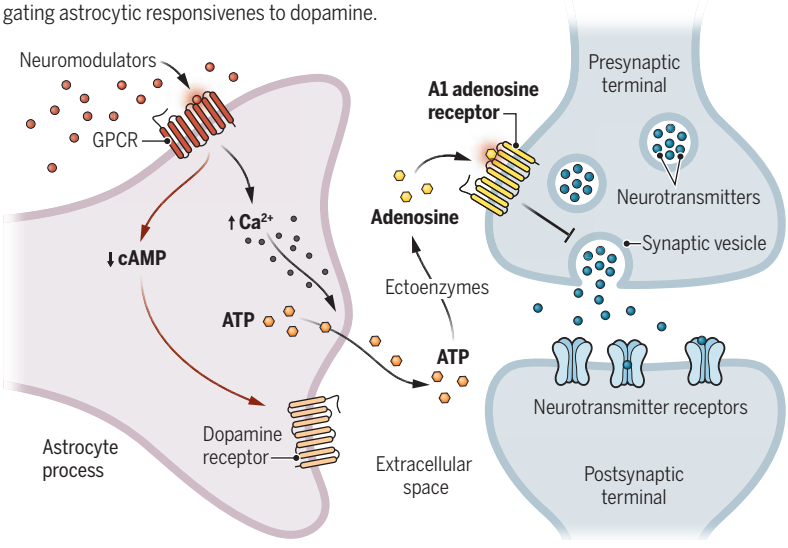

GRAPHIC: K. HOLOSKI/*SCIENCE*

control of behavior; however, the specific astrocytic receptors activated by norepinephrine, and how their activation causes behavioral state transitions, were unknown. Chen *et al.* addressed these gaps in knowledge by showing that norepinephrine from the locus coeruleus—a small brain region important for regulating attention, stress, and arousal—activates astrocytic α1 adrenergic receptors in zebrafish larvae, triggering calcium signaling and ATP release. They also report that astrocyte-derived ATP is rapidly converted extracellularly into adenosine, which acts presynaptically through neuronal adenosine receptors to modulate neuronal activity (see the figure).

To link astrocytic signaling with behavioral states, Chen *et al.* used the active-passive behavioral assay paired with live imaging of a calcium indicator in astrocytes. The authors show a direct correlation between norepinephrine-driven astrocytic calcium elevations and the progressive shift toward this passive behavioral state. Targeted astrocytic manipulations—including chemogenetic and optogenetic control of astrocytic calcium signaling or pharmacological inhibition of ATP-to-adenosine conversion—provided further evidence that astrocytic ATP-to-adenosine signaling is a critical mechanism that modulates neuronal circuits underlying the decision to actively engage or disengage from behavioral actions. Notably, a similar astrocyte-driven mechanism was previously reported in mice, where dopamine-induced astrocytic calcium elevations and ATP release in the nucleus accumbens modulated reward-related synaptic transmission and influenced behavioral responses to psychostimulants (*3*), suggesting broad evolutionary conservation of astrocyte-mediated neuromodulation.

The study by Lefton *et al.* provides compelling evidence from electrophysiological experiments in ex vivo mouse hippocampal brain slices that norepinephrine modulates synaptic transmission exclusively via astrocytes. They identified astrocytic α1A adrenergic receptors as crucial receptors that transduce norepinephrine signals into intracellular calcium increases within astrocytes. In agreement with the observations of Chen *et al.* in zebrafish larvae, the elevation in astrocytic calcium caused release of ATP, which was subsequently metabolized extracellularly to adenosine. This adenosine then bound to A1 adenosine receptors on the presynaptic terminal, thus inhibiting presynaptic neurotransmitter release. Using optogenetics to selectively stimulate norepinephrine release and electrophysiological methods (patch-clamp recordings and paired-pulse facilitation assays) to study synaptic activity and plasticity, Lefton *et al.* demonstrated that norepinephrine-induced synaptic depression depended specifically on astrocytic function. Genetic approaches in which astrocytic or neuronal α1A adrenergic receptors were selectively deleted also provided evidence that astrocytes, not neurons, are the primary mediators of norepinephrine's neuromodulatory effects in hippocampal synaptic plasticity. An important area for future investigation is how this astrocytic mechanism influences hippocampus-dependent behaviors, such as spatial learning and other memory processes.

The studies by Guttenplan *et al.*, Chen *et al.*, and Lefton *et al.* establish astrocytes as active intermediaries linking neuromodulators directly to neuronal activity and behavior. Together, these findings position astrocytes as essential nodes in neural signaling networks. Several key questions remain, such as why did astrocytes evolve to serve as intermediaries in neuromodulation? Furthermore, the roles of astrocytic neuromodulation in higher brain functions such as decision-making, sensory perception, and learning and memory remain largely unexplored. A study using live imaging in awake mice found that hippocampal astrocytes actively encode spatial information about reward locations, suggesting that astrocytes may directly contribute to cognitive functions traditionally attributed solely to neurons (*7*). Future work would benefit from examining astrocytic neuromodulation in other mammalian brain regions, such as the cortex, amygdala, basal ganglia, and thalamus, and in behaviors related to higher brain functions. Some technical issues, particularly regarding cell-type specificity and efficiency of genetic manipulations, also need to be addressed. Advances in genetic tools have enabled the selective attenuation of G_q GPCR signaling in astrocytes (*8*). This attenuation resulted in specific behavioral deficits in mice, underscoring the necessity of precise genetic approaches to dissect astrocytic functions and their effects on behavior.

...astrocytes, not neurons, are the primary mediators of norepinephrine's neuromodulatory effects in hippocampal synaptic plasticity.

The findings of Guttenplan *et al.*, Chen *et al.*, and Lefton *et al.* signify the importance of expanding the conceptual framework for investigating neurological and psychiatric disorders that involve dysregulation of neuromodulation. For instance, disorders such as depression, anxiety, and schizophrenia, which are traditionally attributed to neuronal neuromodulatory receptor dysfunction, may stem from disrupted astrocyte signaling. Exploring the potential clinical applications of astrocyte-targeted interventions may unveil new therapeutic avenues for these disorders. □

REFERENCES AND NOTES

1. Z. Ma, T. Stork, D. E. Bergles, M. R. Freeman, *Nature* **539**, 428 (2016).
2. Y. Mu *et al.*, *Cell* **178**, 27 (2019).
3. M. Corkrum *et al.*, *Neuron* **105**, 1036 (2020).
4. K. A. Guttenplan *et al.*, *Science* **388**, 763 (2025).
5. A. B. Chen *et al.*, *Science* **388**, 769 (2025).
6. K. B. Lefton *et al.*, *Science* **388**, 776 (2025).
7. A. Doron *et al.*, *Nature* **609**, 772 (2022).
8. J. Nagai *et al.*, *Neuron* **109**, 2536 (2021).

ACKNOWLEDGMENTS

C.E. thanks K. Sakers, N. Elazar, J. Ramirez, G. Sejourne, N. Brose, and D. Quintero for critical input. C.E. is a Howard Hughes Medical Institute Investigator.

10.1126/science.adx7102

[1]Department of Cell Biology, Duke University Medical Center, Durham, NC, USA.
[2]Howard Hughes Medical Institute, Duke University Medical Center, Durham, NC, USA.
Email: cagla.eroglu@duke.edu

CONSERVATION

Deliberate extinction by genome modification: An ethical challenge

What circumstances might justify deliberate, full extinction of a species?

Gregory E. Kaebnick[1], James P. Collins[2], Athmeya Jayaram[1], Rebecca G. Tiernan[2], Katie Barnhill[3], Lucy Carter[4], Munamato Chemhuru[5], Pablo Fresia[6], Bruce Jennings[7], Curt Meine[8], Paul Ndebele[9], Clare Palmer[10], Christopher Preston[11], Kent H. Redford[12], Yasha Rohwer[13], Ronald Sandler[14], Maxwell J. Scott[15], Riley Taitingfong[16], Laurie Zoloth[17]

Among the ways that genome modification could be used to modify wild populations of organisms, the deliberate outcome of fully eradicating a species has received little critical attention. The lack of discussion leaves a difficult ethical question unresolved: When so much attention is given to the value of biodiversity and the conservation of species, what circumstances, paradoxically, might justify the deliberate, full extinction of a species? At least one species is now a preliminary candidate for full extinction, and cases under consideration for temporary suppression and local extinction might pose a risk of full extinction. We discuss three cases in which genome modification might be used to eradicate a species. Together, we argue, these cases suggest that deliberate full extinction might occasionally be acceptable, but only extremely rarely. The cases also highlight tensions within some widely held views about the conservation of species and the governance of genome editing.

To encourage more critical attention to these tensions, all of the authors—environmental ethicists, bioethicists, conservation biologists, ecologists, social scientists, and scientists—participated in a May 2024 workshop to study the moral question posed by deliberate extinction through genome editing. The discussion that follows below draws upon that event.

PROSPECTIVE CASES

In principle, a spectrum of techniques for altering genomes could cause or facilitate full extinction of a species. The three cases on which we focus aim either at full extinction (global eradication outside of ex situ holding facilities) or at local extinction (eradication within a limited portion of a species' range) that carries a risk of full extinction.

New World screwworm

The New World screwworm (*Cochliomyia hominivorax*) is a leading, though little-discussed, candidate for full extinction, probably by means of a combination of genomic strategies now under development. Screwworm is a fly that in its larval stage is an obligate parasite of warm-blooded animals. The flies lay eggs on mucosal surfaces and wounds, and the larvae burrow into and consume the host's flesh, causing bacterial infections that can kill the host through sepsis. Screwworm is considered a severe threat to livestock and also infects wild animals and sometimes humans, as suggested by the species name *hominivorax*. Screwworm has already been eradicated from North America, some Caribbean islands, and (until recently) Central America using the sterile insect technique (SIT), in which mass-reared pupae are exposed to ionizing radiation that produces sterilizing genetic mutations. Flies are then allowed to emerge and are released in vast numbers, usually from planes, to saturate a release zone. The goal of the release is that wild-type females mate with sterilized males, preventing the wild population from reproducing.

Screwworm persists across most of South America, where the costs of SIT are likely prohibitively high. SIT can be greatly improved, however, by using a strain of screwworm genetically modified so that female larvae mature only in the presence of tetracycline and can therefore be eliminated from the populations raised for release (*1*). In business-as-usual SIT, both males and females are released. With females eliminated, the cost of rearing flies is reduced and, because females require a higher level of radiation than males, the radiation can be reduced, which means the males remain more fit and are likelier to mate. Additionally, because sterilized females are not among the released flies, the males can mate only with wild-type females, which maximizes their impact.

The modified strain also allows for alternatives to SIT that would be yet more effective. For example, releasing modified males without sterilization would transmit the female-killing modification to all offspring and to residual numbers of a few subsequent generations—an example of the technique known as female-specific release of insect with a dominant lethal (fsRIDL) (*1*). Alternatively, the modification could be coupled with a gene drive so that the trait was transmitted to nearly all offspring through many generations (*2*). A combination of these techniques is sufficiently promising that full eradication of the species has emerged as a future possibility.

Use of SIT to eradicate the New World screwworm locally has been widely supported in North and Central America (*3*). There is also now interest in South America, starting in Uruguay (*4*, *5*) and with the assistance of the International Atomic Energy Agency (IAEA) (which, given its expertise in radiation-based technologies, helps member countries develop and use SIT), the Food and Agriculture Organization of the United Nations, the US Department of Agriculture, and the Panama–United States Commission for the Eradication and Prevention of Screwworm, to continue the effort across the remainder of the screwworm's range. Although a plan published by IAEA envisions eradication solely through standard SIT (*4*), improved SIT and fsRIDL approaches, which have already been developed, would greatly increase both cost-effectiveness and the odds of success, though approval has not yet been sought. A gene drive technique would require further research and approval, but, if successfully developed, would increase effectiveness and reduce costs still further.

The argument for moving forward is multipronged. Screwworm parasitism of animals causes substantial suffering, and parasitism of domestic animals, including livestock, is thought to diminish human food security (*4*) and raises special concerns about animal welfare, because humans arguably bear greater responsibility for animals under their care than for wild animals. Infections are difficult to treat, and, from reports of human cases, death from screwworm infection is painful and slow (*6*). The extent of the public health threat posed by

screwworm is not certain, but any flesh-eating insect that caused occasional human mortality in the Global North would almost certainly be marked for suppression if not eradication.

The case against extinction consists of the species' intrinsic value (that is, any value the species possesses in and of itself—for what it is, rather than for what it provides or does for others) plus the value of any environmental benefits it confers, such as by holding deer populations in check or by providing food for predators. But these claims are limited. Screwworm is considered among the worst of pests in the cultures where it is present. Whatever intrinsic value it possesses must therefore be a value that a species possesses just by virtue of being a species, but claims about that kind of intrinsic value are highly contested. Although the environmental role of screwworm is not well studied, some research suggests that the fly is not ecologically vital (*7*), and its eradication is not known to have had substantial environmental impacts in North and Central America.

The broad support for use of SIT to achieve a series of local extinctions of screwworm suggests that the argument in favor of fully eradicating screwworm is likely to be compelling for many people—especially in light of a recent resurgence of screwworm in Central America, because the resurgence suggests that a permanent solution may be possible only with complete eradication. Most of our own author group agree that it is compelling.

Anopheles gambiae mosquitoes

Possible cases of temporary suppression or local extinction of species through genome editing also raise questions about full extinction, insofar as a risk of inadvertent full extinction should be taken into account in those cases. Mosquito species in the *Anopheles gambiae* complex, which are vectors for *Plasmodium* species that cause human malaria, are possible targets for temporary suppression and, at least in principle, full extinction. Malaria kills upward of half a million people annually and imposes a considerable economic toll on many countries in sub-Saharan Africa (*8*). Elimination of malaria might be facilitated through vector control strategies such as a gene drive that prevents development of one of the sexes, biasing the sex ratio and leading to a population crash (*9*). This strategy poses a possible though very slight risk of full extinction of anopheline vectors of malaria and perhaps, through interbreeding, of nonvector anopheline mosquitoes. Given the enormous human burden of malaria, which has been growing in recent years, the argument for extinction of *An. gambiae* is arguably even stronger than the argument for extinction of screwworm. Nor does the overall value of mosquitoes seem likely to outweigh the harm they cause humans. The ecological role of any one *An. gambiae* species would likely be filled by another (*9*). However, we can avoid deciding in favor of extinction in this case. Eliminating malaria requires eradication only of *Plasmodium*, not of the vectors, and *Plasmodium* can be eliminated with a combination of measures that interrupt its life cycle without necessarily wiping out its vector. Such measures could include bed nets, health care infrastructure that brings infected people indoors and prevents reuptake of *Plasmodium* into mosquitoes, the recently approved malaria vaccine, and perhaps a gene drive that modifies mosquitoes in ways that prevent them from being vectors for *Plasmodium*. In many places, *Plasmodium* has been eliminated in part by attacking the mosquito directly, through insecticides or habitat modification. In Africa, gene drives that cause temporary and local population suppression might prove to be necessary, but most commentators do not call for full extinction of the vector (*9*). Eliminating *Plasmodium* in this way would also be deliberate species extinction through genome modification, but one more easily justified.

House mouse, black rat, Norway rat

Several mammalian species are potential targets for sex-biasing gene drives meant to achieve local extinction in places where they are non-

New World screwworm larvae use tusklike mandibles to consume the flesh of warm-blooded animals, causing infections that can be fatal to the host.

native and pose a severe threat to native species. Foremost among these species are the house mouse (*Mus musculus*), the black rat (*Rattus rattus*), and the Norway rat (*Rattus norvegicus*), which threaten endangered bird species on islands across Oceania (*10*). Such a drive would be more humane, more targeted, and less environmentally damaging than population control by means of traps and poisons, but it might also present a very slight risk of global extinction of the target species, if individuals modified with the drive escaped the geographical containment of the island and if genes targeted by the drive were conserved across the species. Moreover, these species are widely viewed as pests, and they threaten global extinction of a large number of endemic species on islands where they are invasive. Nonetheless, neither we nor any other commentators, even among those who advocate use of such a drive, hold that local extinction of invasive rats or mice is permissible if there is a nonnegligible risk of global extinction (*11*). To help head off such risks, research on gene drives has focused on developing drives that are temporally limited or can be targeted at particular subpopulations of the species in question.

IMPLICATIONS FOR CONSERVATION

As tools for species population control, genomic technologies such as SIT, RIDL, and gene drive are designed to target a species precisely, in contrast to alternative strategies such as habitat modification, poisoning, or trapping, which typically have effects beyond the targeted species. Because these technologies can affect only the target species, avoiding unnecessary collateral effects, the prospect of using them to eradicate a species is a lens for examining the value of species themselves. That value—a combination of any intrinsic value and any benefit it provides others—has been paramount in conservation philosophy and policy, as the Endangered Species Act in the US attests. We believe that the cases above, taken together, illustrate that high value. They show that even decisions to eliminate parasites and vectors of disease require extremely compelling arguments as well as confidence that the eradication poses low risk to other species.

PHOTO: USDA/NATURE SOURCE/SCIENCE SOURCE

The screwworm case, however, shows that the value is not absolute and overriding. Most of our group agree that, under extremely rare and compelling circumstances, deliberate extinction through genome editing is permissible.

The cases may also have repercussions for how species are valued. Western conservation ethicists and biologists often argue that the intrinsic value of species should be equal across species and should not track subjective human preferences (*12*). However, the willingness to eradicate screwworm and risk extinction of anopheline mosquitoes, though justified in terms of the harms these species pose, might be influenced by a dislike of parasitism or a disregard for species perceived as being lower on some understanding of a phylogenetic tree. These views need clarifying and assessment. Similar views are tacitly present elsewhere, such as in the conservation biology practice of eradicating parasitic mites and insects (the condor louse is an example) from endangered fauna on which those parasites depend. The idea that species can be ordered by moral status resembles the ancient Greek and medieval European concept of the *scala naturae*, or "great chain of being."

Western scholars now widely reject the *scala naturae* (*13*), but other philosophical traditions sometimes uphold similar orderings. Some lines of sub-Saharan African environmental thought, for example, recognize a "hierarchy of existence" on the ground that different species have different ontological and teleological characteristics (*14*). Even many in the West may not regard a *Plasmodium* species as equal in value to the mosquitoes that carry it, much less to humanity. A final set of questions that the cases raise for conservation is about the widely shared view that genome modification is particularly unappealing, compared to other ways of intervening in nature, because of a special moral status possessed by genomes or by genetic and evolutionary processes that are closely connected to organisms' identity. In contrast to genome modification, the use of SIT has historically aroused little to no public resistance. Yet, because both genome modification and SIT work by making genetic changes, they appear to be on par with each other in terms of their goals: They alter genomes in ways that lead to population suppression. Perhaps genome modification, which allows for more precise alterations, is more troubling because it seems to impose human design on the genome; because SIT is less precise, it appears to involve less control. Yet the irradiation in SIT is timed and titrated to accomplish exactly enough genomic scrambling to sterilize insects without disabling them. Variance in the genetic effects of radiation is not a lack of control; rather, it's the chosen method to achieve sterilization. The potential improvements in SIT blur the lines further. If SIT already is genetic modification of an organism, then why not carry out SIT on a genetically modified strain of the organism? And if using a genetic modification is acceptable in SIT, then why is it unacceptable to use that same modification in fsRIDL, or coupled with a gene drive, to achieve the same results more efficiently?

IMPLICATIONS FOR GOVERNANCE

Even if there were greater clarity on substantive moral issues such as the value of species or the disvalue of genome modification, there can be no simple, universally applicable criteria for handling decisions about when species extinction through genome editing should be pursued and when the effort should not be made. Both action and inaction have consequences and require justification. Ultimately, these decisions depend on value trade-offs—a weighing of competing fundamental moral commitments—that will be different in each case and will be seen differently in different cultures and communities.

Partly because the trade-offs depend on stakeholders' input, and partly to uphold basic principles of democratic legitimacy, decisions about extinction through genome modification should be made through appropriate collective decision-making processes. A key governance issue for these decision-making processes is the balance of local and wider publics. For most decisions about releasing genetically modified organisms into the shared environment, local publics should have primacy in the decision-making (*15*). Their interests are most clearly at stake, and they likely have specific knowledge of many of the possible social and ecological consequences of the release. Indigenous Peoples, in particular, should have a primary role, as they hold distinct rights to determine the use of their lands and resources. Giving local publics a primary role in the decision can also help prevent the perpetuation of historical injustices that have prevented marginalized people from participating in environmental policy decisions, particularly in postcolonial contexts. Because both technology development and technology governance are dominated by the Global North, care must be taken to ensure that voices from the Global North are not overly influential in decisions about release, especially in the Global South.

In decisions to move forward with local extinction, especially of invasive and nonnative organisms, the preferences of local publics should therefore be weighted most heavily, if the risk of effects outside the local area is very low. Decisions to move forward with full extinction, however, may challenge the priority of local preferences (though on this question, too, there will be no one strategy that can be applied across cases). People who live distant from a species' range have asserted a stake in the planet's shared ecological heritage and have supported international efforts to preserve species. The argument for recognizing that publics in the Global South should have the same freedoms to make decisions about their environment that have long been claimed in the Global North is very powerful. So, too, is the need for a strong, collective approach to the decisions about species' existence. □

REFERENCES AND NOTES

1. C. Concha *et al*., *BMC Biol*. **14**, 72 (2016).
2. M. J. Scott *et al*., *Commun. Biol*. **3**, 424 (2020).
3. S. Zhang, "America's never-ending battle against flesh-eating worms," *The Atlantic*, 26 May 2020.
4. International Atomic Energy Agency, "Propuesta de un Plan Estratégico para la Erradicación de la Miasis Causada por el Gusano Barrenador del Ganado en América del Sur," September 2020; https://www.iaea.org/sites/default/files/21/03/plan-estrategico.pdf.
5. A. Menchaca, *Agrociencia Uruguay* **26**, 1059 (2022).
6. Centers for Disease Control and Prevention, "Clinical Overview of New World Screwworm Myiasis"; https://www.cdc.gov/myiasis/hcp/clinical-overview/index.html.
7. I. Etchevers *et al*., *Agrociencia Uruguay* **26**, 2 (2022).
8. J. Fang, *Nature* **466**, 432 (2010).
9. The High-Level African Panel on Emerging Technologies, *Gene Drives for Malaria Control and Elimination in Africa* (African Union Development Agency and New Partnership for Africa's Development).
10. C. M. Leitschuh *et al*., *J. Responsib. Innov*. **5**, S1 (2018).
11. J. L. Teem *et al*., *Front. Bioeng. Biotechnol*. **8**, 452 (2020).
12. M. E. Soulé, *Bioscience* **35**, 11 (1985).
13. R. Darr, *Religions (Basel)* **15**, 520 (2024).
14. M. Chemhuru, "The Moral Status of Nature: An African Understanding" in *African Environmental Ethics: A Critical Reader*, M. Chemhuru, Ed. (Springer, 2019).
15. N. Kofler *et al*., *Science* **362**, 527 (2018).

ACKNOWLEDGMENTS

This essay builds upon discussions that were held at a workshop organized by The Hastings Center and Arizona State University, held at Arizona State University in May 2024 and funded by National Science Foundation grant 2317702 (G.E.K., J.P.C., A.J.).

10.1126/science.adv4045

[1]The Hastings Center, Garrison, NY, USA. [2]School of Life Sciences, Arizona State University, Tempe, AZ, USA. [3]Genetic Engineering and Society Center, North Carolina State University (NCSU), Raleigh, NC, USA. [4]Commonwealth Scientific and Industrial Research Organisation, Brisbane, Australia. [5]Department of Philosophy and Religious Studies, Great Zimbabwe University, Masvingo, Zimbabwe. [6]Institut Pasteur de Montevideo, Montevideo, Uruguay. [7]Center for Humans and Nature, Libertyville, IL, USA. [8]Aldo Leopold Foundation, Baraboo, WI, USA. [9]Milken Institute School of Public Health, George Washington University, Washington, DC, USA. [10]Department of Philosophy, Texas A&M University, College Station, TX, USA. [11]Department of Philosophy, University of Montana, Missoula, MT, USA. [12]Archipelago Consulting, Portland, ME, USA. [13]Oregon Institute of Technology, Wilsonville, OR, USA. [14]Department of Philosophy, Northeastern University, Boston, MA, USA. [15]Department of Entomology and Plant Pathology, NCSU, Raleigh, NC, USA. [16]Native Nations Institute, University of Arizona, Tucson, AZ, USA. [17]Divinity School, The University of Chicago, Chicago, IL, USA. Email: kaebnickg@thehastingscenter.org

BOOKS ET AL.

LABORATORY ANIMALS

Very good dogs

The beagle has sacrificed much for biomedical research—was it worth it? **Barbara J. King**

In 1962, visitors to the annual Picnic Day at the University of California, Davis, were invited to tour the campus's "world-famous" beagle colony. Six years later, a Davis newspaper reported that for locals, a Sunday drive often included a stop to see those same beagles. As historian Brad Bolman explains in his exquisitely researched *Lab Dog: What Global Science Owes American Beagles*, the Davis colony was one node in a national network of research efforts—some highly public and others more secretive—that spanned decades and put beagles at the heart of scientific endeavors to understand, safeguard, and improve human health.

The Davis dogs were atomic beagles, "high-quality physiological proxies" used to study the effects of radiation on longevity and reproduction in ways that were intended to be translatable to humans. The colony had been founded in 1951 as part of a huge postwar project that reflected Americans' uneasy relationship with radiation after the dropping of atomic bombs on Hiroshima and Nagasaki. Plans for "an eagerly anticipated fleet of nuclear-powered aircrafts and ships" meant that pilots of the future needed irradiated dogs to confirm which features of this plan were safe and which were not.

The history of US biomedical science is, in large part, a history of beagles forced to become laboratory tools, not only for radiation research but also for studies that tested drugs, assessed smoking risks, and analyzed cognitive deterioration. In tracing this history, Bolman effectively deploys two central concepts: conformation and species projection. Conformation describes the worlds of shared meaning and culture that dogs and humans co-construct—a recognition that individuals across species may shape each other's lived experiences. Species projection is the practice of imagining nonhuman laboratory organisms as "living exemplars of past, present, or future forms of life."

In smoking studies, for instance, machines customized for dogs allowed (that is, compelled) beagles to inhale smoke as stand-ins for human smokers. In this case, beagles were required to become not only physiological proxies and withstand lung damage but also emotional proxies as analogs of human smokers. Some beagles expressed signs of great pleasure—tail-wagging, rushing toward the apparatus—as they anticipated an opportunity to inhale smoke, thus becoming true smokers and "experiencing and performing elements of that conformation of life."

But why beagles, specifically? Before delving into the experiments, Bolman describes the entangled nature of beagle breeding and the American eugenics movement. The dogs, he notes, were subject to intense genetic shaping that rendered them small yet long-lived, tractable, and charming. As beagles increasingly began to suit experimental researchers because of these characteristics, "momentum from earlier experiments frequently became its own justification" as scientists preferred to share data on a known animal. (I offer a small critique here: Bolman traces the interconnections among institutions and individual scientists around experimental beagle deployment in such fierce detail across decades that at times I struggled to keep the recitation of names coherently ordered in my mind.)

Scientists and nonscientists alike find it difficult to resist the canine's many charms.

Lab Dog: What Global Science Owes American Beagles
Brad Bolman
University of Chicago Press, 2025. 384 pp.

Between 1985 and 2015, the American laboratory industry produced nearly 50,000 beagles a year. With the rise of companion-animal science, the centrality of the laboratory dog is shifting somewhat now. Bolman notes that this change is especially apparent in the realm of research on cognitive changes in aging through initiatives, such as the Dog Aging Project, that work with "enrolled pet dogs." More and more, researchers invite dog guardians to volunteer their dogs for studies akin to citizen-science initiatives, but with animal partners added. (How might dogs indicate consent, or refusal, for such participation?) This trend, plus current events Bolman discusses, such as the 2022 rescue of 4000 beagles used and abused by the Virginia-based contract research company Envigo, bring beagling science up to date.

In the book's preface, Bolman says that he will adopt "neither a condemnation nor a defense" of animal experimentation. Yet already in the next chapter, he remarks that it is difficult to read about beagles "subjected to lethal doses of radiation" with "a neutral eye" and that many experiments "appear unacceptable, even barbarous." Concluding his analysis, Bolman notes that "some dogs and humans" profited from the research described and then adds that "quite a few dogs were also sacrificed without clearly advancing knowledge in a meaningful way." In my estimation, Bolman fails in his initial intention to remain neutral about beagle experiments, although he is never strident about his views. This refusal of total neutrality serves readers well, and I am grateful for it. With its extensive scholarship and historical analysis framed by attention to issues of multispecies justice, the book is a triumph. □

10.1126/science.adv2848

The reviewer is a research fellow at PAN Works, Wilbraham, MA, USA, and professor emerita of anthropology at William & Mary, Williamsburg, VA, USA. Email: bjking@wm.edu

PHOTO: JUNIORS BILDARCHIV GMBH/ALAMY STOCK PHOTO

ENERGY

Energy's international history and future

Scholars find lessons for today in foundational energy texts with an emphasis on the Global South

Rasoul Sorkhabi

Energy's History: Toward a Global Canon
Edited by Daniela Russ and Thomas Turnbull
Stanford University Press, 2025.
292 pp.

Energy history as a modern field of research emerged prominently in the 1970s when two entirely different movements dominated political and intellectual discourses. On the one hand, the first oil shock in 1973 and the second oil shock in 1979 motivated Western industrial countries to secure energy resilience and diversify energy supplies. On the other hand, a grassroots environmental movement against industrial pollution advocated limiting growth and resource use reform (*1*–*3*).

These two conflicting sociopolitical movements have continued to the present day, and one of the ways to understand and accommodate them is to investigate energy history. There are several excellent histories of energy. Two of my favorites are Vaclav Smil's *Energy and Civilization* and Richard Rhodes's *Energy: A Human History*. However, these "global" histories are heavily West-centered, and their references to the rest of the world, particularly Asia, are largely two-millennia-old, prehistoric, or ancient stories to provide a context for the rise of Western energy technologies. The new book *Energy's History: Toward a Global Canon*, edited by Daniela Russ and Thomas Turnbull, shifts readers' perspectives from a monolithic history of world energy to a pluralistic one—and from global generalizations to important specifications about the modern Global South.

Workers teach trainees how to build a mine tunnel in Kushiro, Japan, in 2023.

Each of the book's 12 chapters revolves around a foundational article published by a pioneering scholar decades ago. For instance, a chapter on the Organization of the Petroleum Exporting Countries (OPEC) and Venezuela's oil centers on a 1967 manifesto by Juan Pablo Pérez Alfonzo (*4*), a key founder of OPEC and Venezuela's first minister of mines and petroleum. In this way, the book links the often-forgotten voices of the past to today's problems of economic development and energy use.

The book opens with the story of Brazil's program to convert the country's vehicles from gasoline to biofuel. This has been the largest and longest experiment of its kind. Brazil, itself an oil-producing country, saved millions of barrels of oil through this initiative, but the massive plantations of sugarcane needed to produce the ethanol required for the conversion have had adverse environmental impacts, including soil erosion, air pollution, and water overuse (*5*). The lesson readers learn throughout the text is that both pros and cons of every type of energy resource and policy must be considered.

Three chapters on Japan, China, and India discuss how these nations—the largest in Asia and all endowed with coal resources—embraced coal as a major fuel source, mimicking similar development paths in the West. The implication made by these three chapters is that current Western efforts to demonize coal use represent a type of "green colonialism." This view may be valid from a historical vantage point, but today's China and India are not the victims of colonial powers, and their energy consumption and environmental footprints are of global significance.

I learned much from the book's chapters on Frederick Tryon, an American economic geologist, and Gleb Krzhizhanovskii, a Russian electrical engineer. These two figures are little known today, but their research work in the 1920s was visionary. Tryon examined the close relationships between energy consumption, or what he called "index of power," and economic growth and output. His thoughts on the impacts of technological changes on human labor and how we can optimally couple energy and development are relevant today. Meanwhile, Krzhizhanovskii recommended that the Soviet Union adopt a centralized economic plan to implement widespread electrification, reasoning that electricity was the power of the future. The Stalin-led Soviet Union instead embraced fossil fuels. The pioneering idea of electrification for development was also shared by the West African barrister Frederick William Dove, who, in 1909, advocated construction of electric power stations in Lagos by private companies because the British colonial government did not prioritize such matters. (This story is covered in chapter 8.)

The book's final chapter is about the 20th-century American economist Julian Simon, who—unlike Paul Ehrlich, author of *The Population Bomb* (1968)—believed that increasing human populations are not a problem, because people are the "master resource" and humans can be counted on to find solutions to both resource production and environmental problems. The "Simon-Ehrlich wager" on how to optimize population growth, economic development, and environmental protection still haunts energy policy today.

Energy's History is a valuable addition to the literature and discourses on energy history and societal progress, problems, and prospects. We need more studies of this sort. Two shortcomings, however, must be mentioned. First, although the book engages with the Global South, all of the contributors live and work in North America or Western Europe. Second, the book's authors are primarily social scientists and historians. Including the perspectives of physical scientists and engineers would have added great value to the volume, especially regarding the upstream (production) side of energy. □

REFERENCES AND NOTES

1. C. A. Reich, *The Greening of America* (Random House, 1970).
2. D. H. Meadows *et al.*, *The Limits to Growth* (Potomac Associates, 1972).
3. E. F. Schumacher, *Small Is Beautiful: A Study of Economics As If People Mattered* (Blond and Briggs, 1973).
4. J. P. Pérez Alfonzo, *El Pentágono Petrolero* (Ediciones Revista Política, 1967).
5. S. Filoso *et al.*, *Renew. Sustain. Energy Rev.* **52**, 1847 (2015).

10.1126/science.ady0842

The reviewer is at the Energy & Geoscience Institute, University of Utah, Salt Lake City, UT, USA. Email: rsorkhabi@egi.utah.edu

PHOTO: BLOOMBERG/CONTRIBUTOR VIA GETTY IMAGES

Flowers near agricultural fields can attract, nourish, and serve as breeding grounds for the natural enemies of invertebrate pests.

PHOTO: CHRISTOPH SCHERBER

Leaving synthetic pesticides behind

In their Research Article, "Pervasive sublethal effects of agrochemicals on insects at environmentally relevant concentrations" (25 October 2024, 10.1126/science.ado0251), L. Gandara *et al.* found that agrochemicals have overwhelmingly negative effects on nontarget insects, even at low dosages. Their results add to an extensive body of evidence (*1*) on the social-environmental costs of synthetic pesticides (*2*). Many of the chronic, sublethal effects that Gandara *et al.* identify may strengthen under global warming, challenging regulatory systems (*3*). Pesticides can also disrupt ecosystems, drive pest resurgence or resistance, and jeopardize food security (*4*). To address the environmental and societal harms caused by pesticides, the global community must act.

Mitigating pesticide effects will require multiple approaches. Chemical pesticides should be progressively replaced with agroecological measures such as invertebrate biological control agents and biopesticides, many of which are cost-effective, environmentally sound, and practicable (*5*). Preventative pest management without chemical pesticides can include planting pest-tolerant varieties (*6*); using light, pheromone, or sticky traps (*7*); removing pest resources, such as harvest residues and alternative host plants; and altering sowing dates (*8*). Other strategies include diversifying crops through intercropping or cover cropping; mulching or organic manuring; establishing flower strips that provide food for predators and parasitic wasps; and raising aquatic animals, such as fish, ducks, or frogs, in cropping fields, where they can prey on insect herbivores or weeds (*9*).

Precision agriculture and digital tools could also decrease pesticide use. Robotics, unmanned aerial vehicles (UAVs), artificial intelligence–based computer vision, and data-driven forecasting or advisory systems can all enable timely, targeted interventions (*10*). Tractor-pulled or autonomous camera–equipped mechanical weeders, for instance, can surgically remove weeds from a standing crop, and UAVs can "precision-drop" natural enemies or deliver biopesticide patch sprays on infestation hotspots. However, the funds and training required to use such technologies limit their accessibility and impact.

Collaboration among farmers; scientists; decision-makers; and supply chain stakeholders, such as suppliers, retailers, and consumers, can facilitate changes that limit pesticide use. For example, financial support can help farmers transition to alternative approaches (*11*). Outreach efforts can adjust consumer expectations about, for example, the aesthetic appeal of harvested produce. Scientists could address farmers' concerns about eventual risks or losses and help adapt strategies to local contexts. Pesticide

policies and regulations should focus on fast-tracking registration for low-risk alternatives, implementing creative incentive schemes, imposing differential pesticide taxation, and valuing the multidimensional benefits of nature-friendly production (*12*).

By clarifying the biophysical, social, and economic determinants of pesticide use and by increasing accessibility to alternatives, global agribusiness and small farmers can improve the ecological resilience of the agrifood system profitably. Committing to this transition will safeguard the interconnected health of plants, people, and the environment.

Nian-Feng Wan[1], Ben A. Woodcock[2], Christoph Scherber[3,4], Kris A. G. Wyckhuys[5,6,7], Zhong Li[1], Xuhong Qian[1,8]

[1]Shanghai Key Laboratory of Chemical Biology, State Key Laboratory of Bioreactor Engineering, School of Pharmacy, East China University of Science and Technology, Shanghai, China. [2]UK Centre for Ecology and Hydrology, Wallingford, UK. [3]Centre for Biodiversity Monitoring and Conservation Science, Leibniz Institute for the Analysis of Biodiversity Change, Museum Koenig, Bonn, Germany. [4]Institute of Organismic Biology, University of Bonn, Bonn, Germany. [5]Chrysalis Consulting, Danang, Vietnam. [6]State Key Laboratory for Biology of Plant Diseases and Insect Pests, Institute for Plant Protection, Chinese Academy of Agricultural Sciences, Beijing, China. [7]School of the Environment, University of Queensland, Saint Lucia, QLD, Australia. [8]Shanghai Engineering Research Center of Molecular Therapeutics and New Drug Development, School of Chemistry and Molecular Engineering, East China Normal University, Shanghai, China. Email: nfwan@ecust.edu.cn

REFERENCES AND NOTES

1. E. Rufo, R. Brouwer, P. van Beukering, *Sci. Rep.* **14**, 31905 (2024).
2. R. Carson. *Silent Spring* (Houghton Mifflin Co., 1962).
3. C. A. Brühl, J. G. Zaller, *Front. Environ. Sci.* **7**, 177 (2019).
4. A. Janssen, P. C. J. van Rijn, *Ecol. Lett.* **24**, 2010 (2021).
5. H. E. Hezakiel, M. Thampi, S. Rebello, J. M. Sheikhmoideen, *Appl. Biochem. Biotechnol.* **196**, 5533 (2024).
6. M. M. Rahaman, K. S. Islam, M. Jahan, *J. Health Poll.* **8**, 181203 (2018).
7. C. Vincent, G. Hallman, B. Panneton, F. Fleurat-Lessard, *Annu. Rev. Entomol.* **48**, 261 (2003).
8. R. D. Harrison *et al*., *J. Environ. Manage.* **243**, 318 (2019).
9. N.-F. Wan, M. Dainese, Y.-Q. Wang, M. Loreau, *Curr. Biol.* **34**, R587 (2024).
10. P. Batz, T. Will, S. Thiel, T. M. Ziesche, C. Joachim, *Front. Plant Sci.* **14**, 1150748 (2023).
11. R. Chaplin-Kramer *et al*., *Front. Sustain. Food Syst.* **3**, 60 (2019).
12. N. Möhring *et al*., *Nat. Food* **1**, 535 (2020).

COMPETING INTERESTS

K.A.G.W. is the chief executive officer of Chrysalis Consulting, a firm that provides tailored support to biological control and biodiversity-friendly agriculture.

10.1126/science.adv7806

Revolutionize textile recycling

The rapid rise in textile waste worldwide has brought growing attention to the environmental consequences of fast fashion. In 2015, the global textiles and clothing industry generated an estimated 92 million metric tons of waste (*1*), and projections suggest that this figure could increase by at least 50% by 2030 under a business-as-usual scenario (*2*). Unsustainable waste management practices, such as landfilling, have exacerbated environmental challenges, contributing to the release of micro- and nanoplastics as well as per- and polyfluoroalkyl substances (PFAS) into ecosystems (*3*, *4*). The textile industry urgently needs sustainable interventions that will promote a circular economy.

Governments worldwide have just begun to address the challenges of textile waste. The US Government Accountability Office has recommended that Congress assign a federal entity to lead efforts in reducing textile waste and advancing recycling technologies (*5*). The European Union's Waste Framework Directive mandates that all member states establish separate collection systems for used textiles by the end of 2025, aiming to promote textile circularity and mitigate risks of increased exports, incineration, and landfilling (*6*). China has set goals to achieve a 25% textile recycling rate and the production of 2 million metric tons of regenerated fibers by the end of 2025, with these goals rising to 30% and 3 million metric tons, respectively, by 2030 (*7*).

Global collaboration is essential to enhance textile circularity, reduce waste, and improve recycling systems. Making the transition will require setting clear and measurable outcomes, identifying resource and data needs, and adopting best practices for collaborative action. Developing advanced technologies for reducing and recycling waste textiles should be a priority (*8*). Creating high-efficiency, low-toxicity, and eco-friendly catalysts for recovering valuable materials from waste textiles can play a transformative role in closing the textile life cycle loop and unlocking new opportunities for the textile recycling industry (*9*). Replacing fossil fuels with renewable energy by incorporating innovative chemical engineering approaches, such as microwave and spatiotemporal heating (*10*, *11*), can enhance the sustainability of waste conversion processes. The United Nations Environment Programme (UNEP) textile initiative, launched in 2021, can provide strategic leadership to accelerate these changes (*12*).

By aligning stakeholders' efforts and focusing on shared goals, these initiatives can contribute to achieving a circular economy, reducing greenhouse gas emissions, and limiting global warming. Such actions not only address environmental challenges but also pave the way for a more resilient and resource-efficient future.

Leilei Dai[1], Roger Ruan[2], Hanwu Lei[3], Rui Xiao[1], Huiyan Zhang[1]

[1]Key Laboratory of Energy Thermal Conversion and Control, School of Energy and Environment, Southeast University, Nanjing, China. [2]Department of Bioproducts and Biosystems Engineering, University of Minnesota, Saint Paul, MN, USA. [3]Department of Biological Systems Engineering, Washington State University, Richland, WA, USA. Email: ruixiao@seu.edu.cn; hyzhang@seu.edu.cn

REFERENCES AND NOTES

1. European Parliamentary Research Service, "Environmental impact of the textile and clothing industry: What consumers need to know" (2019); https://www.europarl.europa.eu/thinktank/en/document/EPRS_BRI(2019)633143.
2. The Boston Consulting Group, "Pulse of the Fashion Industry Report" (2018); https://globalfashionagenda.org/resource/pulse-of-the-fashion-industry-2017/.
3. Y.-Q. Zhang *et al*., *Green Chem.* **23**, 5247 (2021).
4. J. R. Lang, B. McKay Allred, G. F. Peaslee, J. A. Field, M. A. Barlaz, *Environ. Sci. Technol.* **50**, 5024 (2016).
5. US Government Accountability Office, "Textile waste: Federal entities should collaborate on reduction and recycling efforts" (2024); https://www.gao.gov/products/gao-25-107165.
6. Waste Framework Directive, "Management of used and waste textiles in Europe's circular economy" (2019); https://www.eea.europa.eu/publications/management-of-used-and-waste-textiles.
7. WTO Trade and Environmental Sustainability Structured Discussions, "China's practices and business approaches in the recycling of waste textiles" (2025); https://www.wto.org/english/tratop_e/tessd_e/09_circ_economy_presentation_by_china.pdf.
8. E. Andini, P. Bhalode, E. Gantert, S. Sadula, D. G. Vlachos, *Sci. Adv.* **10**, eado6827 (2024).
9. L. D. Ellis *et al*., *Nat. Catal.* **4**, 539 (2021).
10. Q. Dong *et al*., *Nature* **616**, 488 (2023).
11. Y. Kwak *et al*., *Sci. Adv.* **9**, eadi8219 (2023).
12. UNEP, UNEP inputs to the Secretary-General report (2023); https://sdgs.un.org/sites/default/files/2024-08/UNEP%20inputs%20to%20the%20SG%20report.pdf.

COMPETING INTERESTS

R.R. is a chief technical adviser to and owns equity in Resynergi, which holds a license to the patented plastic pyrolysis technology.

10.1126/science.adw0473

El Salvador revives metallic mining risks

In 2017, El Salvador became the first nation to ban metallic mining after a historic legal victory against the Pacific Rim Mining Corporation (*1*). The case exposed the severe environmental and social harm caused by mining, including water contamination in the central region of the country, the deaths of four environmental activists, and criminal charges brought against many others (*2*). Although public perception of metallic mining remains overwhelmingly negative (*3*), on 23 December 2024, the Salvadoran Congress revoked the 2017 ban by passing the Ley General de Minería Metálica (Decree 187) (*4*). Congress excluded civil society while drafting the law, and the final version includes inconsistencies and lacks transparency. El Salvador's government should ensure that its policies reflect the needs of its people by guaranteeing access to water and a healthy environment for all Salvadorans.

El Salvador's Lempa River suffers from contamination and other threats, which new metal mining projects could exacerbate.

PHOTO: SOPA IMAGES VIA GETTY IMAGES

Decree 187 grants the state exclusive authority over exploration, extraction, and processing of metallic minerals, bypassing the need for legislative approval (*4*). It also permits public-private partnerships, raising concerns about a return to the inequitable economic arrangements associated with extractive industries (*2*). Although the law prohibits mercury use and claims to promote sustainable mining practices, it fails to explicitly ban other toxic substances, such as cyanide, arsenic, lead, and cadmium. These substances are known to pose serious threats to aquifers, human health, and biodiversity (*5*). Compounding these issues, the law requires no environmental impact assessments during the mining activity cycle.

Although the law restricts mining in protected areas, aquifer recharge zones, and urban settlements, it paradoxically grants the Directorate of Mines discretion to authorize mining in urban areas, disregarding evidence that mining impacts often extend far beyond operational boundaries (*6*). Old mining sites and the areas that surround them exhibit reduced tree density, carbon stocks, and animal and plant species richness, with effects worsening over time (*6*). Moreover, because 63% of metal deposits are concentrated in intermediate- and high-biodiversity zones, metallic mines are disproportionately located in these areas (*7*). In El Salvador, this pattern threatens fragile biodiversity-rich ecosystems, exacerbating deforestation and environmental degradation.

The Lempa River, El Salvador's main water basin, already faces overexploitation, reduced water retention, and contamination (*8*). The government has committed to restoring this vital resource (*9*), but allowing mining would undermine these efforts. Given El Salvador's severe water stress (*10*) and ecological vulnerability (*11*) and the potential socioenvironmental conflicts that mining could trigger (*3*), the government must listen to the scientific community (*12*) and revoke the Ley General de Minería Metálica. To achieve global environmental goals, El Salvador must prioritize environmental and public health over profit.

Diego J. Arévalo-Ayala[1], Guillermo Funes[2], José D. Pablo-Cea[3]

[1]Departament de Biologia Evolutiva, Ecologia i Ciències Ambientals, Facultat de Biologia, Universitat de Barcelona, Barcelona, Spain. [2]San Salvador, El Salvador. [3]Escuela de Biología, Facultad de Ciencias Naturales y Matemática, Universidad de El Salvador, San Salvador, El Salvador. Email: darevaloayala@gmail.com

REFERENCES AND NOTES

1. M. L. Dougherty, "El Salvador makes history" (NACLA, 2017); https://nacla.org/news/2017/04/19/el-salvador-makes-history.
2. J. A. Artiga-Purcell, *Extr. Ind. Soc.* **9**, 101035 (2022).
3. Instituto Universitario de Opinión Pública, "La población salvadoreña opina sobre la minería metálica" (2024); https://uca.edu.sv/iudop/wp-content/uploads/2024/12/Bol.-Mineria-2024.pdf [in Spanish].
4. Diario Oficial, "Decreto No. 187. Ley General de Minería Metálica" (2024); https://www.asamblea.gob.sv/sites/default/files/documents/decretos/E9287517-FFF5-42CA-B65E-DCDD48E5EDCA.pdf [in Spanish].
5. M. Jaishankar, T. Tseten, N. Anbalagan, B. B. Mathew, K. N. Beeregowda, *Interdiscip. Toxicol.* **7**, 60 (2014).
6. H. A. Seki *et al*., *Biol. Conserv.* **275**, 109782 (2022).
7. D. I. Murguía, S. Bringezu, R. Schaldach, *J. Environ. Manag.* **180**, 409 (2016).
8. United Nations Environment Programme, "Hydropolitical Vulnerability and Resilience Along International Waters: Latin America and the Caribbean" (2007); https://www.unep.org/resources/report/hydropolitical-vulnerability-and-resilience-along-international-waters-latin.
9. El País, "El Salvador alcanza un acuerdo para la mayor reconversión de de deuda de su historia" (2024); https://elpais.com/america-futura/2024-10-18/el-salvador-alcanza-un-acuerdo-para-la-mayor-reconversion-de-de-deuda-de-su-historia.html [in Spanish].
10. J. E. Cuéllar, *NACLA Rep. Am.* **52**, 317 (2020).
11. D. Manuel-Navarrete, J. J. Gómez, G. Gallopín, *Glob. Environ. Change* **17**, 207 (2007).
12. K. Muñoz, "La explotación minera en El Salvador es inviable señalan expertos científicos de la UES" (YSUCA, 2025); https://ysuca.org.sv/2025/01/la-explotacion-minera-en-el-salvador-es-inviable-senalan-expertos-cientificos-de-la-ues/ [in Spanish].

10.1126/science.adv8619

RESEARCH

IN *SCIENCE* JOURNALS

Edited by **Michael Funk**

RANGE SHIFTS

Unexpected resilience of mountain species

Mountain species are expected to move upslope or face extinction as temperatures rise. Evidence for upslope range shifts has been observed in some regions but not others. Chen *et al.* used temporal datasets of plant and animal species ranges from five continents to determine whether species are indeed moving upslope and if this is occurring more than would be expected by a null model accounting for the area they occupy. They found that both upward and downward range shifts occurred, with narrow-ranged and lowland species more likely to expand their ranges upward. However, ranges did not generally contract, and trends fell within the range of null model expectations, suggesting that, so far, species are not showing the expected responses to climate change. —Bianca Lopez

Science p. 741, 10.1126/science.adq9512

Mountain species, such as the golden mantella found in Madagascar, are not shifting upward as much as expected in response to climate change.

PHOTO: CHIEN LEE/MINDEN PICTURES

MESOSCOPIC PHYSICS

Measuring the braiding phase

Anyons, quasiparticles that obey fractional exchange statistics, are known to emerge in fractional quantum Hall (FQH) systems. When one anyon is exchanged with another, the many-body wave function acquires a phase that can be measured using Fabry-Pérot interferometers. Werkmeister *et al*. used such a technique to measure this so-called braiding phase for two different filling factors in a graphene device. The researchers expect that the approach can also be used for even-denominator FQH states, where non-abelian anyons are predicted to arise. —Jelena Stajic

Science p. 730, 10.1126/science.adp5015

MECHANOTRANSDUCTION

Stretch-induced ligand shedding

Mechanically induced activation of the kinase ERK is important for epithelial homeostasis and morphogenesis. Houtekamer *et al*. found that ERK was activated upon stretching of cultured epithelial monolayers (see the Focus by Potoczky and Yap). Stretch-induced ERK activation was driven by ligand-mediated activation of the epidermal growth factor receptor (EGFR) and depended on the adherens junction protein E-cadherin and the activation of ADAM proteases that mediate the shedding of EGFR ligands. This work shows that mechanical tension transmitted through cell-cell junctions can elicit ERK activation by promoting EGFR ligand shedding. —Annalisa VanHook

Sci. Signal. (2025) 10.1126/scisignal.adr7926; see also 10.1126/scisignal.adx0682

BATTERIES

Mixing up better electrodes

All-solid-state lithium-sulfur batteries offer significantly increased energy density, safety, and cost-effectiveness compared with existing lithium-ion batteries. However, optimizing the solid-solid interface remains a grand challenge to achieve high sulfur utilization and long cycle life. Lee *et al*. used ultra-high-speed mixing of a sulfur cathode with a halide-based solid electrolyte to fabricate composite electrodes. This process leads to interfacial segregation and formation of a lithium chloride–rich shell on the surface of the particles. This structure enhances charge transport kinetics, boosts interfacial stability, and mitigates mechanical failure in solid-state batteries. The formation and efficacy of the halide segregation was confirmed using cryogenic transmission electron microscopy and synchrotron x-ray

diffraction and spectroscopy techniques. —Marc S. Lavine

Science p. 724, 10.1126/science.adt1882

PALEONTOLOGY

Lessons from the past

Horses evolved in North America and traveled across Beringia, where they further speciated and expanded their ranges. As far as we know, modern North American horses are descended from Eurasian lineages later brought by Europeans. Running Horse Collin *et al.* looked across modern and ancient samples and found that horse movement between North America and Asia was common across Beringia between 50,000 and 13,000 years ago. In the late Pleistocene, this route was lost, and connectivity between these populations ended, leading to the extinction of horses on their natal continent. Understanding how such losses of connectivity have affected species in the past should shape our efforts to maintain species into the future. —Sacha Vignieri

Science p. 748, 10.1126/science.adr2355

NEUROPHYSIOLOGY

Rethinking neuron-astrocyte communication

Astrocytes have been shown to modulate neuronal activity, and dysfunction in neuron-astrocyte communication causes alterations in many cognitive processes. However, the fundamental mechanisms by which astrocytes might be integrated into neuronal circuitry has remained largely unclear. Three independent studies investigated the mechanisms and molecular players involved in astrocyte-neuron communication using multiple in vivo and in vitro models (see the Perspective by Eroglu). Guttenplan *et al*. used fruit fly larvae and mammalian astrocyte cultures to show that exposure to the norepinephrine (NE) homolog tyramine enables astrocytes to suddenly respond potently to a range of neurotransmitters to which they are normally nonresponsive. In zebrafish, Chen *et al*. found that NE modulates larval behavior through NE receptor activation on astrocytes, astrocyte secretion of ATP, extracellular metabolism of ATP into adenosine, and activation of neuronal adenosine receptors. Finally, Lefton *et al*. showed that, in mice, NE modulates synaptic function through a signaling pathway involving astrocytic adrenergic receptors. These three studies point to a model of neural network function in which neuronal signaling and network function can be gated by computations in astrocytes. —Mattia Maroso

Science p. 763, 10.1126/science.adq5729, p. 769, 10.1126/science.adq5233, p. 776, 10.1126/science.adq5480; see also p. 705, 10.1126/science.adx7102

GENETIC DISEASE

Prenatal treatment for genetic disease

Treatment of spinal muscular atrophy (SMA) ideally starts in the early postnatal period, but patients with severe forms of the disease may still develop substantial neurological deficits even if treated early. Borges *et al.* showed that prenatal treatment with antisense oligonucleotides (ASOs) through intra-amniotic injection improved outcomes in two mouse models of severe SMA. They also tested the feasibility of intra-amniotic ASO administration in a fetal lamb model, which resulted in broad ASO distribution, including to the central nervous system, although ASO concentrations in different brain regions were expected to be therapeutic in only a subset of animals. These findings highlight the potential utility of intra-amniotic delivery as a route of administration for prenatal treatment for SMA, although further optimization will likely be required before translation to the clinic. —Melissa L. Norton

Sci. Transl. Med. (2025) 10.1126/scitranslmed.adv4656

IN OTHER JOURNALS

Edited by **Corinne Simonti** *and* **Jesse Smith**

CANCER

The lymph node and metastasis

Metastasis refers to the spreading of cancer cells from the primary site of formation to another part of the body. Lymph nodes are critical sites for deploying antitumor immune responses, but they can also be hijacked by cancer cells to facilitate metastasis. Kahn *et al.* explored the ways in which tumors can colonize lymph nodes. Using mouse models, the researchers report that regulatory T lymphocytes (Tregs) in tumor-draining lymph nodes thwart the ability of $CD8^+$ T cells to kill tumors. By expressing high-affinity interleukin-2 (IL-2) receptors, Tregs can limit IL-2 availability, which impairs the activity of tumor-specific cytotoxic $CD8^+$ T cells. As a result, an immunosuppressive environment is created within the lymph node that appears susceptible to local metastatic colonization. —Priscilla N. Kelly

Cancer Discov. (2025) 10.1158/2159-8290.CD-24-1847

METABOLISM

Running on myelin

Running a marathon requires an extraordinary amount of energy expenditure, and exercise has been associated with structural brain changes in animal models. Ramos-Cabrer *et al.* investigated the short- and long-term effects of running a marathon on brain structure using functional magnetic resonance imaging (fMRI). The authors found a temporary reduction in myelin in regions of the brain associated with motor activity, sensory perception, and emotional responses in subjects after they completed a marathon. Two months after the marathon, myelin levels were fully restored, suggesting that myelin might be used as fuel during long-lasting activities when energy demands are extreme. —Mattia Maroso

Nat. Metab. (2025) 10.1038/s42255-025-01244-7

PHOTO: U.S. NATIONAL PARK SERVICE

BIOMATERIALS

When diamonds help hearts

The myocardium, the middle muscular layer and the thickest layer of the heart, causes contraction and relaxation of the heart walls to pump blood throughout the body. The efficiency of this layer is due partly to the specific arrangement of the cardiomyocytes and their associated extracellular matrix. Iglesias-García *et al.* used melt electrowriting to explore the roles of scaffolds and pore shape in the beating of cardiac tissues grown

RESTORATION ECOLOGY

Beans benefit from bacteria

Legumes, plants in the bean and pea family (Fabaceae), play a unique ecological role through their association with rhizobium bacteria that fix nitrogen in soil. Restoring legumes to grasslands may be limited by the availability of rhizobia, as has been shown for some prairie plants, the establishment of which depends on the presence of symbiotic mycorrhizal fungi. Magnoli and Bever tested whether adding rhizobia benefits legume species with varying life histories. Their survey of soils from various land uses in western Kansas showed significantly lower rhizobial abundance in agricultural soils. In a set of greenhouse and field experiments, they found that native legumes benefited from rhizobial interaction, and slow-growing, long-lived legumes especially benefited from rhizobia from undisturbed sites. —Bianca Lopez

Ecol. Appl. (2025) 10.1002/eap.70027

Rhizobia limit the establishment of legumes such as lupine in restoration.

from human pluripotent stem cells. They found that tissues with diamond-shaped pores beat faster, with increased force and higher conduction velocity compared with those having square or rectangular pores. The authors also tested their cardiac tissues in an infarction model in athymic rats, where they showed better contractility and diminished ventricular dilatation. —Marc S. Lavine

Adv. Funct. Mater. (2025) 10.1002/adfm.202420106

EARTHQUAKE ALERTS

Locating deep-sea ruptures in real time

Earthquake early warning systems, such as ShakeAlert along the West Coast of the US, send emergency cell phone alerts within seconds of an earthquake. The timing and distribution of an alert depends on accurate real-time location of the initial rupture, which is more difficult for offshore earthquakes. During the 2024 M7 Cape Mendocino earthquake and aftershocks, Williamson *et al*. tested a modification to ShakeAlert's standard location algorithm that adds prior seismicity. Tuning to historical patterns helped the algorithm detect more earthquakes with smaller location and magnitude errors at no extra computational cost. —Angela Hessler

TSR (2025) 10.1785/0320250009

ORGANIC CHEMISTRY

Boron gets strained

Four-membered carbon rings, or cyclobutanes, are important substructures in a variety of molecules. Their intrinsic strain renders them highly susceptible to ring-opening or ring-expansion reactions. Wang *et al.* now report a versatile method to make boron analogs of these rings: C_3B motifs sharing an edge with a phenyl group. The route to these benzoborotenes relies on energy transfer from a photosensitizer to an aryl precursor with boryl and vinyl substituents. A diradical intermediate then forms the strained boron-carbon bond. —Jake S. Yeston

Nat. Chem. (2025) 10.1038/s41557-025-01807-x

NEUROSCIENCE

Simultaneous imaging and recording

With genetically encoded calcium indicators and two-photon microscopy, neuronal population dynamics can be measured in intact tissues. However, calcium indicators provide only an indirect measure of neuronal spiking. Rupprecht *et al*. performed simultaneous cell-attached recordings and calcium imaging of spinal cord neurons to study the relationship between calcium signals and electrophysiological action potentials. They then tested a supervised deep learning algorithm that infers spike rates from calcium imaging data. The algorithm, originally trained on cortical neuron data, generalized well to these spinal cord neurons. Specific retraining on spinal cord electrophysiological recordings improved the retrieval of high-frequency spike events and resulted in an improved prediction of relative spike rates across and within neurons. —Peter Stern

J. Neurosci. (2025) 10.1523/JNEUROSCI.1187-24.2025

RESEARCH ARTICLE SUMMARY

POPULATION GENETICS

Admixture's impact on Brazilian population evolution and health

Kelly Nunes†, Marcos Araújo Castro e Silva†, Maíra R. Rodrigues†, Renan Barbosa Lemes†, Patricio Pezo-Valderrama, Lilian Kimura, Lucas Schenatto de Sena, José Eduardo Krieger, Margareth Catoia Varela, Luiz Otávio de Azevedo, Luis Marcelo Aranha Camargo, Ricardo G. M. Ferreira, Henrique Krieger, Maria Cátira Bortolini, José Geraldo Mill, Putira Sacuena, João F. Guerreiro, Celia M. B. de Souza, Francisco V. Veronese, Fernanda S. L. Vianna, David Comas, Alexandre C. Pereira*, Lygia V. Pereira*, Tábita Hünemeier*

Full article and list of author affiliations: https://doi.org/10.1126/science.adl3564

INTRODUCTION: Brazil is a vast continental country home to the largest population in Latin America and boasts the world's largest recently admixed population. The colonization process brought ~5 million Europeans to Brazil, alongside the forced migration of at least 5 million Africans and the decimation of Indigenous populations, which once included >10 million people speaking more than 1000 languages. This distinctive historical interplay shaped a complex mosaic of genetic diversity, underscoring the importance of detailed genomic studies. However, similar to other populations in the Global South, the Brazilian population remains notably underrepresented in genomic research, where there is a lack of studies investigating the effects of this population's admixture on its evolution, diversity, and health status.

RATIONALE: To address these gaps, we generated 2723 high-coverage whole-genome sequences of the Brazilian population, encompassing urban, rural, and riverine communities from all five geographical regions of Brazil. This dataset reflects a diverse group of ethnic backgrounds, including Afro-Brazilians and descendants of Indigenous people, and provides a comprehensive representation of Brazilian genomic diversity. Advanced methods, such as local ancestry inference and haplotype-based analyses, enabled us to characterize ancestry-specific genomic regions in different time periods and geographic regions and detect signatures of natural selection. Our research highlights admixture's evolutionary and health implications, focusing on the historical and demographic dynamics that shaped Brazilian genomes. Our results contribute to a deeper understanding of how global haplotypes and admixture patterns resulting from an intricate evolutionary history could affect an admixed population's health.

RESULTS: We identified >8 million previously unknown variants, 36,637 of which are putatively deleterious, and elucidated a positive correlation between these deleterious variants and genetic ancestry components. We also showed that the Brazilian population is a tapestry of global haplotypes shaped by nonrandom mating, with the peak of admixture occurring in the 18th and 19th centuries. Multiple or continuous admixture events between Indigenous American, African, and European parental sources have formed Brazilian populations. These processes align with major historical events that have shaped the Brazilian state over the past five centuries. We also identified that, after a prolonged period of sex-biased mating in the initial centuries, a strong pattern of assortative mating has more recently emerged in the Brazilian population, regardless of the region studied. These patterns reveal both the violent dynamics of European colonization and the lasting imprints of this process on contemporary South America. Within the extensive diversity found in Brazil, ancestral-specific genomic regions originating from different populations are unevenly spread across Brazilian regions and historical time frames. This distribution demonstrates the lasting impact of the hundreds of ethnicities that arrived in the country through millions of Europeans and Africans at different times, admixing with and replacing the original Indigenous population. Furthermore, our study identifies several candidate genes that were subject to selection both before and after contact in the Brazilian admixed population. These genes are primarily associated with heightened fertility rates, immune response, and distinctive metabolic traits.

CONCLUSION: Our findings underscore the discernible influence of different ancestral backgrounds on Brazilian admixed individuals' health and genetic makeup. We show that this genetic landscape finds its roots in the evolutionary history of Brazilian Indigenous communities and the intricate demographic interplay stemming from both coerced and voluntary historical immigration to Brazil. □

*Corresponding author. Email: alexandre.pereira@incor.usp.br (A.C.P.); lpereira@usp.br (L.V.P.); hunemeier@usp.br (T.H.) †These authors contributed equally to this work. **Cite this article as K. Nunes *et al.*, *Science* 388, eadl3564 (2025). DOI: 10.1126/science.adl3564**

Brazilian genomic diversity. A comprehensive study of 2723 high-coverage whole-genome sequences from diverse Brazilian regions reveals >8 million newly identified single-nucleotide variants (SNVs), highlighting Brazil's pronounced genomic diversity, shaped by natural selection, nonrandom mating, and continuous admixture pulses since 1500. These findings underscore the influence of ancestral backgrounds on the health and genetic profile of the Brazilian population, rooted in Indigenous history and diverse immigration waves.

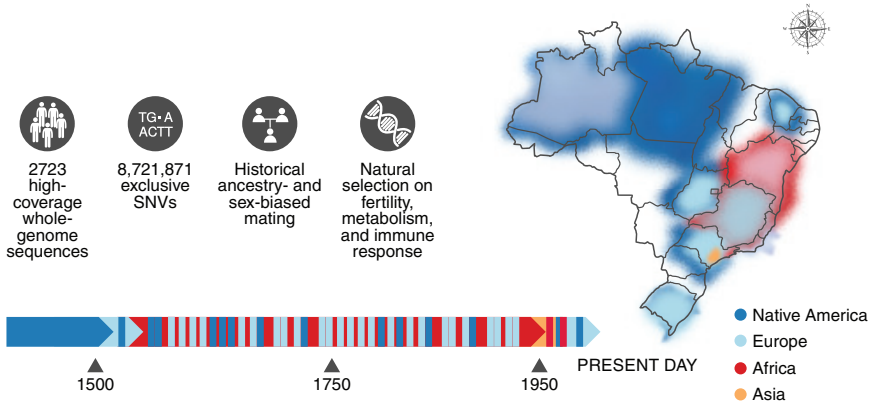

RESEARCH ARTICLE SUMMARY

POPULATION GENETICS

From North Asia to South America: Tracing the longest human migration through genomic sequencing

Elena S. Gusareva *et al.*

Full article and list of author affiliations: https://doi.org/10.1126/science.adk5081

INTRODUCTION: During the late Pleistocene, humans expanded across Eurasia and eventually migrated to the Americas. Those who reached Patagonia, at the southern tip of South America, completed the longest migration out of Africa.

RATIONALE: The extent of basal divergences, admixture, and degrees of isolation among Indigenous North Eurasian and Native South American populations remain debated, with most insights derived from genome-wide genotyping data. This study aims to deepen our understanding of the ancient dynamics that shaped contemporary populations in North Eurasia and the Americas. By using large-scale whole-genome sequencing of 1537 individuals from 139 ethnic groups in these regions, we examined population structures, elucidated prehistoric migrations, and explored the influence of past environmental factors on the diversification of human populations.

RESULTS: Advances in large-scale genomic sequencing have considerably enhanced our understanding of the genetic ancestry of human populations across North Eurasia and South America. Our analysis reveals that all contemporary Siberians, as well as some Northeast Europeans and Central Asians, share ancestry with the West Siberian groups, represented by the Kets and Nenets. Their ancestors were widespread across Siberia 10,000 years ago (ya), but now these groups face population decline by 73.6% and are becoming a minority.

The populations of west Beringia, including the Koryaks, Inuit, and Luoravetlans, are the most genetically distinct from other Siberians. These groups have adapted to Arctic conditions with genetic variations related to lipid metabolism, thermogenesis, sensory perception, and the regulation of reproductive and immune functions.

We were not able to identify a specific Siberian group as the direct ancestors of Native Americans owing to deep divergence and limited genetic continuity. However, west Beringian populations remain closely related to Native Americans. Koryaks and Inuit show 5 and 28% Native American ancestry, respectively, owing to gene flow between 700 and 5100 ya.

We estimated the split time of Native South Americas into Amazonians, Andeans, Chaco Amerindians, and Patagonians to have occurred 13,900 to 10,000 ya. Migration and settlement across the continent led to population isolations due to geographic boundaries and a reduction in their genetic diversity, particularly affecting immune genes, such as the human leukocyte antigen (*HLA*) genes. Over the past 10,000 years, all four Native South American lineages have experienced population declines ranging from 38 to 80%. This dramatic decline, combined with the loss of traditional lifestyles, cultural practices, and languages, has pushed some Indigenous communities, such as the Kawésqar, to the brink of extinction.

CONCLUSION: The migration to an uninhabited continent of South America through the narrow Isthmus of Panama resulted in a founder effect among Native South Americans, leading to reduced genetic diversity compared with that of Indigenous populations of North Eurasia. Over 13,900 years, geographic barriers within the continent further isolated Indigenous groups, subsequently reducing genetic diversity. These groups faced a profound challenge with the arrival of European colonists in the 1600s, who introduced new adversities that threatened their long-standing endurance. □

*Corresponding author: Hie Lim Kim (HLKIM@ntu.edu.sg). Cite this article as E. S. Gusareva *et al.*, *Science* **388**, eadk5081 (2025). DOI: 10.1126/science.adk5081

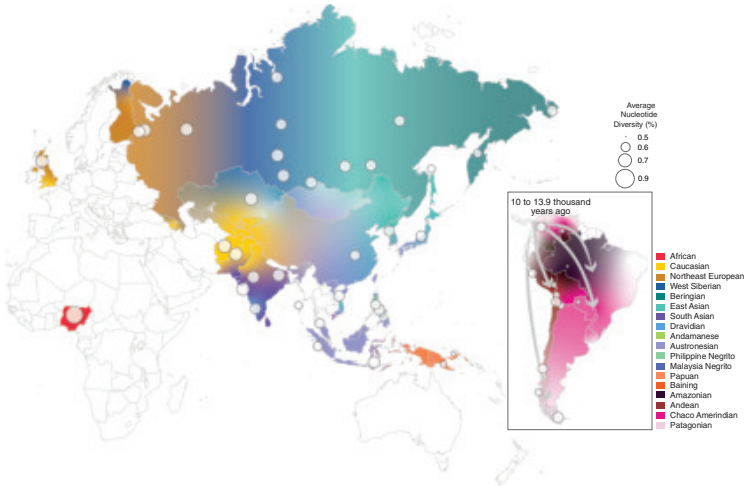

Genetic ancestry and nucleotide diversity. Colors represent genetic ancestries estimated by whole-genome sequencing data of contemporary human populations. Countries having no data remained empty. Circle size indicates the average nucleotide diversity of each population.

RESEARCH ARTICLE SUMMARY

VIROLOGY

Cryptic infection of a giant virus in a unicellular green alga

Maria P. Erazo-Garcia†, Uri Sheyn†, Zachary K. Barth, Rory J. Craig, Petronella Wessman, Abdeali M. Jivaji, W. Keith Ray, Maria Svensson-Coelho, Charlie K. Cornwallis, Karin Rengefors, Corina P. D. Brussaard*, Mohammad Moniruzzaman*, Frank O. Aylward*

Full article and list of author affiliations: https://doi.org/10.1126/science.ads6303

INTRODUCTION: The recent discovery of giant endogenous viral elements (GEVEs) across a wide range of protist genomes presents an opportunity to investigate a possible latent viral infection strategy within giant viruses. Although these elements can be prominent features of eukaryotic genomes, GEVEs frequently exhibit clear signs of genomic erosion, including duplications, methylation, and intron invasion, raising questions about their viability. *Chlamydomonas reinhardtii* is a unicellular green alga long recognized as a model organism, but its potential interaction with viruses in the environment has remained elusive. The recent observation that some field isolates of *C. reinhardtii* harbor signatures of GEVEs suggests that this alga could also serve as a valuable model for investigating the dynamics of endogenous giant viruses in nature.

RATIONALE: Although latency is a common strategy in a wide range of viral lineages, it remains unknown whether GEVEs originate from a viral life cycle involving a latent phase or whether they are the result of another route of gene transfer. Latency was proposed as a potential strategy used by viruses of eukaryotic algae by numerous studies dating to the 1970s that described the formation of large icosahedral particles in otherwise healthy cultures. Methodological challenges, particularly in isolating and tracing the origin of these large particles, have hindered efforts to determine whether these particles result from active latent giant viruses or other factors such as persistent infections or contaminated cultures.

RESULTS: Using long-read sequencing, we resolved a 617–kilo–base pair (kbp) GEVE located on chromosome 15 of *C. reinhardtii* strain CC-2937. The GEVE is flanked by 6-bp target site duplications (TSDs), which are signatures of distinct families of DD(E/D) integrase enzymes. We found a candidate integrase encoded by the GEVE, which is related to polintovirus (phylum *Preplasmiviricota*) integrases, suggesting that interactions with hyperparasites could drive the evolution of cryptic infection strategies in giant viruses. We demonstrate that the GEVE is transcriptionally active and produces viral particles that accumulate primarily during the stationary growth phase of liquid cultures that exhibit no evident signatures of infection. The GEVE encodes several selfish genetic elements, including several transposases that encode Fanzor nucleases, which are active during infection and show signatures of recent mobility. In addition, we provide evidence that *Chlamydomonas* spp. isolates from freshwater environments harbor giant viruses closely related to the *C. reinhardtii* CC-2937 GEVE, suggesting that cryptic infections involving genome integration are prevalent among large DNA viruses of green algae.

CONCLUSION: Our study describes an unusually large temperate virus that infects the model green alga *C. reinhardtii*. Our evidence indicates that the GEVE can reactivate and produce viral particles, although many aspects of the infection program, including the potential molecular signals that control reactivation, remain unclear. Additionally, the presence of several viral-encoded selfish genetic elements suggests that giant viruses may serve as vectors of selfish DNA in eukaryotes. Last, our discovery of signatures of giant viruses related to the GEVE in field isolates of *Chlamydomonas* spp. points to cryptic infections as potentially widespread among natural algal populations. Our findings broaden the scope of cryptic infections in the virosphere and emphasize genome integration as a potentially important component of the infection cycle of many giant viruses. □

*Corresponding author. Email: corina.brussaard@nioz.nl (C.P.D.B.); m.monir@miami.edu (M.M.); faylward@vt.edu (F.O.A.) †These authors contributed equally to this work. Cite this article as M. P. Erazo-Garcia *et al.*, *Science* **388**, eads6303 (2025). DOI: 10.1126/science.ads6303

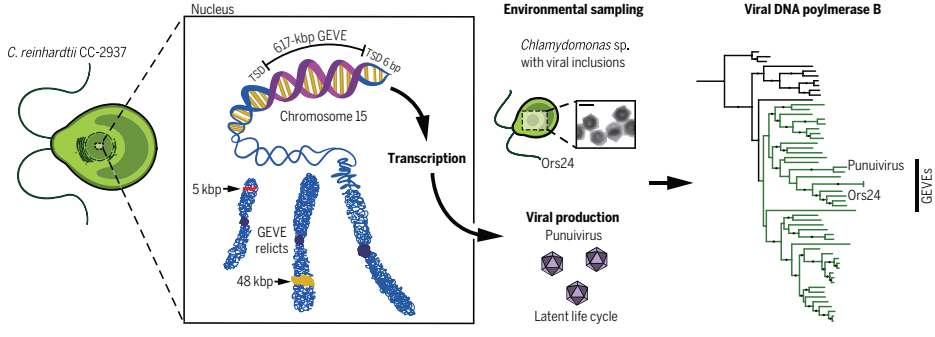

An active GEVE in *C. reinhardtii* produces virions and establishes a cryptic infection. A 617-kbp GEVE and two relicts were resolved in *C. reinhardtii* CC-2937 using long-read sequencing. The GEVE is transcriptionally active in stationary-phase cultures, producing particles of the virus "punuivirus," named after the Inca deity of untroubled sleep, Puñuy. Related giant viruses are associated with natural *Chlamydomonas* isolates and exhibit comparable infection dynamics, which suggests that cryptic infection strategies are common among large protist viruses. Ors24 is a *Chlamydomonas* isolate from Örsjön, a lake located in southern Sweden. Scale bar is 200 nm.

RESEARCH ARTICLE SUMMARY

VIROLOGY

Molecular basis of influenza ribonucleoprotein complex assembly and processive RNA synthesis

Ruchao Peng†, Xin Xu†, Binod Nepal, Yikang Gong‡, Fenglin Li‡, Max B. Ferretti, Mingyang Zhou, Kristen W. Lynch, George M. Burslem, Sandhya Kortagere, Ronen Marmorstein, Yi-Wei Chang*

Full article and list of author affiliations: https://doi.org/10.1126/science.adq7597

INTRODUCTION: Influenza virus poses a long-standing public health issue worldwide, causing both recurring seasonal flu and occasional pandemics in humans and other animals. Current vaccines and antivirals predominantly target the envelope proteins, which are prone to mutations, leading to decreased efficacy as well as drug resistance over time. By contrast, the ribonucleoprotein (RNP) complexes inside the virus are more evolutionarily conserved, which makes them promising targets for broad-spectrum antiviral development. Each RNP complex consists of a viral genomic RNA segment bound with multiple nucleoprotein (NP) subunits and a polymerase complex, which carries out transcription and replication of the viral genome in the host cell. Despite their critical functional roles, a high-resolution structural understanding of RNP assembly and its working mechanism has remained elusive.

RATIONALE: Although the structures of individual influenza NP and polymerase have been characterized, the complete RNP complex has been refractory to high-resolution structural analysis owing to its inherent flexibility. Previous cryo–electron microscopy (cryo-EM) studies of influenza RNP were limited to nanometer resolution, and the polymerase complex within the RNP could not be visualized. To address this gap, we combined cryo-EM single-particle analysis (SPA) and cryo–electron tomography (cryo-ET) to investigate both reconstituted and native RNPs in distinct functional states. Specifically, we reconstituted the shortest RNP segment—the nonstructural (NS) segment—of influenza D virus to reduce flexibility for detailed structural analysis of the NP-RNA packaging, and we used cryo-ET to capture the polymerase functioning on individual RNPs in three dimensions for subtomogram averaging. The overall picture of the RNP in the act could highlight important molecular interactions for RNP function and guide the focus of influenza inhibitor design.

RESULTS: Cryo-EM SPA of the reconstituted influenza D NS RNP revealed a right-handed, antiparallel double helix of NP polymers, with the RNA encapsidated in the minor groove and adjacent NP subunits linked by a conserved tail loop. Subtomogram averaging of native RNP purified from influenza A virus particles confirmed these features and further identified multiple different conformations indicative of dynamic inter-strand motion within the double helix. The polymerase complex, visualized in preinitiation and elongation states, consistently associates with the RNP exterior, which supports a helical strand sliding model in which the polymerase processes along the RNA template for RNA synthesis while maintaining the overall double-helical architecture of RNP. This mechanism is enabled by the flexible tail loop connecting neighboring NPs, which renders the double-helical RNP highly dynamic and prone to sliding motion with a low energy barrier. Virtual screening against the tail loop binding interface of NP identified lead compounds that effectively inhibited influenza virus replication in cell-based assays.

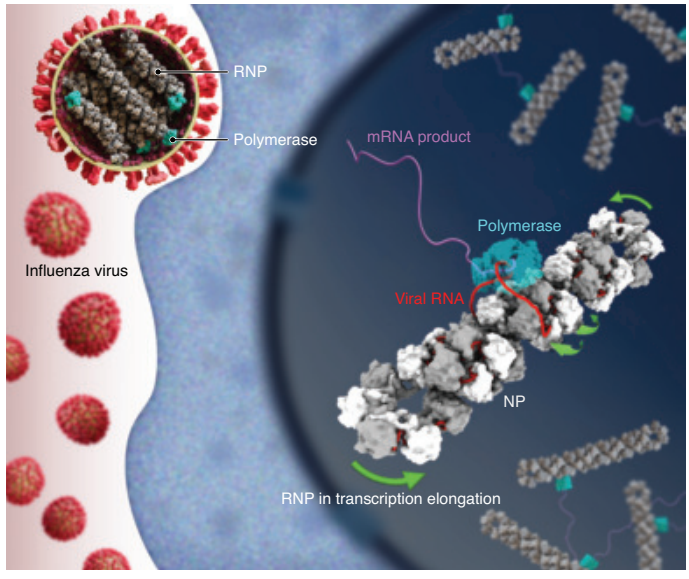

Molecular architecture and working mechanism of influenza RNP. Influenza viruses package their genomic RNA segments into right-handed, double-helical RNPs, each harboring a viral polymerase at one end. During infection, these RNPs enter the host nucleus, orchestrating viral genome transcription and replication through sliding between the two antiparallel strands (green arrows). This mechanism enables the polymerase to process along the RNA while preserving the double-helical arrangement.

CONCLUSION: By integrating high-resolution cryo-EM and cryo-ET approaches, we delineate the structural basis of influenza RNP assembly and reveal how the polymerase-driven RNA synthesis proceeds without disrupting the helical framework—potentially enhancing processivity and/or evading host immune detection. These findings offer insights for the design of next-generation, broad-spectrum anti-influenza therapeutics targeting the conserved RNP components. □

*Corresponding author. Email: ywc@pennmedicine.upenn.edu †These authors contributed equally to this work. ‡These authors contributed equally to this work. Cite this article as R. Peng *et al.*, *Science* **388**, eadq7597 (2025). DOI: 10.1126/science.adq7597

RESEARCH ARTICLE SUMMARY

CRISPR

Programmable gene insertion in human cells with a laboratory-evolved CRISPR-associated transposase

Isaac P. Witte†, George D. Lampe†, Simon Eitzinger†, Shannon M. Miller, Kiara N. Berríos, Amber N. McElroy, Rebeca T. King, Olivia G. Stringham, Diego R. Gelsinger, Phuc Leo H. Vo, Albert T. Chen, Jakub Tolar, Mark J. Osborn, Samuel H. Sternberg*, David R. Liu*

Full article and list of author affiliations: https://doi.org/10.1126/science.adt5199

INTRODUCTION: The efficient insertion of gene-sized DNA sequences at user-specified genomic sites is a long-standing goal in genome editing. Although current editing methods can correct most disease-causing mutations, the genetic diversity underlying many disorders will require the design and regulatory approval of many mutation-specific strategies—substantially limiting the number of patients who can benefit from therapeutic genome editing. Programmed genomic integration of a healthy gene copy could offer a mutation-agnostic treatment for loss-of-function genetic diseases. Additionally, targeted gene integration enables other applications, including cancer immunotherapies, transgenic cell and animal models for basic research, and metabolic engineering.

RATIONALE: CRISPR-associated transposases (CASTs) are naturally occurring bacterial systems that exploit nuclease-deficient CRISPR machinery to integrate DNA at genomic locations specified by guide RNAs. CASTs offer many attractive qualities as a genome editing tool, including facile programmability, compatibility with multi-kilobase-scale DNA cargo, and avoidance of genomic double-strand DNA breaks. Despite this promise, wild-type CASTs reported to date support minimal integration in human cells (often ≤0.1% of treated cells). We reasoned that this low efficiency may stem from naturally evolved, suboptimal transposition catalysis that mitigates mobilization-induced fitness cost to the host. To enable efficient CAST integration in human cells, we developed a phage-assisted continuous evolution (PACE) system that rapidly evolves CAST variants capable of fast targeted transposition and applied CAST-PACE to a prototypical Type I-F CAST system from *Pseudoalteromonas*.

RESULTS: We linked on-target DNA integration in *Escherichia coli* to the propagation of continuously mutating phage genomes encoding evolving CAST components. After hundreds of generations of continuous selection, replication, and mutation in which the resulting phage survived an overall 10^{322}-fold dilution, we generated an evolved variant of the CAST transposase protein TnsB that mediated >200-fold improved integration activity in human cells. The evolved TnsB contains 10 activity-enhancing mutations located throughout the protein, which likely modulate several distinct interactions with other CAST components. Notably, the evolved TnsB mediated efficient integration activity in human cells without requiring codelivery of the bacterial CAST accessory protein, ClpX, which is cytotoxic. We combined this evolved TnsB with other PACE-evolved and rationally engineered CAST components to yield evoCAST, a system optimized for human-cell integration activity. EvoCAST achieved 10 to 30% integration efficiencies across 14 genomic targets in human cells, representing a 420-fold average improvement over wild-type CAST. EvoCAST supported large DNA cargoes >10 kb and mediated the integration of several therapeutic payloads at disease-relevant genomic sites, including safe harbor loci, sites for cancer immunotherapy engineering, and genes implicated in loss-of-function genetic diseases. EvoCAST also performed targeted integration in multiple human cell types, including primary human fibroblasts, and exhibited high product purity, with no detected insertions and deletions (indels), predominantly unidirectional cargo insertion, single–base pair precision of integration, and low levels of off-target integration.

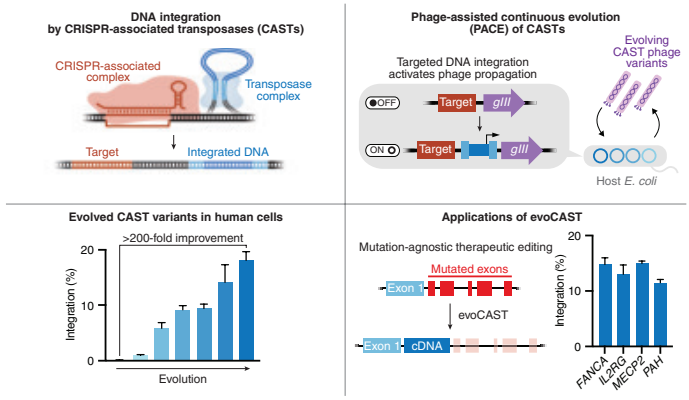

PACE-evolved CASTs mediate efficient, programmable gene integration in human cells. CASTs exploit a nuclease-deficient CRISPR-Cas system to recruit a transposase complex that catalyzes DNA integration (top left). We developed a PACE selection that links integration to propagation of phage that encode transposase components (top right), yielding an evolved CAST that supports >200-fold improved integration in human cells (bottom left). EvoCAST enables efficient and targeted integration of therapeutically relevant genes at many genomic loci (bottom right), paving the way for mutation-agnostic therapies for loss-of-function genetic diseases.

CONCLUSION: This work establishes CAST as a powerful platform technology for efficient, RNA-guided gene integration in human cells. The advantages of evoCAST—including its simple programmability, single-step integration mechanism, and avoidance of genomic double-strand breaks—make it well-suited for many applications in the life sciences and therapeutics, including the capability to address genetically diverse patient populations through a single editing agent. The CAST PACE system developed in this work also provides a strategy for improving the properties of other naturally occurring CASTs toward their use for efficient human-cell genome editing. □

*Corresponding author. Email: drliu@fas.harvard.edu (D.R.L.), shsternberg@gmail.com (S.H.S.) †These authors contributed equally to this work. **Cite this article as** I. P. Witte *et al.*, *Science* **388**, eadt5199 (2025). DOI: 10.1126/science.adt5199

RESEARCH ARTICLE SUMMARY

SIGNAL TRANSDUCTION

Activation dynamics traced through a G protein–coupled receptor by 81 ^{1}H-^{15}N NMR probes

Feng-Jie Wu*, Pascal S. Rieder, Layara Akemi Abiko, Anne Grahl, Daniel Häussinger, Stephan Grzesiek*

Full article and list of author affiliations: https://doi.org/10.1126/science.adq9106

INTRODUCTION: G protein–coupled receptors (GPCRs) are the largest family of integral membrane proteins and key mediators of cellular signaling. They are targets of about a third of marketed drugs and the focus of promising new drug development against many challenging diseases, such as diabetes, Alzheimer's and Parkinson's disease or cancer. Despite decades of progress, the details of atomic motion during ligand-induced GPCR activation and coupling to intracellular transducers remain unresolved.

RATIONALE: Resolving these motions at atomic resolution is essential to understand the underlying principles governing GPCR ligand efficacy, potency, and signaling bias toward intracellular pathways, which can then provide guidance for designing drugs with desired signaling outputs. Dynamical information is generally missing in existing static GPCR structures, and most biophysical dynamics experiments provide only low resolution. Nuclear magnetic resonance (NMR) spectroscopy can resolve the dynamical interchange of GPCR conformations, including intermediates not visible in static structures, at atomic resolution.

RESULTS: Using a recently developed technique for the assignment of nuclear magnetic signals based on paramagnetic resonance shifts, we could follow the behavior of all 162 ^{1}H and ^{15}N atomic nuclei of the valine, isoleucine, tryptophan, and tyrosine residues of the β_1-adrenergic receptor (β_1AR) during ligand activation. This large number of probes traces the activation through the entire receptor from the extracellular ligand pocket to the intracellular transducer binding site. Four distinct interchanging receptor conformations are clearly distinguished: inactive, preactive, active, and transducer-bound active.

The most inactive conformation is detected in the complex between β_1AR and the antagonist carvedilol. In this state, the receptor is overall rigidified and the extracellular ligand pocket filled by the large antagonist. Binding of the agonist isoprenaline to the apo receptor induces first a preactive conformation where the ligand pocket is not yet rigidly closed. In this state, the activating signal from the ligand travels already toward the intracellular ends of transmembrane helices TM3, 5, and 6, and primes the receptor for a slow (>0.15 s), high activation-barrier transition to the active conformation.

The preactive-active transition involves a large rearrangement of many parts of the receptor, including the highly conserved, central xWIPF$_3$ transmission switch. Perturbing this switch through an I-V mutation substantially modulates the preactive-active equilibrium thereby revealing a key mechanical element of the signal transduction pathway. The binding of a transducer further changes the intracellular sides of TM3 and TM5 to TM7, but not the intracellular sides of TM1 and TM2 or the extracellular side. Thus, the latter part is already in its final conformation in the active binary complex and rigidly coupled to the state of the xWIPF$_3$ switch. The rest of the intracellular side is loosely coupled. This plasticity may allow for the accommodation of various transducer proteins and the breathing motion of the G protein during nucleotide exchange. The boundary between rigid and loose coupling is located at the most conserved residues in TM5 to TM7, i.e., the prolines, which enable the loose coupling by their helix-breaking properties.

CONCLUSION: The obtained detailed description of the β_1AR activation dynamics appears widely general to GPCRs. It bridges the gap between static GPCR structures and function. □

*Corresponding author. Email: stephan.grzesiek@unibas.ch (S.G.); fengjie.wu@unibas.ch (F.-J.W.) Cite this article as F.-J. Wu *et al.*, *Science* **388**, eadq9106 (2025). DOI: 10.1126/science.adq9106

High-resolution detection of GPCR dynamics by solution NMR. A large number of GPCR nuclear signals are assigned using the GPS-PCS NMR method based on paramagnets. Their analysis reveals four distinct ligand-induced receptor states. The main activating motion is governed by the central highly conserved xWIPF3 switch that is rigidly coupled to the extracellular receptor half but loosely coupled to most of the intracellular side.

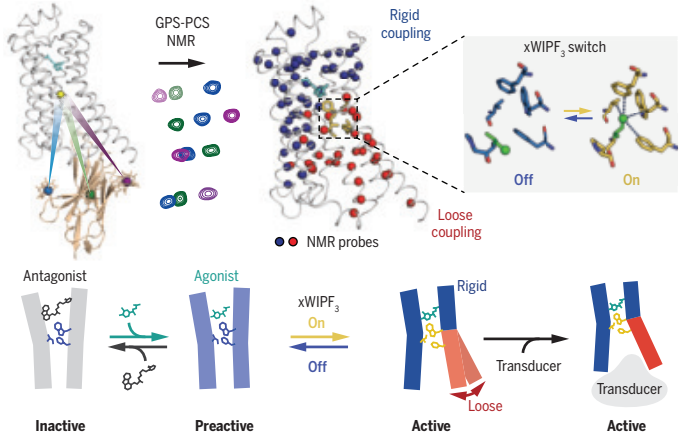

BATTERIES

Halide segregation to boost all-solid-state lithium-chalcogen batteries

Jieun Lee[1]†‡, Shiyuan Zhou[1]†, Victoria C. Ferrari[1], Chen Zhao[1], Angela Sun[1], Sarah Nicholas[2], Yuzi Liu[3], Chengjun Sun[4], Dominik Wierzbicki[2], Dilworth Y. Parkinson[5], Jianming Bai[2], Wenqian Xu[4], Yonghua Du[2], Khalil Amine[1,6]*, Gui-Liang Xu[1,6]*

Mixing electroactive materials, solid-state electrolytes, and conductive carbon to fabricate composite electrodes is the most practiced but least understood process in all-solid-state batteries, which strongly dictates interfacial stability and charge transport. We report on universal halide segregation at interfaces across various halogen-containing solid-state electrolytes and a family of high-energy chalcogen cathodes enabled by mechanochemical reaction during ultrahigh-speed mixing. Bulk and interface characterizations by multimodal synchrotron x-ray probes and cryo–transmission electron microscopy show that the in situ segregated lithium halide interfacial layers substantially boost effective ion transport and suppress the volume change of bulk chalcogen cathodes. Various all-solid-state lithium-chalcogen cells demonstrate utilization close to 100% and extraordinary cycling stability at commercial-level areal capacities.

All-solid-state lithium-sulfur (Li-S) batteries (ASSLSBs) are highly desirable for electric vehicles because of their high theoretical energy density, safe operation, cost-effectiveness, and low supply chain risk (*1*). Despite the development of solid-state electrolytes (SSEs) with high room-temperature ionic conductivity (>10 mS cm^{-1}) (*2*–*4*), the cell performance of all-solid-state batteries still largely hinges on the charge transport and chemomechanical stability of the electrode-SSE interface (*5*, *6*). Although the challenges of the Li-SSE interface are acknowledged, the poor electronic and ionic conductivity and large volume swelling (~80%) of sulfur result in severe intra- and interparticle reaction heterogeneity and chemomechanical failure of solid-solid interfaces after cycling (fig. S1) (*7*, *8*).

Present efforts to improve the cell performance of ASSLSBs include nanostructured hosts (*9*–*11*), catalysts (*12*), additives (*13*–*15*), doping (*1*, *16*), atomic layer deposition coating (*17*), and new SSEs (*18*–*20*). Although improvements have been achieved, these approaches still suffer from sluggish interfacial ion transport, resulting in low sulfur utilization (≤80%) and insufficient cycle life, particularly with increased areal sulfur loading (table S1). As a result, the projected cell energy densities of existing ASSLSBs remain low even when paired with thin SSEs (fig. S2). Moreover, elevated temperatures are often needed to improve the reaction kinetics of thick electrodes (*1*, *12*, *13*, *17*, *19*), which would facilitate the formation of soluble polysulfides that has been deemed a critical barrier for long-life Li-S batteries (*21*) and would thus require specific cell design to prevent cross-talk (*1*). Last, these material innovations require multiple steps or long processing times to fabricate sulfur cathodes or composite electrodes (table S1), adding extra manufacturing cost.

It has been a common practice to mix electroactive materials, SSEs, and conductive carbon together to fabricate composite electrodes owing to the poor wetting ability of SSEs. This critical step dictates, to a great extent, the interfacial stability and charge transport of the composite electrodes but has long been deemed as a merely physical mixing process while underestimating the underlying interfacial chemistry. The existing efforts mostly focus on the physical properties of the composite electrodes, such as porosity, tortuosity, and the distribution of electrode components (*22*, *23*). Leveraging chemical reactions between sulfur and SSEs represents an alternative strategy to forming an intimate interface through a wet mix process (*24*). However, owing to the insulating nature of sulfur, the ionic conductivity of the formed lithium polysulfidophosphate remains very low (*25*), leading to a low capacity retention of 63.9% after 250 cycles (*24*). In addition, this strategy relied on using sulfur-impregnated hosts and polar organic solvents that can potentially dissolve sulfide SSEs.

Having observed that nanocrystalline SSEs such as LiF could favor interfacial Li^+ transport despite the ionic insulating nature of the bulk phase (*13*, *26*, *27*), we considered whether nanosized lithium halides could segregate from bulk halogen–containing SSEs, such as argyrodites (*28*) and halides (*29*), and work as a plausible ion-transport booster. Inspired by the photoinduced phase segregation in mixed-halide perovskite solar cells (*30*), we observed a universal halide segregation at interfaces across a series of halogen-containing SSEs and a family of high-energy chalcogen (S, Se, SeS_2, Te) cathodes enabled by an ultrahigh mixing speed of 2000 rpm. The synergistic effects of heat striking and shear fracturing by the ultrahigh speed (UHS) mixing make it feasible to induce mechanochemical reaction to drive halide segregation from halogen-containing SSEs and the subsequent homogeneous deposition onto cathode particles during mixing (fig. S1). Such in situ segregated lithium halide interfacial layers boost the interfaces of various all-solid-state lithium-chalcogen cells, leading to exceptionally high utilization and long cycling stability (up to 450 cycles) at commercial-level areal capacities and room temperature (figs. S2 and S3). Moreover, no extra components (e.g., hosts, catalysts, dopants, etc.) and processing are required, contributing to substantial cost advantages compared with traditional material innovation approaches.

Mixing and structure analysis

We began our validation of the universal halogen-chalcogen chemistry for all-solid-state batteries by using a sulfur cathode and argyrodite Li_6PS_5Cl (LPSCl) SSE as an example. We prepared the optimal composite sulfur cathode by one-step UHS mixing of raw sulfur, LPSCl, and conductive carbon at 2000 rpm for 5 hours. Scanning electron microscopy (SEM) elemental mapping (fig. S4) showed an obvious separation of Cl and P (two signature elements of LPSCl) at the surface of LPSCl and a homogeneous distribution of Cl with S cathode particles after UHS mixing. By contrast, no Cl segregation was observed when lowering the mixing time to 1 hour (fig. S5) or reducing the mixing speed to 400 rpm (fig. S6).

A major challenge in using transmission electron microscopy (TEM) to achieve atomic-level insights into ASSLSBs lies in sulfur's vulnerability to local heat and high vacuum and the extreme sensitivity of LPSCl electrolyte to moisture and e-beam damage (*7*, *31*). These limitations hinder high-resolution structural, chemical, and valence analysis at critical interfaces (*32*, *33*), hampering the development of advanced solid-state batteries. To overcome this, aberration-corrected cryo-TEM and low-dose imaging were developed through extensive instrumental

[1]Chemical Sciences and Engineering Division, Argonne National Laboratory, Lemont, IL, USA. [2]National Synchrotron Light Source II, Brookhaven National Laboratory, Upton, NY, USA. [3]Center for Nanoscale Materials, Argonne National Laboratory, Lemont, IL, USA. [4]X-ray Science Division, Argonne National Laboratory, Lemont, IL, USA. [5]Advanced Light Source, Lawrence Berkeley National Laboratory, Berkeley, CA, USA. [6]Pritzker School of Molecular Engineering, The University of Chicago, Chicago, IL, USA. ***Corresponding author. Email: amine@anl.gov (K.A.); xug@anl.gov (G.-L.X.)** †These authors contributed equally to this work. ‡ Present address: Energy Storage Research Center, Korea Institute of Science and Technology (KIST), Seoul, Republic of Korea.

and experimental advancements (figs. S7 to S10), enabling direct observation of surface-to-bulk microstructural evolution in LPSCl and composite sulfur cathodes as well as their interface.

High-angle annular dark-field scanning transmission electron microscopy (HAADF-STEM) imaging and energy-dispersive x-ray spectroscopy (EDS) mappings revealed a uniform distribution of S, P, and Cl within the microsized LPSCl particle (Fig. 1A). Line scan analysis further confirmed an atomic ratio of 5:1:1 for S, P, and Cl, respectively (Fig. 1B). Quantitative analysis across surface and bulk regions (#1 to #3 in Fig. 1A) showed a Cl-to-P atomic ratio close to 1:1 (Fig. 1E), which was consistent with the bulk LPSCl structure. After UHS mixing, HAADF-STEM and EDS mapping revealed a clear Z-contrast variation and a Cl-rich segregation layer at the particle surface (Fig. 1C). The EDS line scan (Fig. 1D) confirmed a sharp increase in Cl concentration at the particle edges. Quantitative analysis in areas #4 to #6 of UHS-mixed LPSCl particles further showed a two to three times increase in the Cl-to-P ratio at the surface compared with the bulk (Fig. 1E). S-$L_{2,3}$ and Cl-$L_{2,3}$ edge electron energy loss spectroscopy (EELS) spectra at multiple regions further distinguished the distribution of sulfur and chlorine signals at the interface, which shows that the high-contrast regions (#8 to #10) are mainly composed of bulk LPSCl without Cl segregation, whereas the low-contrast regions (#7 and #11) consist of elemental sulfur and Cl-rich compounds (Fig. 1F and fig. S11).

The observed Cl segregation from LPSCl SSE is hypothesized to result from a mechanochemical reaction induced by UHS mixing (fig. S12). The frictional forces between particles generated localized heat sufficient to promote the Cl segregation, whereas shear forces contributed to particle size reduction and homogeneous mixing (*34*). As Li^+ is the only cation within the composite cathode and LiCl is a major electrochemical decomposition component of LPSCl (*35*, *36*), we believe that the segregated Cl tends to exit as LiCl. In situ synchrotron x-ray diffraction (SXRD) during heating of a hand-mixed composite S/LPSCl/C mixture clearly evidenced the formation of LiCl (111) and (200) peaks as well as the reduction of LPSCl peaks with increased temperature (Fig. 1G and fig. S13). Similar results were observed during the heating of LPSCl and conductive carbon without sulfur, indicating that the LiCl segregation was not driven by the reaction with sulfur (fig. S14). EDS mapping (fig. S15) and quantification analysis results (Fig. 1E) of hand-mixed and heated composite S/LPSCl/C cathodes revealed similar Cl segregation, confirming the effect of the heating-striking force. In situ heating TEM experiments (figs. S16 and S17, and movies S1 and S2) further highlight the crucial role of the interplay between heating and shearing force during UHS mixing in addition to the microstructures of carbon additives (fig. S18) and electroactive materials (e.g., melting point) in promoting the halide segregation of halogen-containing solid electrolytes.

The microstructures of composite S cathodes prepared with different mixing times and speeds were unveiled by the SXRD (fig. S19A) and Rietveld refinement results (tables S2 to S5), x-ray pair distribution function analysis (fig. S19C), and Raman spectra (fig. S19D). No

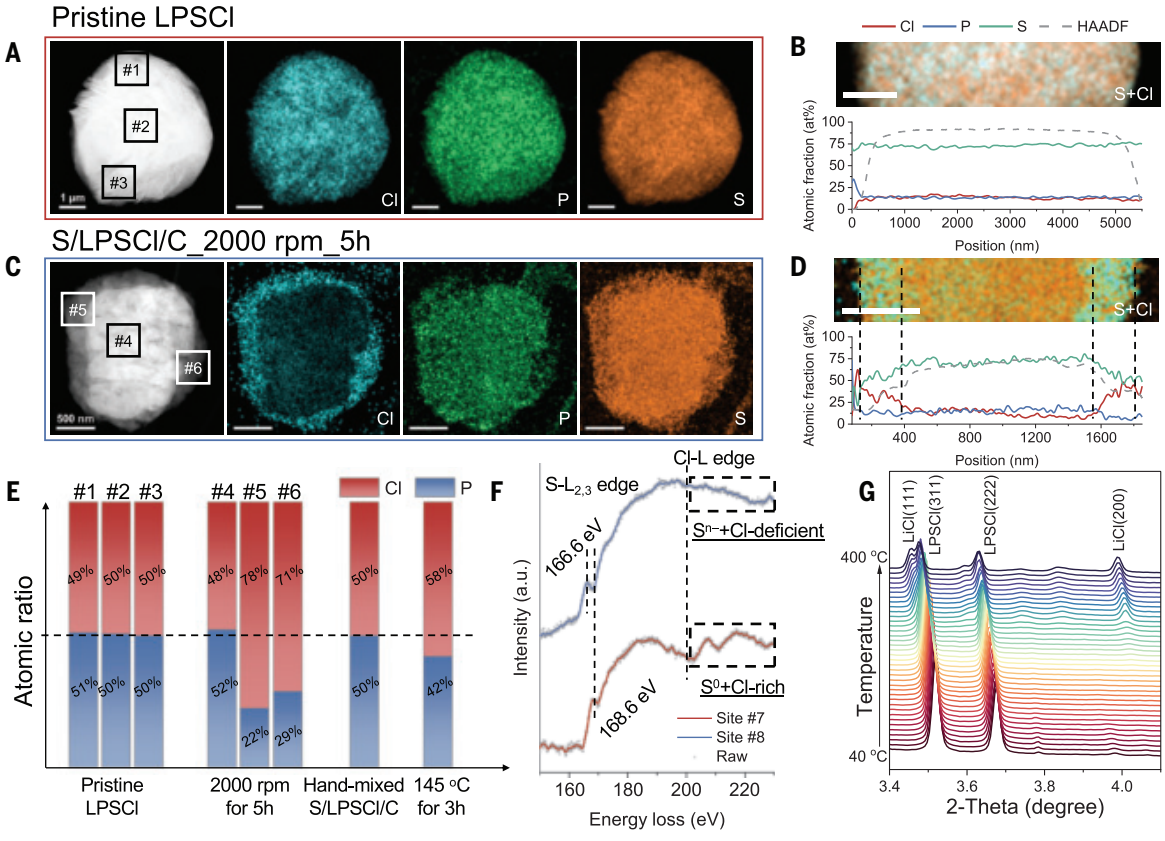

Fig. 1. Structure analysis of various composite S/LPSCl/C cathodes. (**A**) HAADF image with elemental mappings and (**B**) EDS line scan analysis of pristine LPSCl. (**C**) HAADF image with elemental mappings and (**D**) EDS line scan analysis of composite S/LPSCl/C cathode prepared with an ultrahigh mixing speed of 2000 rpm for 5 hours. The scale bars in (B) and (D) are the same as in (A) and (C), respectively. (**E**) Quantification of Cl-to-P atomic ratios for pristine Li_6PS_5Cl, composite S/LPSCl/C cathode with mixing at 2000 rpm for 5 hours, hand-mixed S/LPSCl/C cathode, and hand-mixed S/LPSCl/C cathode after heating at 145°C for 3 hours. (**F**) S-$L_{2,3}$ and Cl-$L_{2,3}$ edges EELS spectra of selected regions (fig. S11) in the composite S/LPSCl/C cathode with mixing at 2000 rpm for 5 hours. a.u., arbitrary units. (**G**) In situ SXRD patterns of the hand-mixed S/LPSCl/C cathode during heating from 40° to 400°C with a heating ramp rate of 10°C min^{-1}.

crystalline sulfur features were observed in all the composite S cathodes, indicating strong crystallinity loss of sulfur after mixing. By contrast, the 5-hour UHS-mixed sample showed pronounced reduction in both crystallite size and lattice parameter *a* of LPSCl (fig. S19B), presumably owing to the LiCl segregation. These findings were corroborated by x-ray photoelectron spectroscopy (XPS) characterization (figs. S20 to S22), reaffirming the formation of LiCl through partial segregation of LPSCl while ruling out the severe collapse of LPSCl to form Li_3P (*37*).

Universal halide segregation with chalcogen cathodes

We extended such a halide segregation strategy to a family of chalcogen cathodes and halogen-containing SSEs. Although cryo-TEM can preserve the native state of sulfur and its species, the real challenge lies in distinguishing critical interfaces due to the similar atomic numbers of sulfur and LPSCl anions. Introducing chalcogen cathodes such as Se and Te not only differentiates chalcogen signals from halogen-containing SSEs (Cl, Br, I) but also improves the understanding of cathode interfaces, as Se and Te exhibit greater stability than sulfur against e-beam damage and high vacuum. The UHS-mixed composite Se, SeS_2, and Te cathodes using LPSCl SSE demonstrated distinct Cl segregation from LPSCl and a strong overlap of Cl with Se or Te signals (figs. S23 and S24) regardless of the chalcogen type. Similarly, the composite S cathodes with various halogen-containing SSEs [Li_6PS_5Br (LPSBr), $Li_6PS_5Cl_{0.5}Br_{0.5}$ (LPSClBr), and $Li_6PSCl_{0.9}I_{0.1}$(LPSClI)] all demonstrated halide segregation after UHS mixing (fig. S25). HAADF-STEM images and EDS mappings revealed halide segregation of both Cl and Br at the surface of Se in UHS-mixed composite Se/LPSCl/C (Fig. 2A) and Se/LPSBr/C cathodes (Fig. 2B). Quantitative analysis of multiple regions confirmed a substantial increase in the Cl-to-P and Br-to-P ratios, which rose by 1.5 to 4.6 times (Fig. 2C), similar to the Cl segregation observed in UHS-mixed composite S cathodes (Fig. 1). The composite Se cathodes did not form similar core-shell structures as the UHS-mixed composite S cathode owing to the difference in material properties between S and Se, such as melting point and ductility. Nevertheless, a uniform halide segregation (fig. S26) and carbon distribution (fig. S27) within the composite Se cathode was clearly evidenced by EDS mapping of multiple particles and regions.

To investigate the chemical state and spatial distribution of the segregated layer, we obtained EELS spectra and element mapping at specific sites in the annular dark-field STEM (ADF-STEM) image. Compared with the bulk LPSCl (i) and blank area (v), Cl-$L_{2,3}$ edge peaks located at 200 to 220 eV intensified at sites ii to iv (fig. S28), indicating Cl^- anion enrichment, based on standard KCl edge peaks. EELS mapping (Fig. 2D) further confirmed the formation of a LiCl-rich interfacial layer on the surfaces of Se particles after UHS mixing. Furthermore, Li-K (55 eV), P-$L_{2,3}$ (132 eV), S-$L_{2,3}$ (165 eV), and Cl-$L_{2,3}$ (200 eV) edge EELS characterization (Fig. 1E and fig. S29) revealed the formation of LiCl and Li- and Cl-deficient Li-P-S phase at the interface with a distinct Cl-to-P ratio. Interestingly, Cl-rich phases were consistently

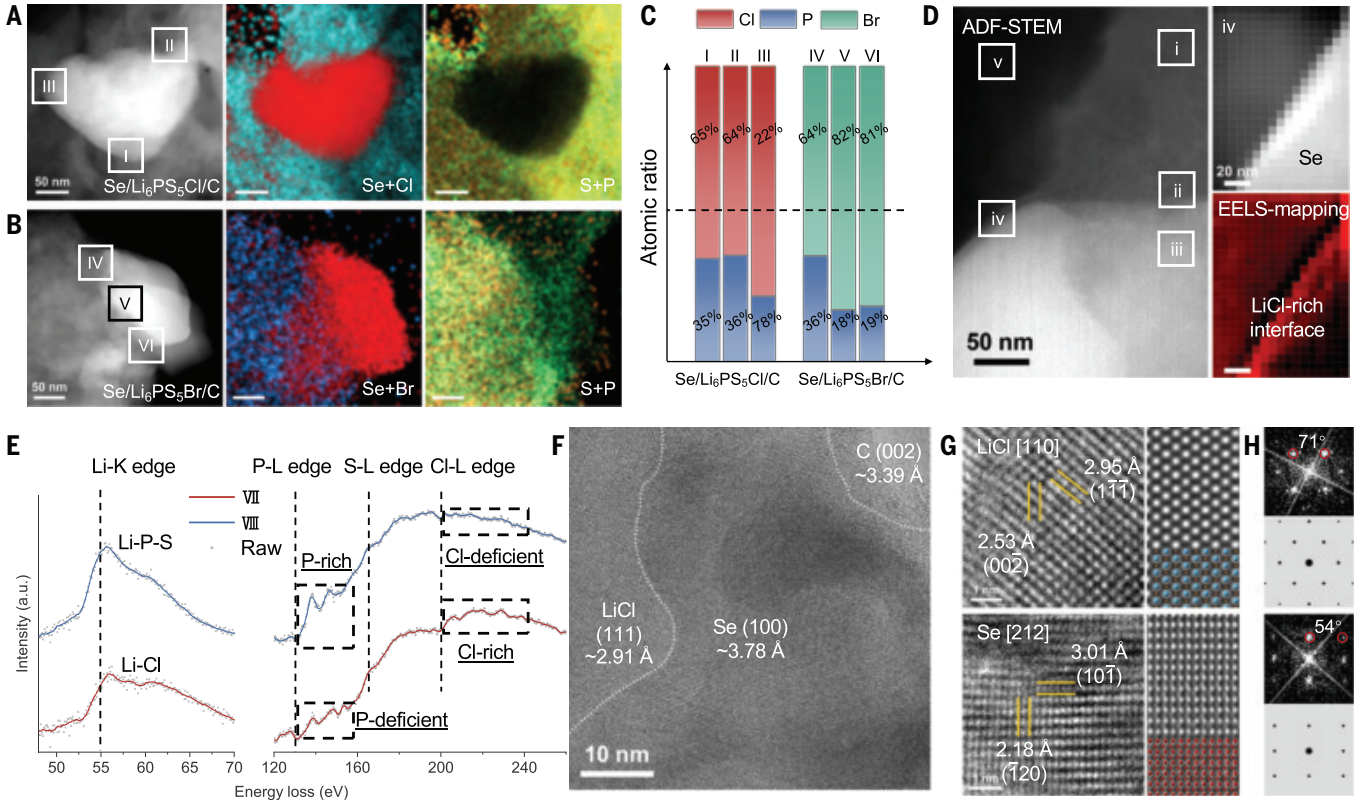

Fig. 2. Cryo-TEM validation of universal halide segregation. (**A**) HAADF image and the elemental mapping of composite Se/LPSCl/C cathode prepared with mixing at 2000 rpm for 5 hours. (**B**) HAADF image and the elemental mappings of composite Se/LPSBr/C cathode prepared with mixing at 2000 rpm for 5 hours. (**C**) Comparison of Cl-to-P and Br-to-P atomic ratios in the UHS-mixed composite Se cathodes, with data obtained from three different regions in each particle, as marked by the boxes in (A) and (B). (**D**) HAADF-STEM image (left), an enlarged view of the region marked as iv (top right), and EELS mapping of the same region (bottom right). (**E**) Li-K, P-$L_{2,3}$, S-$L_{2,3}$, and Cl-$L_{2,3}$ edges EELS spectra of selected regions (fig. S29) in the composite Se/LPSCl/C cathode with mixing at 2000 rpm for 5 hours. (**F**) HRTEM image showing Se covered by a layer of nanosized LiCl and carbon. (**G**) Acquired and simulated results of HRTEM images and (**H**) the corresponding FFT patterns and standard FFT patterns for cubic LiCl (top) and hexagonal Se (bottom) along the [110] and [212] directions, respectively. The Li, Cl, and Se atoms are represented by orange, blue, and red balls, respectively.

associated with P-deficient phases, whereas Cl-deficient phases corresponded to P-rich areas. High-resolution TEM (HRTEM) imaging of multiregions consistently revealed that nanocrystalline LiCl segregated alongside Se domains (Fig. 2F and figs. S30 and S31). A comparison of HRTEM images with simulated images (Fig. 2G), along with corresponding fast Fourier transform (FFT) patterns and standard FFT patterns (Fig. 2H), showed cubic Fm-3m LiCl with $(1\bar{1}\bar{1})$ and $(00\bar{2})$ crystal facets along the [110] zone axis and hexagonal P3121 Se with $(10\bar{1})$ and $(\bar{1}20)$ surfaces along the [212] direction. These results provided solid evidence for the segregation of nanosized lithium halide from bulk halogen–containing SSEs and the subsequent deposition onto chalcogen cathode particles by UHS mixing.

Electrochemical performance

We examined the effect of halide segregation on the electrochemical performance of various chalcogen cathodes in all-solid-state cells with a Li-In anode, areal active material (e.g., S) loading of 4 mg cm^{-2}, and a stack pressure of ~70 MPa, unless specified otherwise. Moreover, we tested all the cells at room temperature (~25°C), lifting the limits of many reported ASSLSBs that relied on elevated working temperature (e.g., 60°C) to improve ion transport (table S1). Figure 3A shows the cycling performance of the UHS-mixed composite S cathodes with different processing times (1, 5, and 10 hours) at a current density of 0.67 mA cm^{-2}. Compared with the 1-hour and lower-speed (figs. S32 to S34) composite S cathodes without marked LiCl segregation, the 5-hour UHS-mixed composite S cathode delivered a high initial areal capacity of 6.28 mA·hour cm^{-2} and still retained 6.21 mA·hour cm^{-2} after 100 cycles, corresponding to a high capacity retention of 98.9%. Further increasing the mixing time to 10 hours still preserved the feature of LiCl segregation but resulted in a notable crystal structure collapse of LPSCl (fig. S35). As a result, both the 1- and 10-hour composite S cathodes exhibited rapid capacity decline during prolonged cycling. Whereas the ionic conductivity of bulk LPSCl SSEs decreased along with the time of UHS mixing, the Li^+ diffusion coefficient of the UHS-mixed composite cathodes increased substantially, with the 5-hour UHS-mixed composite S cathode demonstrating an increase 196 times greater than that of the 400-rpm cathode (fig. S36). These results highlight the crucial role of lithium halide segregation at the cathode-SSE interface in boosting the effective ion transport of the composite S cathodes, leading to exceptionally high sulfur utilization beyond many reported ASSBs under high S loading (fig. S3). Online cell stack pressure measurement during discharge and charge revealed a minimum pressure loss in the 5-hour UHS-mixed composite S cathode, indicating that the segregated LiCl layer could also suppress the volume change of sulfur particles during cycling (fig. S37). As a result, the voltage profiles during cycling of the 5-hour UHS-mixed composite S cathode showed a minimal polarization increase (Fig. 3B).

Long-term cycling performance of the 5-hour UHS-mixed composite S cathode was evaluated with an areal S loading of 2 mg cm^{-2} at 0.67 mA cm^{-2}. As shown, the all-solid-state cell could retain a reversible capacity of 3.00 mA·hour cm^{-2} after 450 cycles (Fig. 3C), leading to a high capacity retention of 93.2% after extended cycling. With an increased areal S loading of 4 mg cm^{-2} and a higher current density of 1.4 mA cm^{-2}, the all-solid-state cell could still deliver an initial discharge areal capacity of 6.35 mA·hour cm^{-2} (i.e., a high sulfur utilization of 95%) and a capacity retention of 80% after 450 cycles (Fig. 3D). The excellent cycling stability of the UHS-mixed composite S cathode was also demonstrated using Li metal as the anode (fig. S38). The 5-hour UHS-mixed composite S cathode still presented a high areal capacity and stable cycle life with a further increase of sulfur content to 32.5 wt % (fig. S39), leading to increased overall energy density. Evaluation under lower stack pressures of 36 and 18 MPa also demonstrated high capacity retention (fig. S40). These results corroborate

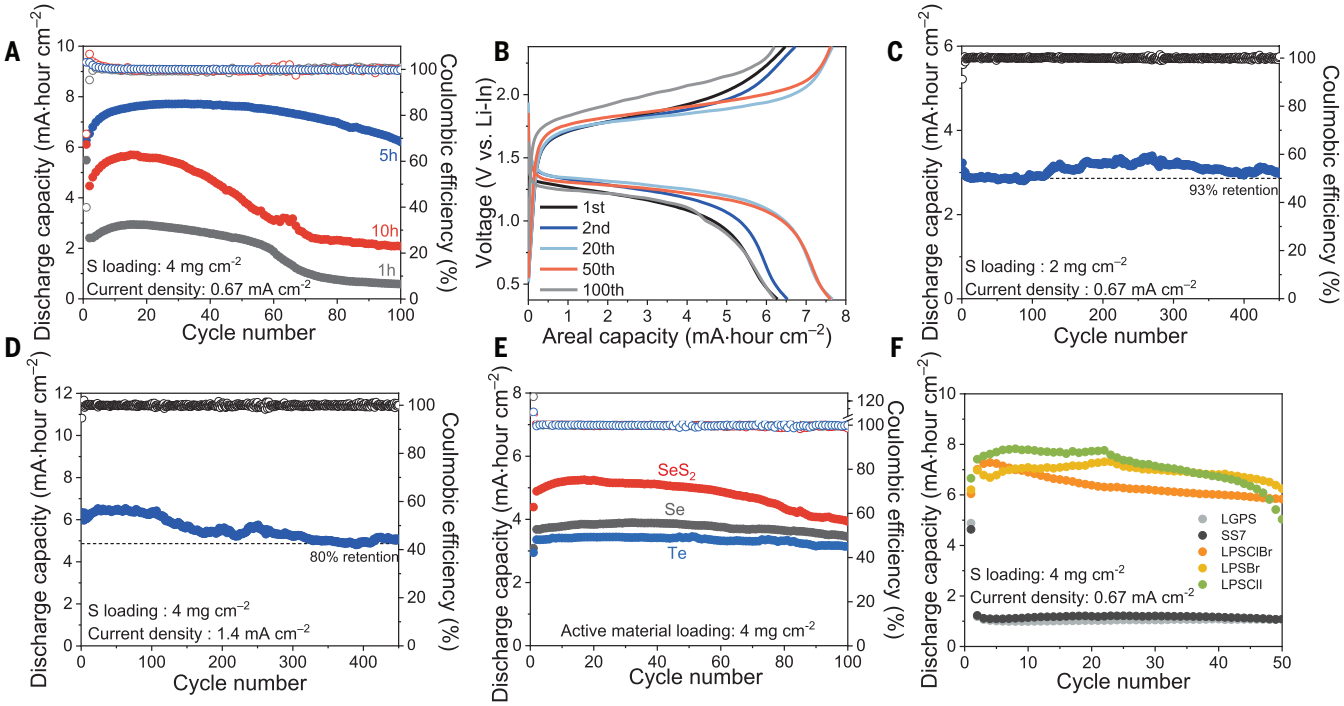

Fig. 3. Electrochemical performance of all-solid-state Li-chalcogen batteries. (**A**) Cycling performance of the UHS-mixed composite S/LPSCl/C cathodes with different times. (**B**) The corresponding discharge-charge curves of the 5-hour UHS-mixed composite S/LPSCl/C cathode. Long-term cycling performance of the 5-hour UHS-mixed composite S/LPSCl/C cathode with an areal S loading of (**C**) 2 mg cm^{-2} and (**D**) 4 mg cm^{-2} at room temperature. (**E**) Cycle performance of 5-hour UHS-mixed composite chalcogen cathodes at 0.27 (Se), 0.54 (SeS_2), and 0.56 (Te) mA cm^{-2} at room temperature. (**F**) Cycle performance of various 5-hour UHS-mixed composite S cathodes incorporating halogen-containing and halogen-free SSEs at room temperature.

the notable advantages of the present halide segregation strategy over many reported approaches in promoting the reaction kinetics and cycling stability of high-loading ASSLSBs (table S1 and figs. S2 and S3). Specifically, such in situ segregated nanosized lithium halide layers at the cathode-SSE interface produce results that differ greatly from those using bulk lithium halide additives, which suffer from intrinsic poor ion conductivity and low coverage (*13*–*15*).

The cycling performance of all-solid-state cells with various UHS-mixed composite chalcogen cathodes, including SeS_2, Se, and Te, are presented in Fig. 3E. As a result of the universal LiCl segregation, all these cells also demonstrated high utilization, stable cycling life, and good rate performance (fig. S41) at commercial-level areal capacities (3 to 5 mA·hour cm^{-2}) and room temperature. The broad effectiveness of halide segregation was further demonstrated through cycling tests of UHS-mixed composite S cathodes with various SSEs (Fig. 3F). Despite similar ionic conductivities among all the used SSEs (fig. S42), only cells incorporating halogen-containing SSEs (LPSBr, LPSClBr, and LPSClI) consistently exhibited high reversible capacity, whereas those with halogen-free SSEs (SS7 and $Li_{10}GeP_2S_{12}$) showed markedly lower capacity. Additionally, separate tests of hand-mixed composite S cathodes with and without heating treatment showed that the sulfur utilization was improved after heat treatment (fig. S43), which was well aligned with heat-induced LiCl segregation as revealed by the cryo-TEM results (fig. S15).

In addition, it was noted that the UHS-mixed composite chalcogen cathodes exhibit greater capacity than their theoretical capacity limits (table S6), which can be attributed to the capacity contribution of the LPSCl SSE (*36*, *38*). Although it has been shown that carbon would accelerate the decomposition of sulfide SSEs, particularly at high and low potential (*39*), the superior cycling stability of the 5-hour UHS-mixed composite chalcogen cathodes revealed that the interfacial halide segregation might help suppress these side reactions as well (figs. S44 to S46), adding extra capacity and energy density to the cell without sacrificing stability.

Postmortem characterization

We conducted multimodal synchrotron x-ray probes and cryo-TEM characterization of the cycled composite cathodes to elucidate the effect of halide segregation on the reaction pathways of all-solid-state lithium-chalcogen batteries. Figure 4A shows the S K-edge x-ray absorption near-edge structure (XANES) spectra of the 5-hour UHS-mixed composite S cathode at different discharge and charge states, along with the reference S, LPSCl, and Li_2S spectra. As shown, the pristine composite S cathode showed both features of S (2473 and 2480 eV) and LPSCl (2472 eV). At half discharge or charge, no peaks at ~2470 eV were observed (*13*), indicating no formation of soluble polysulfides. After the first full discharge, the peak of LPSCl remained, but the peak of sulfur (2473 eV) shifted to higher energy (2474 eV), well aligned with the peak of reference Li_2S. After the first full charge, the peak of Li_2S disappeared along with the return of the S signal to its original position before discharge. Such high delithiation-lithiation reversibility enabled by LiCl segregation was still well maintained during extended cycling. The structural features of the 30th discharge composite S cathode well reassembled those of the first discharge feature. For comparison, the 10-hour UHS-mixed composite S cathode showed a notable residue of Li_2S features after the first charge, indicating decreased reaction reversibility (fig. S47).

As both the sulfur cathode and LPSCl SSEs contain S signals, in situ Se K-edge XANES of the 5-hour UHS-mixed composite Se/LPSCl/C cathode was conducted to better probe whether any soluble long-chain polyselenides form during discharge and charge (Fig. 4B and fig. S48). As shown, the absorption edge position of Se did not undergo an obvious shift during the entire cycling process, whereas the absorption intensity gradually decreased during discharge and completely recovered at the end of charge, which was reaffirmed by the first derivatives of the Se K-edge XANES (Fig. 4C). These structural features are consistent with the reaction pathway of the Se cathode in polyselenide-free carbonate electrolytes (*40*) while being in sharp contrast with those involving conventional ether electrolytes with high polyselenide

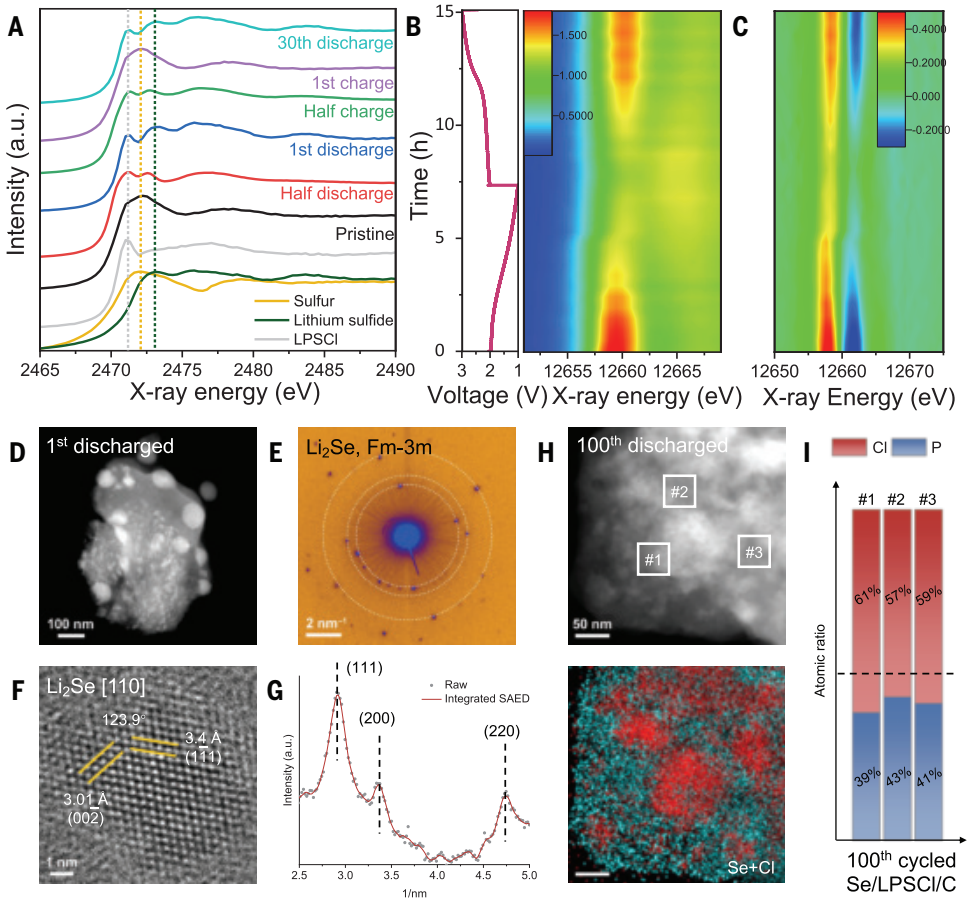

Fig. 4. Postmortem analysis of UHS-mixed composite chalcogen cathodes. (**A**) S K-edge XANES spectra of the 5-hour UHS-mixed composite S/LPSCl/C cathode at different discharge and charge states. (**B**) Normalized two-dimensional contour plot of in situ Se K-edge XANES spectra of the 5-hour UHS-mixed composite Se/LPSCl/C cathode along with the discharge-charge profiles and (**C**) the corresponding derivative curve. (**D**) HAADF-STEM image, (**E**) SAED pattern, (**F**) HRTEM image, and (**G**) intensity integration profile from (E) of the 5-hour UHS-mixed composite Se/LPSCl/C cathode after the first discharge. (**H**) HAADF-STEM image and the elemental mappings of the 5-hour UHS-mixed composite Se/LPSCl/C cathode after 100 cycles. (**I**) Cl-to-P atomic ratios, with data from the three different regions in (H) marked by boxes.

solubility (*41*). In combination with S XANES, these results firmly reveal no formation of soluble intermediates in the LiCl-segregated composite chalcogen cathodes during discharge and charge, preserving the inherent nature of all-solid-state batteries that eliminate the use or formation of any liquid species. Comparison with composite Se cathodes prepared at different conditions further confirm the effect of halide segregation in promoting the reaction reversibility of composite cathodes (fig. S49).

The influences of LiCl segregation on the microstructures of discharge products and the consequent effects on the reaction kinetics and mechanical stability of composite chalcogen cathodes were further revealed. The in situ microcomputed tomography (μ-CT) of the 5-hour UHS-mixed composite S cathode during discharge and charge showed minimal electrode expansion and no formation of visible cracks or pores (fig. S50), confirming that the segregated LiCl interfacial layer could well suppress the volume change during cycling. Owing to the extreme sensitivity of sulfur and related species, such as Li_2S, we conducted HAADF-STEM on the 5-hour UHS-mixed composite Se/LPSCl/C cathode after the first discharge. As shown in Fig. 4D, a uniform distribution of nanoparticles (brighter contrast) embedded within the LPSCl matrix (darker contrast) was observed. The corresponding selected-area electron diffraction (SAED) pattern indicated a polycrystalline feature (Fig. 4E), with intensity integration peaks matching the (111), (200), and (220) planes of cubic Fm-3m Li_2Se (Fig. 4G). This suggests that these larger nanoparticles are aggregates of numerous smaller nanocrystalline particles. HRTEM imaging confirmed nanocrystalline Li_2Se oriented along the [110] direction, with particle sizes of about 10 nm (Fig. 4F). The formation of nanocrystalline discharge products not only reduces the energy barriers for nucleation and decomposition of Li_2Se, enabling more efficient reactions, but also mitigates the volume swelling and shrinkage during repeated cycling, ensuring long-term stability (*42*). Additionally, HAADF-STEM imaging and elemental mapping of the 5-hour UHS-mixed composite Se cathode after 100 cycles show that Cl segregation and deposition at the cathode surface remains well preserved (Fig. 4, H and I), with a Cl-to-P ratio close to that of the pristine state (Fig. 2C).

Overall, such universal halide segregation enabled by UHS mixing expands the scope of interface design to develop high-energy and long-life all-solid-state batteries. The in situ segregated nanosized lithium halide interfacial layer from a series of halogen-containing SSEs substantially boosts the interfaces for a family of chalcogen cathodes, even with commercially viable areal capacities and room temperature. The discovery of unexpected mixing-directed interfacial chemistries might inspire fundamental understandings and optimization of existing and emerging mixing technologies and pave the way to development and manufacturing of advanced ASSLSBs with future optimization of anode interface design and solid electrolyte engineering.

REFERENCES AND NOTES

1. J. Zhou *et al.*, *Nature* **627**, 301–305 (2024).
2. Y. Li *et al.*, *Science* **381**, 50–53 (2023).
3. Y. Zeng *et al.*, *Science* **378**, 1320–1324 (2022).
4. Y. Kato *et al.*, *Nat. Energy* **1**, 16030 (2016).
5. S. Kalnaus, N. J. Dudney, A. S. Westover, E. Herbert, S. Hackney, *Science* **381**, eabg5998 (2023).
6. B. Zahiri *et al.*, *Nat. Mater.* **20**, 1392–1400 (2021).
7. J. T. Kim *et al.*, *Nat. Chem. Eng.* **1**, 400–410 (2024).
8. J. Lee *et al.*, *Chem. Soc. Rev.* **53**, 5264–5290 (2024).
9. T. Jin *et al.*, *Nano Lett.* **24**, 6625–6633 (2024).
10. X. Yao *et al.*, *Adv. Energy Mater.* **7**, 1602923 (2017).
11. S. Xu *et al.*, *Adv. Funct. Mater.* **31**, 2004239 (2021).
12. H. Zhong *et al.*, *Adv. Energy Mater.* **13**, 2300767 (2023).
13. J. T. Kim *et al.*, *Nat. Commun.* **14**, 6404 (2023).
14. H. Li *et al.*, *Adv. Compos. Hybrid Mater.* **6**, 162 (2023).
15. M. Liu *et al.*, *Nat. Commun.* **12**, 5943 (2021).
16. X. Li *et al.*, *Adv. Mater.* **31**, 1808100 (2019).
17. H. Zhong *et al.*, *Adv. Funct. Mater.* **34**, 2315925 (2024).
18. F. Pei *et al.*, *Nat. Commun.* **15**, 351 (2024).
19. D. Wang *et al.*, *Nat. Commun.* **14**, 1895 (2023).
20. S. Kim *et al.*, *Nat. Commun.* **10**, 1081 (2019).
21. Q. Pang *et al.*, *Nat. Energy* **3**, 783–791 (2018).
22. G. F. Dewald, S. Ohno, J. G. C. Hering, J. Janek, W. G. Zeier, *Batter. Supercaps* **4**, 183–194 (2021).
23. L. Fernandez-Diaz *et al.*, *Chem. Eng. J.* **464**, 142469 (2023).
24. H. Kim, H.-N. Choi, J.-Y. Hwang, C. S. Yoon, Y.-K. Sun, *ACS Energy Lett.* **8**, 3971–3979 (2023).
25. Z. Lin, Z. Liu, W. Fu, N. J. Dudney, C. Liang, *Angew. Chem. Int. Ed.* **52**, 7460–7463 (2013).
26. Y. Liu *et al.*, *Science* **375**, 739–745 (2022).
27. L. Hu *et al.*, *ACS Nano* **18**, 8463–8474 (2024).
28. H.-J. Deiseroth *et al.*, *Angew. Chem. Int. Ed.* **47**, 755–758 (2008).
29. X. Li *et al.*, *Nat. Commun.* **15**, 53 (2024).
30. J.-P. Correa-Baena *et al.*, *Science* **363**, 627–631 (2019).
31. Y. Nomura, K. Yamamoto, *Adv. Energy Mater.* **13**, 2203883 (2023).
32. J. E. Lee *et al.*, *Adv. Mater.* **34**, e2200083 (2022).
33. Y. B. Song *et al.*, *Nano Lett.* **20**, 4337–4345 (2020).
34. R. Schlem *et al.*, *Adv. Energy Mater.* **11**, 2101022 (2021).
35. C. D. Alt *et al.*, *Joule* **8**, 2755–2776 (2024).
36. D. H. S. Tan *et al.*, *ACS Energy Lett.* **4**, 2418–2427 (2019).
37. J. Auvergniot *et al.*, *Solid State Ion.* **300**, 78–85 (2017).
38. S. Wang *et al.*, *Adv. Energy Mater.* **11**, 2101370 (2021).
39. S. Ohno, C. Rosenbach, G. F. Dewald, J. Janek, W. G. Zeier, *Adv. Funct. Mater.* **31**, 2010620 (2021).
40. Y. Cui, A. Abouimrane, C.-J. Sun, Y. Ren, K. Amine, *Chem. Commun.* **50**, 5576–5579 (2014).
41. Y. Cui *et al.*, *J. Am. Chem. Soc.* **135**, 8047–8056 (2013).
42. S. Zhou *et al.*, *Nature* **621**, 75–81 (2023).

ACKNOWLEDGMENTS

This research used resources of the Advanced Photon Source and Center for Nanoscale Materials, both of which are US Department of Energy (DOE) Office of Science User Facilities operated for the DOE Office of Science by Argonne National Laboratory under contract no. DE-AC02-06CH11357. This research used 28-ID-2, 8-BM, and 8-ID beamlines of the National Synchrotron Light Source II, DOE Office of Science User Facilities, operated for the DOE Office of Science by Brookhaven National Laboratory under contract no. DE-SC0012704. This research also used resources of the Advanced Light Source (ALS), a DOE Office of Science User Facility under contract no. DEAC02-05CH11231. We are grateful for the use of microtomography measurement at beamline 8.3.2 of the ALS. **Funding:** Research at Argonne National Laboratory was funded by the DOE's Vehicle Technologies Office. Funding support from S. Thompson and T. Duong of the DOE's Vehicle Technologies Office program is gratefully acknowledged. **Author contributions:** G.-L.X. and K.A. supervised this project. G.-L.X., J.L., and S.Z. conceptualized the idea and designed the experiments. J.L., V.C.F., and A.S. synthesized composite cathode materials. J.L., V.C.F., and S.Z. conducted electrochemical tests for various cells and carried out SEM and XPS characterizations. S.Z. and Y.L. conducted TEM characterizations and analysis. G.-L.X., J.B., and W.X. conducted synchrotron XRD characterization and analysis. J.L., S.N., D.W., and Y.D. conducted S x-ray absorption spectroscopy (XAS) characterization. J.L., C.Z., and C.S. conducted the Se XAS experiment. J.L., S.Z., and D.Y.P. conducted the μ-CT experiment, and D.Y.P. conducted the data analysis. G.-L.X., J.L., and S.Z. drafted the paper with the help of all the other authors. All authors participated in the analysis of experimental data and discussions of the results, as well as in the writing and revision of the manuscript. **Competing interests:** G.-L.X., J.L., and K.A. report a US nonprovisional patent application filed on 13 February 2024, serial no. 18/440,838, based on this work. All other authors declare no competing interests. **Data and materials availability:** All data are available in the main text or the supplementary materials.

License information: Copyright © 2025 the authors, some rights reserved; exclusive licensee American Association for the Advancement of Science. No claim to original US government works. https://www.science.org/about/science-licenses-journal-article-reuse

SUPPLEMENTARY MATERIALS

science.org/doi/10.1126/science.adt1882
Materials and Methods; Figs. S1 to S50; Tables S1 to S6; References (*43*–*68*); Movies S1 and S2

Submitted 16 September 2024; accepted 25 March 2025

10.1126/science.adt1882

MESOSCOPIC PHYSICS

Anyon braiding and telegraph noise in a graphene interferometer

Thomas Werkmeister[1]†, James R. Ehrets[2]†, Marie E. Wesson[1], Danial H. Najafabadi[3], Kenji Watanabe[4], Takashi Taniguchi[5], Bertrand I. Halperin[2], Amir Yacoby[1,2], Philip Kim[1,2]*

The search for anyons, quasiparticles with fractional charge and exotic exchange statistics, has inspired decades of condensed matter research. Quantum Hall interferometers enable direct observation of the anyon braiding phase through discrete interference phase jumps when the number of encircled localized quasiparticles changes. In this study, we observed this braiding phase in both the filling factor 1/3 and 4/3 fractional quantum Hall states by probing three-state random telegraph noise (RTN) in real time. We found that the observed RTN stems from anyon quasiparticle number n fluctuations, and we reconstructed three Aharonov-Bohm oscillation signals phase shifted by $2\pi/3$, corresponding to the three possible interference branches from braiding around n (mod 3) anyons. Our methods can be readily extended to interference of non-abelian anyons.

The fractional quantum Hall (FQH) effects, where electrons are confined to two spatial dimensions and exposed to large magnetic fields, have long been predicted to host emergent fractionally charged excitations that obey neither fermionic nor bosonic exchange statistics (*1*–*5*). These quasiparticles fall into two classes, abelian and non-abelian anyons, associated with FQH states at different filling factors ν. For abelian anyons, exchanging two quasiparticles (i.e., braiding) results in the many-body wave function acquiring a complex phase, as demonstrated by anyon collision and interferometry experiments (*6*, *7*). For non-abelian anyons, the wave function evolves by a unitary transformation, enabling fault-tolerant topological quantum computation that has yet to be experimentally realized (*8*–*12*).

FQH Fabry-Pérot (FP) interferometers enable direct measurements of the anyon braiding phase (*13*, *14*). By partially backscattering current at two quantum point contact (QPC) constrictions, the conductance through the FP cavity modulates with the phase accumulated by edge-traveling quantum Hall (QH) quasiparticles (*5*, *15*). When the number of localized cavity quasiparticles encircled by the interfering edge changes, the resulting phase shift in the interference signal is equivalent to twice the fundamental exchange phase (modulo 2π) (*7*, *16*). However, because the observed discrete phase jumps represent charging events in the cavity, resultant Coulomb coupling between the bulk and edge must be accounted for when extracting the anyon braiding phase from a small number of phase jump events (*17*). Consequently, mitigating Coulomb coupling while maintaining electrostatic tunability has been a major challenge in semiconductor-based interferometers (*7*, *18*).

Graphene-based interferometers offer several advantages for realizing anyon braiding, both for the abelian and non-abelian cases. First, both QPCs (*19*, *20*) and interferometers (*21*–*26*) exhibit robust electrostatic tunability for integer QH states. Second, graphite gates reduce Coulomb coupling to reveal Aharonov-Bohm (AB) oscillations (*22*), which previously required complex quantum well structures in gallium arsenide (GaAs) (*7*, *18*). Simultaneously, these atomically flat gates enhance FQH states by screening out charge disorder (*27*, *28*) while allowing precise control of QPC transmission (*22*, *29*, *30*) and FP cavity filling factor (*25*). Encouragingly, bilayer graphene has displayed a multitude of even-denominator FQH states that may host non-abelian anyons with relatively large energy gaps (*31*–*35*). Here we report direct observation of abelian anyon braiding using high-visibility Aharonov-Bohm interference and anyon fluctuations in single-atomic-layer graphene.

Constructing a graphene fractional quantum Hall interferometer

We constructed our device by performing previously described nanolithography steps (*22*, *25*) on a heterostructure consisting of monolayer graphene encapsulated with insulating hexagonal boron nitride (*36*) and conducting graphite layers. By gating with separated top graphite regions, we defined the interferometer cavity and constructed two QPCs that introduce backscattering between the opposite chirality QH edge channels (Fig. 1A). The quality of the graphene is maintained in part thanks to the encapsulating graphite gates, as evident by well-developed FQH states (Fig. 1, B and C) at $T = 20$ mK. Unlike previous FQH interferometers in GaAs, we tuned the electron density in situ in graphene to access many FQH states while holding the magnetic field fixed. We set magnetic field B to 12 T (unless noted otherwise) and changed density to tune between filling factors $\nu = 4/3$, 1, and 1/3, enabling a direct comparison of interference between each state.

We began by tuning the device such that the interferometer cavity and adjoining contact regions are set to $\nu = 4/3$ by applying appropriate voltages V_{MG}, V_{LG}, and V_{RG} (MG, middle gate; LG, left gate; RG, right gate). The cavity boundary is defined by setting the plunger gate (V_{PG}) and QPC split-gate (SG) regions ($V_{LSG/RSG}$) to lie within $\nu = 0$. Two additional metallic bridge gates (BG) over the QPCs ($V_{LBG/RBG}$) allow for independent control of QPC transmissions while keeping all other gates fixed. The conductance across each QPC evolves from near 0 to a plateau at e^2/h, and finally to near $(4/3)e^2/h$ with increasing $V_{LBG/RBG}$, where e is the electron charge and h is Planck's constant (Fig. 1D). The resonances in the conductance in these scans indicate a relatively soft confining potential at this QPC tuning (*29*, *37*). It is then straightforward to tune each QPC to weakly backscatter the fractional edge channel of $\nu = 4/3$ by setting $V_{LBG/RBG}$ as indicated in Fig. 1D.

Three-state anyon telegraph noise

By measuring the conductance through the interferometer with the fractional edge of $\nu = 4/3$ weakly backscattering at both QPCs, we discovered sporadic switches between three discrete levels as a function of time, that is, three-state random telegraph noise (RTN) (Fig. 1E). From a histogram showing how these levels are weighted over 8 min, we extracted the average conductance and the total weight in time associated with each level. Then, we stepped the plunger gate V_{PG} to modify the area (*18*, *22*, *38*, *39*), or equivalently the total charge (*25*, *40*) contained in the FP cavity, and repeated the process. Plotting the resulting average conductance values shaded by their weight in time as a function of V_{PG} revealed three interwoven, phase-shifted sinusoidal oscillations (Fig. 1F).

Each sinusoid represents one of the three n (mod 3) possible phase "branches" associated with braiding the interfering edge quasiparticles around a system composed of n $e/3$ abelian anyons (*41*–*43*). By fitting the phase shift between the sinusoids using an improved measurement style (see section "Aharonov-Bohm magnetic field dependence"), we were able to extract the braiding phase at high precision.

Demonstrating exchange statistics with RTN is a departure from the method used in previous interferometer studies, in which discrete

[1]John A. Paulson School of Engineering and Applied Sciences, Harvard University, Cambridge, MA, USA. [2]Department of Physics, Harvard University, Cambridge, MA, USA. [3]Center for Nanoscale Systems, Harvard University, Cambridge, MA, USA. [4]Research Center for Electronic and Optical Materials, National Institute for Materials Science, Tsukuba, Japan. [5]Research Center for Materials Nanoarchitectonics, National Institute for Materials Science, Tsukuba, Japan. ***Corresponding author. Email: pkim@physics.harvard.edu** †These authors contributed equally to this work.

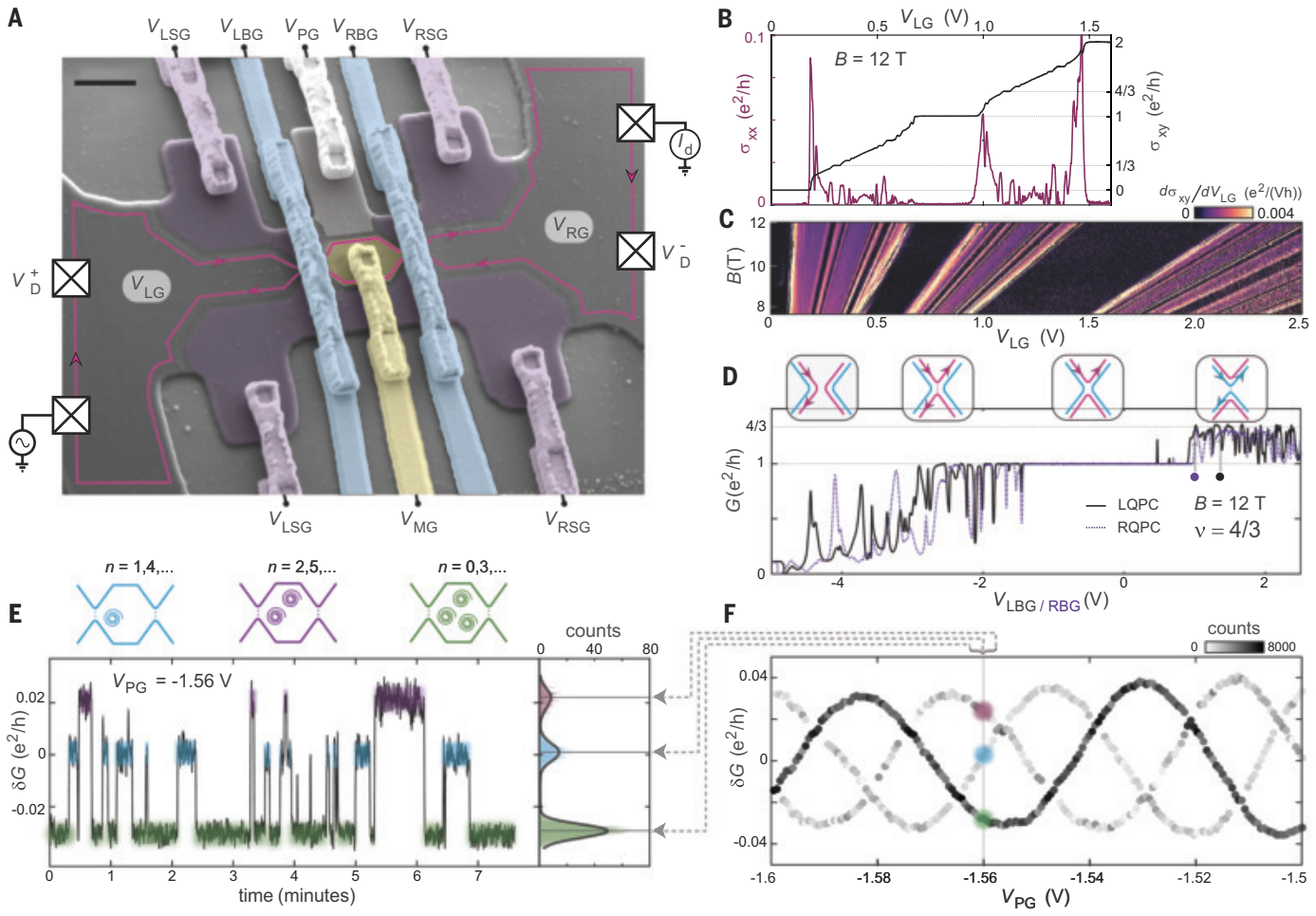

Fig. 1. Graphene FQH interferometer telegraph noise. (**A**) False-color scanning electron microscope image of a representative device depicting an interference measurement with a single edge channel. Scale bar: 1 μm. We measured the conductance $G = I_d / \left(V_D^+ - V_D^-\right)$ where I_d is the measured drain current and $V_D^{\pm}$ are the measured voltages at the indicated locations. The top graphite gate is etched into eight separately tunable regions controlled by voltages V_{LG}, V_{LSG}, V_{PG}, V_{MG}, V_{RSG}, and V_{RG}. Additionally, voltages $V_{LBG/RBG}$ applied to suspended bridges above the two QPCs independently set their transmissions. See fig. S1 for more details. (**B**) Hall conductivity σ_{xy} and longitudinal conductivity σ_{xx} measured with contacts in the left reservoir of the device highlighting the robust plateaus at $\nu = 0, 1/3, 1$, and $4/3$, the quantum Hall states that we studied. (**C**) Derivative of σ_{xy} showing the expected magnetic field dependence of the well-developed quantum Hall states. (**D**) Conductance G across the left/right QPC tuned by $V_{LBG/RBG}$ with the right/left QPC deactivated and the bulk in $\nu = 4/3$. See fig. S2 for details. (Inset) Schematics of the edge channel configuration and tunneling at a QPC. As $V_{LBG/RBG}$ increases, the constriction opens and transmits the outer integer edge (pink) first and eventually transmits the inner fractional edge (blue). (**E**) Three-state RTN in the conductance G when the fractional edge of $\nu = 4/3$ is weakly backscattering, corresponding to the tuning $V_{LBG} = 1.37$ V and $V_{RBG} = 1.01$ V, marked by the black and purple dots, respectively in (D), which are chosen to set $G \approx 1.28\, e^2/h$ or roughly 15% backscattering at each QPC. (Top inset) Cartoons of the three possible interference branches from braiding around n (mod 3) anyons, corresponding to the three conductance levels. (Right inset) Histogram of the conductance over time with 1000 bins. (**F**) Extracted sinusoidal oscillations from histograms over ~8 min for each V_{PG} voltage. Each data point shows the central conductance value of a Gaussian fit to a histogram peak, shaded by the total counts summed under the Gaussian. See fig. S3 for similar data in $\nu = 1/3$.

phase jumps in the continuously modulating AB phase $\theta_{AB}(B,V_{PG})$ were argued to represent the addition or subtraction of a quasiparticle in the interferometer bulk (*7*, *17*, *44*). These studies relied on modulating the AB phase using magnetic field B and plunger gate V_{PG} to probe irregularly spaced phase jumps due to anyon localization. To extract the anyon braiding phase, however, the experimentally observed phase jumps need to be analyzed with consideration given to the electrostatic coupling between the QH edge and localized bulk states. These analyses often become complicated because the bulk-edge capacitive coupling, the position of the chemical potential relative to the bulk Landau levels, and interferometer area A can drastically affect interference behavior, such as pivoting the interference signal into the well-studied "Coulomb-dominated" regime (*14*, *17*, *38*, *45*, *46*). It has also been shown that integer QH fillings can produce similar fractional phase jumps owing to the Coulomb coupling effect described above (*25*, *26*, *47*, *48*).

The measurement scheme presented in our work—observing a time-dependent interference phase ϕ through the RTN signal—offers a key benefit in this regard. Here, the parameters (B,V_{PG}) used to modulate the AB phase

$$\theta_{AB}\left(B, V_{PG}\right) = 2\pi \frac{e^*}{e} \frac{A\left(V_{PG}\right)B}{\phi_0}$$

can be held fixed while the quasiparticle number $n(t)$ fluctuates in time. Then, the expression for the total interference phase may be simplified as

$$\phi = \theta_{AB}\left(B, V_{PG}\right) + n\left(B, V_{PG}, t\right)\ \theta_a \rightarrow \theta_{AB} + n(t)\ \theta_a \qquad (1)$$

where $\theta_\alpha = 2\pi/3$ is the braiding phase for an $e^* = e/3$ anyon around a localized counterpart (assuming that Coulomb interactions are well screened) and $\phi_0 = h/e$. Considering the 2π periodicity of ϕ, the resulting braiding phase can only be one of three values varying by $2\pi/3$, reflecting the total number of localized anyons $n(t)$ (mod 3) at a given time. The device accordingly remains static in configurable parameter space (B,V_{PG}) while observing conductance switching from real-time fluctuations $n(t)$. Therefore, as this method demonstrates the existence of all three branches associated with the exchange statistics of charge $e/3$ anyons, we have constructed a complete representation of the state's braiding outcomes near a fixed device configuration set by B, V_{PG}, and density (tuned through V_{MG}).

Aharonov-Bohm magnetic field dependence

Measuring how the magnetic field B changes the total interference phase is crucial for determining whether the interferometer falls into the AB or the Coulomb-dominated regime (*5*, *14*). We started by measuring interference in the $\nu = 1$ integer QH state. By repeatedly sweeping the plunger gate, we observed the expected single-sinusoidal oscillations devoid of phase jumps (Fig. 2A). As we changed B, we observed magnetic field–dependent AB interference (Fig. 2B), where the magnetic field period ΔB_1 yields an area $\phi_0 = \Delta B_1 = 0.80\ \mu m^2$, as expected for interference of electrons in $\nu = 1$. A similar measurement in $\nu = 1/3$ with varying B and V_{PG} produced an irregular two-dimensional (2D) map because repeated plunger gate sweeps are not consistent owing to the frequent RTN fluctuations (Fig. 2C). However, we observed that each plunger gate scan contains stochastic switching between three sinusoidal branches, again shifted by $2\pi/3$ (Fig. 2D). By superimposing 100 of these sweeps and plotting the histogram of total recorded conductance values over V_{PG}, we were able to sample enough instances of the AB oscillation signal of each branch to recreate the three interwoven sinusoids seen in the previous measurement technique discussed in Fig. 1. Figure 2E exhibits the three interwoven branches at different magnetic fields. As the magnetic field decreases (from the top to bottom panels), we observe that each branch continuously drifts toward increasing V_{PG} values, creating a negative slope of constant phase (dashed line) analogous to the integer case of Fig. 2B. For $\nu = 1/3$, the corresponding flux superperiodicity $\Delta B_{1/3}$ (the magnetic field period for a single branch to return to its initial V_{PG} coordinate) yields $3\phi_0/\Delta B_{1/3} = 0.83 \pm 0.04\ \mu m^2$. This value is what one expects for interfering $e/3$ quasiparticles such that $\phi_0 \rightarrow h/(e/3) = 3\phi_0$. We similarly observe AB interference and a flux superperiodicity on the fractional edge of $\nu = 4/3$ (fig. S4), whereas the integer edge shows typical electron AB interference with no observable RTN. Note that even if the charge within the interferometer fluctuates in the integer case, the change in the interference phase caused by integer

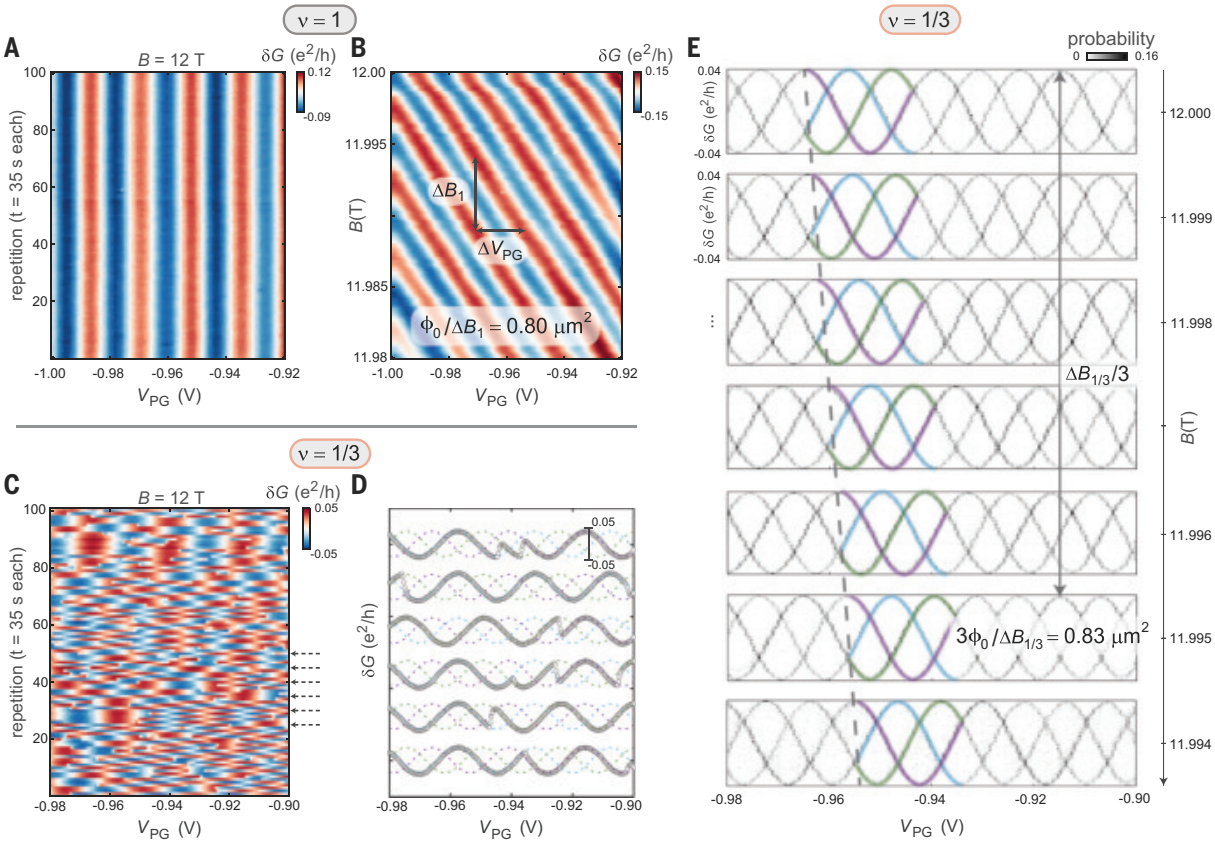

Fig. 2. Aharonov-Bohm magnetic field trend of $\nu = 1/3$ branches. (**A**) One hundred repeated V_{PG} sweeps in $\nu = 1$, where each sweep takes 35 s, demonstrating the temporal stability of oscillations in the integer state. (**B**) Magnetic field dependence of the oscillations in $\nu = 1$ demonstrating Aharonov-Bohm periodicity; the magnetic field period yields $\phi_0/\Delta B_1 = 0.80\ \mu m^2$, consistent with a small reduction of the area enclosed by the edge state within the designed area of 1.1 μm^2. (**C**) One hundred repeated V_{PG} sweeps in $\nu = 1/3$, using the same sweeping parameters as in (A), demonstrating the stochastic fluctuations induced by the RTN that could easily be mistaken for structureless noise, especially if averaged over by a slow sweep. (**D**) Six of the V_{PG} sweeps plotted to demonstrate switching between the three sinusoidal branches within a single scan. (**E**) 2D histograms showing the probability of measuring a given conductance for each V_{PG} value and its trend with the magnetic field. All three branches (partially highlighted) are made evident by this plot, and each branch trends identically with a flux superperiod in the magnetic field corresponding to $e/3$ anyons. Note that (E) is effectively presenting the AB oscillation demonstrated in the B versus V_{PG} plane for the $\nu = 1/3$ case, where RTN is present during each scan of V_{PG}.

changes in electron charge will be a multiple of 2π and therefore unobservable (*40*).

The fact that all tested configurations show AB interference (i.e., a negative slope of constant phase with respect to V_{PG} and B) instead of Coulomb-dominated effects indicates that our graphene interferometer is sufficiently screened by the graphite gates to suppress long-range Coulomb interaction, as required for observing braiding signatures (*7*, *14*, *17*). Furthermore, the observed $3\phi_0$ magnetic-flux superperiod in both $\nu = 1/3$ and $\nu = 4/3$ agrees with the $3\phi_0$ superperiod observed near the center of the $\nu = 1/3$ plateau in GaAs-based FP interferometers (*7*, *17*), suggesting that the quasiparticle gap is large enough to prevent continuous addition of quasiparticles (*49*).

The repeated sweep method exhibited in Fig. 2, which includes hundreds of phase jumps, provides an opportune dataset to extract a precise value for the anyon braiding phase and associated uncertainty [see section 3 of (*50*) for methodology and detailed discussion]. For the subplots shown in Fig. 2E, each containing 100 repeated sweeps and several hundred branch switches, we extracted an average braiding phase of $2\pi(0.3336 \pm 0.0051)$, or $120.1° \pm 1.8°$. The phase shift closely agrees with the theoretical value $2\pi/3$ and with the value extracted from previous interferometer (*7*, *17*) and anyon collider (*6*) experiments. Additionally, the smallness of the fitting error to the theoretical value $2\pi/3$, which neglects Coulomb corrections to the interferometer area with each quasiparticle fluctuation, demonstrates that Coulomb corrections are indeed negligible in our device.

Telegraph noise across the quantum Hall plateau

We gained insight into the nature of the quasiparticle fluctuations by tracking how the RTN evolves with density (filling) across the FQH plateau. Figure 3A exhibits subsets of 50-min measurements of the conductance, showing the V_{MG}-dependent RTN across the $\nu = 1/3$ plateau. The trace colors indicate the select values of V_{MG} that correspond to the subrange of the $\nu = 1/3$ QH plateau as shown in Fig. 3B. Of immediate note are clear changes in both the switching rate and amplitude as V_{MG} steps across the plateau. The average switching rate from the complete 50-min traces, τ_s^{-1}, shown in Fig. 3C, exhibits steep rises near the edges of the plateau and a relatively constant switching rate in between. Figure 3D shows the standard deviation, σ_G, of the diagonal conductance $G(t)$, providing a direct measure of switching amplitude.

The distinctive behavior of the anyon branch switching rate and amplitude along the plateau reveals that the quasiparticle fluctuations and coherence are closely correlated with the compressibility of the FQH state. A natural explanation would be that the switching rate increases as the number of localized states and anyon trapping sites increases near the edges of the FQH plateau. However, a simple increase in the individual switching rates of a constant number of traps across the plateau cannot be ruled out from this observation alone.

The noise spectral density of the diagonal conductance, S_G, can provide additional information supporting the hypothesis of an increasing trap number near the edge of the plateau. Figure 3E shows S_G as a function of frequency f, obtained from the Fourier transform of $G(t)$ at

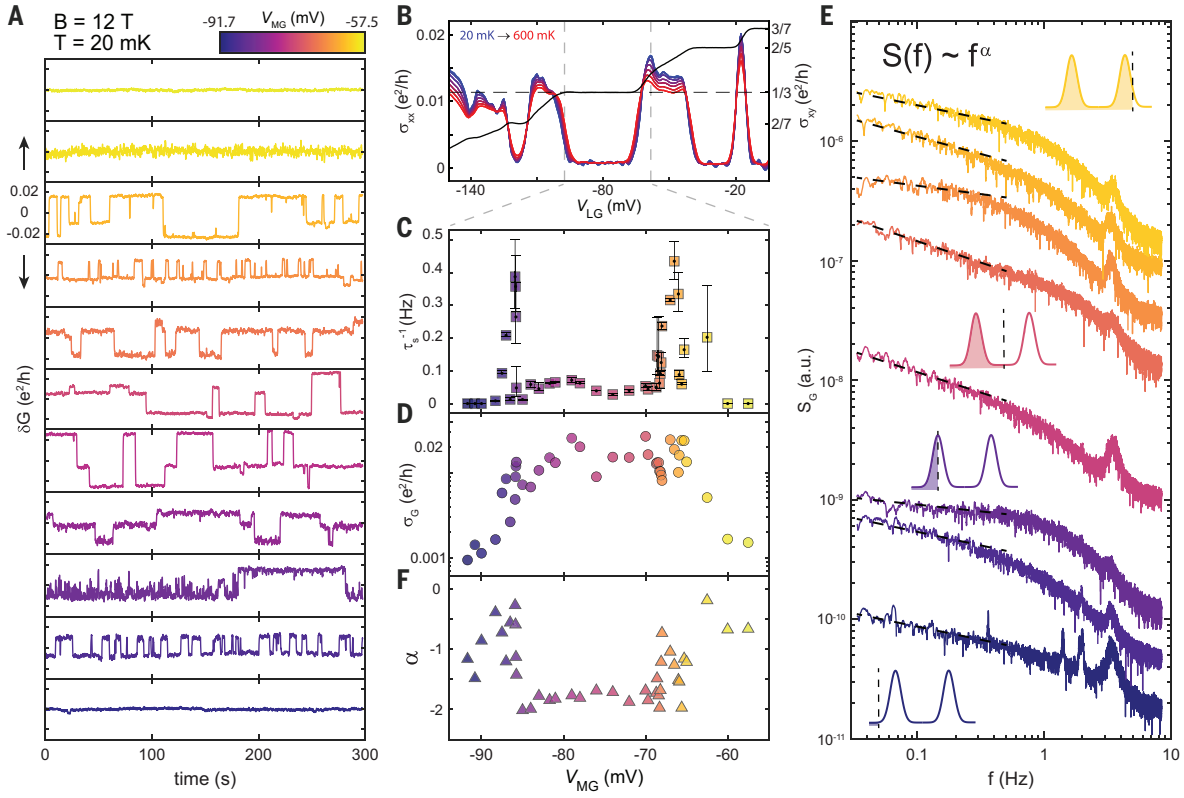

Fig. 3. Telegraph noise dependence on filling in $\nu = 1/3$. (**A**) Conductances versus time taken at different values for V_{MG}, indicated by color bar. The 300 s shown are from longer 50-min datasets. (**B**) Hall data taken from the left half of the device with density tuned through V_{LG}. The dashed lines indicate the associated range shown for V_{MG} in (C) to (E) below. The color scale on σ_{xx} spans from 20 mK (blue) to 600 mK (red). (**C**) Average branch switching rate along the plateau. Error bars indicate uncertainty associated with the switching identification algorithm and background noise [see section 2 of (*50*)]. (**D**) Standard deviation of conductance computed for $G(t)$ at fixed V_{MG}. (**E**) The spectral densities of conductance plotted on a log-log scale (traces are arbitrarily vertically shifted by ordering of V_{MG}). Dotted lines are fit to the power law dependence f^{α} in the low-frequency regime. Inset cartoons indicate the anyonic quasiparticle density of states versus energy, with the vertical dashed lines indicating the Fermi level for a given filling. a.u., arbitrary units. (**F**) The exponent α extracted from the fits of the power spectrum in (E) within the frequency range associated with the RTN.

various V_{MG} values across the plateau region. We find that $S_G(f)$ follows a power law scaling behavior $\sim f^{\alpha}$ in the low-frequency regime corresponding to the RTN signal. Figure 3F exhibits the scaling exponent α obtained from the line fits shown in Fig. 3E. In the middle of the plateau, the exponent α remains close to −2, which is expected from RTN with a single switching timescale (*51*). However, near the edges, α sharply increases and deviates from this stable value. It is known that when many instances of RTN with different switching timescales are convolved together, S_G is expected to approach $1/f$, or $\alpha = -1$ (*52*). Accordingly, the change of α near the edges of the plateau suggests that there are more distinctive switching timescales at the edge of the plateau than in the middle. This observation, together with the switching rate behavior discussed above, supports that the increased branch-switching incidents are indeed associated with increased localized anyon states in the bulk.

Temperature scaling

We also studied how the RTN changes as a function of temperature T. Figure 4A shows $G(t)$ near the middle of the $\nu = 1/3$ plateau at T ranging from 20 to 220 mK. As temperature increases, the switching amplitude decreases corresponding to a decrease in AB oscillation visibility. Figure 4B shows separately measured AB oscillation visibility as a function of T using plunger gate sweep measurements (similar to Fig. 2, C to E). The visibility decreases following an exponential decay as T increases, with a characteristic energy scale $T_0 = 110$ mK similar to that observed in $\nu = 1/3$ in GaAs (*7*).

In addition to the decrease in visibility, the RTN also shows an increase in switching rate as temperature increases. Figure 4C shows temperature-dependent τ_s^{-1} for two representative datasets, one at the center (red) and the other at the edge (yellow) of the plateau. Whereas the switching rate increases quickly at the high temperature limit, there is a drastic flat saturation of τ_s^{-1} for both datasets at low temperatures, below about 100 and 50 mK for the plateau center and edge, respectively. We find that an empirical formula that combines a term motivated by an Efros-Shklovskii (ES) form of variable-range hopping (VRH) (*53*, *54*) with an additional temperature-independent transition rate $\tau_{s,0}^{-1}$

$$\tau_s^{-1} = \tau_{s,0}^{-1} + \tau_{s,1}^{-1}(T)\, e^{-(T_{ES}/T)^{1/2}} \quad (2)$$

can provide a reasonable fit to the data, as shown by the dashed lines in Fig. 4C. Here $\tau_{s,1}^{-1}(T) \sim 1/T$ and T_{ES} is the characteristic ES VRH temperature scale. Although VRH has been used in the past to model longitudinal conduction caused by localized states in the QH effect (*54*–*57*), the physical mechanism behind the temperature scaling of τ_s^{-1} here remains nebulous.

Although we were able to provide evidence that the anyon fluctuations are closely associated with the number of anyon localized states and that they have consistent temperature scaling properties, a precise mechanism for their origin remains unclear. On the basis of the uniformity of the AB-modulating sinusoids in Figs. 1F and 2E, we postulate that the anyons are neither hopping from nor getting trapped within regions close to the QPCs, as even small changes in environmental charge would drastically change their tunings and the resultant visibility of the interference signal over time. We also observe that enclosing the sample in an additional radiation shield strongly reduces the switching rate (fig. S9), indicating that photons stimulate the fluctuations. Lastly, although fluctuations have not been reported in GaAs heterostructure–based interferometry experiments (*7*, *17*, *44*, *58*, *59*) or more recently in bilayer graphene (*60*), we note that the presence of slower or faster switching timescales could make initial observations of anyon fluctuations challenging with standard dc measurement techniques.

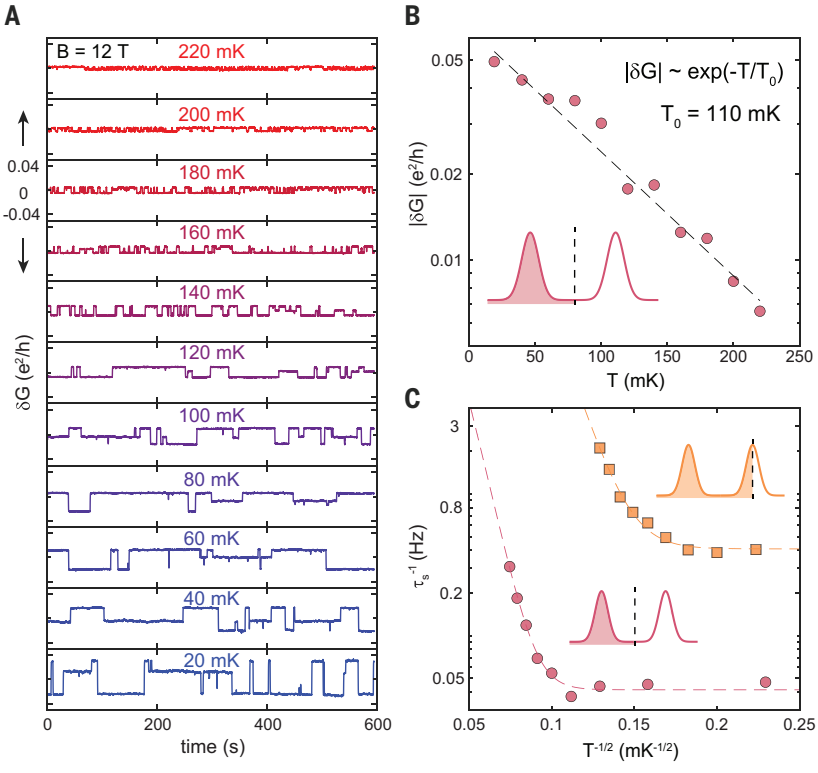

Fig. 4. Temperature-dependent telegraph noise and visibility in $\nu = 1/3$. (**A**) Conductance versus time taken at different temperatures T. The 600 s shown are subsets of longer 50-min datasets used for subsequent analysis. (**B**) Oscillation visibility extracted from V_{PG} sweep measurements (21 repeated scans averaged per point). The exponential decay fit to the oscillation visibility results in a characteristic temperature $T_0 = 110$ mK. (**C**) Low-temperature saturation and high-temperature activation of the average switching rate τ_s^{-1} observed for two fillings: at the center and at the edge of the $\nu = 1/3$ plateau, as shown in the insets. Shown fit lines follow the empirical formula of Eq. 2, where $T_{ES} = 22$ K (middle of plateau) and $T_{ES} = 9.5$ K (edge of plateau), which correspond to VRH hopping lengths of 130 and 300 nm, respectively (*55*, *65*).

Discussion and outlook

Here, we have shown that anyonic quasiparticle fluctuations and the resulting RTN in an FP interferometer are a powerful tool for exhibiting the complete set of braiding phases present in abelian states. These techniques pave the way for future interferometer measurements of non-abelian anyon braiding in even-denominator FQH states, where the small energy gap may enhance the RTN and limit the range of AB phase modulation. Several theoretical studies have already discussed which signatures would be expected in such a case where RTN is present for non-abelian states (*41*–*43*). Moreover, our ability to observe the slow equilibration of anyons enables future experiments to probe nontrivial anyon dynamics and to dynamically control anyon number in similar devices. This is particularly relevant to the ultimate goal of constructing a topological qubit with non-abelian anyons, which requires an understanding of how to selectively control and modulate the quasiparticle number (*61*–*63*).

Note added in proof: During the preparation of this manuscript, we became aware of a concurrent work using a similar graphene device (*64*).

REFERENCES AND NOTES

1. R. B. Laughlin, *Phys. Rev. Lett.* **50**, 1395–1398 (1983).
2. B. I. Halperin, *Phys. Rev. Lett.* **52**, 1583–1586 (1984).
3. D. Arovas, J. R. Schrieffer, F. Wilczek, *Phys. Rev. Lett.* **53**, 722–723 (1984).
4. A. Stern, *Ann. Phys.* **323**, 204–249 (2008).
5. D. E. Feldman, B. I. Halperin, *Rep. Prog. Phys.* **84**, 076501 (2021).
6. H. Bartolomei *et al.*, *Science* **368**, 173–177 (2020).
7. J. Nakamura, S. Liang, G. C. Gardner, M. J. Manfra, *Nat. Phys.* **16**, 931–936 (2020).
8. A. Kitaev, *Ann. Phys.* **321**, 2–111 (2006).
9. C. Nayak, S. H. Simon, A. Stern, M. Freedman, S. Das Sarma, *Rev. Mod. Phys.* **80**, 1083–1159 (2008).
10. A. Stern, N. H. Lindner, *Science* **339**, 1179–1184 (2013).
11. S. D. Sarma, M. Freedman, C. Nayak, *NPJ Quantum Inf.* **1**, 15001 (2015).
12. A. Yazdani, F. von Oppen, B. I. Halperin, A. Yacoby, *Science* **380**, eade0850 (2023).
13. C. de C. Chamon, D. E. Freed, S. A. Kivelson, S. L. Sondhi, X. G. Wen, *Phys. Rev. B* **55**, 2331–2343 (1997).
14. B. I. Halperin, A. Stern, I. Neder, B. Rosenow, *Phys. Rev. B* **83**, 155440 (2011).
15. M. Carrega, L. Chirolli, S. Heun, L. Sorba, *Nat. Rev. Phys.* **3**, 698–711 (2021).
16. N. Read, S. Das Sarma, *Nat. Phys.* **20**, 381–382 (2024).
17. J. Nakamura, S. Liang, G. C. Gardner, M. J. Manfra, *Nat. Commun.* **13**, 344 (2022).
18. J. Nakamura *et al.*, *Nat. Phys.* **15**, 563–569 (2019).
19. K. Zimmermann *et al.*, *Nat. Commun.* **8**, 14983 (2017).
20. H. Overweg *et al.*, *Nano Lett.* **18**, 553–559 (2018).
21. C. Déprez *et al.*, *Nat. Nanotechnol.* **16**, 555–562 (2021).
22. Y. Ronen *et al.*, *Nat. Nanotechnol.* **16**, 563–569 (2021).
23. L. Zhao *et al.*, *Nano Lett.* **22**, 9645–9651 (2022).
24. H. Fu *et al.*, *Nano Lett.* **23**, 718–725 (2023).
25. T. Werkmeister *et al.*, *Nat. Commun.* **15**, 6533 (2024).
26. W. Yang *et al.*, *Nat. Commun.* **15**, 10064 (2024).
27. Y. Zeng *et al.*, *Phys. Rev. Lett.* **122**, 137701 (2019).
28. R. Ribeiro-Palau *et al.*, *Nano Lett.* **19**, 2583–2587 (2019).
29. L. A. Cohen *et al.*, *Nat. Phys.* **19**, 1502–1508 (2023).
30. L. A. Cohen *et al.*, *Science* **382**, 542–547 (2023).
31. A. A. Zibrov *et al.*, *Nature* **549**, 360–364 (2017).
32. J. I. A. Li *et al.*, *Science* **358**, 648–652 (2017).
33. K. Huang *et al.*, *Phys. Rev. X* **12**, 031019 (2022).
34. A. Assouline *et al.*, *Phys. Rev. Lett.* **132**, 046603 (2024).
35. Y. Hu *et al*., arXiv:2308.05789 [cond-mat.mes-hall] (2023).
36. C. R. Dean *et al.*, *Nat. Nanotechnol.* **5**, 722–726 (2010).
37. S. Baer *et al.*, *Phys. Rev. B* **89**, 085424 (2014).
38. N. Ofek *et al.*, *Proc. Natl. Acad. Sci. U.S.A.* **107**, 5276–5281 (2010).
39. D. T. McClure, W. Chang, C. M. Marcus, L. N. Pfeiffer, K. W. West, *Phys. Rev. Lett.* **108**, 256804 (2012).
40. D. E. Feldman, B. I. Halperin, *Phys. Rev. B* **105**, 165310 (2022).
41. C. L. Kane, *Phys. Rev. Lett.* **90**, 226802 (2003).
42. E. Grosfeld, S. H. Simon, A. Stern, *Phys. Rev. Lett.* **96**, 226803 (2006).
43. B. Rosenow, S. H. Simon, *Phys. Rev. B* **85**, 201302 (2012).
44. J. Nakamura, S. Liang, G. C. Gardner, M. J. Manfra, *Phys. Rev. X* **13**, 041012 (2023).
45. Y. Zhang *et al.*, *Phys. Rev. B* **79**, 241304 (2009).
46. C. W. von Keyserlingk, S. H. Simon, B. Rosenow, *Phys. Rev. Lett.* **115**, 126807 (2015).
47. M. P. Rösli *et al.*, *Phys. Rev. B* **101**, 125302 (2020).
48. M. P. Rösli *et al.*, *Sci. Adv.* **7**, eabf5547 (2021).
49. B. Rosenow, A. Stern, *Phys. Rev. Lett.* **124**, 106805 (2020).
50. See supplementary materials.
51. M. B. Weissman, *Rev. Mod. Phys.* **60**, 537–571 (1988).
52. Sh. Kogan, in *Electronic Noise and Fluctuations in Solids* (Cambridge Univ. Press, 1996), pp. 203–286.
53. A. L. Efros, B. I. Shklovskii, *J. Phys. C Solid State Phys.* **8**, L49–L51 (1975).
54. G. Ebert *et al.*, *Solid State Commun.* **45**, 625–628 (1983).
55. K. Bennaceur, P. Jacques, F. Portier, P. Roche, D. C. Glattli, *Phys. Rev. B* **86**, 085433 (2012).
56. A. J. M. Giesbers *et al.*, *Phys. Rev. B* **80**, 241411 (2009).
57. J. Martin *et al.*, *Science* **305**, 980–983 (2004).
58. R. L. Willett *et al.*, *Phys. Rev. X* **13**, 011028 (2023).
59. H. K. Kundu, S. Biswas, N. Ofek, V. Umansky, M. Heiblum, *Nat. Phys.* **19**, 515–521 (2023).
60. J. Kim *et al.*, *Nat. Nanotechnol.* **19**, 1619–1626 (2024).
61. S. Das Sarma, M. Freedman, C. Nayak, *Phys. Rev. Lett.* **94**, 166802 (2005).
62. A. Stern, B. I. Halperin, *Phys. Rev. Lett.* **96**, 016802 (2006).
63. P. Bonderson, A. Kitaev, K. Shtengel, *Phys. Rev. Lett.* **96**, 016803 (2006).
64. N. L. Samuelson *et al*., arXiv:2403.19628 [cond-mat.mes-hall] (2024).
65. A. L. Efros, N. Van Lien, B. I. Shklovskii, *Solid State Commun.* **32**, 851–854 (1979).
66. T. Werkmeister, J. Ehrets, Data for "Anyon braiding and telegraph noise in a graphene interferometer" [Data set], Zenodo (2025); https://doi.org/10.5281/zenodo.14947934.

ACKNOWLEDGMENTS

We thank A. Banerjee, N. Poniatowski, Y. Ronen, S. H. Simon, and J. Zauberman for stimulating and helpful discussions. **Funding:** The major part of the experiment was supported by the US Department of Energy (DOE) (DE-SC0012260). J.R.E. acknowledges support from ARO MURI (N00014-21-1-2537) for sample preparation, measurement, characterization, and analysis. K.W. and T.T. acknowledge support from the JSPS KAKENHI (grants 20H00354 and 23H02052) and World Premier International Research Center Initiative (WPI), MEXT, Japan. M.E.W. and A.Y. acknowledge support from Quantum Science Center (QSC), a National Quantum Information Science Research Center of the DOE. B.I.H. acknowledges support from NSF grant DMR-1231319. Nanofabrication was performed at the Center for Nanoscale Systems at Harvard University, supported in part by an NSF NNIN award ECS-00335765. **Author contributions:** T.W., J.R.E., and P.K. conceived of and designed the experiment. T.W. and D.H.N. created the van der Waals heterostructure. T.W. performed the nanofabrication. T.W. and J.R.E. performed the measurements. M.E.W. and A.Y. provided the measurement cryostat and collaborated on discussions and analysis. K.W. and T.T. provided the hexagonal boron nitride crystals. T.W., J.R.E., and P.K. analyzed the data and wrote the manuscript, with contributions from B.I.H. **Competing interests:** The authors declare that they have no competing interests. **Data and materials availability:** All gathered data and code used to generate the plots within this paper are available at a repository hosted on Zenodo (*66*).

License information: Copyright © 2025 the authors, some rights reserved; exclusive licensee American Association for the Advancement of Science. No claim to original US government works. https://www.science.org/about/science-licenses-journal-article-reuse

SUPPLEMENTARY MATERIALS

science.org/doi/10.1126/science.adp5015
Materials and Methods; Supplementary Text; Figs. S1 to S9; References

Submitted 28 March 2024; resubmitted 23 September 2024; accepted 28 March 2025; published online 10 April 2025

10.1126/science.adp5015

2D MATERIALS

Imaging quantum melting in a disordered 2D Wigner solid

Ziyu Xiang[1,2,3]†, Hongyuan Li[1,2,3]†, Jianghan Xiao[1,2,3]†, Mit H. Naik[1,3], Zhehao Ge[1], Zehao He[1], Sudi Chen[1,3,4], Jiahui Nie[1], Shiyu Li[1], Yifan Jiang[1], Renee Sailus[5], Rounak Banerjee[5], Takashi Taniguchi[6], Kenji Watanabe[7], Sefaattin Tongay[5], Steven G. Louie[1,3], Michael F. Crommie[1,3,4]*, Feng Wang[1,3,4]*

Two-dimensional strongly interacting electrons crystalize into a solid phase known as the Wigner crystal at low densities and form a Fermi liquid at high densities. At intermediate densities, the two-dimensional solid evolves into a strongly correlated liquid phase around a critical density. We observed this quantum melting of a disordered Wigner solid in bilayer molybdenum diselenide ($MoSe_2$) using a noninvasive scanning tunneling microscopy imaging technique. At low densities, the Wigner solid forms nanocrystalline domains pinned by local disorder. It exhibits a quantum densification behavior with increased densities in the solid phase. Above a threshold density, the Wigner solid melts locally and enters a mixed phase in which solid and liquid regions coexist. The liquid regions expand and form a percolation network at even higher densities.

Understanding strongly correlated electron phenomena arising from the interplay between Coulomb energy and electron kinetic energy is a central topic in condensed matter physics (*1*–*9*). The two-dimensional electron gas (2DEG) at very high densities is well described by a weakly interacting Fermi liquid theory (*10*), whereas in the low-density limit, electrons solidify into a Wigner crystal in which Coulomb energy dominates over kinetic energy (*1*, *11*, *12*). At intermediate densities, however, the competition between Coulomb energy and kinetic energy is more pronounced and drives the emergence of exotic strongly correlated phases (*12*, *13*). Great experimental and theoretical effort has been made to understand the quantum melting of Wigner crystals and the resulting correlated electron phenomena at intermediate electron densities (*13*–*22*). Notable non–Fermi liquid transport behavior, including an insulator-to-metal transition and anomalous temperature-dependent and magnetic field–dependent resistivity, have been observed experimentally in various 2DEG systems (*8*, *13*, *21*–*26*). Although different theoretical pictures have been proposed to describe the experimental data (*14*–*20*, *27*), no consensus on the proper description of Wigner crystal quantum melting and resulting correlated electron states at intermediate electron densities has been reached. For substantial further understanding of the microscopic nature of Wigner solid quantum melting, experimental measurements capable of probing correlated electronic structure at both atomic and mesoscopic scales are necessary.

Here, we describe the use of a noninvasive imaging technique to visualize a Wigner solid of holes, including its densification and quantum melting, in bilayer molybdenum diselenide ($biMoSe_2$). At low hole density, we observed a disordered Wigner solid that exhibits a local triangular lattice but no long-range crystalline order owing to point defects that pin the Wigner solid and induce nanocrystalline domains. The Wigner solid exhibits an unusual densification behavior as the hole density is increased: Instead of a continuous contraction of the lattice constant as expected for a perfect Wigner crystal, the holes appear to evolve by means of a quantum superposition state. Above a critical hole density of $n_c = 5.7 \times 10^{12}$ cm^{-2}, the Wigner solid starts to melt and enters a mixed phase, with coexisting solid and liquid regions.

Noninvasive STM imaging in $biMoSe_2$

The ratio between Coulomb energy and kinetic energy in a 2DEG is characterized by a single dimensionless parameter $r_s = \frac{a_0}{a_B} = \frac{m^* e^2}{4\pi\varepsilon\hbar^2\sqrt{\pi n}}$ where a_0 is the average interparticle distance, a_B is the effective Bohr radius, n is the electron/hole density, ε is the effective dielectric constant, and m^* is the electron effective mass. Quantum Monte Carlo simulations suggest that 2D Wigner crystals melt into a liquid phase for $r_s^* \approx 38$ (*12*, *14*, *28*). Atomically thin 2D materials provide a rich platform to explore Wigner crystal physics. Previously, generalized Wigner crystals stabilized by a moiré superlattice have been imaged in tungsten diselenide (WSe_2)/tungsten disulfide (WS_2) heterostructures (*6*), and more recently, magnetic field–stabilized Wigner crystals have been imaged in graphene samples (*9*). Optical spectroscopy, on the other hand, has suggested that "bare" Wigner crystals (without assistance from a moiré superlattice or magnetic field) can exist in transition-metal dichalcogenide (TMD) layers (*29*, *30*). We chose the 2D hole gas (2DHG) in $biMoSe_2$ as a model system to image bare Wigner solid and its quantum melting behavior because of the large hole effective mass $m^* \approx 1.26 m_e$ predicted by our ab initio calculation [(*31*), section 3], which helps to increase r_s. Increased r_s facilitates the formation of Wigner solids over a large hole density range and helps them to be more robust against temperature fluctuation and weak disorder. The experimental setup used to incorporate $biMoSe_2$ into a van der Waals heterostructure device stack is illustrated in Fig. 1A. We tuned the hole density in $biMoSe_2$ by applying a bottom gate voltage (V_{BG}) between a graphite bottom gate (BG) and the $biMoSe_2$. A graphene nanoribbon (GNR) array was specially prepared as the electrical contact to $biMoSe_2$, thus reducing contact resistance and facilitating effective gating. An optical micrograph of the $biMoSe_2$ heterostructure device is shown in Fig. 1B, with $biMoSe_2$, GNR, and BG regions indicated with green, blue, and red dashed lines, respectively.

We used a noninvasive valence band edge (VBE) tunnel current measurement technique (*32*) that enables the probing of Wigner solids in hole-doped $biMoSe_2$ with minimal tip perturbation. The schematic in Fig. 1C outlines the basic principle of the measurement by showing the band alignment between the tip of scanning tunneling microscopy (STM) and hole-doped $biMoSe_2$. Because of the non-negligible work function difference between the STM tip (made of platinum/iridium) and $biMoSe_2$, the tip perturbation cannot be neglected in most cases and often has a fatal impact on fragile correlated electrons. To overcome this issue, we tuned the sample-tip bias voltage (V_{bias}) so that the vacuum energy levels of both the tip and $biMoSe_2$ were aligned, thus canceling the work function difference. This minimizes the local electric field near the tip apex and ensures that the integrity of the Wigner solid is maintained [(*31*), section 1]. The alignment of the TMD and tip vacuum levels can be achieved by moving the tip chemical potential within the $biMoSe_2$ bandgap. In this case, the tunnel current arises exclusively from doped holes at the $biMoSe_2$ VBE without impact from higher-energy states. The VBE tunnel current directly reflects the spatial distribution of doped holes similar to previous demonstrations of VBE current mapping of Wigner molecules (*32*).

The tunnel current (*I*-*V*) characteristic on a log scale is shown in Fig. 1D as a function of V_{BG} for hole-doped $biMoSe_2$, with a relatively large tip-sample separation [determined by the setpoint condition $V_{bias} = -3$ V, setpoint currrent (I_{sp}) = 20 pA, tip lift height (h_{tip}) = –30 pm,

[1]Department of Physics, University of California at Berkeley, Berkeley, CA, USA. [2]Graduate Group in Applied Science and Technology, University of California at Berkeley, Berkeley, CA, USA. [3]Materials Sciences Division, Lawrence Berkeley National Laboratory, Berkeley, CA, USA. [4]Kavli Energy Nano Sciences Institute, University of California Berkeley and the Lawrence Berkeley National Laboratory, Berkeley, CA, USA. [5]School for Engineering of Matter, Transport and Energy, Arizona State University, Tempe, AZ, USA. [6]International Center for Materials Nanoarchitectonics, National Institute for Materials Science, Tsukuba, Japan. [7]Research Center for Functional Materials, National Institute for Materials Science, Tsukuba, Japan. ***Corresponding author. Email: crommie@berkeley.edu (M.F.C.); fengwang76@berkeley.edu (F.W.)** †These authors contributed equally to this work.

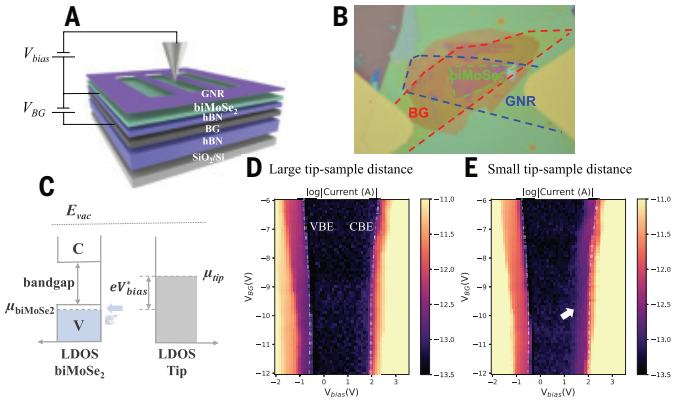

Fig. 1. Noninvasive VBE tunnel current measurement of biMoSe$_2$. (**A**) A schematic of the STM measurement setup for gate-tunable biMoSe$_2$. The biMoSe$_2$ is placed on top of a 50-nm-thick hexagonal boron nitride (hBN) layer and a graphite substrate that defines the back gate (BG). A back gate voltage V_{BG} is applied to control the charge carrier density in the biMoSe$_2$. A bias voltage V_{bias} is applied to the biMoSe$_2$ relative to the STM tip to induce tunnel current. A graphene nanoribbon (GNR) array is placed on top of the biMoSe$_2$ as a contact electrode. (**B**) Optical microscope image of the device heterostructure. The biMoSe$_2$, GNR, and BG are outlined in green, blue, and red, respectively. (**C**) Schematic energy diagram for the valence band edge (VBE) tunnel current measurement of hole-doped biMoSe$_2$. The biMoSe$_2$ chemical potential, μ_{biMoSe_2}, is near the valence band edge. When μ_{tip} is aligned within the bandgap of biMoSe$_2$, the tunnel current arises from doped holes at the VBE. V_{bias} is tuned to roughly align the vacuum energy levels of the tip and biMoSe$_2$ so that the electric field near the tip apex is minimized. The gap between μ_{tip} and μ_{biMoSe_2} is denoted V^*_{bias} instead of V_{bias} because the real bias on the tunneling junction V^*_{bias} is reduced by the large contact resistance (the Schottky barrier). (**D**) The tunnel current *I*-*V* characteristics as a function of V_{BG} for hole-doped biMoSe$_2$ with a large tip-sample distance. The current is plotted on an absolute log scale. The VBE and CBE are indicated with white dashed curves. (**E**) The tunnel current *I*-*V* characteristics as a function of V_{BG} for hole-doped biMoSe$_2$ with a small tip-sample distance, similar to that in (D). The white arrow indicates the VBE tunnel current. $T = 5.4$ K for all the above measurements.

and temperature (T) = 5.4 K] (*31*). Negligible tunnel current occurs for $-0.5\text{V} < V_{bias} < 2$ V, which corresponds to the biMoSe$_2$ semiconducting band gap [the VBE and conduction band edge (CBE) are indicated in Fig. 1D with dot-dashed lines]. The bandgap shows an apparent increase as V_{BG} is increased. This is likely because the contact resistance between the biMoSe$_2$ and GNR contacts increases at lower hole doping, causing part of the bias voltage to drop at the contact rather than at the tip-sample gap. At large tip-sample separation, the VBE tunnel current is lower than the measurement noise floor in the bandgap region and is not observable. When the tip-sample distance is reduced (setpoint condition: $V_{bias} = -3$ V, $I_{sp} = 20$ pA, $h_{tip} = -90$ pm), however, VBE tunnel current starts to appear in the band gap (Fig. 1E, white arrow).

Visualizing the hole Wigner solid

Spatially mapping the VBE tunnel current allows us to visualize the Wigner solid within biMoSe$_2$. The VBE tunnel current map obtained at a hole density of $n = 5.3 \times 10^{12}$ cm^{-2} is shown in Fig. 2A [with $V_{BG} = -8$V, $V_{bias} = 1.9$V to minimize tip perturbation; details on determining V_{bias} with minimized tip perturbation are available in (*31*), section 1]. Each bright dot in Fig. 2A indicates a localized hole in biMoSe$_2$. The corresponding STM topographic image by using conventional constant current mode is shown in Fig. 2B ($V_{bias} = -3$V, $I_{sp} = 20$ pA). The bright defects in Fig. 2B correspond to charged defects, which act as local pinning centers in the Wigner solid of Fig. 2A (Fig. 2B also contains weaker features arising from isovalent defects) [(*31*), section 11] (*33*–*35*). The Wigner solid exhibits a nanocrystalline phase with different nanocrystalline domains but no long-range crystalline order owing to defect-induced disorder. The fast Fourier transform (FFT) patterns in Fig. 2, D to F, correspond to regions (i), (ii), and (iii), respectively, in Fig. 2A. Each shows a local hexagonal lattice with six distinct diffraction spots (Fig. 2, D to F, solid red dots), but the lattice orientation is random in different regions. The orientational coherence of the Wigner solid is disrupted by disorder in the biMoSe$_2$ semiconductor.

We used the Delaunay triangulation and Voronoi cell partition method to systematically analyze the disordered Wigner solid. This methodology is useful for quantitatively analyzing the lattice structure of disordered crystals [it has been used, for example, to analyze vortex lattice in layered superconductors (*36*, *37*)]. We show in Fig. 2C the Voronoi cell diagram for the disordered Wigner solid shown in Fig. 2A [(*31*), section 2]. Each vertex corresponds to a single hole, and each edge connects nearest-neighbor holes. In an ideal Wigner crystal, each hole would have six nearest neighbors, whereas in our disordered Wigner solid, a substantial number of dislocations can be seen (a dislocation is a five-membered ring of nearest neighbors adjacent to a seven-membered ring). We counted 43 dislocations out of the 237 holes shown in Fig. 2C. We have color-coded in Fig. 2C the Voronoi cell: Blue dashed lines connect the vertices of dislocations, and solid lines connect to holes without dislocations. The three different colors of the solid lines in Fig. 2C (light blue, light orange, and dark red) trace the lattice orientation of the crystalline domains. Dislocations frequently appear in pairs or defect lines that separate regions without dislocations into randomly oriented nanocrystalline domains.

We studied the evolution of the disordered Wigner solid as a function of hole density by varying the gate voltage V_{BG}. In Fig. 2, A and G to I, we show the VBE tunnel current maps for biMoSe$_2$ as the hole density is increased from 4.2×10^{12} to 7.0×10^{12} cm^{-2} [discussion of choosing a noninvasive V_{bias} is available in (*31*), section 1]. For low charge density ($V_{BG} \geq -8$V), the holes remain well separated and form a solid phase. As V_{BG} is reduced, however, the Wigner solid becomes denser, and the spatial extent (full width at half maximum) of each hole wave function shrinks. As V_{BG} is reduced beyond the threshold of $V_{BG} = -8$V, regions of the Wigner solid become "blurred" and no longer exhibit well-separated holes. This behavior indicates the onset of local melting of the Wigner solid. Further reduction of V_{BG} causes the melted regions to expand and eventually form a percolation network at very high hole density ($n \approx 7.0 \times 10^{12}$ cm^{-2}).

Quantum densification

The mechanism by which the density of holes increases with decreased V_{BG} for our disordered Wigner solid is different from the smooth lattice constant variation expected for an ideal Wigner crystal. We observed instead a highly local process that we call "quantum densification." In this process, individual holes are added quantum mechanically into local regions constrained by disorders, and partially delocalized hole wave functions are observed during the transition between two well-defined solid lattice configurations.

The quantum densification process can be seen in Fig. 3, which shows a small region of the Wigner solid imaged under conditions in which the hole density is gradually increased through a combination of increased V_{bias} and decreased V_{BG} as shown in Fig. 3, A to F (increasing V_{bias} has the same effect locally as decreasing V_{BG}). In these conditions, the vacuum levels near the tip and sample surface are nearly in alignment to perform a noninvasive measurement. The dashed white circle in Fig. 3A outlines the region where the most dramatic changes occur during the quantum densification process when the local hole number increases from four to five as V_{bias} is increased as shown in Fig. 3, A to C. The red dots throughout Fig. 3 indicate the same locations of the holes in Fig. 3A so that changes in hole positions can be easily seen. The white arrow in Fig. 3B indicates the region where a new charge carrier arises as V_{bias} is raised from 1.9 to 2.0 V. A new

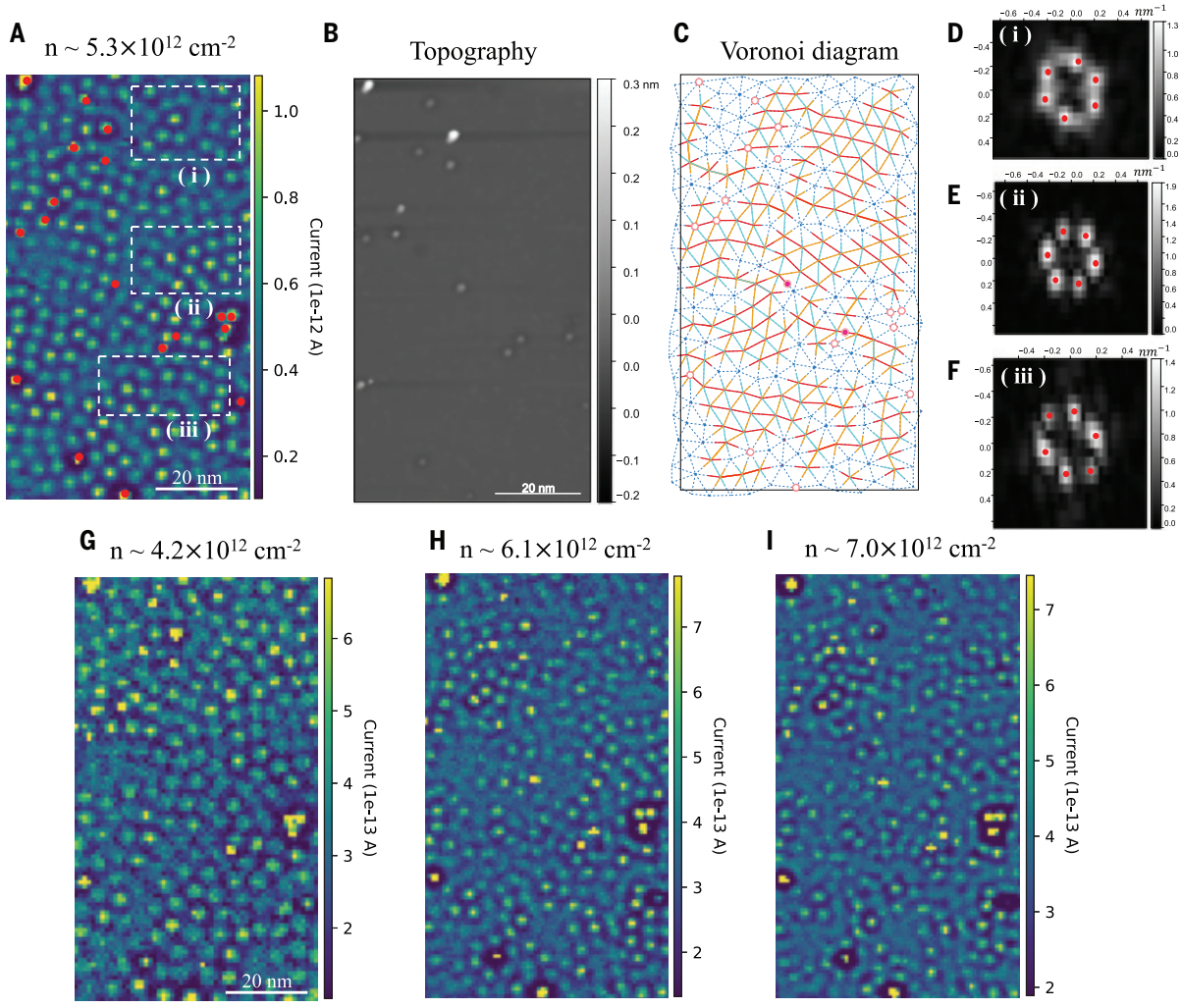

Fig. 2. Hole density dependence of a Wigner solid. (**A**) VBE tunnel current map of a Wigner solid in a 60- by 100-nm region of biMoSe$_2$ (V_{BG} = −8 V, V_{bias} = 1.9 V). The bright dots in the VBE tunnel current maps correspond to individual holes in the Wigner solid. Charged defects are indicated with red solid dots. (**B**) STM topographic image of the biMoSe$_2$ surface taken in the same region as (A) and (G) to (I). Most charged defects in the VBE maps correspond to defects in the topography image. (**D** to **F**) FFT images for regions (i), (ii), and (iii) showed in (A). A Nuttall window was used. The solid red dots indicate the peaks in the FFT images. (**C**) Crystal structure analysis of (A). Each intersection indicates a hole position calculated by applying a Voronoi cell partition method [(*31*), section 2]. Points connected with blue dashed lines indicate holes that have five or seven nearest neighbors, whereas points connected with colored solid lines indicate holes that have six nearest neighbors. The open red circles indicate charged defect positions as shown in (A). Solid red points indicate defects without a trapped hole. (**G** to **I**) VBE tunnel current maps of the same region shown in (A) for different hole densities controlled by using the bottom gate voltage V_{BG}. (G) V_{BG} = −6 V, V_{bias} = 2.2 V. (H) V_{BG} = −10 V, V_{bias} = 1.8 V. (I) V_{BG} = −12 V, V_{bias} = 1.5 V. T = 5.4 K for all the above measurements.

coalescence of charge is seen to gather at the location inidcated in Fig. 3B with the white arrow, whereas the charge that was previously at the location of the red dot just above and to the right of the arrow is seen to slightly rise. All other holes remain close to the locations of the red dots. The process continued when the sample bias was raised to V_{bias} = 2.1 V (Fig. 3C). The new charge carrier was at that point fully incorporated in the Wigner solid. This process continued as shown in Fig. 3, C and D (V_{BG} decreasing to −8V), in which the hole density further increased, causing a new coalescence of hole gathering around the location indicated in Fig. 3C with the white arrow. When V_{bias} = 1.9 V, six holes exist in the center region (Fig. 3E) where previously (Fig. 3A) only four holes resided. The process continued as shown in Fig. 3, E and F, where an increase in V_{bias} caused a new coalescence of charge to appear at the region indicated with the arrow in Fig. 3F.

During the transition between integer-hole-number states under quantum densification, there is notable elongation or delocalization of the hole wave functions. We observed similar behavior in other local regions during hole densification of the Wigner solid [additional data are provided in (*31*), section 7]. This behavior is a manifestation of the quantum mechanical nature of the hole lattice, in which quantum tunneling and delocalization of isolated holes can be substantial under suitable conditions even in the solid phase. By contrast, atom positions are almost always localized in disordered natural solids because of the much heavier mass of atoms.

Quantum melting

We next focused more strongly on the quantum melting behavior of the Wigner solid. This melting process is shown in Fig. 4 as the hole density ranges from $n = 5.3 \times 10^{12}$to 7.0×10^{12} cm^{-2}. At the highest hole density, we observed a mixed phase composed of solid regions with nanocrystalline domains and liquid regions with a smoother hole density distribution. We define liquid and solid regions as areas where

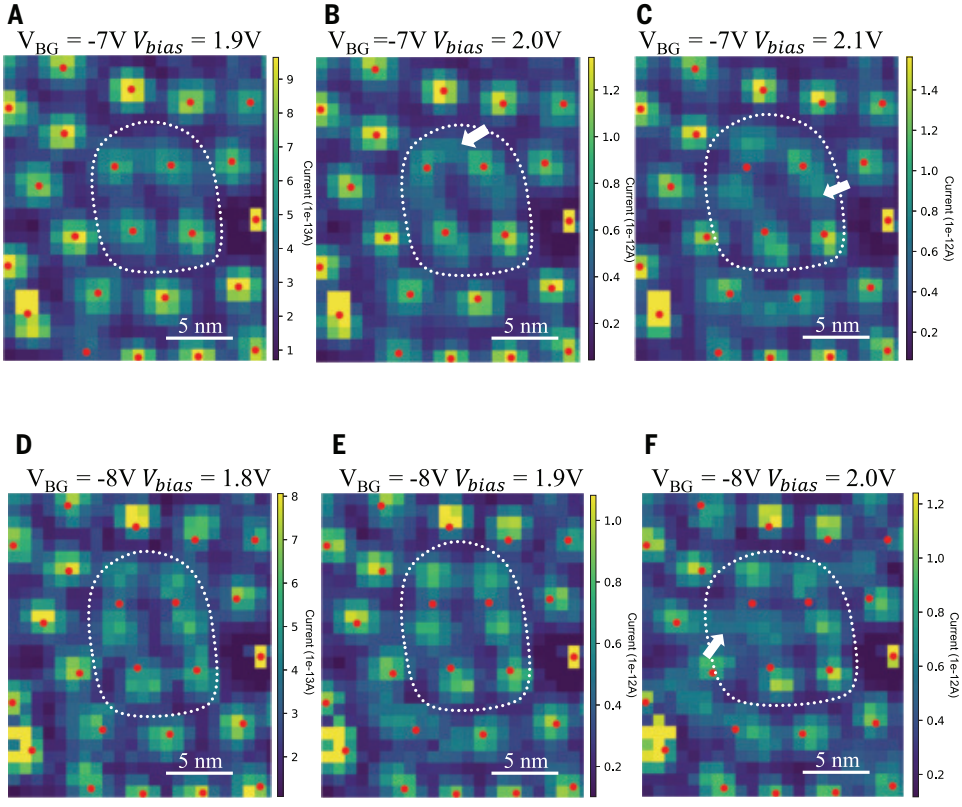

Fig. 3. Quantum densification of holes in a Wigner solid. VBE tunnel current maps show a Wigner solid with hole density increasing in fine steps by using both V_{BG} and V_{bias} (with negligible tip perturbation) [(*31*), section 1]. (**A**) $V_{BG} = -7$ V, $V_{bias} = 1.9$ V. (**B**) $V_{BG} = -7$ V, $V_{bias} = 2.0$ V. (**C**) $V_{BG} = -7$ V, $V_{bias} = 2.1$ V. (**D**) $V_{BG} = -8$ V, $V_{bias} = 1.8$ V. (**E**) $V_{BG} = -8$V, $V_{bias} = 1.9$ V. (**F**) $V_{BG} = -8$V, $V_{bias} = 2.0$ V. Solid red dots throughout indicate the initial location of holes shown in (A). The region indicated with a white dashed line in (A) to (F) shows (A) a local four-hole configuration, which evolves into (C) a well-resolved five-hole configuration and (E) six-hole configuration at higher densities. At the intermediate densities in (B) and (D), the wave function of local holes becomes partially delocalized (white arrows), a manifestation of the quantum nature of the Wigner hole solid. $T = 5.4$ K for all the above measurements.

the local tunnel current variation is lower and higher, respectively, than 28% over one Voronoi-cell size [(*31*) section 8]. The resulting boundaries between solid and liquid regions are indicated with two-toned solid lines in Fig. 4. The low-contrast liquid regions where holes are delocalized and have more widespread wave functions (close to the white boundary lines) can be clearly distinguished from the high-contrast solid regions where holes are more highly localized (close to the red boundary lines). The liquid-solid mixed phase extends over a rather broad hole density range of $5.7 \times 10^{12} < n < 7.0 \times 10^{12}$ cm^{-2}, which corresponds to the range of $19.7 < r_s < 21.8$ if we use a hole effective mass of $1.26m_e$ in $biMoSe_2$, based on the ab inito calculation [(*31*), section 3]. The value of r_s in this range is smaller than the theoretically predicted melting density of $r_s^* \approx 38$ for an ideal Wigner crystal (*12*, *14*, *28*). However, there is currently no experimentally measured hole effective mass for $biMoSe_2$. Previous studies have shown that measured effective masses for 2D TMDs can be much larger than theoretical predictions, creating a large uncertainty in our estimated r_s values (*38*).

Our melting data are qualitatively consistent with a percolation picture. For $n = 5.7 \times 10^{12}$ cm^{-2}, only small bubbles of the liquid phase are present (Fig. 4B), whereas at increased hole density, the liquid bubbles gradually expand (Fig. 4C). The bubbles are seen to eventually coalesce into an interconnected percolation network (Fig. 4D). Such percolation

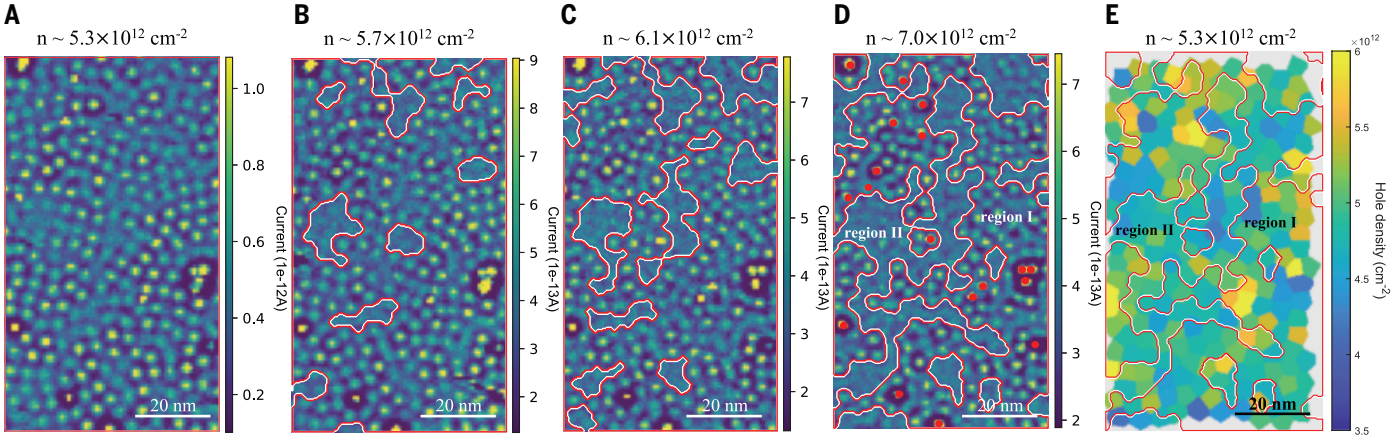

Fig. 4. Quantum melting of a Wigner solid. VBE tunnel current maps of a Wigner solid in $biMoSe_2$ show a gradual melting at high charge densities. (**A**) $V_{BG} = -8$ V, $V_{bias} = 1.9$ V. (**B**) $V_{BG} = -9$ V, $V_{bias} = 1.8$ V. (**C**) $V_{BG} = -10$ V, $V_{bias} = 1.8$ V. (**D**) $V_{BG} = -12$V, $V_{bias} = 1.5$ V. The boundary between solid and liquid phase is distinguished by its local contrast difference and is outlined by two-colored solid lines. The red side indicates solid phase, whereas the white side indicates liquid phase. Wigner solid domains pinned by defects shrink with increasing charge density, whereas liquid regions expand and eventually induce percolative connectivity. We labeled the liquid phase and solid phase regions in (D) as region I and region II, respectively. The charged defects are indicated in (D) with solid red dots and are all localized in region I, suggesting that defect sites perform as pinning points. (**E**) The hole density distribution at $V_{BG} = -8$ V, $V_{bias} = 1.9$ V (yellow is high, blue is low). The overlaid solid lines indicate region I and region II as defined in (D). The measured average charge densities in the two regions are identical within an experimental uncertainty of 2%. $T = 5.4$ K for all the above measurements.

behavior could potentially explain insulator-to-metal transitions seen for Wigner solids in previous transport studies (*19*, *20*).

Discussion and outlook

Two very different theoretical mechanisms in the literature can potentially give rise to a solid-liquid mixture phase during the quantum melting of a 2D Wigner solid. In one mechanism, the disordered 2D material has long-range potential fluctuations that lead to spatially varying hole density regions within the sample. When the average hole concentration is close to the critical density of the Wigner solid, low-density regions will be in the solid phase ($r_s > r_s^*$), whereas the high-density regions will be in the liquid phase ($r_s < r_s^*$);solid and liquid regions are directly correlated with the long-range potential disorder. In the second mechanism, a solid and a liquid phase may coexist in an ideal 2DEG without defects. This spontaneous coexistence of solid and liquid phases during the quantum melting of a Wigner solid is called the "microemulsion" phase (*39*, *40*). It is caused by a negative surface energy between the two different phases.

We can test the first mechanism by characterizing the long-range potential fluctuations in our system. If long-range potential fluctuations are the dominant effect, they should lead to persistent hole density fluctuation patterns at all gate voltages. To test this idea, we defined the liquid and solid regions in the mixed phase at $n = 7 \times 10^{12}$ cm^{-2} ($V_{BG} = -12$ V, $V_{bias} = 1.5$ V) as regions I and II, respectively, and compared the average hole density in these two regions at lower gate voltages where the holes are in a solid phase everywhere. We used the inverse of the Voronoi cell area ($1/A_{Voronoi}$) to define the local hole density for low-density Wigner solid states at $n < 5.5 \times 10^{12}$ cm^{-2} [details to determine solid and liquid boundaries are provided in (*31*), section 8]. In Fig. 4E, we show the hole density distribution based on the Voronoi cell analysis at $V_{BG} = -8$V, $V_{bias} = 1.9$V, which is overlayed with the boundaries of region I and region II. Substantial spatial variations are seen in the hole density at the unit cell level, but there are no pronounced long-range variations. The calculated average hole densities in region I and region II are identical within an experimental uncertainty of 2% [(*31*), section 10], and so no correlation exists between solid regions in the mixed phase and decreased local hole density, or between liquid regions in the mixed phase and increased local hole density. Therefore, the liquid-solid mixture phase in our system is not induced by a long-range potential fluctuation.

The second mechanism based on the microemulsion picture can generate a solid-liquid mixture phase in the absence of a long-range potential fluctuation. However, the microemulsion phase in an ideal 2DEG is expected to exist only in a very narrow phase region (*41*). This is in contradiction to the relatively wide phase coexistence density range ($\Delta n/n_c \geq 0.3$) observed in our experiment. Our data suggest that short-range disorders play a critical role in the Wigner crystal melting behavior, which is not included in the existing microemulsion theory.

We have visualized the quantum melting of a disordered Wigner solid, revealing the coexistence of solid and liquid phases during the melting process. The solid-liquid phase mixture observed in the presence of disorder cannot be fully captured by existing theories. Our observations provide insight into quantum melting behavior for Wigner crystals in 2D materials that exhibit defects.

REFERENCES AND NOTES

1. E. Wigner, *Phys. Rev.* **46**, 1002–1011 (1934).
2. R. S. Crandall, R. Williams, *Phys. Lett. A* **34**, 404–405 (1971).
3. Y. Cao *et al.*, *Nature* **556**, 80–84 (2018).
4. E. C. Regan *et al.*, *Nature* **579**, 359–363 (2020).
5. G. Chen *et al.*, *Nature* **579**, 56–61 (2020).
6. H. Li *et al.*, *Nature* **597**, 650–654 (2021).
7. J. Cai *et al.*, *Nature* **622**, 63–68 (2023).
8. J. Sung *et al.*, Observation of an electronic microemulsion phase emerging from a quantum crystal-to-liquid transition. arXiv:2311.18069 [cond-mat.str-el] (2023).
9. Y.-C. Tsui *et al.*, *Nature* **628**, 287–292 (2024).
10. A. A. Abrikosov, I. M. Khalatnikov, *Rep. Prog. Phys.* **22**, 329–367 (1959).
11. Yu. P. Monarkha, V. E. Syvokon, *Low Temp. Phys.* **38**, 1067–1095 (2012).
12. N. D. Drummond, R. J. Needs, *Phys. Rev. Lett.* **102**, 126402 (2009).
13. B. Spivak, S. V. Kravchenko, S. A. Kivelson, X. P. A. Gao, *Rev. Mod. Phys.* **82**, 1743–1766 (2010).
14. B. Tanatar, D. M. Ceperley, *Phys. Rev. B Condens. Matter* **39**, 5005–5016 (1989).
15. B. Spivak, S. A. Kivelson, *Ann. Phys.* **321**, 2071–2115 (2006).
16. C. Attaccalite, S. Moroni, P. Gori-Giorgi, G. B. Bachelet, *Phys. Rev. Lett.* **88**, 256601 (2002).
17. V. T. Dolgopolov, A. Gold, *JETP Lett.* **71**, 27–30 (2000).
18. G. Zala, B. N. Narozhny, I. L. Aleiner, *Phys. Rev. B Condens. Matter* **64**, 214204 (2001).
19. M. J. Manfra *et al.*, *Phys. Rev. Lett.* **99**, 236402 (2007).
20. S. Das Sarma *et al.*, *Phys. Rev. Lett.* **94**, 136401 (2005).
21. X. P. A. Gao *et al.*, *Phys. Rev. B Condens. Matter Mater. Phys.* **73**, 241315 (2006).
22. E. P. De Poortere, E. Tutuc, Y. P. Shkolnikov, K. Vakili, M. Shayegan, *Phys. Rev. B Condens. Matter* **66**, 161308 (2002).
23. M. S. Hossain *et al.*, *Phys. Rev. Lett.* **129**, 036601 (2022).
24. J. Falson *et al.*, *Nat. Mater.* **21**, 311–316 (2022).
25. V. J. Goldman, M. Santos, M. Shayegan, J. E. Cunningham, *Phys. Rev. Lett.* **65**, 2189–2192 (1990).
26. J. Yoon, C. C. Li, D. Shahar, D. C. Tsui, M. Shayegan, *Phys. Rev. Lett.* **82**, 1744–1747 (1999).
27. S. T. Chui, B. Tanatar, *Phys. Rev. Lett.* **74**, 458–461 (1995).
28. K.-S. Kim, C. Murthy, A. Pandey, S. A. Kivelson, *Phys. Rev. Lett.* **129**, *227202* (2022).
29. Y. Zhou *et al.*, *Nature* **595**, 48–52 (2021).
30. T. Smoleński *et al.*, *Nature* **595**, 53–57 (2021).
31. Supplementary text and data are available as supplementary materials.
32. H. Li *et al.*, *Science* **385**, 86–91 (2024).
33. S. Liu *et al.*, *ACS Nano* **17**, 16587–16596 (2023).
34. S. Barja *et al.*, *Nat. Commun.* **10**, 3382 (2019).
35. B. Schuler *et al.*, *Sci. Adv.* **6**, eabb5988 (2020).
36. C. A. Murray, P. L. Gammel, D. J. Bishop, D. B. Mitzi, A. Kapitulnik, *Phys. Rev. Lett.* **64**, 2312–2315 (1990).
37. P. Kim, Z. Yao, C. M. Lieber, *Phys. Rev. Lett.* **77**, 5118–5121 (1996).
38. Y. Zhang *et al.*, *Nat. Nanotechnol.* **9**, 111–115 (2014).
39. B. Spivak, *Phys. Rev. B Condens. Matter* **67**, 125205 (2003).
40. B. Spivak, S. A. Kivelson, *Phys. Rev. B Condens. Matter Mater. Phys.* **70**, 155114 (2004).
41. S. Joy, B. Skinner, *Phys. Rev. B* **108**, L241110 (2023).
42. Z. Xiang, Replication data for: Imaging quantum melting in a disordered 2D Wigner solid. *Harvard Dataverse*, V1 (2025); https://doi.org/10.7910/DVN/CDWJEH

ACKNOWLEDGMENTS

The authors acknowledge helpful discussion with S. Kivelson and P. Kim. **Funding:** This work was primarily funded by the US Department of Energy, Office of Science, Basic Energy Sciences, Materials Sciences and Engineering Division under contract DE-AC02-05-CH11231 within the van der Waals heterostructure program KCWF16 (device fabrication, STM spectroscopy, theoretical analysis, and computations). Support was also provided by the National Science Foundation award DMR-2221750 (surface preparation). This research used the Lawrencium computational cluster provided by the Lawrence Berkeley National Laboratory (supported by the US Department of Energy, Office of Basic Energy Sciences under contract DE-AC02-05-CH11231). This research also used resources of National Energy Research Scientific Computing Center (NERSC), a US Department of Energy Office of Science User Facility located at Lawrence Berkeley National Laboratory, operated under contract DE-AC02-05CH11231. S.T. acknowledges primary support from US Department of Energy SC0020653 (materials synthesis), NSF CMMI1825594 (nuclear magnetic resonance and transmission electron microscopy studies on crystals), NSF DMR-1955889 (magnetic measurements on crystals), NSF ECCS2052527 (for bulk electrical tests), DMR 2111812, and CMMI 2129412 (for optical tests on bulk crystals). K.W. and T.T. acknowledge support from the JSPS KAKENHI (grants 21H05233 and 23H02052) and World Premier International Research Center Initiative (WPI), MEXT, Japan. **Author contributions:** M.F.C. and F.W. conceived the project. Z.X., J.X., H.L., J.N., S.L., and Y.J. fabricated the heterostructure device. Z.X. and S.C. fabricated the shadow mask. Z.X., H.L., and J.X. performed the STM/scanning tunneling spectroscopy measurement. M.H.N. and S.G.L. performed the DFT calculations of the biMoSe$_2$ effective mass. Z.X., H.L., J.X., Z.G., Z.H., M.F.C., and F.W. discussed the experimental design and analyzed the experimental data. R.S., R.B., and S.T. grew the MoSe$_2$ crystals. K.W. and T.T. grew the hBN single crystal. All authors discussed the results and wrote the manuscript. **Competing interests:** The authors declare that they have no competing interests. **Data and materials availability:** All data shown in the main text and supplementary materials are available in the Havard Dataverse (*42*).

License information: Copyright © 2025 the authors, some rights reserved; exclusive licensee American Association for the Advancement of Science. No claim to original US government works. https://www.science.org/about/science-licenses-journal-article-reuse

SUPPLEMENTARY MATERIALS

science.org/doi/10.1126/science.ado7136
Materials and Methods; Supplementary Text; Figs. S1 to S9; Table S1; References (*43*–*49*)

Submitted 17 February 2024; accepted 14 March 2025

10.1126/science.ado7136

RANGE SHIFTS

Limited evidence for range shift–driven extinction in mountain biota

Yi-Hsiu Chen[1], Jonathan Lenoir[2], I-Ching Chen[1]*

Mountain biodiversity reorganizes rapidly as species shift upslope to track temperatures. Pervasive species redistribution poses substantial threats to mountain ecosystems, a phenomenon sometimes described as an "escalator to extinction," primarily through mountaintop extinctions, range shift gaps (i.e., rapid shifts of suitable temperatures getting ahead of narrow-range species' upper limits), and lowland biodiversity attrition, yet empirical evidence remains scarce. In this study, our analysis of 8800 records of historical and modern elevational range limits for 440 animal and 1629 plant species revealed little evidence supporting the proposed threats. Observed changes largely fell within random expectations, accounting for geometric constraints. Although delayed mountaintop extinctions point to accumulating extinction debt, concurrent range expansions of both narrow-range and lowland species suggest thermal niche underfilling, processes that collectively drive biotic homogenization across biologically complex mountain ecosystems.

Mountain ecosystems face rapid changes in response to increasing temperatures, including glacier retreat and disappearance (*1*) as the freezing level, i.e., the zero-degree isotherm, shifts upslope and vanishes beyond the summits. Although mountains can be efficient refugia for species to track temperature along the elevation gradient (*2*), biodiversity changes are highly susceptible to the constraints of mountain topography (*3*–*5*). Nearly two decades ago, Colwell *et al.* (*6*) perceptively proposed that the vulnerability of mountain biota to climate warming is intrinsically linked to their elevational positions and range extents within a finite and geometrically delimited elevational gradient (*6*) (Fig. 1), leading to specific phenomena: mountaintop extinctions, range shift gaps, and lowland biotic attrition. Mountaintop extinctions threaten high-elevation species through extirpation of local populations and range reductions, given the limited space to move upslope. Range shift gaps pose challenges for narrow-ranged species, which are more likely to face nonoverlap between their current and future elevational distributions, impeding their ability to stay within suitable climate niches. Biotic attrition may occur in tropical lowlands, where biodiversity loss is anticipated, as no other species adapted to warmer climates are available to replace those shifting upslope.

To date, there are varying degrees of support for these predictions of temperature-driven risks on mountain biodiversity. For example, climate change has already caused upslope shifts and mountaintop extirpations in a tropical bird community in the Peruvian Andes (*7*). However, vascular plant species richness has increased on more than 300 mountain summits in Europe without any clear signs, so far, of mountaintop extirpations (*8*). Empirical evidence for range shift gaps remains scarce. A recent report concluded that International Union for Conservation of Nature red-listed plant species in the European Alps were not able to track climate warming at the leading edge of their distribution and further experienced a substantial erosion of their rear margins, resulting in an overall rapid range contraction, which increases the risk for range shift gaps (*9*). Apart from that one example, most studies examining range shift gaps rely on model predictions rather than empirical evidence (*10*–*12*). Lowland biotic attrition in the wet tropics (*5*) has mixed support from predictions, depending on the level of niche filling or underfilling between the realized and fundamental thermal niche of a given species (*13*, *14*). Colwell and Feeley's (*15*) comprehensive review notes that only elevational, not latitudinal, range shifts were reported for tropical species so far, indirectly supporting a potential risk for lowland biotic attrition (*13*). In fact, a recent report has shown sharp declines in observation and capture rates of Amazon birds based on 22 years of empirical data from the Tiputini Biodiversity Station in Ecuador, a lowland rain forest within the Yasuní Biosphere Reserve, one of the world's most biodiverse regions (*16*). Therefore, the potential consequences of species redistribution in mountain systems and their associated risks are far more complex than just a simple lift of entire biodiversity assemblages marching upslope on the escalator to extinction (*17*, *18*), in lockstep with the shifting temperature isotherms (*19*). Given the abundant literature on elevational range shifts published during recent decades (*20*), the time is ripe for investigating these three predictions of temperature-induced changes on mountain biodiversity worldwide.

To analyze species range-shift data, recent syntheses and meta-analyses of biodiversity redistribution have recommended several best-practice standards, including the use of appropriate null models as well as models that account for differences in methodological attributes among the studies from which the raw range shift data originate (*20*–*23*). Notably, geometric constraints in bounded domains, such as mountain ranges, inherently shape biodiversity patterns (*4*, *24*) and their redistribution, a challenge seldom tackled comprehensively in empirical studies. Even under stable climatic conditions, comparing elevational limits of mountain species distributions between two time periods can yield apparent range shifts due to chance alone (*23*). Mountaintop species' upper limits tend to shift downslope, whereas lowland species' lower limits tend to shift upslope, a statistical phenomenon known as regression toward the mean (*25*). Thus, geometric constraints alone can generate a negative correlation between species range shifts and elevation (fig. S1 illustrates a hypothetical example of random species movement).

Under warming scenarios, however, geometric constraints further interact with species' upslope movements, producing distinct patterns of shifts in distribution limits and range midpoints (*26*) [Fig. 2, red lines depict a simulated warming case following Colwell *et al.*'s (*6*) assumption of 600-m shifts upslope in response to a +3.12°C temperature increase over a century]. Species living near the summits face restricted expansions at their upper elevational limits (Fig. 2A, red line). By contrast, the degree of freedom for upslope shifts is greater at the lower elevational limit, especially for lowland species (Fig. 2B, red line). When combined, these expectations should significantly reduce the range extent of mountaintop species (Fig. 2C, red line) and render a more pronounced midpoint shift for lowland species (Fig. 2D, red line). Geometric constraints imposed by the elevational gradient of the focal mountain also interact with the historical range extent of the focal species such that species with a historically large elevational range are more likely to hit the upper or lower limit of the available gradient than narrow-range species. Thus, the magnitude of upslope shifts at the upper limit of wide-range species is more limited than for narrow-range species sharing the same midpoint position (Fig. 2E, red line). On the contrary, at the lower limit, wide-range species are intrinsically less constrained to shift upslope than narrow-range species sharing the same midpoint position (Fig. 2F, red line). Combining both constraints, we expect greater range contractions for widespread than narrow-range species (Fig. 2G, red line) and greater upslope shifts for narrow-range species (Fig. 2H, red line).

[1]Department of Life Sciences, National Cheng Kung University, Tainan City, Taiwan. [2]UMR CNRS 7058, Ecologie et Dynamique des Systèmes Anthropisés (EDYSAN), Université de Picardie Jules Verne, Amiens, France. *Corresponding author. Email: chenic@ncku.edu.tw

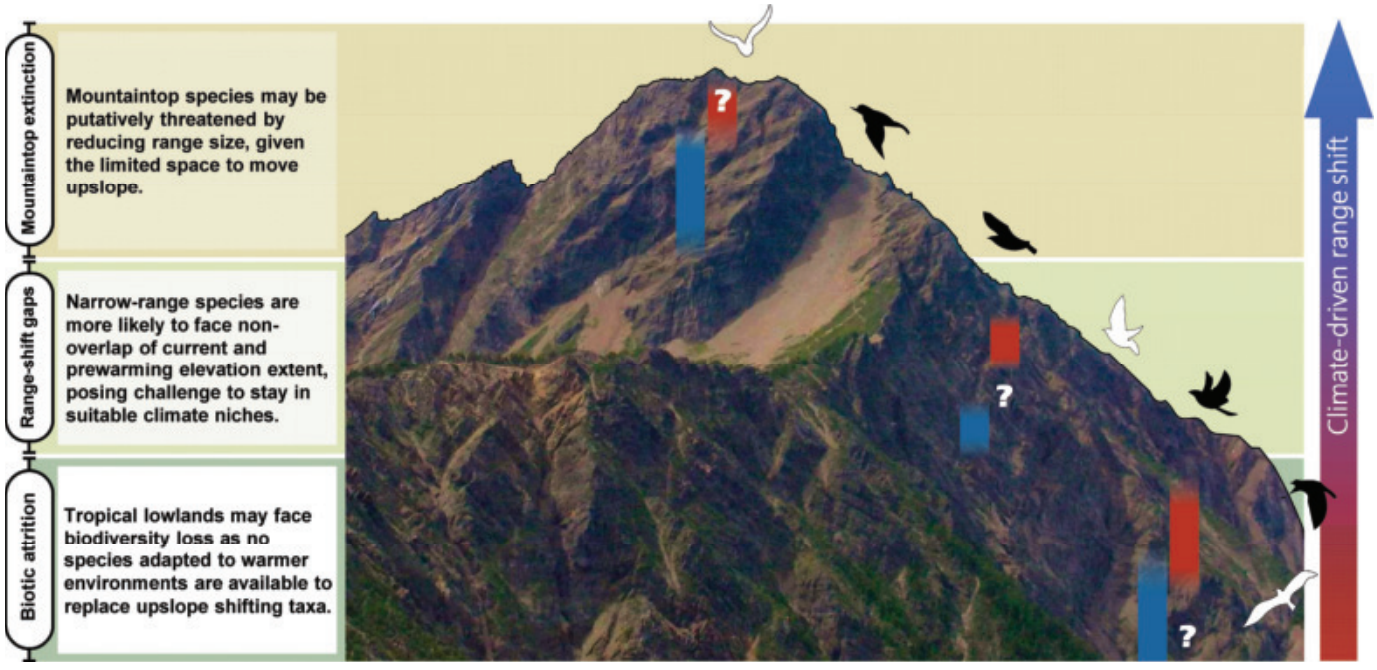

Fig. 1. Schematic of hypothesized impacts on mountain biodiversity under climate warming. Owing to climate warming, mountain species continue to shift uphill from prewarming (blue bars) to postwarming elevational extents (red bars). In that case, three consequences (*6*)—mountaintop extinctions, range shift gaps, and biotic attrition—are predicted to result in greater species extirpation risk and biodiversity loss (white icons and question marks, respectively) along elevational gradients.

As described above, observed range shift responses to temperature forcing inevitably include the confounding effects of geometric constraints. Deriving meaningful biological interpretations of temperature warming requires disentangling these responses from spatial limitations. We modeled null expectations of shifts for range limits, extents, and midpoints using a randomization approach [Fig. 2, A to D (purple shading) and E to H (orange shading)]. The null models we developed randomly assign observed shifts to species along elevational gradients while accounting for the geometric constraints of elevational gradients on the magnitude and direction of range shifts (*26*). Significant deviations of empirical observations from null expectations would indicate substantial effects despite the geographically bounded nature of elevational gradients in the mountains. To assess the three warming-driven consequences to mountain biodiversity, we tested whether (i) range contractions near mountaintops exceed null expectations (mountaintop extinction: Fig. 2C, gray arrow), (ii) narrow-range species maintain stable range extents while shifting midpoints further upslope than expected (range shift gap: Fig. 2, G and H, gray dot and arrow), and (iii) upslope shifts at lowland species' lower range limits surpass null expectations (lowland biotic attrition: Fig. 2B, gray arrow).

We compiled 2200 quadruplets of historic (1849 to 1998) and modern (2003 to 2017) elevational range limits (both upper and lower) for a total of 2069 terrestrial plant and animal species, extracted from 21 peer-reviewed studies conducted across 23 montane regions between 14°S and 61°N (fig. S2 and table S1). To test the three above-listed predictions of warming-induced consequences on mountain biota, we analyzed pairs of response variables: lower and upper limit shifts combined (Model 1, Fig. 2) as well as range extent change and midpoint shift combined (Model 2, Fig. 2). It is worth noting that the response variables within each pair are often discussed together in ecological studies, but they are not independent of each other. This interdependence stems from the same principle that governs geometric constraints under warming conditions. For example, the lower limit cannot shift and exceed the upper limit. Consequently, we needed to use models with two response variables to accurately capture and analyze these interrelated ecological processes. We fitted two separate Bayesian multivariate response models (Model 1 and Model 2), applying a multivariate mixed-effects modeling (MMM) approach (*27*), to estimate correlations between pairs of response variables as well as the correlations between each pair of response variables and two fixed-effect variables, the elevational position (defined as the distance from a species' historical upper limit to the local mountaintop) (Fig. 2, A to D) and the historical range extent of each of the 2069 studied species (Fig. 2, E to H). To account for the effect of different methodological attributes stemming from the original studies, we added several covariates as control variables and the publication identification number as a random effect (*20*) (see materials and methods). Model significance for the three predictions of warming-induced changes was obtained by comparisons against expectations from null models (*23*) (see materials and methods) (Fig. 2).

To assess potential biotic homogenization induced by species range shifts, we analyzed temporal changes between the historical and contemporary period in distance-decay patterns of similarity in species assemblages along elevational gradients (*28*). We divided mountain areas into 100-m elevational bands and generated each species list or assemblage per 100-m elevational band by assuming that all species were continuously distributed within their reported range limits. Pairwise Jaccard's similarity indices between all possible pairs of elevational assemblages were calculated by using the beta.pair function from the R package *betapart* (*29*). We modeled the similarity patterns using both power-law and negative exponential functions, which represent the primary theoretical forms for distance-decay relationships (*30*). The models were implemented in a nonlinear regression framework using the Levenberg-Marquardt algorithm, with a model selection procedure based on Akaike information criterion values. We compared the slope estimates between the historical and contemporary distance-decay relationship using the z_{dep} statistic in *betapart* (*29*), a method designed for comparing model parameters with pairwise dependent data (*31*).

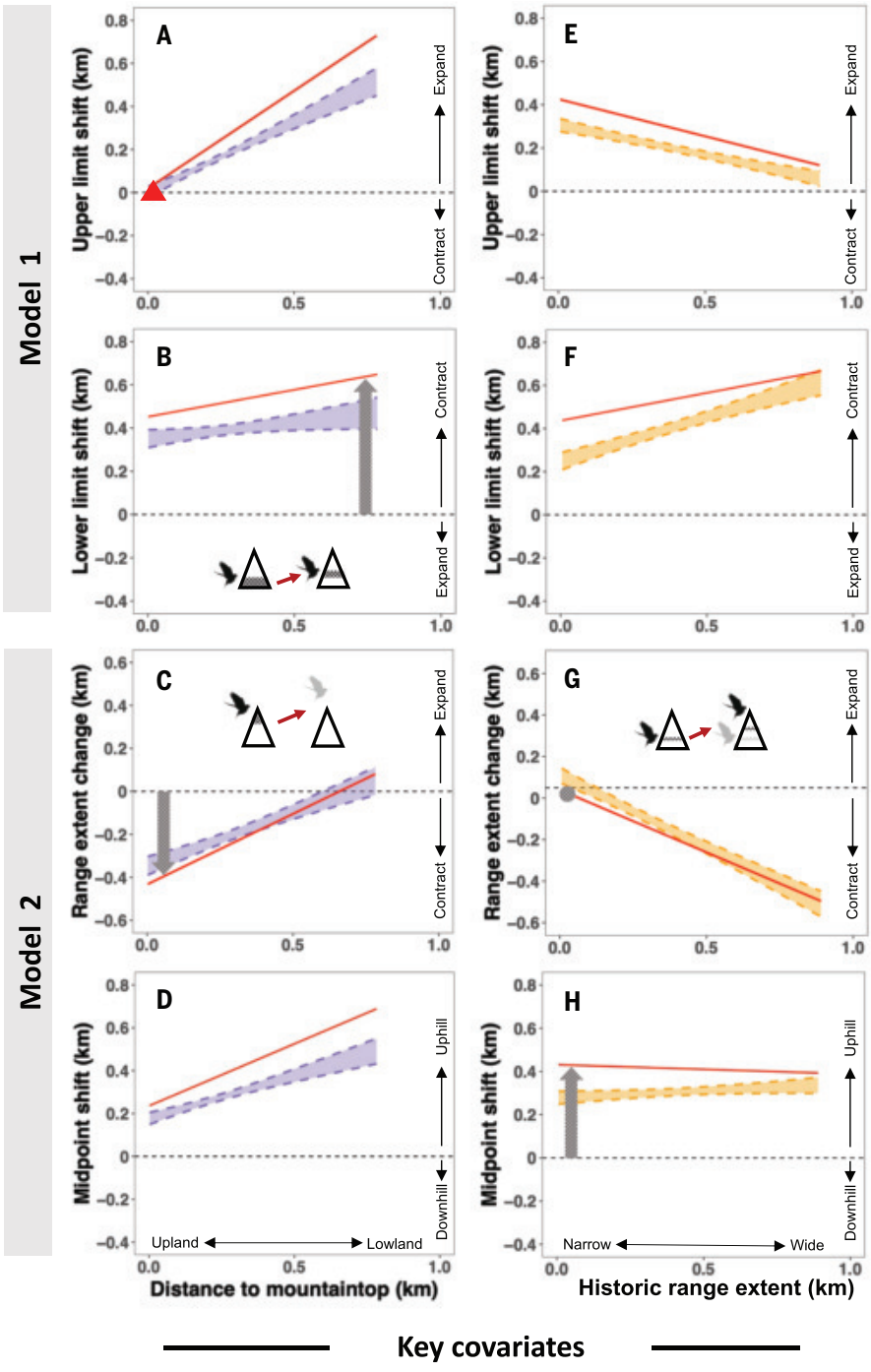

Fig. 2. Expected patterns of species range shifts under null models, taking mountain geometric constraints into account, during climate-driven migration. Predicted observations (red lines) and null expectations (shaded dashed lines) for: (i) elevational range shifts at the upper (**A** and **E**) and lower (**B** and **F**) limits; (ii) changes to the elevational range extent (i.e., expansions or contractions) (**C** and **G**); and (iii) range midpoint shifts (**D** and **H**). All expectations are displayed separately for the two predictors of baseline elevational positions (defined as the distance from a species' historical upper limit to the local mountaintop; left column) and historical elevational range extent (right column). Following the assumption of Colwell *et al*. (6), species' range limits are projected to shift 600 m upward in response to a +3.12°C temperature increase over a century, with the shifts truncated at the mountaintop [indicated by the red triangle in (A)]. In practice, we simulated 100 virtual species on a virtual mountain that is 1000 m high, with distribution limits randomly generated ($n = 1000$ iterations) from a uniform distribution bounded between 0 and 1000. The red line represents the fitted relationship of range shifts for the 100 virtual species based on an MMM approach, pairing lower and upper limit shifts (Model 1) as well as range extent change and midpoint shift (Model 2) as response variables. Given the geometric constraints, we further generated null expectations for species range shifts, with the shaded area between the dashed lines representing the 95% confidence interval based on 1000 resamples (with replacement) of the 100 species' upper and lower limit shifts. The horizontal dashed line indicates no change in species range limits. Comparing Colwell's projections under temperature forcing with null expectations that account for geometric constraints, we expected "mountaintop extinctions" to manifest as range contractions greater than null expectations near mountaintops [indicated by the gray arrow in (C)], "lowland biotic attrition" to manifest as contractions at lower limits greater than null expectations near mountain bases [indicated by the gray arrow in (B)], and range shift gaps to manifest as relatively unchanged range extents but midpoints shifting more than null expectations [indicated by the gray dots and arrow in (G) and (H), respectively].

Little evidence to date for mountaintop extinction and extinction debt

Our analysis revealed that changes in range extent near summits did not deviate significantly from the 95% confidence intervals generated by the null model (Fig. 3C, fig. S3C, and table S3), contradicting the prediction of mountaintop extinction (Fig. 2E, gray arrow). Both upper and lower elevational range limit shifts near summits fell within the null model's 95% confidence intervals (Fig. 3, A and C; fig. S3, A and C; and table S3). Mountaintop range contractions, often precursors to population extirpation and local extinction, were not prominent in our analyses. Thus, we found modest evidence, to date supporting global mountaintop extinctions under contemporary climate warming. By analyzing range extent changes near summits separately for each taxonomic group, we found empirical range contractions that exceed null model predictions, but only for amphibians inhabiting near-summit areas (Fig. 4, figs. S6c and S7c, and table S5).

Our findings were contrary to recent conclusions that suggest an escalator to extinction (*18*). Amphibian declines reflect more complex changes than just the sole effect of temperature increases, involving interactions with epidemic diseases and habitat loss, which accounted for 91% of observed status deteriorations from 1980 to 2004 (*32*). Under a severe warming scenario (+3.12°C over a century), Colwell *et al.* (*6*) projected only four mountaintop extinctions by 2108 among 1902 species along the Barva Transect in Costa Rica, suggesting that this process may proceed gradually. Nevertheless, although patterns of observed distribution changes remain, so far and overall, within the scope of random expectations respecting mountain geometric constraints, it is important to note that the widespread upslope movement of species persists. The null expectation of upper limits and midpoint shifts across elevational gradients are above zero (Fig. 3, A and D), reflecting the overall upward trend observed in the empirical data. The persistence of mountaintop species for some taxonomic groups, as reported for vascular plants across European mountain summits (*8*), may be only temporary, allowed by delaying competitive exclusion caused by slow but progressive local extinction and colonization processes (*33*–*36*). Other nonclimatic abiotic constraints at high elevations (e.g., poor soil development, high ultraviolet radiation, low air density, and low oxygen availability) may delay competitor establishment (*33*, *37*), extending the transient period before the extinction debt is paid off.

Range dynamics and climatic disequilibrium

Our analysis revealed that narrow-range species' distributional changes fell within null model expectations, contradicting the prediction of range shift gaps. Two main patterns emerged. First, narrow-range species expanded their ranges (Fig. 3G, fig. S3G, and tables S3 and S7) rather than marching upslope in lockstep with isotherms, as originally assumed (Fig. 2G, gray dot). Narrow-range species generally expanded upslope at their upper elevational limits (Fig. 3E, fig. S3E, and tables S3 and S8) without clear contractions at their lower elevational limits (Fig. 3F, fig. S3F, and tables S3 and S8). Secondly, their midpoint elevation shifts did not exceed null model expectations, also contrary to the prediction (Figs. 2G, gray arrow, and 3H; fig. S3H; and table S3). Notably, an upslope expansion increases the likelihood of persistent overlap with historical ranges. Consequently, the threat of range shift gaps for narrow-range species so far appears limited under current climate warming.

In fact, empirical evidence indicates simultaneous range expansions in narrow-range species and contractions in wide-range species, both conforming to geographic expectations from the null model (Fig. 3G). The observed range dynamics imply that the assumption of species equilibrium with temperature conditions is not common for mountain species (*38*). In other words, range shift gaps may not be common if some species are, in fact, filling up their fundamental thermal niche as the climate warms, which is likely to be the case for temperate species (*14*). The concept of "climatic disequilibrium," the idea that a given species' distribution might not be in full equilibrium with its climatic niche requirements, is not new for mountain species, which showed evidence of disequilibrium even before the onset of contemporary climate change (*38*). Several nonclimatic factors, such as biotic interactions, microhabitat availability, and behavioral thermoregulation for ectotherms, may contribute to climatic disequilibrium (*39*–*42*). Warmer temperatures may disrupt and potentially alleviate these constraints, allowing for niche filling, especially for temperate species underfilling their potential thermal niche on land (*14*). Hence, niche underfilling may further complicate the detection of actual range shift gaps.

Lowland species expansions without biotic attrition

Focusing on range shifts at the lower elevational limit of mountain species, we found no evidence for contraction upslope, even in the lowlands (Fig. 3B, fig. S3B, and table S3). The empirical relationship between range shifts at the lower elevational limit and distance to mountaintop did not deviate from the 95% confidence interval around predictions generated by the null model. This contradicts our initial expectation of more pronounced contractions at the lower elevational limit of mountain species, especially in the tropical lowlands (Fig. 2B, red line). Instead, the lower elevational limits of temperate species shifted downslope more than expected (figs. S4F and S5F and table S4). Lowland species significantly expanded their upper limits beyond null expectations (Fig. 3A, fig. S3A, and table S3), particularly for temperate species (fig. S4), resulting in widespread range expansions (Fig. 3C) without immediate threats of lowland mountain biodiversity loss from contraction of lower range limits.

Asymmetric boundary shifts have been widely discussed and attributed to various biotic and abiotic causes (*43*, *44*). However, we emphasize that asymmetric boundary shifts can simply result from mountains' geometric constraints (as illustrated in Fig. 2), a methodological artifact that has been largely unaddressed in previous research. Thus, to adequately examine the relationship between upper and lower boundary shifts, careful analyses should be undertaken by not only accounting for species' historic range size and elevational position relative to the nearest mountain summit but also undertaking a thoughtful and appropriate null-model approach, ideally, as we did in our analyses. Yet, even after accounting for those geometric constraints, we still found a consistent signal of range expansion for lowland species, specifically for lowland birds (Fig. 4). Mountain species found in lowlands may occupy only a fraction of their potential thermal niches and elevational ranges, even in wet tropical regions. This observation challenges previous findings that suggest that tropical species inhabit areas closely matching their thermal tolerances (*13, 45*–*47*). Therefore, lowland species may benefit from a wide elevational gradient available to further fill in their potential thermal niche as temperature increases and thus expand upslope with little or no change in the elevation of their lower range limits.

Biotic homogenization

Delayed mountaintop extinctions coupled with upslope range expansion of lowland and/or narrow-range species are expected to reduce the spatial turnover—i.e., increase similarity—in species composition along elevational gradients compared with historical baselines. Our global analysis of the steepness of distance-decay patterns along elevational gradients revealed that 5 out of the 20 studied mountain gradients exhibited significantly shallower slopes during contemporary periods, indicating more homogenized assemblages compared with their historical counterparts. These patterns emerged from multiple datasets across California and Europe, spanning birds, insects, mammals, and plants (Fig. 5, asterisks). Nevertheless, we also observed the opposite trend of steeper distance-decay patterns along three other elevational gradients (Fig. 5, plus signs), whereas the remaining 12 elevational gradients showed no significant temporal change in the steepness of the distance-decay relationship. These findings suggest an ongoing biotic homogenization but only for a limited set of mountain

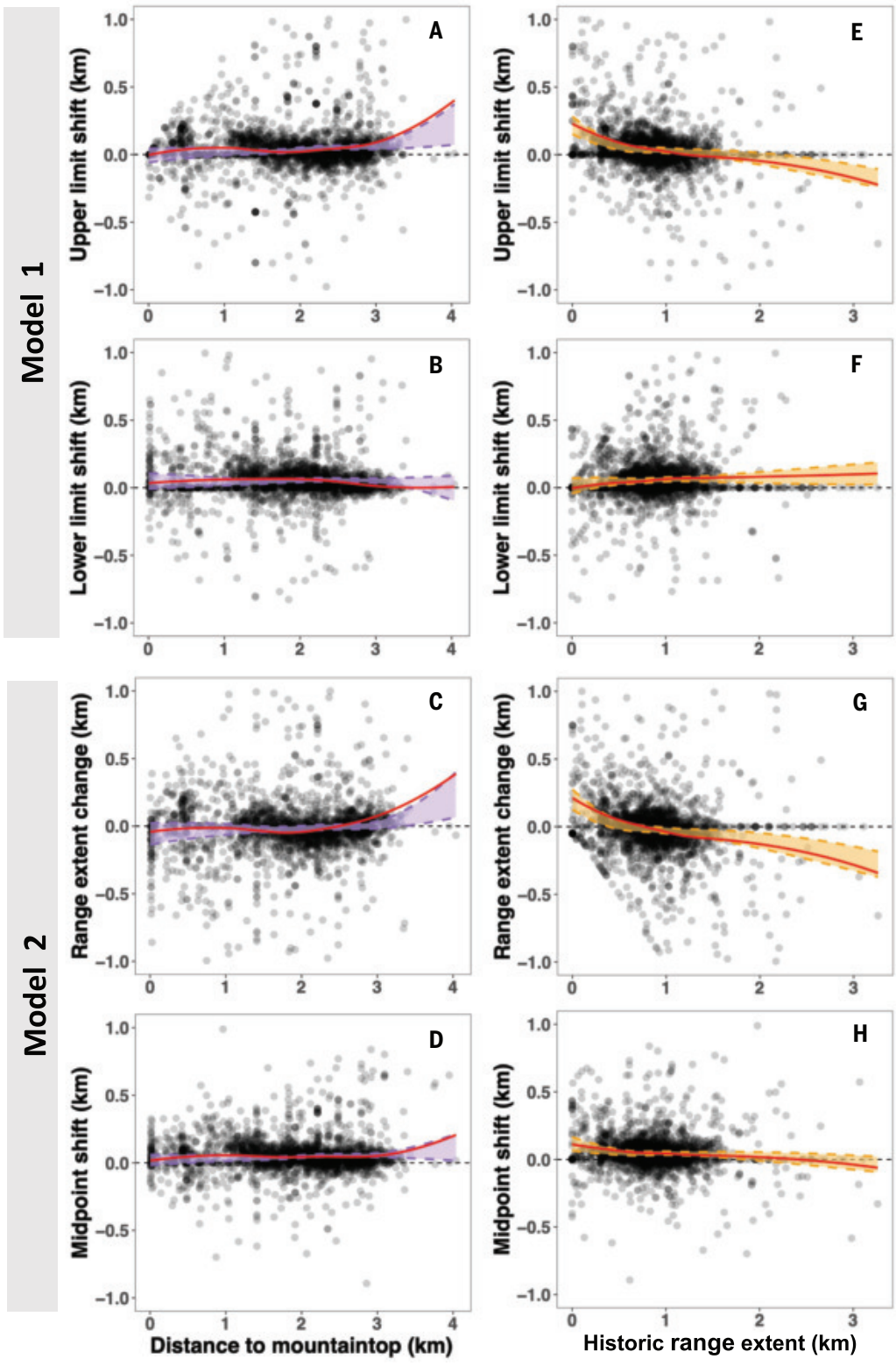

Fig. 3. Empirical results of species range shifts under geometric constraints during climate-driven migration. From 2200 species' range shift records (dots), the figure shows observed relationships (red lines) and null expectations (colored fill between dashed lines) for elevational range shifts at the upper (**A** and **E**) and lower (**B** and **F**) limits, elevational range changes (**C** and **G**), and range midpoint shifts (**D** and **H**), based on elevational positions (defined as the distance from a species' historical upper limit to the local mountaintop; left column) and historical elevational range extents (right column). The horizontal dashed line indicates no change in species range position or extent. Red lines represent averaged fitted relationships for observed range shifts based on the estimates of posterior mean correlations from MMMs, pairing lower and upper limit shifts (Model 1) as well as range extent change and midpoint shift (Model 2) as response variables (tables S7 and S8), smoothed by using locally weighted smoother (LOESS) with a span of 0.75. Colored dashed lines and shaded areas indicate LOESS-smoothed 95% confidence intervals of null expectations based on 1000 resamples (with replacement) of the observed upper and lower limit shifts, accounting for the geometric constraints, with a span of 0.75.

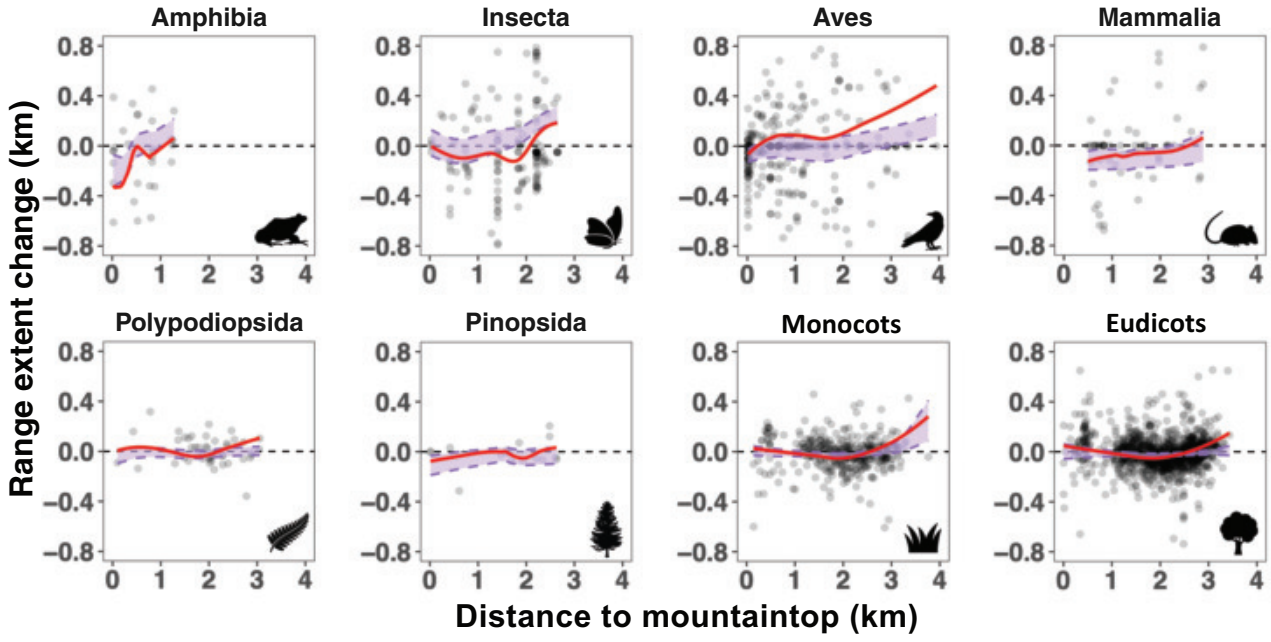

Fig. 4. Changes in species' elevational extents along elevational gradients across taxa. This figure illustrates the relationships between distance to mountaintop [baseline elevational positions, indicated by the distance from species' historical upper elevational limits to local summits (kilometers)] and range extent change (kilometers) for 2200 records of species range shifts (dots), grouped by taxonomic group, including Amphibia, Insecta, Aves, Mammalia, Polypodiopsida, Pinopsida, monocots, and eudicots. The horizontal dashed lines represent no change in species' elevational extents. Red lines represent averaged fitted relationships for observed range extent changes based on the estimates of posterior mean correlations from MMMs (tables S7 and S8) and LOESS, which had a span of 0.75. Colored dashed lines and filled areas indicate LOESS-smoothed 95% confidence intervals of null expectations based on 1000 resamples (with replacement) of the observed lower limit shifts, accounting for geometric constraints, with a span of 0.75.

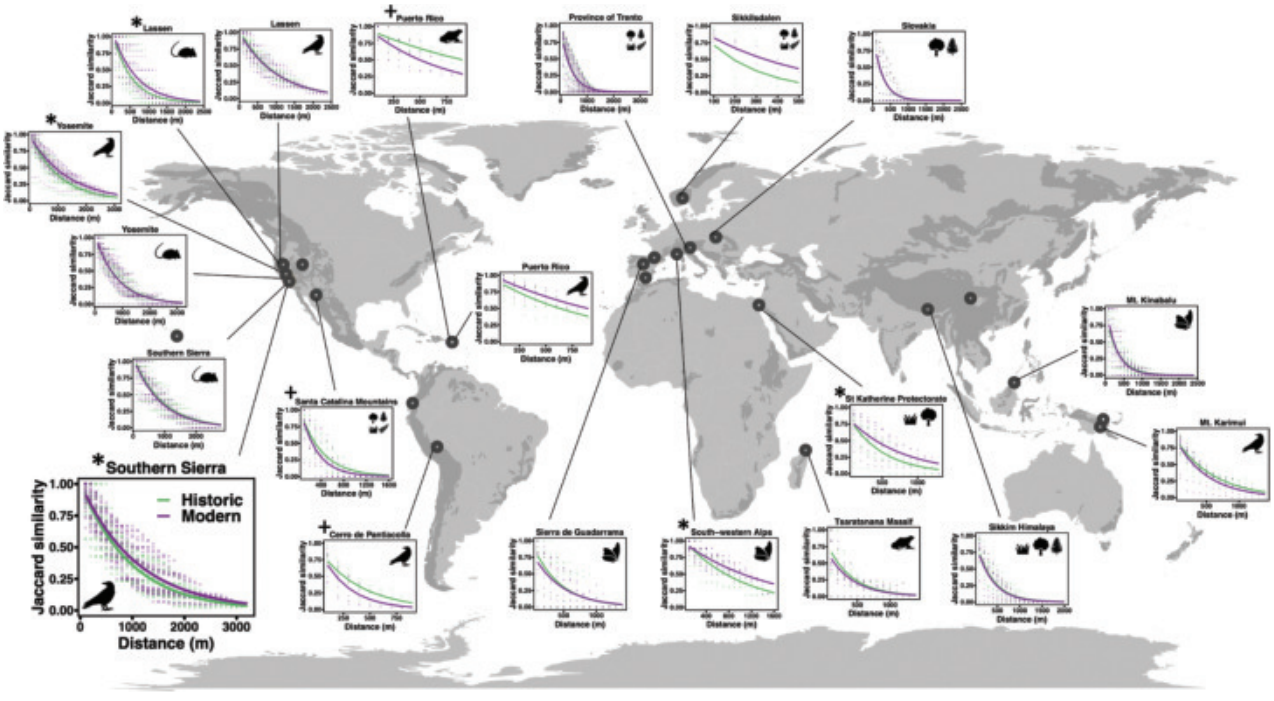

Fig. 5. Distance-decay patterns of assemblage similarity between historical and contemporary periods in global mountains. Pairwise Jaccard similarity indices were calculated between assemblages in 100-m elevational bands based on interpolated species distributions within their documented elevational ranges. Negative exponential models were fitted separately for each period, with differences tested through z_{dep} statistics (1000 resamples), a method optimized for comparing parameters from pairwise autocorrelated data. Asterisks and plus signs denote significantly shallower slopes in contemporary and historical periods, respectively, where shallower slopes indicate more homogenized assemblages. Mountain ranges (dark gray) follow Körner *et al*. (*57*). Studies with <10 species were excluded.

regions so far, whereas an increase in the spatial turnover in species composition along elevational gradients cannot be excluded. These discrepancies call for more field studies and detailed monitoring of community data to confirm the generality (or scarcity) of a biotic homogenization signal. Warming-driven range shifts under mountain geometric constraints may act in concert with multiple mechanisms to contribute to biodiversity homogenization, such as the upslope expansion of non-native species from lowland sources (*48*) and the proliferation of wide-ranging species at the expense of narrow-range species (*49*–*51*). Consequently, biotic homogenization in mountain ecosystems may occur earlier than the anticipated mountaintop extinctions, range shift gaps, and lowland biotic attrition. Such compositional changes could alter species interactions and trophic relationships, potentially triggering cascading effects throughout mountain food webs (*52*).

Complexities of climate-induced range shifts and future risks

Species range shifts exhibit greater dynamism and complexity than predicted by the simplified "escalator to extinction" model of isotherm tracking. Our research highlights the critical importance of mountain geometric constraints when investigating biological responses to climate change, as these constraints fundamentally influence the interpretation of underlying mechanisms (*53*, *54*). To better understand biodiversity redistribution, future research should examine both additional climatic variables, particularly moisture conditions (*2*, *55*), and other abiotic drivers, such as nitrogen deposition in the European Alps (*56*). The observed range dynamics and climatic disequilibrium in montane species suggest that biotic interactions jointly shape species distributions, warranting further investigation (*41*). Although current evidence for mountaintop extinctions, range shift gaps, and lowland biotic attrition remains modest, we have observed early signs of ongoing biotic homogenization along a few mountain slopes. We anticipate that continued warming will amplify these risks, fundamentally reshaping species composition and ecosystem functioning, ultimately leading to the ongoing extinction debts being paid off on mountaintops.

REFERENCES AND NOTES

1. R. Hugonnet *et al.*, *Nature* **592**, 726–731 (2021).
2. W. P. Chan *et al.*, *Nature* **629**, 114–120 (2024).
3. P. R. Elsen, M. W. Tingley, *Nat. Clim. Chang.* **5**, 772–776 (2015).
4. R. K. Colwell, D. C. Lees, *Trends Ecol. Evol.* **15**, 70–76 (2000).
5. J. Lenoir, J. C. Gégout, P. A. Marquet, P. de Ruffray, H. Brisse, *Science* **320**, 1768–1771 (2008).
6. R. K. Colwell, G. Brehm, C. L. Cardelús, A. C. Gilman, J. T. Longino, *Science* **322**, 258–261 (2008).
7. B. G. Freeman, M. N. Scholer, V. Ruiz-Gutierrez, J. W. Fitzpatrick, *Proc. Natl. Acad. Sci. U.S.A.* **115**, 11982–11987 (2018).
8. M. J. Steinbauer *et al.*, *Nature* **556**, 231–234 (2018).
9. C. Geppert, A. Bertolli, F. Prosser, L. Marini, *Proc. Natl. Acad. Sci. U.S.A.* **120**, e2211531120 (2023).
10. F. A. La Sorte, W. Jetz, *Proc. Biol. Sci.* **277**, 3401–3410 (2010).
11. A. Mekasha, L. Nigatu, K. Tesfaye, A. J. Duncan, *Biol. Conserv.* **168**, 169–175 (2013).
12. J. Kreyling, D. Wana, C. Beierkuhnlein, *Divers. Distrib.* **16**, 593–605 (2010).
13. K. J. Feeley, M. R. Silman, *Glob. Change Biol.* **16**, 1830–1836 (2010).
14. N. A. Moore *et al.*, *Nat. Ecol. Evol.* **7**, 1993–2003 (2023).
15. R. K. Colwell, K. J. Feeley, *Biotropica* **57**, e13358 (2024).
16. J. G. Blake, B. A. Loiselle, *Glob. Ecol. Conserv.* **51**, e02902 (2024).
17. E. Marris, *Nat. Clim. Chang.* **1**, 94–96 (2007).
18. M. C. Urban, *Proc. Natl. Acad. Sci. U.S.A.* **115**, 11871–11873 (2018).
19. B. G. Freeman, J. A. Lee-Yaw, J. M. Sunday, A. L. Hargreaves, *Glob. Ecol. Biogeogr.* **27**, 1268–1276 (2018).
20. J. Lenoir *et al.*, *Nat. Ecol. Evol.* **4**, 1044–1059 (2020).
21. C. J. Brown *et al.*, *Glob. Chang. Biol.* **22**, 1548–1560 (2016).
22. S. Taheri, B. Naimi, C. Rahbek, M. B. Araújo, *Sci. Adv.* **7**, 1–12 (2021).
23. E. Iseli *et al.*, *Nat. Ecol. Evol.* **7**, 405–413 (2023).
24. R. K. Colwell, G. C. Hurtt, *Am. Nat.* **144**, 570–595 (1994).
25. L. Mazalla, M. Diekmann, *J. Veg. Sci.* **33**, 1–8 (2022).
26. Materials and methods are available as supplementary materials.
27. J. E. Brommer, B. Class, G. Covarrubias-Pazaran, Multivariate mixed models in ecology and evolutionary biology: Inference and implementation in R, EcoEvoRxiv [Preprint] (2019); https://doi.org/10.32942/osf.io/hs38a.
28. J. D. Olden, T. P. Rooney, *Glob. Ecol. Biogeogr.* **15**, 113–120 (2006).
29. A. Baselga *et al.*, betapart: Partitioning beta diversity into turnover and nestedness components, R package version 1.6, (2023); https://doi.org/10.32614/CRAN.package.betapart.
30. J. C. Nekola, B. J. Mcgill, *Ecography* **37**, 309–320 (2014).
31. R. Martín-Devasa, S. Martínez-Santalla, C. Gómez-Rodríguez, R. M. Crujeiras, A. Baselga, *Ecol. Inform.* **72**, 101894 (2022).
32. J. A. Luedtke *et al.*, *Nature* **622**, 308–314 (2023).
33. J. M. Alexander *et al.*, *Glob. Chang. Biol.* **24**, 563–579 (2018).
34. S. B. Rumpf *et al.*, *Nat. Commun.* **10**, 4293 (2019).
35. L. Figueiredo, J. Krauss, I. Steffan-Dewenter, J. Sarmento Cabral, *Ecography* **42**, 1973–1990 (2019).
36. J. C. Svenning, B. Sandel, *Am. J. Bot.* **100**, 1266–1286 (2013).
37. A. R. Spence, M. W. Tingley, *Ecography* **43**, 1571–1590 (2020).
38. S. J. Ivory, R. Early, D. F. Sax, J. Russell, *Glob. Ecol. Biogeogr.* **25**, 693–703 (2016).
39. J. M. Sunday *et al.*, *Proc. Natl. Acad. Sci. U.S.A.* **111**, 5610–5615 (2014).
40. J. Lenoir, T. Hattab, G. Pierre, *Ecography* **40**, 253–266 (2017).
41. I.-C. Chen, S.-F. Shen, S.-F. Chan, *Annu. Rev. Ecol. Evol. Syst.* **55**, 449–469 (2024).
42. J. W. Williams, A. Ordonez, J. C. Svenning, *Nat. Ecol. Evol.* **5**, 17–26 (2021).
43. A. Paquette, A. L. Hargreaves, *Ecol. Lett.* **24**, 2427–2438 (2021).
44. M. H. C. Neate-Clegg, M. W. Tingley, *PLOS Clim.* **2**, e0000174 (2023).
45. D. H. Janzen, *Am. Nat.* **101**, 233–249 (1967).
46. C. A. Deutsch *et al.*, *Proc. Natl. Acad. Sci. U.S.A.* **105**, 6668–6672 (2008).
47. J. J. Tewksbury, R. B. Huey, C. A. Deutsch, *Science* **320**, 1296–1297 (2008).
48. J. M. Alexander *et al.*, *Proc. Natl. Acad. Sci. U.S.A.* **108**, 656–661 (2011).
49. I. R. Staude *et al.*, *Ecol. Lett.* **25**, 466–482 (2022).
50. I. R. Staude *et al.*, *Nat. Ecol. Evol.* **4**, 802–808 (2020).
51. B. H. Daru *et al.*, *Nat. Commun.* **12**, 6983 (2021).
52. M. Di Marco, L. Santini, D. Corcos, H.-P. Tschorsnig, P. Cerretti, *Proc. Natl. Acad. Sci. U.S.A.* **120**, e2308273120 (2023).
53. L. Comte *et al.*, *Glob. Change Biol.* **30**, e17271 (2024).
54. J. A. Lawlor *et al.*, *Nat. Rev. Earth Environ.* **5**, 351–368 (2024).
55. C. M. McCain, R. K. Colwell, *Ecol. Lett.* **14**, 1236–1245 (2011).
56. P. Sanczuk *et al.*, *Science* **386**, 193–198 (2024).
57. C. Körner *et al.*, *Alp. Bot.* **127**, 1–15 (2017).
58. Y.-H. Chen, J. Lenoir, I.-C. Chen, Data from: Limited Evidence for Range-Shift-Driven Extinction in Mountain Biota, Dryad (2024); https://doi.org/10.5061/dryad.83bk3jb1m.
59. D. N. Karger, N. E. Zimmermann, CHELSAcruts - High resolution temperature and precipitation timeseries for the 20th century and beyond. EnviDat [Preprint] (2018). https://doi.org/10.16904/envidat.159.
60. D. N. Karger *et al.*, *Sci. Data* **4**, 170122 (2017).
61. D. N. Karger *et al.*, Data from: Climatologies at high resolution for the earth's land surface areas, Dryad (2018); https://doi.org/10.5061/dryad.kd1d4.
62. J. J. Danielson, D. B. Gesch, Global Multi-resolution Terrain Elevation Data 2010 (GMTED2010): Open-File Report 2011-1073, USGS (2010); https://doi.org/10.3133/ofr20111073.

ACKNOWLEDGMENTS

We sincerely thank R. Colwell, the two anonymous reviewers, and B. Lopez for their insightful and constructive feedback, which considerably improved this article. We also thank H.-C. Hsu for kindly providing the photograph of Mount Jade for inclusion in Fig. 1 and Y.-W. Chen for the design of Fig. 1. **Funding:** National Science and Technology Council, Taiwan, grants 113-2628-B-006-012, 112-2628-B-006-005, and 111-2628-B-006-016 (I.-C.C.); Forestry and Nature Conservation Agency, Taiwan, grant 113-09.1-EP-03 (Y.-H.C.). **Author contributions:** Conceptualization: I.-C.C., Y.-H.C.; Methodology: Y.-H.C., I.-C.C., J.L.; Analysis: Y.-H.C.; Visualization: Y.-H.C., I.-C.C.; Writing – original draft: Y.-H.C., I.-C.C.; Writing – review & editing: Y.-H.C., I.-C.C., J.L. **Competing interests:** The authors declare that they have no competing interests. **Data and materials availability:** The data and code to reproduce analyses in this study are available at https://doi.org/10.5061/dryad.83bk3jb1m (*58*). CHELSA data are available at https://chelsa-climate.org/ (*59*–*61*). GMTED2010 data are available at https://www.usgs.gov/coastal-changes-and-impacts/gmted2010 (*62*).

License information: Copyright © 2025 the authors, some rights reserved; exclusive licensee American Association for the Advancement of Science. No claim to original US government works. https://www.science.org/about/science-licenses-journal-article-reuse

SUPPLEMENTARY MATERIALS

science.org/doi/10.1126/science.adq9512
Materials and Methods; Supplementary Text; Figs. S1 to S14; Tables S1 to S9; References (*63*–*80*); MDAR Reproducibility Checklist

Submitted 11 June 2024; accepted 27 March 2025

10.1126/science.adq9512

PALEONTOLOGY

Sustainability insights from Late Pleistocene climate change and horse migration patterns

Yvette Running Horse Collin (Tašunke Iyanke Wiŋ)[1,2,3]*, Clément P. Bataille[4,5]*, Samantha Hershauer[6], Mila Hunska Tašunke Icu (Chief Joe American Horse)[2,3], (Akil Nujipi) Chief Harold Left Heron[2,3], Wilson Justin[7,8,9], Jane (q^{w}yxnmitk^{w}) Stelkia[10], C'wyelx (Thomas Pierre)[11], James Aaron Stelkia[12], Sean Asikłuk Topkok[13], Beth Ginondidoy Leonard[14,15], Beatle (Naatoonistaahs) Soop[16], Mario Gonzalez (Nantan Hinapan)[2,3], Anpetu Luta Wiŋ (Antonia Loretta Afraid of Bear-Cook)[2,3], Wakiŋyala Wiŋ (Anita Afraid of Bear)[2,3], Tanka Omniya (Robert Milo Yellow Hair)[2,3], Barbara Dull Knife (Mah'piya Keyaké Wiŋ)[2,3], Mažasu (Wendell W. Yellow Bull)[2,3], Bill Means[2,3], Cruz Tecumseh Collin (Wanka'tuya Kiya)[2,3], Michael Koskey[12], Joshua D. Kapp[17], Zoe Landry[4], Danielle Fraser[18,19,20], John Southon[21], Eve E. Lindroos[4], Auguste Hassler[4,22], Lorelei Chauvey[1], Gaetan Tressières[1], Laure Tonasso-Calvière[1], Stéphanie Schiavinato[1], Andaine Seguin-Orlando[1], Aude Perdereau[23], Pedro H. Oliveira[24], Jean-Marc Aury[24], Patrick Wincker[24], Irina V. Kirillova[25], Sergey K. Vasiliev[26], Mariya A. Kusliy[1,27], Alexander S. Graphodatsky[27], Alexey A. Tishkin[28], Ian Barnes[29], Pat Druckenmiller[30,31], Christopher N. Jass[32], Ross D. E. MacPhee[33], Christina I. Barrón-Ortiz[32], Pam Groves[34], Dan Mann[33], Duane G. Froese[35], Matthew Wooller[36], Joshua H. Miller[20,37], Brooke Crowley[37,38], Grant Zazula[39], Elizabeth Hall[39], Susan Hewitson[39], Beth Shapiro[17]*, Ludovic Orlando[1]*

Climate affects habitat, food availability, and the movement and sustainability of all life. In this work, we apply Indigenous and Western scientific methods, including genomics and isotope profiling, on fossils from across Beringia to explore the effect of climate change on horses. We find that Late Pleistocene horses from Alaska and northern Yukon are related to populations from Eurasia and crossed the Bering land bridge multiple times during the last glacial interval. We also find deeply divergent lineages north and south of the American ice sheets that genetically influenced populations across Beringia and into Eurasia. As climate warmed and horses entered the ice-free corridor connecting Beringia and midcontinental America, restricted mobility and food availability impeded population growth. Our combined Western and Indigenous framework offers critical guidance for wildlife conservation amid ongoing climate change.

Many Indigenous scientific systems are premised on the knowledge that all life is in constant motion (*1*), moving and adapting as climate shifts (*2*). Megafauna (animals that are >45 kg) fill keystone roles in ecosystems, shaping biodiversity (*3*) and safeguarding carbon stocks in soils and vegetation (*4*). Their decline can trigger cascading effects on ecosystem function, habitats, and people (*5*, *6*). This is especially acute in the Arctic, which is warming considerably faster compared with other ecosystems (*7*, *8*). Understanding the long-term interplay between megafaunal dynamics and climate change is urgently needed to aid conservation and ecosystem restoration in the Artic and beyond (*9*).

Indigenous science has accumulated invaluable knowledge on habitat change and its effects on the movement of peoples, megafauna, and other life forms (*10*, *11*). The fossil record—with its deep temporal archive of responses to changing environments—also provides insights into the relationship between climate and megafaunal dynamics (*12*–*14*). For example, Pleistocene fossils of Beringia, the unglaciated landmass that connected present-day Yukon, Alaska, and northeastern Asia across the exposed Bering land bridge (Fig. 1A), reveals notably shifting patterns of habitat availability concurrent with climate swings. During the last cold period [35 to 16 thousand years before the present (kyr B.P.)], lower sea levels allowed dispersal into and out of North America via the exposed land bridge, although ice sheets limited movement southward into lower American latitudes (*15*). As the climate warmed (16 to 10 kyr B.P.), ice sheet melting opened the ice-free corridor to midcontinental America (*16*) and submerged the land bridge, forming the Bering Strait (*17*), which remains a barrier to the dispersal of terrestrial species [although examples of human-mediated exchanges seasonally and by sea are abundant in Iñupiaq and Dene' (Athabascan) oral traditions]. These changes altered habitat availability, connectivity, and food resources as cryoxeric steppe-tundra fragmented into boggy tundra, shrublands, wetlands, and boreal forests (*18*), which are less favorable habitats for some megafaunal species (*19*).

Despite substantial habitat changes in Beringia during Pleistocene climate cycles, the effects on megafaunal populations remain elusive (*13*, *14*). In this work, we combine geochemical and genomic analyses of horse fossils with traditional science to track changing habitats, population dynamics, and dispersal in Beringia from ~13 to >50 kyr B.P. Pleistocene horses offer a model to explore climate effects on megafauna, particularly in Beringia (*20*–*22*), where the *Equus* fossil record is exceptional (*23*). The Horse Nation and its movement and evolution are sacred to many Indigenous knowledge keepers in the Americas (*1*). Following the movement and evolution of the horse to reveal traditional knowledge fully aligns with many Indigenous scientific protocols. We thus integrate the biological signatures identified with Indigenous knowledge regarding ecosystem balance and sustainability to highlight the importance of corridors in safeguarding life.

Genomic, radiocarbon, and isotopic datasets

We applied Western and Lakota protocols to generate genomic data from 67 fossils originating in Beringia, Siberia, and continental North America (Fig. 1, A and B; fig. S1; and table S1). These data, which showed expected signatures of postmortem DNA damage (figs. S2 and S3) and limited error rates at transversion sites (fig. S4 and table S1), were compared with 158 genomes representing all known horse lineages (*24*–*26*) plus two donkeys (table S1). Additionally, we integrated genomic data with 200 radiocarbon dates and stable carbon and nitrogen isotope measurements ($\delta^{13}C$ and $\delta^{15}N$) from fossil horse collagen. To extend reconstruction of environmental conditions, dietary behavior, and habitats across the Northern Hemisphere, we prepared a database of 3809 $\delta^{13}C$ and $\delta^{15}N$ data from radiocarbon-dated Late Pleistocene megafauna (table S2). Combined, these data tracked habitat, diet, and genetic diversity changes across Beringia and beyond from ~13 to >50 kyr B.P.

Horses crossed Beringia multiple times

Phylogenetic analyses of mitochondrial and Y chromosome DNA suggest that horses crossed the Bering land bridge in both directions during the Pleistocene. Most horse fossils from North America cluster into two distinct major clades (Fig. 1C and figs. S5 and S6). The first ranged from south of the continental ice sheets (present-day US lower 48 states) to easternmost East Beringia via the ice-free corridor. Fossils from eastern Eurasia, including *Equus dalianensis* specimens from China (*27*) and South-East Russia near Vladivostok, appear sister to this clade at the mitochondrial level (Fig. 1C). Because *Equus* originated in North America (*28*), this phylogenetic structure supports dispersal into Eurasia beyond the limits of radiocarbon dating (i.e., >50 kyr B.P.). The second clade includes individuals from the

most western and northern extent of East Beringia (Fig. 1C and figs. S5 and S6) and clusters within broader Eurasian diversity, with closest relatives in northeastern Siberia, which supports migration back into America >46.8 kyr B.P.

Dispersals from Eurasia into North America

Analyses of genome-wide autosomal variation identified two major horse genetic lineages in North America. Principal components analysis (PCA) (Fig. 2A and figs. S7 to S9) and f3-outgroup statistics (fig. S10) showed strong differentiation between one cluster of specimens spanning easternmost East Beringia, the ice-free corridor, and south of the continental ice sheets, and a second cluster comprising the remaining American and Eurasian lineages. Within the latter, PC2 revealed a genetic cline stretching longitudinally from the Ural Mountains (≥15.4 kyr B.P.) to Alaska and northwestern Yukon (Fig. 2B) [Pearson correlation, adjusted coefficient of determination (R^2) = 0.941, $P < 2.2 \times 10^{-16}$]. Longitude was also correlated with the ADMIXTURE (*29*) component maximized in Alaskan individuals (adjusted R^2 = 0.949, $P < 2.2 \times 10^{-16}$) (fig. S11), all of which belonged to a highly supported monophyletic group, deriving from a larger Siberian cluster (Fig. 3, A and B, and fig. S12). These results support isolation-by-distance east of the Ural Mountains and across the Arctic into North America.

Temporal branching patterns within Alaskan and northwestern Yukon individuals support multiple dispersals across the Bering land bridge. Whereas a single dispersal event would produce a temporally sorted phylogenetic clade, no clear time structure emerged within Alaska (Fig. 3A), with the two most recent specimens (AV089 and AV096) branching off first. Their basal position is not a result of admixture with a divergent lineage because D-statistics and F4 ratio calculation (*30*) indicated significantly less genetic sharedness with the geographically closest, most divergent population from East Beringia versus with the other individuals from Alaska or northwestern Yukon (Fig. 3D and fig. S14). These results, alongside radiocarbon dating, support multiple independent dispersal events into North America from genetically close Siberian sources followed by limited genetic admixture (F4 ratios, 0.5 ± 0.3% to 6.1 ± 0.6%) with the other main American lineage.

Dispersals from North America into Eurasia

Several individuals deviated from the genetic cline linking the Eurasian and American Arctic (Fig. 2B and fig. S11). These included three >50–kyr B.P. specimens from northeastern Siberia (PH156, PH172, and R17x2), one ~23.6–kyr B.P. specimen from southwestern Siberia (Rus45), and two *E. dalianensis* specimens from more southerly latitudes (Fig. 1 and fig. S1). The latter showed ancestry from the lineage spanning easternmost East Beringia, the ice-free corridor, and south of the continental ice sheets, as revealed by ADMIXTURE (*29*) (1.3 ± 0.3% to 1.7 ± 0.2%; fig. S12 and table S1) and Struct-f4 (*31*) analyses (3.0 ± 0.3% to 3.6 ± 0.2%) (Fig. 3, B and C; fig. S14; and table S1). Similar ancestry was identified among the >50–kyr B.P. outliers from northeastern Siberia (0.8 to 1.7%), Rus45 (1.3%), and some Holocene (~3.9 to 4.7 kyr B.P.) remains from Iberia (2.3 to 4.2%; fig. S13 and table S1). F4 ratio analysis found 0.6 ± 0.2% to 0.7 ± 0.2% of such ancestry in two northeastern Siberian specimens dated to ~20.4 (PH147) and ~36.6 kyr B.P. (PH159) (Fig. 3D and table S1). Combined, these analyses support genetic contribution of North American horses to Eurasia before ~20.4 kyr B.P., extending from northeastern Siberia southward to the Russian Far East (*E. dalianensis*) and west to Iberia.

Understanding the frequency and limits of American horse dispersal across the Bering land bridge requires extensive genetic surveys of Pleistocene eastern Eurasia. Our findings reveal genetic exchanges across Beringia and well into Eurasia. This aligns with the movement patterns described within the sciences of the Iñupiaq and Dene' (Athabascan) (*2*) and with the Lakota and Syilx understanding of the evolution of their Peoples and the Horse Nation. Current labeling practices of Beringian fossils, influenced by geography and historical bias, overlook the dynamic history of species movement and reduce the multidimensionality of life forms. They ignore the Lakota mitakuye oyasin concept, which emphasizes "the relationality between life forms"—i.e., the interdependence between organisms, including microbes. We believe that the reliance on contemporary geographical labels, although convenient to Western paleontologists, has hindered constructive dialogs with Indigenous scientists.

Opening of the ice-free corridor

Beringia served as a dispersal corridor between Siberia and America until rising sea levels reformed the Bering Strait ~11 to 13 kyr B.P. (*17*). Meanwhile, the Laurentide and Cordilleran ice sheets coalesced from ~25 kyr B.P., depopulating Alberta until the ice-free corridor reopened ~13.8 ± 0.5 kyr B.P. (*16*) (Fig. 1B). The 19 horses analyzed from the Edmonton area, Alberta, lived ~13.1 kyr B.P., immediately after deglaciation (Fig. 1A and table S1). Although phylogenetically close, these horses diverged before the divergence of populations in easternmost East Beringia and those south of the continental ice sheets (Fig. 3A), which indicates that the ice-free corridor population did not emerge from either group expanding into the region.

To characterize the genetic source or sources entering the ice-free corridor, we performed population graph modeling with AdmixtureBayes (*32*) and OrientAGraph (*33*), considering key lineages in and around Beringia (Fig. 4 and figs. S15 and S16). These analyses confirmed the deep phylogenetic split within America between Alaska and/or northwestern Yukon and other regions, with the former receiving a minor genetic contribution from a source related to easternmost East Beringia (AdmixtureBayes, 3.0%; OrientAGraph, 2.5%). The genetic affinities linking the Ural Mountains to East Beringia, as well as the early divergence of the outlier northeastern Siberian and *E. daliensis* lineages, were also validated.

[1]Centre for Anthropobiology and Genomics of Toulouse, CNRS UMR 5288, Université de Toulouse, Toulouse, France. [2]Taku Skan Skan Wasakliyapi: Global Institute for Traditional Sciences, Keystone, SD, USA. [3]Oglala Lakota, Pine Ridge Reservation, SD, USA. [4]Department of Earth and Environmental Sciences, University of Ottawa, Ottawa, ON, Canada. [5]Department of Forestry and Natural Resources, Purdue University, West Lafayette, IN, USA. [6]Department of Biomolecular Engineering, University of California Santa Cruz, Santa Cruz, CA, USA. [7]Mt. Sanford Tribal Health Corporation, Hq Chistochina, AK, USA. [8]Ahtna Inc., ANCSA Regional Corporation, Slana, AK, USA. [9]Cheesh'Na Tribal Council, Gakona, AK, USA. [10]sqilxʷ/suknaqin or Okanagan Nation, Osoyoos Indian Band, Oliver, BC, Canada. [11]sqilxʷ/suknaqin or Okanagan Nation, snpink'tn Indian Band, Penticton, BC, Canada. [12]sqilxʷ/suknaqin or Okanagan Nation, Osoyoos Indian Band, Spetlumkn Oliver, BC, Canada. [13]Center for Cross-Cultural Studies, University of Alaska Fairbanks, Fairbanks, AK, USA. [14]Shageluk Tribe of Interior Alaska, Shageluk, AK, USA. [15]Institute of Culture and Environment, Alaska Pacific University, Anchorage, AK, USA. [16]Blackfoot Nation, Horse Spirit Healing and Wellness, McLean, SK, Canada. [17]Department of Ecology and Evolutionary Biology, University of California Santa Cruz, Santa Cruz, CA, USA. [18]Palaeobiology, Canadian Museum of Nature, Gatineau, QC, Canada. [19]Department of Earth Sciences and Biology, Carleton University, Ottawa, ON, Canada. [20]Smithsonian National Museum of Natural History, Washington, DC, USA. [21]Department of Earth System Science, University of California Irvine, Irvine, CA, USA. [22]Department of Archaeology, School of Geosciences, University of Aberdeen, Aberdeen, Scotland. [23]Genoscope, Institut de Biologie François Jacob, CEA, CNRS, Université d'Évry, Université Paris-Saclay, Évry, France. [24]Génomique Métabolique, Genoscope, Institut François Jacob, CEA, CNRS, Université d'Évry, Université Paris-Saclay, Évry, France. [25]Ice Age Museum, Shidlovskiy National Alliance "Ice Age," Moscow, Russia. [26]ArchaeoZOOlogy in Siberia and Central Asia – ZooSCAn, CNRS–IAET SB RAS International Research Laboratory, IRL 2013, Institute of Archaeology and Ethnography SB RAS, Novosibirsk, Russia. [27]Department of the Diversity and Evolution of Genomes, Institute of Molecular and Cellular Biology SB RAS, Novosibirsk, Russia. [28]Department of Archaeology, Ethnography and Museology, Altai State University, Barnaul, Russia. [29]Earth Sciences Department, Natural History Museum, London, UK. [30]University of Alaska Museum, Fairbanks, AK, USA. [31]Department of Geosciences, University of Alaska Fairbanks, Fairbanks, AK, USA. [32]Quaternary Palaeontology Program, Royal Alberta Museum, Edmonton, AB, Canada. [33]Department of Mammalogy, American Museum of Natural History, New York, NY, USA. [34]Institute of Arctic Biology, University of Alaska Fairbanks, Fairbanks, AK, USA. [35]Department of Earth and Atmospheric Sciences, University of Alberta, Edmonton, AB, Canada. [36]Alaska Stable Isotope Facility, University of Alaska Fairbanks, Fairbanks, AK, USA. [37]Department of Geosciences, University of Cincinnati, Cincinnati, OH, USA. [38]Department of Anthropology, University of Cincinnati, Cincinnati, OH, USA. [39]Government of Yukon, Palaeontology Program, Whitehorse, YT, Canada. ***Corresponding author. Email: runninghorse@takuskanskan.org (Y.R.H.C.); cbataill@uottawa.ca (C.P.B.); bashapir@ucsc.edu (B.S.); ludovic.orlando@univ-tlse3.fr (L.O.)**

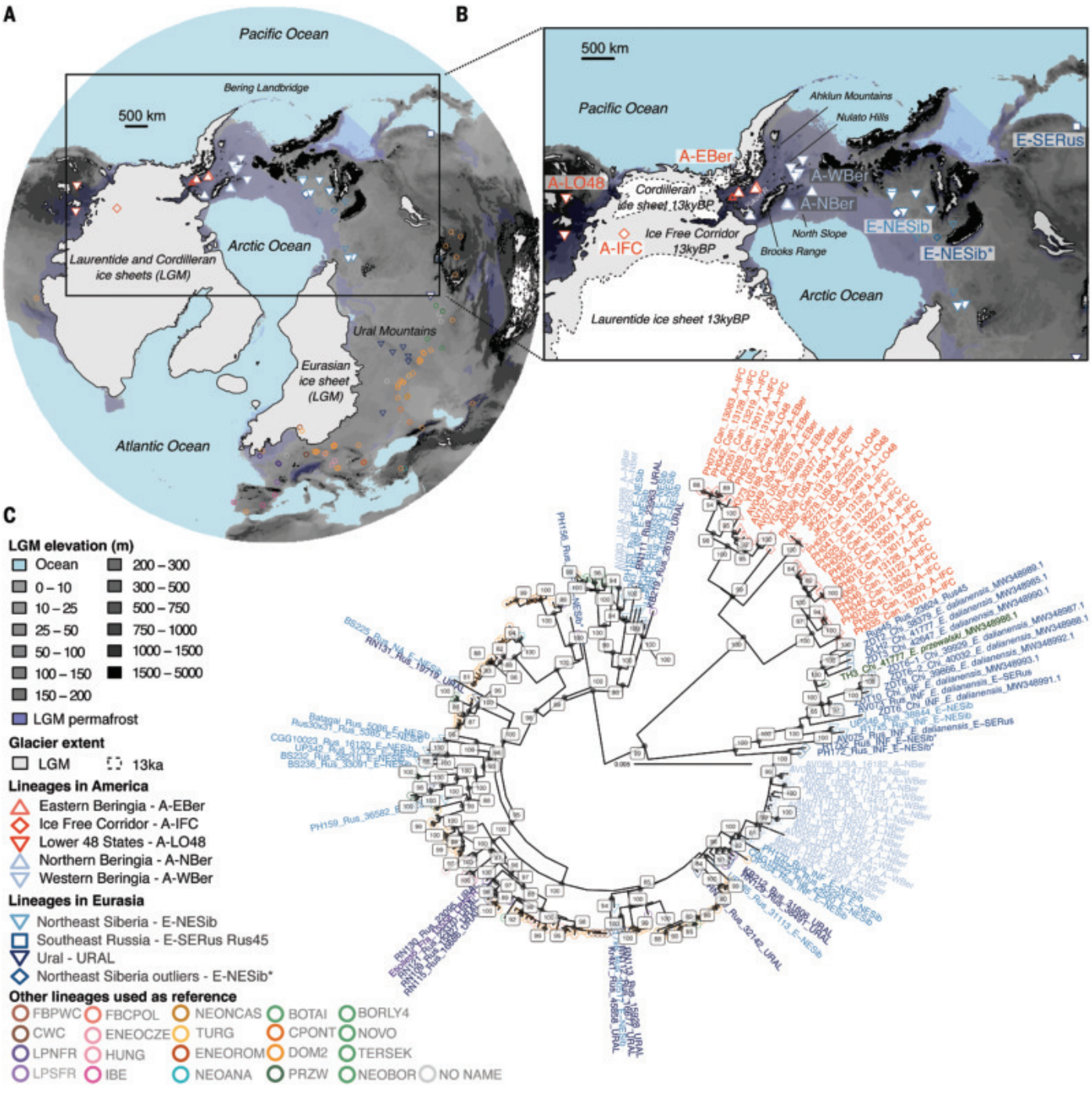

Fig. 1. Samples and mitochondrial phylogeny. (**A**) Sample location, with Last Glacial Maximum (LGM) geographic and climate features. LGM elevation and ocean extent were obtained by adding 130 m to the GEBCO 2014 bathymetric model (v20150318, http://www.gebco.net). LGM ice-sheet extent and permafrost are from Dalton *et al*. (*43*) and Lindgren *et al*. (*50*), respectively. Large, white-filled symbols indicate samples sequenced in this study, whereas small, open symbols indicate samples sequenced in previous studies. The colors of symbols reflect their main clusters of genetic affinities (table S1). (**B**) Inset zoom on Beringia and North America ~13 kyr B.P., showing key geographic features discussed in the main text. (**C**) Maximum likelihood (ML) tree for mitochondrial DNA manually rooted using a donkey outgroup, not shown ($N = 16{,}420$ base pairs, GTR+F+R10). Node supports (percentages) are displayed when greater than 80%, as estimated from 1000 replicates and ultrafast bootstrap approximation.

Graph models could not clearly resolve the history of the ice-free corridor population. AdmixtureBayes indicated early divergence (Fig. 4, A and B), whereas OrientAGraph grouped this population with easternmost East Beringia (Fig. 4C), suggesting that the ice-free corridor was primarily populated from north of the ice sheets. Both models showed significant contributions from deeply divergent groups—south of the continental ice sheets in AdmixtureBayes (5.0%) and easternmost East Beringia and the ice-free corridor in OrientAGraph (5.0% and 20.2%, respectively). This reflects a complex history of isolation and admixture during the earliest evolutionary stages, which remains unresolved without population-scale data from the deeper evolutionary past of America.

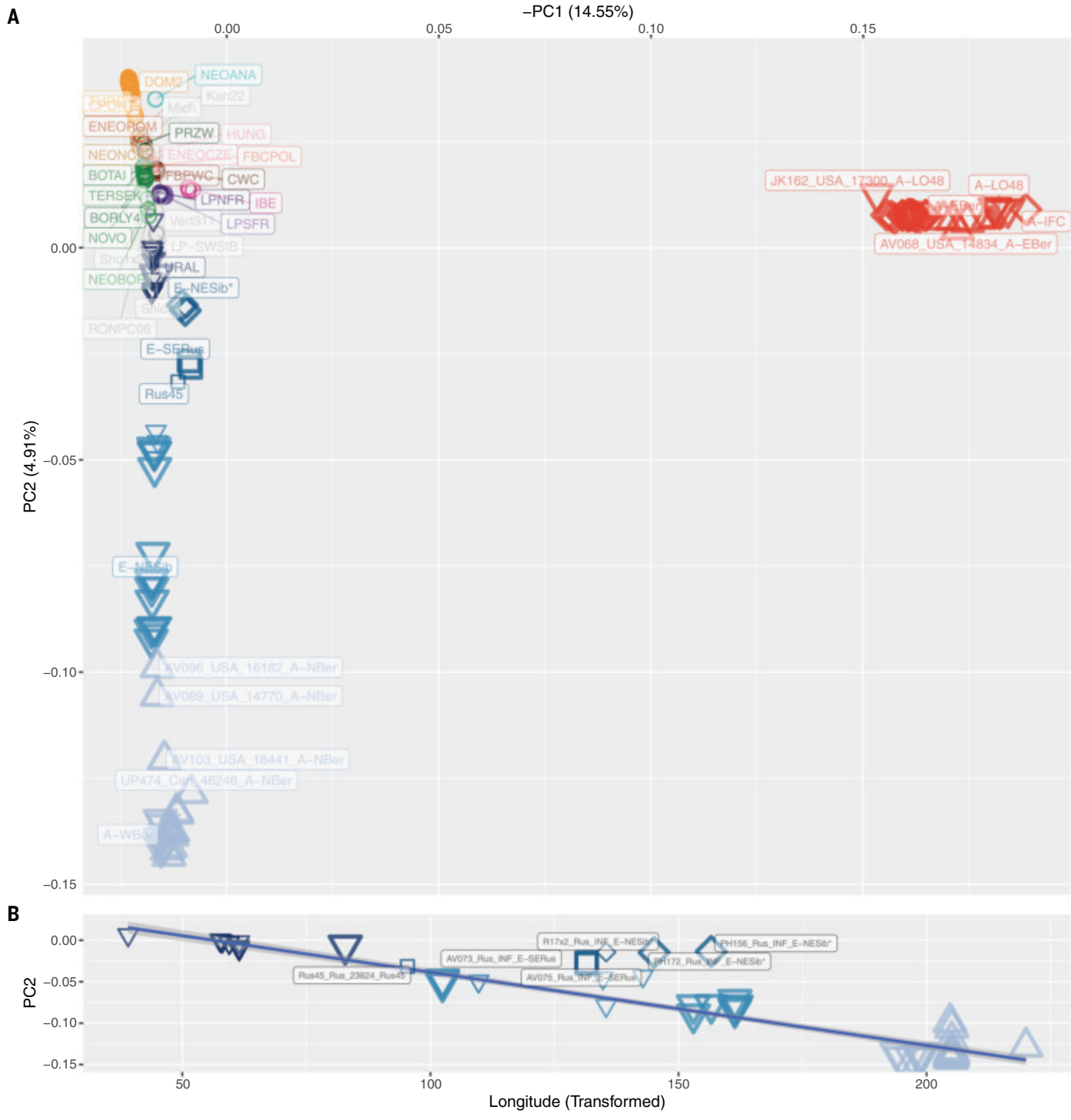

Fig. 2. Population structure. (**A**) PCA with percentages reflecting the variance proportions explained by PC1 and PC2. The AUTOSHRINK mode was applied, and a total of eight samples were projected on the PC space defined by the remaining samples. PC1 is reversed to mirror the geographic position of Eurasia and America in Fig. 1, A and B. Labels indicate the main lineages, except for a few notable samples. Newly sequenced samples are highlighted with larger sizes. (**B**) Linear regression of PC2 against longitude. The fitted Pearson linear regression model is shown with a blue line, with standard errors in gray. The labeled samples, including E-NESib*, E-SERus, and Rus45 individuals, were not included in the model because they are from different genetic backgrounds. Longitude was transformed by adding 360° when inferior to −30° to place the American continent in continuity with Eurasia.

Demographic modeling using GONE (*34*) revealed a brief population bottleneck (2.3-fold) 104 to 91 generations before ~13.1 kyr B.P. (~13,761 to 13,858 yr B.P.), aligning with the ice-free corridor opening (13.8 ± 0.5 kyr B.P.) (*16*) (Fig. 5A). We interpret this as the founder event of the ice-free corridor population, which maintained low effective sizes for 39 generations [91 to 52 generations; effective population size (N_e) = 2607] and collapsed further over 32 generations (52 to 20; N_e = 617) with no subsequent recovery (N_e = 842). These findings suggest that the ice-free corridor could not support substantial population growth at the time.

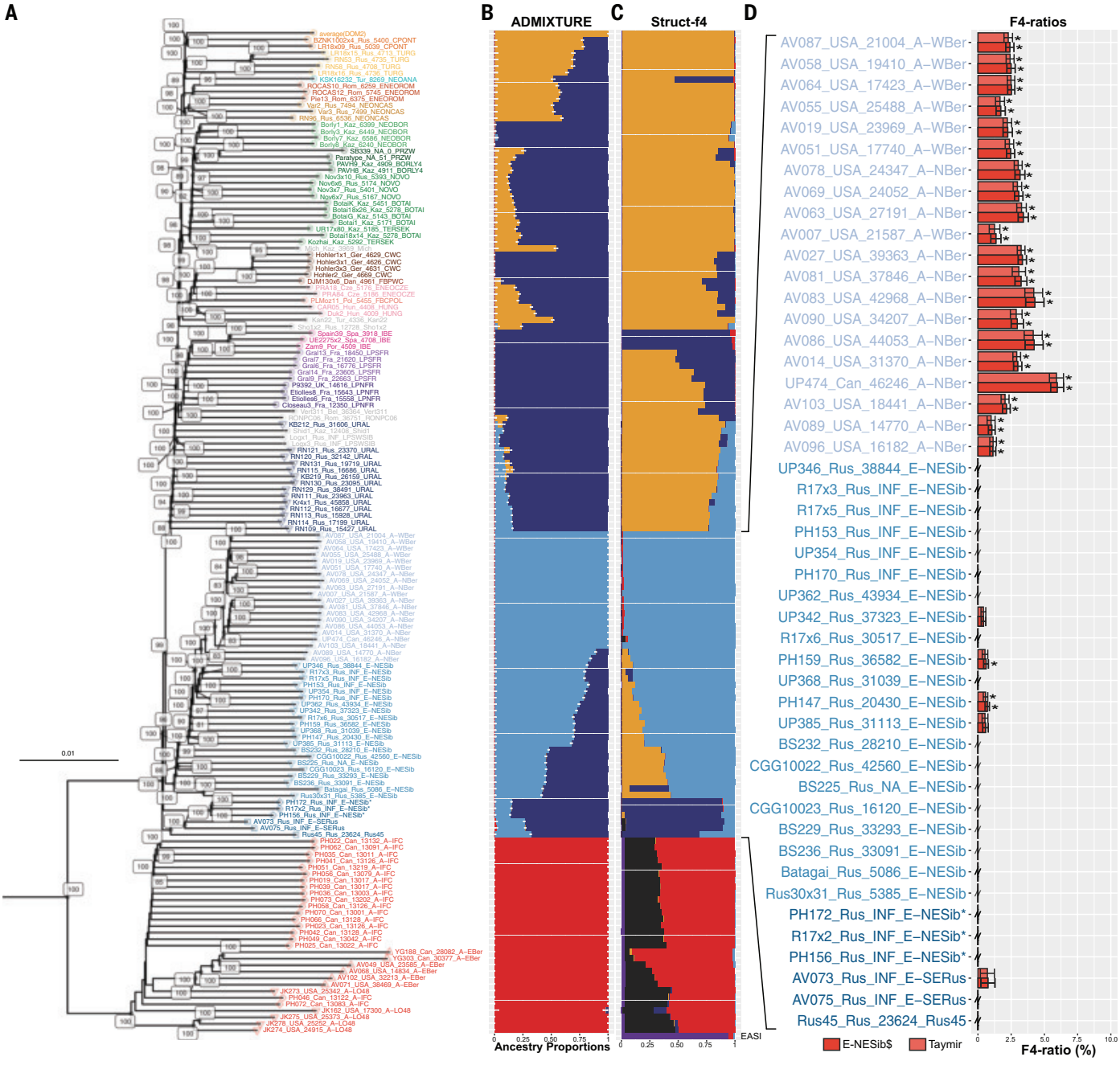

Fig. 3. Autosomal genetic affinities. (**A**) Neighbor-joining phylogeny for 9,386,235 autosomal transversion sites, with node supports estimated from 100 bootstrap pseudoreplicates. The DOM2 clade of modern domestic horses (*25*) shown at the top is collapsed, and the two donkeys used as outgroup are masked for clarity. (**B**) Genetic ancestry profiles from Admixture (*29*) ($K = 4$), with confidence range (white bars) estimated from 100 bootstrap pseudoreplicates. (**C**) Struct-f4 (*31*) profiles ($k = 6$), including EASI outgroup. (**D**) F4 ratio (*30*) estimates of A-EBer genetic ancestry in A-NBer, A-WBer, E-NESib, E-NESib*, E-SERus, and Rus45 horses. Estimates assume populations A-IFC or A-LO48 as the closest to the source of genetic ancestry native from America (A-EBer), and those E-NESib individuals from Taymir, or those devoid of A-EBer genetic ancestry (E-NESib$), as proxies for the northeastern Siberian source.

To explore the interplay between climate, habitat, and demography, we analyzed $\delta^{13}C$ and $\delta^{15}N$ values in megafaunal bone collagen from high latitudes (table S2) as proxies for diet, soil moisture conditions, habitat quality, and food availability (*19*). Ice-free corridor horses had extremely low $\delta^{15}N$ values (Fig. 5B) but $\delta^{13}C$ values typical of those of other Pleistocene horses (fig. S17), which indicates a consistent diet but exceptionally high soil moisture (*19*) associated with permafrost and glacial thaw (*16*). Replacement of cryoxeric steppe-tundra, which is ideal habitat for horses (*35*), by swampy tundra or forests reduced mobility, fragmented habitats, and limited food availability (*19*). Enamel hypoplasias indicate increased systemic stress—possibly nutrition related—at this time in North American horse populations (*36*). Our demographic modeling shows that the reduced carrying capacity of this environment constrained horse expansion in the ice-free corridor (Fig. 5A). A drop in $\delta^{15}N$ values occurred in other grazers between ~15 and 13 kyr B.P. in East Beringia (Fig. 5B) and beyond (fig. S18), a

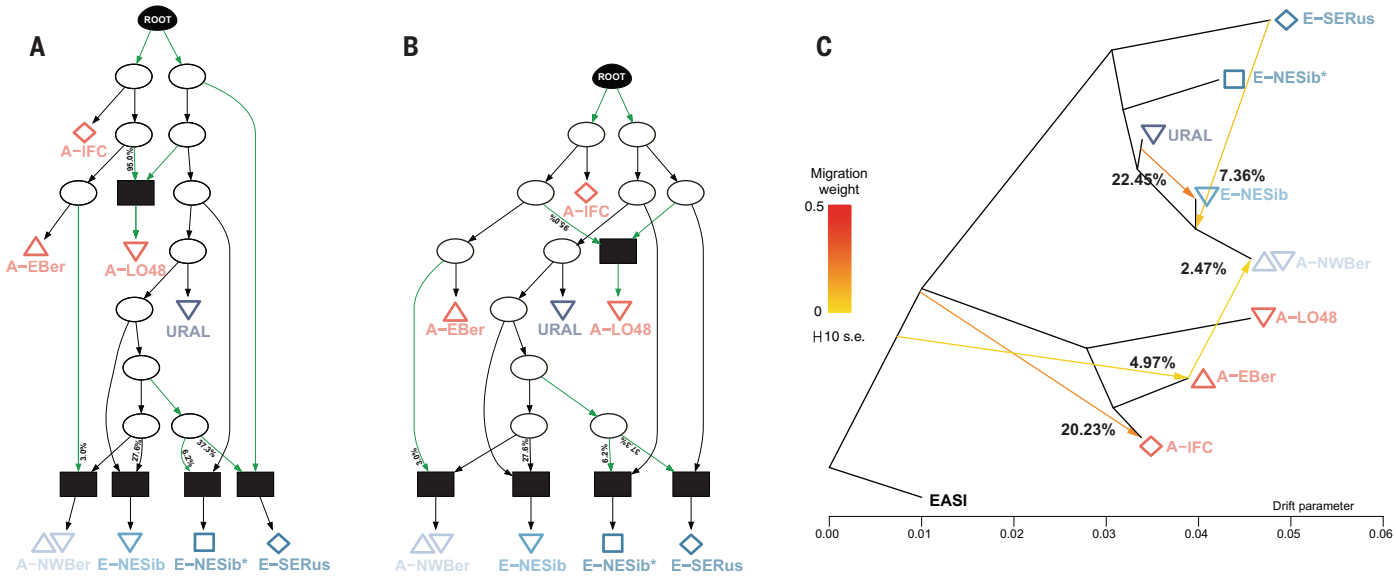

Fig. 4. Population graphs. (**A** and **B**) Two population graphs showing greatest posterior probability (36.7% and 22.6%, respectively) in AdmixtureBayes (*32*). Ancestral and admixture nodes are shown with circles and squares, respectively. Admixture proportions are shown in percentages. Branches substantially drifted are colored in green. The consensus graph and all other graphs accounting for ≥5% of the posterior graph distribution are shown in fig. S15, with drift and admixture estimates. Shapes and colors reflect the main genetic lineages investigated. (**C**) Best-supported graph model from OrientAGraph (*33*), considering $M = 5$ migration edges. Models considering up to five migration edges, and their residuals, are recapitulated in fig. S16.

phenomenon known as the Late Glacial Nitrogen Excursion (*19*). Loss of cryoxeric steppe-tundra because of climate warming and the resulting demographic impacts explain the decline in horse and other megafaunal grazer fossils at the Pleistocene-Holocene transition (*19*).

Discussion

This study extends previous paleogenomic research (*22*, *25*, *37*–*39*) reporting an extensive diversity of late Pleistocene horse lineages that contrasts sharply with horse diversity today. Deeply divergent lineages in Eurasia and North America suggest strong geographic and environmental barriers isolating populations during Pleistocene climate cycles (*40*). Despite this, multiple dispersals between continents occurred during favorable glacial conditions. The genetic cline linking the Eurasian Arctic and Alaska indicates that the cryoxeric steppe-tundra defining the "mammoth steppe" (*41*, *42*) provided a favorable dispersal corridor ranging across the Bering land bridge. However, this transcontinental cline barely extended into America, as northwestern Alaskan populations were predominantly Eurasian genetically (93.7 to 99.5%), whereas northeastern Siberian populations had minimal eastern Beringian ancestry (≤0.8 ± 0.2%). Natural barriers, such as the Ahklun Mountains, Nulato Hills, and Brooks Range, considerably limited, but did not entirely prevent, horse dispersal between ~14.8 and 46.2 kyr B.P. (*43*).

Northeastern Siberian horses from ~5.1 to >48.4 kyr B.P. largely lacked American ancestry, but earlier dispersal(s) from eastern Beringia left lasting genomic footprints in Eurasia, such as in the Russian Far East >50 kyr B.P. (*E. dalianensis*) and Holocene Iberia (Fig. 3C). Struct-f4 and population graph modeling placed these dispersals beyond the limits of radiocarbon dating, aligning with a divergence of at least 285 kyr B.P. between Holocene Iberian and other Eurasian lineages (*38*). Horses near the Ural Mountains strongly influenced the genomic makeup of Eurasian horses: They group basally to most late Pleistocene and Holocene lineages in Anatolia, Central Asia, and Europe (Fig. 3A) and were part of a genetic cline connecting Arctic Eurasia and America. This lineage likely extended farther east than the Urals, as evidenced by the ~45.8–kyr B.P. Kr4x1 specimen from southwestern Siberia near Novosibirsk. Their range likely shifted with time and climate because their genetic sharedness with the ~5.1–kyr B.P. Batagai sample from northeastern Siberia (*39*) was unprecedented in older Siberian specimens (fig. S14).

Further east than Alaska and northwestern Yukon, populations north and south of the continental ice sheets formed distinct genetic subgroups, supporting the role of glacial-interglacial cycles in driving megafauna population dynamics (*20*, *44*). Horses entered the ice-free corridor after the ice sheets retreated but did not expand, likely owing to unfavorable conditions. As permafrost thawed and glaciers retreated ~12 to 15 kyr B.P. (*19*), high soil moisture in deglaciated areas (indicated by $\delta^{15}N$ data) hindered the formation of cryoxeric steppe-tundra crucial for horses. Moist environments replaced the mammoth steppe-tundra with swampy tundra and boreal forest dominated by woody, grazing-resistant plants (*18*, *19*), which in turn resulted in reduced mobility (*45*) and demographic decline (*46*) of large grazers. By contrast, mixed feeders and browsers, such as wapiti and moose, thrived and expanded their ranges (*19*, *47*, *48*). These observations align with the Lakota mitakuye oyasin scientific principle (*1*), which defines a species' habitat by its relationality with other life forms essential for its survival rather than by geography. As climate shifts affect the life forms that each species needs to thrive, their need to exist within their relational habitat serves as the driving force for movement or migration.

Permafrost is projected to largely disappear within a century (*49*), replicating conditions in Alberta ~13 kyr B.P. across much of the Arctic, with severe implications for life. The global loss of the circumpolar permafrost-tundra belt, creating environments less favorable to movement, may also challenge de-extinction prospects for the megafauna grazers that roamed the high latitudes during the late Pleistocene (*8*).

Chief Harold Left Heron, a traditional scientist, Elder, and knowledge keeper for the Lakota Peoples, offers the following perspective: "We understand individual bodies as balanced ecosystems hosting a diversity of life forms, including microbial, all aligned towards health. When survival becomes challenging, life forms whose relationality is being affected utilize ouŋye (most closely translated in English as 'agency') to reach out to other related but different forms

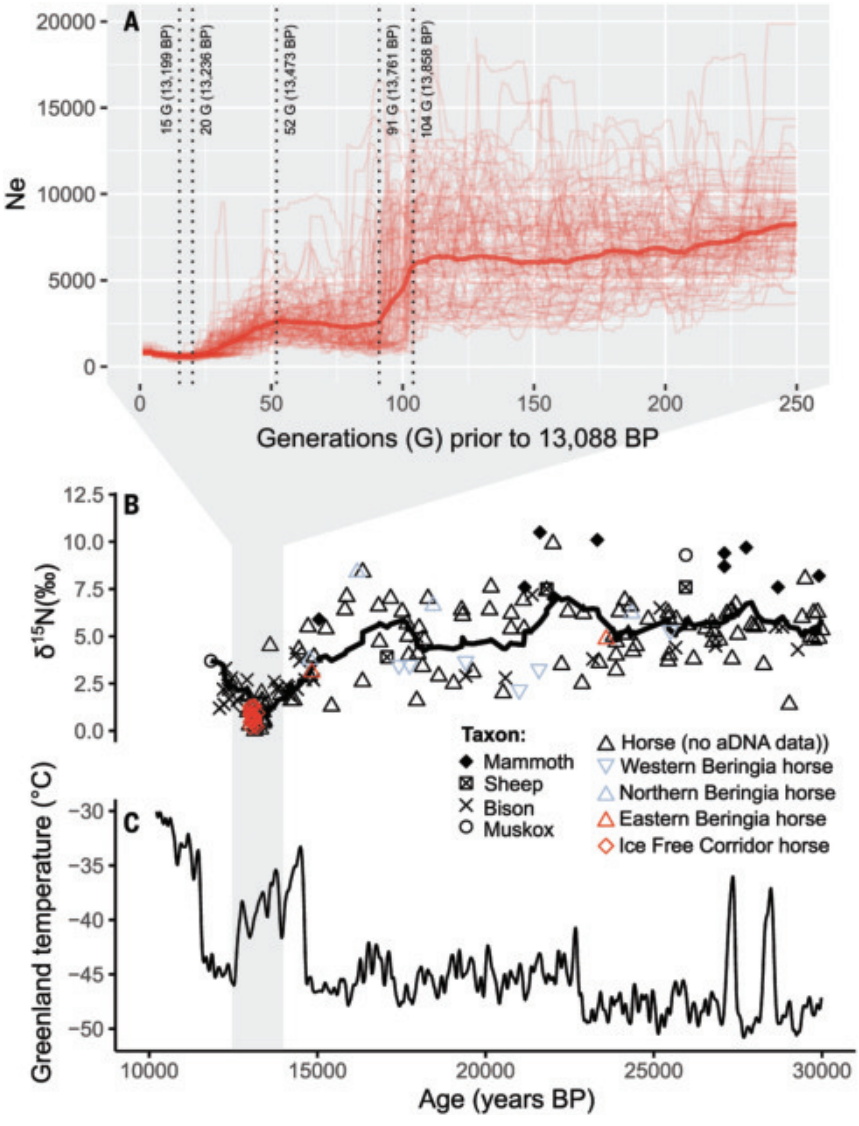

Fig. 5. Demographic and isotopic profiles of the ~13–kyr B.P. A-IFC population from Alberta, Canada. (**A**) GONE (*34*) demographic trajectory, with confidence intervals estimated from 100 bootstrap pseudoreplicates. Dashed vertical lines delineate time periods with changing demographic regimes. Time is shown in numbers of generations ("G") relative to the A-IFC population (bottom *x* axis). An equivalence in calibrated B.P. years is provided between parentheses, considering the average calibrated B.P. radiocarbon date of the specimens (i.e., 13,088 yr B.P.) and the average generation time from (*25*) (i.e., 7.4 years). (**B**) Time series of stable nitrogen isotope values in bone collagen of East Beringia megafauna (table S2) and temperature record for Greenland (*51*). The curves represent the average in sliding windows of 10 samples, with shapes according to common name. Data compiled from the literature or generated in this work are shown with black and colored symbols, respectively. (**C**) Greenland temperature variation between 10 and 30 kyr B.P. [data from (*51*)]. aDNA, ancient DNA.

of life to preserve sustainability. Joining improves their ability not just to survive, but to thrive. This process is called yutaŋ'kil and it combines and diversifies life genetically to ensure an ebb and flow by adjusting and responding to changing conditions. As Lakota, we acknowledge this with each breath." He further explains that respecting the inherent need for life forms to freely move within their optimal relational home provides the ideal conditions for sustainability. Therefore, attempts to preserve megafauna species as they were genetically at one specific point in time disregards this complex diversity of alliances with other life forms and is unlikely to strengthen sustainability. Conversely, ensuring the movement of life through physical corridors connecting a diversity of habitats allows life to adapt and survive in changing environmental conditions.

Wilson Justin is an Upper Ahtna/Upper Tanana Dene' (Athabascan) Elder and knowledge keeper of the Alth'setnay clan, born at Nabesna, Alaska. Addressing the movement inherent in all life and the scope of his People's world, he recalls a well-traveled, physical pathway referred to as the "Medicine Man Trail," which ensured diversity and sustainability for many thousands of years. The Trail reaches from Alaska, across Siberia into Mongolia, but also through Canada, across Lakota territory, and into Maya territory, branching off throughout. "Traveling the trail as far as the horizon could be seen introduced us to a diversity of life forms in constant motion. We learned the way natural systems work and how all life is interconnected and interdependent. This knowledge is held in our songs, stories and in the sciences and life ways we carry. Whether human, horse or the microbial life that moves with them, singing the song of life is a gift that ensures sustainability."

Jane Stelkia is an Elder for the sqilxʷ/suknaqin or Okanagan Nation, which is based on her People's traditional lands in Canada. As a native Nsyilxcen speaker and a keeper of traditional science surrounding Snklc'askaxa, the Horse Nation, she confirms her People's experience with the "Medicine Man Trail" and adds: "Snklc'askaxa serve as balancers in the ecosystem, and when we Indians are in the mountains on Snklc'askaxa, we connect with the water, the rain, the trees, the flowers blooming. Together we experience all of life. Today, we live in a world where the boundaries and obstacles created by mankind do not serve the majority of life. In this study, Snklc'askaxa is offering us medicine by reminding us of the path all life takes together to survive and thrive. It is time that humans help life find the openings and points to cross and move safely."

The ability for life forms to migrate as relationality around them changes is key for long-term survival. Genetic change as a result of yutaŋ'kil should not be feared or artificially blocked but respected as proof of life's strength and resilience. Our ability and willingness to support this process determines our sustainable future.

REFERENCES AND NOTES

1. M. Hunska Tašunke Icu *et al.*, "Standing for *Unči Maka* (Grandmother Earth) and All Life: An Introduction to Lakota Traditional Sciences, Principles and Protocols and the Birth of a New Era of Scientific Collaboration" (Maxwell Museum Technical Series, no. 42, 2023).
2. W. A. Oquilluk, L. L. Bland, *People of Kauwerak: Legends of the Northern Eskimo* (AMU Press, 1973).
3. F. A. Smith *et al.*, *Proc. Natl. Acad. Sci. U.S.A.* **119**, e2115015119 (2022).
4. Y. Malhi *et al.*, *Proc. Natl. Acad. Sci. U.S.A.* **113**, 838–846 (2016).
5. E. J. Lundgren *et al.*, *Science* **383**, 531–537 (2024).
6. P. Jaureguiberry *et al.*, *Sci. Adv.* **8**, eabm9982 (2022).
7. J. Huang *et al.*, *Nat. Clim. Chang.* **7**, 875–879 (2017).
8. M. Macias-Fauria, P. Jepson, N. Zimov, Y. Malhi, *Phil. Trans. R. Soc. B* **375**, 20190122 (2020).
9. W. J. Ripple *et al.*, *Bioscience* **67**, 197–200 (2017).
10. R. E. Morlan, J. Cinq-Mars, in *Paleoecology of Beringia*, D. M. Hopkins, J. V. Matthews, C. E. Schweger, S. B. Young, Eds. (Academic Press, 1982), pp. 353–381.
11. E. Y. Pavlova, V. V. Pitulko, *Quat. Int.* **549**, 5–25 (2020).
12. J. A. Swift *et al.*, *Bioscience* **69**, 877–887 (2019).

13. D. H. Mann *et al.*, *Proc. Natl. Acad. Sci. U.S.A.* **112**, 14301–14306 (2015).
14. M. Stewart, W. C. Carleton, H. S. Groucutt, *Nat. Commun.* **12**, 965 (2021).
15. E. J. Gowan *et al.*, *Nat. Commun.* **12**, 1199 (2021).
16. C. D. Clark *et al.*, *Boreas* **51**, 699–758 (2022).
17. J. R. Farmer *et al.*, *Proc. Natl. Acad. Sci. U.S.A.* **120**, e2206742119 (2023).
18. J. W. Williams, B. N. Shuman, T. Webb III, P. J. Bartlein, P. L. Leduc, *Ecol. Monogr.* **74**, 309–334 (2004).
19. M. T. Rabanus-Wallace *et al.*, *Nat. Ecol. Evol.* **1**, 0125 (2017).
20. E. D. Lorenzen *et al.*, *Nature* **479**, 359–364 (2011).
21. P. D. Heintzman *et al.*, *eLife* **6**, e29944 (2017).
22. A. O. Vershinina *et al.*, *Mol. Ecol.* **30**, 6144–6161 (2021).
23. C. R. Harington, *Quat. Sci. Rev.* **30**, 2341–2354 (2011).
24. L. Orlando, *Annu. Rev. Genet.* **54**, 563–581 (2020).
25. P. Librado *et al.*, *Nature* **631**, 819–825 (2024).
26. W. T. T. Taylor *et al.*, *Science* **379**, 1316–1323 (2023).
27. J. Yuan *et al.*, *Quat. Sci. Rev.* **250**, 106691 (2020).
28. B. J. MacFadden, O. Carranza-Castañeda, *Bull. Fla. Mus. Nat. Hist.* **43**, 163–185 (2002).
29. D. H. Alexander, J. Novembre, K. Lange, *Genome Res.* **19**, 1655–1664 (2009).
30. N. Patterson *et al.*, *Genetics* **192**, 1065–1093 (2012).
31. P. Librado, L. Orlando, *Bioinformatics* **38**, 2070–2071 (2022).
32. S. V. Nielsen *et al.*, *PLOS Genet.* **19**, e1010410 (2023).
33. E. K. Molloy, A. Durvasula, S. Sankararaman, *Bioinformatics* **37**, i142–i150 (2021).
34. E. Santiago *et al.*, *Mol. Biol. Evol.* **37**, 3642–3653 (2020).
35. G. M. MacDonald, T. K. McLeod, *Quat. Int.* **32**, 87–95 (1996).
36. C. I. Barrón-Ortiz, C. N. Jass, R. Barrón-Corvera, J. Austen, J. M. Theodor, *Paleobiology* **45**, 484–515 (2019).
37. M. Schubert *et al.*, *Proc. Natl. Acad. Sci. U.S.A.* **111**, E5661–E5669 (2014).
38. A. Fages *et al.*, *Cell* **177**, 1419–1435.e31 (2019).
39. P. Librado *et al.*, *Proc. Natl. Acad. Sci. U.S.A.* **112**, E6889–E6897 (2015).
40. D. Froese *et al.*, *Proc. Natl. Acad. Sci. U.S.A.* **114**, 3457–3462 (2017).
41. R. D. Guthrie, *Frozen Fauna of the Mammoth Steppe: The Story of Blue Babe* (Univ. Chicago Press, 1990).
42. S. A. Zimov, N. S. Zimov, A. N. Tikhonov, F. S. Chapin III, *Quat. Sci. Rev.* **57**, 26–45 (2012).
43. A. S. Dalton *et al.*, *Quat. Sci. Rev.* **321**, 108345 (2023).
44. P. F. Campos *et al.*, *Proc. Natl. Acad. Sci. U.S.A.* **107**, 5675–5680 (2010).
45. A. G. Rowe *et al.*, *Sci. Adv.* **10**, eadk0818 (2024).
46. A. D. Barnosky, P. L. Koch, R. S. Feranec, S. L. Wing, A. B. Shabel, *Science* **306**, 70–75 (2004).
47. M. Meiri *et al.*, *Proc. R. Soc. B* **281**, 20132167 (2014).
48. M. Meiri, A. Lister, P. Kosintsev, G. Zazula, I. Barnes, *J. Biogeogr.* **47**, 2223–2234 (2020).
49. D. Guo *et al.*, *Proc. Natl. Acad. Sci. U.S.A.* **120**, e2301954120 (2023).
50. A. Lindgren, G. Hugelius, P. Kuhry, T. R. Christensen, J. Vandenberghe, *Permafrost Periglac. Process.* **27**, 6–16 (2016).
51. P. Kindler *et al.*, *Clim. Past* **10**, 887–902 (2014).
52. C. Bataille, L. Orlando, Following Late Pleistocene horse migration toward our sustainable future, Open Science Framework (2025). https://doi.org/10.17605/OSF.IO/Z2XT4

ACKNOWLEDGMENTS

We thank the Vuntut Gwitchin and Tr'ondëk Hwëch'in for enabling research on Yukon fossils collected from within their Traditional Territories. This research and all Indigenous scientific contributions were conducted under the formal Indigenous Review Board (IRB) process put in place by Oglala Lakota Elder traditional government representatives on the Board of Taku Skan Skan Wasakliyapi: Global Institute for Traditional Sciences (GIFTS), joined by their counterparts in the Iñupiaq, Dene' (Athabascan), Blackfoot, and sqilx^{w}/suknaqin or Okanagan Nation. Wopila Tanka to Sam High Crane (Wapageya Mani) for his vision and leadership and to Šungwakaŋ, the Horse Nation, for their collaboration and for continuing to show us the way. **Funding:** Y.R.H.C. was supported by the European Union's Horizon 2020 research and innovation program under the Marie Skłodowska-Curie (grant agreement890702-MethylRIDE). C.P.B. was supported by the NSERC Discovery Grant RGPIN-2019-05709, the New Frontiers in Research Fund Exploration NFRFE-2023-00365, and by the Visiting Professor scholarship 2023 at Université Paul Sabatier (Université de Toulouse). A.H. was supported by UKRI MSCA guarantee fund (PleistoDem, EP/X023249/1). J.H.M. was supported by National Science Foundation (NSF) grant DEB-2135479. This work was supported by France Génomique National infrastructure, funded as part of the "Investissement d'avenir" program managed by Agence Nationale pour la Recherche (ANR-10-INBS-09); the France Génomique Appel à Grand Projet (ANR-10-INBS-09-08, BUCEPHALE and MARENGO projects); the CNRS International Research Project AnimalFarm; the TIRIS "Scaling-Up Science Program" BasicExtinct from the Université de Toulouse; and ERC under the European Union's Horizon 2020 research and innovation program (grant agreements 681605-PEGASUS and 101071707-HorsePower). **Author contributions:** Bioinformatics: L.O., with input from Y.R.H.C.; Databasing: C.P.B., Z.L., D.F., E.L., P.D., C.N.J., C.I.B.-O., D.M., M.W., J.H.M., G.Z.; First Nations protocols: Y.R.H.C., Chief J.A.H., Chief H.L.H.; Funding acquisition: Y.R.H.C., C.P.B., A.H., J.H.M., B.S., L.O.; Material, reagents, and infrastructure: C.P.B., B.C., A.P., P.H.O., J.-M.A., P.W., I.V.K., S.K.V., M.A.K., A.S.G., A.A.T., I.B., P.D., C.N.J., R.D.E.M., P.G., D.M., D.G.F., G.Z., B.S., L.O.; Molecular investigations: Y.R.H.C., S.H., J.D.K., L.C., G.T., L.T.-C., S.S., A.S.-O., M.A.K., with input from L.O.; Radiocarbon dating: J.S.; Study coordination: Y.R.H.C., L.O.; Study design: Y.R.H.C., C.P.B., Chief J.A.H., B.S., L.O.; Supervision: Y.R.H.C., C.P.B., B.S., L.O.; Visualization: Y.R.H.C., C.P.B., L.O.; Writing – original draft: Y.R.H.C., C.P.B., L.O.; Writing – review & editing: all coauthors. **Diversity, equity, ethics, and inclusion:** In part, this study was designed to communicate knowledge that is part of the Indigenous scientific base regarding how to sustain life. Anything not expressly published is being kept under the guardianship of traditional knowledge protocols consistent with those of the Indigenous coauthors. The traditional IRB process that enabled this study served as an umbrella for all aspects of research. Although the Lakota initiated this project, they did so after consultation with Indigenous leaders, knowledge keepers, and scholars from other Nations whose traditional lands were the source of many of the life samples analyzed. The participants from other Indigenous Nations expressly requested coverage under this IRB owing to its comprehensive approach. Under this Lakota-designed IRB process, the outcome of this research could not have been published if the process undertaken had not met all Indigenous scientific protocols at issue. The leading author of this study joined the genomics team at CAGT (France), expressly at the request of Lakota community leaders to conduct this research in collaboration and to aid in establishing new protocols for future cross-cultural scientific collaborations involving Indigenous Peoples, the life forms they protect, and traditional knowledge and sciences. The IRB leadership became coauthors to express their level of responsibility, contribution, and engagement at each stage of the process. Extensive travel between France and Lakota territory occurred for in-person meetings and cross-cultural exchange. This included laboratory facility visits, discussion and interpretation of results, and ceremonial participation. Each of these leaders represented community members and groups with specific interest in the research outcomes. As is aligned with Lakota protocols, representatives from the Indigenous Nations whose territories are covered in this research were consulted and invited to join this study. In-person meetings with these knowledge keepers and scientists took place in their respective territories, and their scientific contributions were included in a manner aligned with their protocols. **Competing interests:** B.S. is the chief science officer at Colossal Biosciences, a company working on de-extinction. The authors declare no other competing interests. **Data and materials availability:** In agreement to all stakeholders of this study, the sequence data generated are available for download at the European Nucleotide Archive (accession no. PRJEB74327). The radiocarbon dates and isotopic data generated in this study are provided in table S1, with reference to their official experimental code. The compiled database of radiocarbon dates and isotopic data is provided in table S2 and is available on the Open Science Framework (*52*) together with the matrix of autosomal transversion variation, mitochondrial, and Y chromosomal sequence alignments. **License information:** Copyright © 2025 the authors, some rights reserved; exclusive licensee American Association for the Advancement of Science. No claim to original US government works. https://www.science.org/about/science-licenses-journal-article-reuse. This research was funded in whole or in part by UKRI (MSCA guarantee fund PleistoDem, EP/X023249/1) and ANR (ANR-10-INBS-09), cOAlition S organizations. The author will make the Author Accepted Manuscript (AAM) version available under a CC BY public copyright license.

SUPPLEMENTARY MATERIALS

science.org/doi/10.1126/science.adr2355
Materials and Methods; Figs. S1 to S18; Tables S1 and S2; References (*53*–*83*); MDAR Reproducibility Checklist

Submitted 21 June 2024; accepted 19 March 2025

10.1126/science.adr2355

ORGANOIDS

Diverse bat organoids provide pathophysiological models for zoonotic viruses

Hyunjoon Kim[1]†, Seo-Young Heo[1,2]†, Young-Il Kim[1]†, Dongbin Park[1], Monford Paul Abishek N[1], Suhee Hwang[1,2], Yong-ki Lee[1], Hobin Jang[1], Jae-Woo Ahn[1], Jeongmin Ha[3], Sujin Park[3], Ho Young Ji[1,2], Semi Kim[1], Isaac Choi[1], Woohyun Kwon[4], Jaemoo Kim[1], Kanghee Kim[4], Juryeon Gil[4], Boyeong Jeong[4], Josea Carmel D. Lazarte[4], Rare Rollon[4], Jeong Ho Choi[4], Eun Ha Kim[1], Seung-Gyu Jang[4], Hye Kwon Kim[5], Bo-Young Jeon[6], Ghazi Kayali[7], Richard J. Webby[8], Bon-Kyoung Koo[3,9,10]*, Young Ki Choi[1,2,4]

Bats are important reservoirs of zoonotic pathogens, but suitable model systems for comprehensively exploring host-pathogen interactions and assessing spillover risks remain limited. To address this gap, we developed a collection of bat organoid models spanning five species and four organ types. This multispecies, multiorgan organoid panel showed species- and tissue-specific replication patterns for several viruses, offering robust pathophysiological models for studying respiratory, renal, and enteric zoonotic viruses. Using this platform, we successfully isolated and characterized bat-borne mammalian orthoreoviruses and paramyxoviruses, demonstrating the utility of these organoid panels for virome surveillance. Furthermore, we successfully tested known antiviral drugs for their efficacy against bat virus isolates.

The World Health Organization defines zoonosis as any disease or infection naturally transmissible from vertebrates to humans (*1*). Historically, many pandemics, such as the Black Death, Spanish Flu, Hong Kong Flu, and COVID-19, originated from zoonotic pathogens (*2*). It is estimated that approximately 75% of new or emerging infectious diseases in humans are zoonotic in origin (*3*).

Bats appear to be important mammalian reservoirs for several zoonotic viruses, including the coronaviruses responsible for SARS, MERS, and COVID-19, as well as henipaviruses, lyssaviruses, and filoviruses (*4*–*6*). Transmission of these pathogens often involves intermediate hosts, which help to bridge the ecological and molecular gaps between bats and humans (*4*, *7*). With ongoing climate change and human encroachment into wildlife habitats, natural ecological barriers separating bats and humans are diminishing, increasing the risk of virus spillover (*7*, *8*).

Despite the clear threat posed by bat-borne viruses, current physiological models to study these pathogens are limited. Most bat viruses identified through metagenomic studies have not been isolated (*4*), primarily because of a lack of suitable bat model systems to culture these viruses. Most existing organoid models representing bat airway (*9*–*11*) and gastrointestinal epithelia (*11*–*14*) have been obtained from tropical fruit bats (*9*–*12*, *14*). These regional and species particularities limit their applicability for global zoonotic research.

To address this gap, we have established multispecies, multiorgan epithelial organoids from four East Asian insectivorous bat species within the Vespertilionidae (*15*), and one species in the Rhinolophidae. The latter have previously been used for establishing intestinal organoids (*13*). Our organoid collection, representing trachea, lung, kidney, and small intestine, offers access for experimental investigation of physiological features of bat epithelial tissues but can also serve as a platform for virome surveillance and pathogen isolation, as well as drug testing.

Results

Establishment of multiple species and tissue types of bat organoids

Previous organoid models for bats have mostly used tissues from tropical frugivorous bats in the Phyllostomidae (e.g., *Carollia perspicillata* and *Artibeus jamaicensis*) (*9*, *14*) and Pteropodidae (e.g., *Eonycteris spelaea*, *Rousettus leschenaultii*, and *Rousettus aegyptiacus*) (*10*–*12*) families, with one example from an insectivorous bat from the Rhinolophidae family (*Rhinolophus sinicus*) (*13*) (fig. S1, A and B, and table S1). We established organoids from multiple East Asian insectivorous bats in the Vespertilionidae and Rhinolophidae families. The Vespertilionidae family, comprising 531 species across 54 genera, is noted for its diversity and wide distribution, while the Rhinolophidae family includes 112 species of *Rhinolophus* (horseshoe bats), found across Asia, Europe, and Africa (fig. S1C) (*15*, *16*).

We collected wild-caught bats, obtained tissue samples, and authenticated species of *Rhinolophus ferrumequinum*, *Myotis aurascens*, *Pipistrellus abramus*, *Eptesicus serotinus* and *Hypsugo alaschanicus* using the cytochrome b gene (fig. S1D). These species have broader geographic distributions than those used in previous organoid studies (fig. S1, B and E, and table S1) (*9*–*14*). We used established methods to generate organoids (*9*–*11*, *17*–*20*) and succeeded in maintaining organoids and primary cells for at least six months in vitro (Fig. 1A, figs. S1F and S2, A and B, and table S2). There were no species-specific differences in the culture conditions required, except for small intestinal organoids of *M. aurascens*, which required commercial human IntestiCult™ Organoid Growth Medium (STEMCELL Technologies) instead of WENRnic Medium (Egf, Noggin, R-spondin1, Wnt surrogate-Fc fusion protein, and nicotinamide) (table S3; see also materials and methods for details).

Metagenomic studies have identified many bat viruses with zoonotic potential (table S4), yet the isolation and characterization of these viruses has been limited by a lack of bat models (*4*). The bat species used in previous organoid studies (*9*–*14*) and in our current study are known to host viruses from multiple families including the *Coronaviridae*, *Paramyxoviridae*, and *Reoviridae* (fig. S1, G and H).

Characterization of cellular diversity and epithelial tissue composition of organoids

In respiratory tissues, the mucociliary epithelium forms a physical barrier against pathogens while the alveolar epithelium facilitates gas exchange in the lungs (*21*). To evaluate how accurately our respiratory bat organoids recapitulated this complex composition, we conducted multiplexed immunohistochemistry on tracheal organoids using markers for ciliated cells [acetylated tubulin (Ac-Tub)] (*22*), goblet cells (MUC5AC) (*22*, *23*), basal stem cells (KRT5) (*24*), and epithelial cell junctional integrity (β-Catenin) (*25*) (Fig. 1, B and C, and figs. S3 and S4A). We obtained different numbers of organoid types (i.e., ciliated cell–rich or basal cell–rich) from different bat species (Fig. 1C, fig. S4, A and B, and table S5), but the overall epithelial composition was well-preserved (fig. S4A). Single-cell RNA sequencing (scRNA-seq) of *R. ferrumequinum* and *E. serotinus* tracheal organoids confirmed cellular

[1]Center for Study of Emerging and Re-emerging Viruses, Korea Virus Research Institute, Institute for Basic Science, Daejeon, Republic of Korea. [2]Department of Metabiohealth, Sungkyun Convergence Institute, Sungkyunkwan University (SKKU), Suwon, Republic of Korea. [3]Center for Genome Engineering, Institute for Basic Science, Daejeon, Republic of Korea. [4]College of Medicine and Medical Research Institute, Chungbuk National University, Cheongju, Republic of Korea. [5]Department of Biological Sciences and Biotechnology, College of Natural Science, Chungbuk National University, Cheongju, Republic of Korea. [6]Department of Biomedical Laboratory Science, College of Software and Digital Healthcare Convergence, Yonsei University, Wonju, Republic of Korea. [7]Human Link, Dubai, United Arab Emirates. [8]Department of Infectious Diseases, St. Jude Children's Research Hospital, Memphis, TN, USA. [9]Graduate School of Stem Cell and Regenerative Biology, KAIST, Daejeon, Republic of Korea. [10]Department of Life Sciences, Pohang University of Science and Technology (POSTECH), Pohang, Republic of Korea. ***Corresponding author. Email: koobk@ibs.re.kr (B.-K.K.); choiki55@ibs.re.kr (Y.K.C.)** †These authors contributed equally to this work.

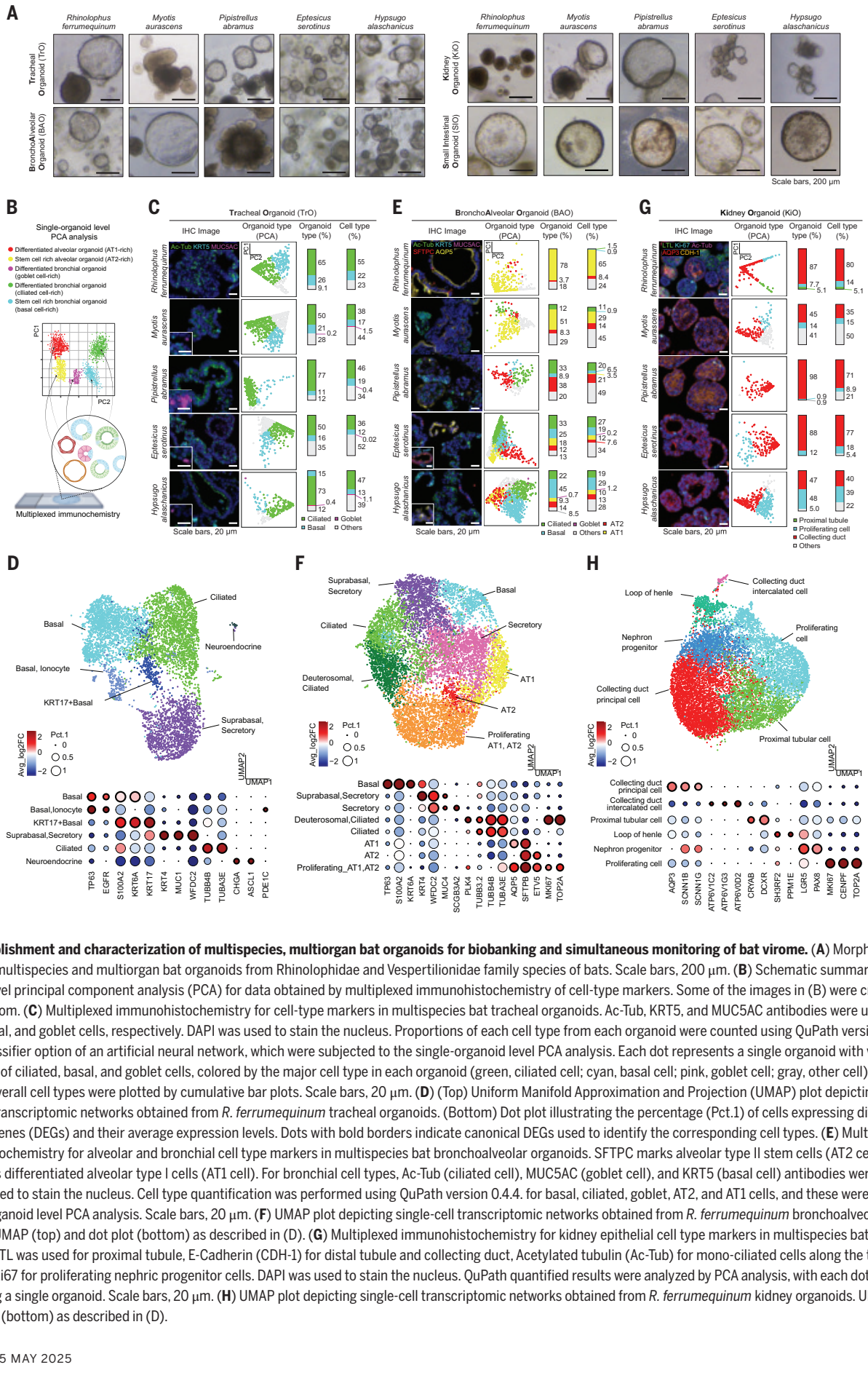

Fig. 1. Establishment and characterization of multispecies, multiorgan bat organoids for biobanking and simultaneous monitoring of bat virome. (**A**) Morphological features of multispecies and multiorgan bat organoids from Rhinolophidae and Vespertilionidae family species of bats. Scale bars, 200 μm. (**B**) Schematic summary of organoid-level principal component analysis (PCA) for data obtained by multiplexed immunohistochemistry of cell-type markers. Some of the images in (B) were created with BioRender.com. (**C**) Multiplexed immunohistochemistry for cell-type markers in multispecies bat tracheal organoids. Ac-Tub, KRT5, and MUC5AC antibodies were used to stain ciliated, basal, and goblet cells, respectively. DAPI was used to stain the nucleus. Proportions of each cell type from each organoid were counted using QuPath version 0.4.4. with the classifier option of an artificial neural network, which were subjected to the single-organoid level PCA analysis. Each dot represents a single organoid with varying proportions of ciliated, basal, and goblet cells, colored by the major cell type in each organoid (green, ciliated cell; cyan, basal cell; pink, goblet cell; gray, other cell). Organoid types and overall cell types were plotted by cumulative bar plots. Scale bars, 20 μm. (**D**) (Top) Uniform Manifold Approximation and Projection (UMAP) plot depicting single-cell transcriptomic networks obtained from *R. ferrumequinum* tracheal organoids. (Bottom) Dot plot illustrating the percentage (Pct.1) of cells expressing differentially expressed genes (DEGs) and their average expression levels. Dots with bold borders indicate canonical DEGs used to identify the corresponding cell types. (**E**) Multiplexed immunohistochemistry for alveolar and bronchial cell type markers in multispecies bat bronchoalveolar organoids. SFTPC marks alveolar type II stem cells (AT2 cell) whereas AQP5 marks differentiated alveolar type I cells (AT1 cell). For bronchial cell types, Ac-Tub (ciliated cell), MUC5AC (goblet cell), and KRT5 (basal cell) antibodies were used. DAPI was used to stain the nucleus. Cell type quantification was performed using QuPath version 0.4.4. for basal, ciliated, goblet, AT2, and AT1 cells, and these were subjected to single-organoid level PCA analysis. Scale bars, 20 μm. (**F**) UMAP plot depicting single-cell transcriptomic networks obtained from *R. ferrumequinum* bronchoalveolar organoids. UMAP (top) and dot plot (bottom) as described in (D). (**G**) Multiplexed immunohistochemistry for kidney epithelial cell type markers in multispecies bat kidney organoids. LTL was used for proximal tubule, E-Cadherin (CDH-1) for distal tubule and collecting duct, Acetylated tubulin (Ac-Tub) for mono-ciliated cells along the tubules and ducts, and Ki67 for proliferating nephric progenitor cells. DAPI was used to stain the nucleus. QuPath quantified results were analyzed by PCA analysis, with each dot representing a single organoid. Scale bars, 20 μm. (**H**) UMAP plot depicting single-cell transcriptomic networks obtained from *R. ferrumequinum* kidney organoids. UMAP (top) and dot plot (bottom) as described in (D).

diversity (Fig. 1D and fig. S5, A and B), which was confirmed by single-organoid immunohistochemical analysis (Fig. 1C) and cell type characterization by transmission electron microscopy (TEM) (fig. S4C). Notably, MUC5AC+ goblet cells were scarce, as measured from the immunohistochemical analysis, in all our tracheal organoids (Fig. 1C and fig. S4, A to E), consistent with observations in the native tracheal epithelia of intact bats (fig. S3) and with other bat organoids from previous studies (*9*, *11*).

We also looked for markers in the bronchoalveolar organoids for bronchial [ciliated (Ac-Tub), goblet (MUC5AC), and basal cells (KRT5)] (*21*), as well as alveolar epithelia type II (SFTPC) and type I cells (AQP5) (*26*). These organoids display a diverse mix of bronchial and alveolar epithelia, reflecting the complex cellular architecture of the distal lung (*21*) (Fig. 1, B and E, figs. S6 and S7, and table S5). The scRNA-seq of *R. ferrumequinum* bronchoalveolar organoids gave similar results (Fig. 1F).

In renal organoids, we observed the presence of key cellular markers indicative of various nephron segments using Ac-Tub for monociliated cells along the tubular and ductal epithelia, LTL for proximal tubule, CDH-1 for distal tubule and collecting duct, AQP3 for collecting duct, and K_i-67 for proliferating nephric progenitor cells (figs. S8 and S9). The kidney organoids expressed these markers in varying proportions (Fig. 1, B and G, fig. S9, and table S5), which were further verified in *R. ferrumequinum* kidney organoids by scRNA-seq (Fig. 1H) and showed that the intricate composition of the renal epithelium could be replicated in the organoids.

We also confirmed the presence of markers for small intestinal epithelia [enterocytes (Villin), goblet (MUC2), enteroendocrine (Chga), and proliferating cells (K_i-67)] in organoids and native bat tissue counterparts (figs. S10 and S11A). Notably, small intestinal organoids of *P. abramus* displayed more proliferative (Ki67+) but less differentiated cells (fig. S11A). These results were further complemented and confirmed by TEM analysis (fig. S11B). Overall, our multispecies, multiorgan organoid collection, representing four tissue types across five bat species, recapitulated native bat epithelial tissues and showed species- and tissue-specific variations in cell proliferation and differentiation (fig. S12).

Differential susceptibilities of respiratory organoids to SARS-CoV-2 and MERS-CoV

We exposed bat respiratory organoids to the pathogenic human coronaviruses SARS-CoV-2 and MERS-CoV to investigate species specificity for these viruses among the Rhinolophidae and Vespertilionidae families (fig. S13A) (*27*–*30*). None of the respiratory organoids supported active SARS-CoV-2 replication (Fig. 2, A and B), despite ACE2 RNA expression and the relatively high computationally predicted binding affinities of *R. ferrumequinum*, *M. aurascens*, and *E. serotinus* ACE2s with the SARS-CoV-2 Spike receptor binding domain (RBD) (Fig. 2C and fig. S13, B to E). However, if human TMPRSS2 was ectopically expressed using the lentiviral system, bronchoalveolar organoids of *E. serotinus* and *R. ferrumequinum* could be infected with SARS-CoV-2 (Fig. 2D and fig. S13F). Notably, small intestinal organoids from *R. ferrumequinum* supported active SARS-CoV-2 replication whereas those from the other species—including *M. aurascens*, *P. abramus*, *E. serotinus*, *and H. alaschanicus*—did not (fig. S13G). This finding, in addition to previous studies using *R. sinicus* small intestinal organoids (*13*, *31*), confirmed species specificity of SARS-CoV-2 for Rhinolophus bats. Moreover, MERS-CoV showed robust replication in the respiratory organoids of *R. ferrumequinum*, *M. aurascens*, and *E. serotinus*, but not in those of *P. abramus* and *H. alaschanicus* (Fig. 2, E and F, and fig. S14, A and B). These species-specific patterns correlated with high expression levels of the MERS-CoV receptor DPP4 seen in *E. serotinus* organoids (Fig. 2G), the greater conservation of the MERS-CoV interacting interface of *R. ferrumequinum* DPP4 with that of human DPP4 (fig. S14C), and relatively higher in silico binding affinities of *R. ferrumequinum* DPP4 to the MERS-CoV RBD (fig. S14, D to F). However, cell type compositions seemed to play limited roles in the species-specificity of MERS-CoV infections. Although AT2 and ciliated cells strongly correlated with MERS-CoV infectivity in *R. ferrumequinum* bronchoalveolar organoids (fig. S14G), their distribution across different bat species did not align with the observed species-specific patterns of MERS-CoV infections (Fig. 2, E and F).

High sensitivities of bat respiratory organoids to avian influenza A viruses

Unlike other mammalian and avian species, influenza viruses have only recently been found to occur in bats (*32*–*34*). An H9N2 influenza A virus (IAV) has been detected in Egyptian fruit bats (*Rousettus aegyptiacus*), indicating that bird-to-bat transmission could occur (*34*, *35*). We found that tracheal organoids from *R. ferrumequinum* and bronchoalveolar organoids from *M. aurascens* were broadly sensitive to avian IAVs, including the H8N4 type (fig. S15A), which typically replicates in wild birds but not in poultry (*36*, *37*). We then challenged bat respiratory organoids with human H1N1 (CA04), avian H5N1, and bat-derived H9N2 IAVs. All organoids tested, except the bronchoalveolar organoids of *P. abramus*, showed comparable sensitivities to all the influenza A virus strains (Fig. 2, H to K, and fig. S15B), but not to influenza B virus strains (fig. S15C). This wide sensitivity to IAVs correlated with co-staining for α-2,3 and α-2,6 sialic acids (Fig. 2H and fig. S15D), which are the avian and human influenza virus receptors, respectively.

Expression of interferon-stimulated genes in bat respiratory organoids on virus infection

To investigate induction of interferon-stimulated genes (ISGs) by viral infection, RNA sequencing (RNA-seq) was performed in tracheal and bronchoalveolar organoids of *R. ferrumequinum* inoculated with MERS-CoV or IAV (human H1N1 CA04). Both viruses stimulated ISG expression (Fig. 2, L to Q), with higher ISG levels, encompassing type I and II ISGs, observed following IAV infection (fig. S16, A and B). Upon MERS-CoV infection, *R. ferrumequinum* tracheal organoids expressed comparable but slightly higher levels of ISGs than bronchoalveolar organoids (fig. S16, C and D).

Similarly, RNA-seq on *E. serotinus* tracheal organoids infected with MERS-CoV or IAV showed induction of ISGs (fig. S16, E to H). A subset of type II ISGs, such as CD74, ASS1, and CCL5, were distinctly elevated in *R. ferrumequinum* organoids compared with *E. serotinus* (fig. S16, I and J). Again, IAV infection induced more ISGs than MERS-CoV infection in *E. serotinus* tracheal organoids (fig. S16, K and L).

Organ-specific susceptibilities to influenza virus and orthohantavirus seoulense

We exposed organoids to representative respiratory (influenza virus) (*38*) and renal (*orthohantavirus*) (*39*) viruses to evaluate whether our bat organoid platform could differentially support tissue-specific viruses. First, we challenged organoids from *M. aurascens* with human influenza A virus H1N1 (CA04) or avian influenza A virus H5N1 (pseudotyped, Δ401). Both viruses replicated efficiently in respiratory and kidney organoids, and modestly in the small intestinal organoids (Fig. 3, A to C). In addition, the small intestinal organoids of *E. serotinus* and bronchoalveolar organoids of *H. alaschanicus* showed infection-induced cell death upon infections with green fluorescent protein (GFP) labeled human H1N1 (PR8-GFP) (fig. S17, A to D and movies S1 to S5).

Kidney organoids from *R. ferrumequinum* and *E. serotinus* were susceptible to Orthohantavirus seoulense (SEOV), an old-world hantavirus, showing nuclear fragmentation and disrupted epithelial integrity, indicating cytopathic effects (Fig. 3, D and E). These species specificities could not have been imposed by putative host receptors, such as PCDH1 and CD55, since no differential expression of these receptors were found among kidney organoids of different species (fig. S18, A and B). ISG expression increased upon SEOV infection in *R. ferrumequinum* kidney organoids (Fig. 3, F and G), indicating that innate immune responses were retained. Further investigation using tracheal, bronchoalveolar, kidney, and small intestinal organoids from

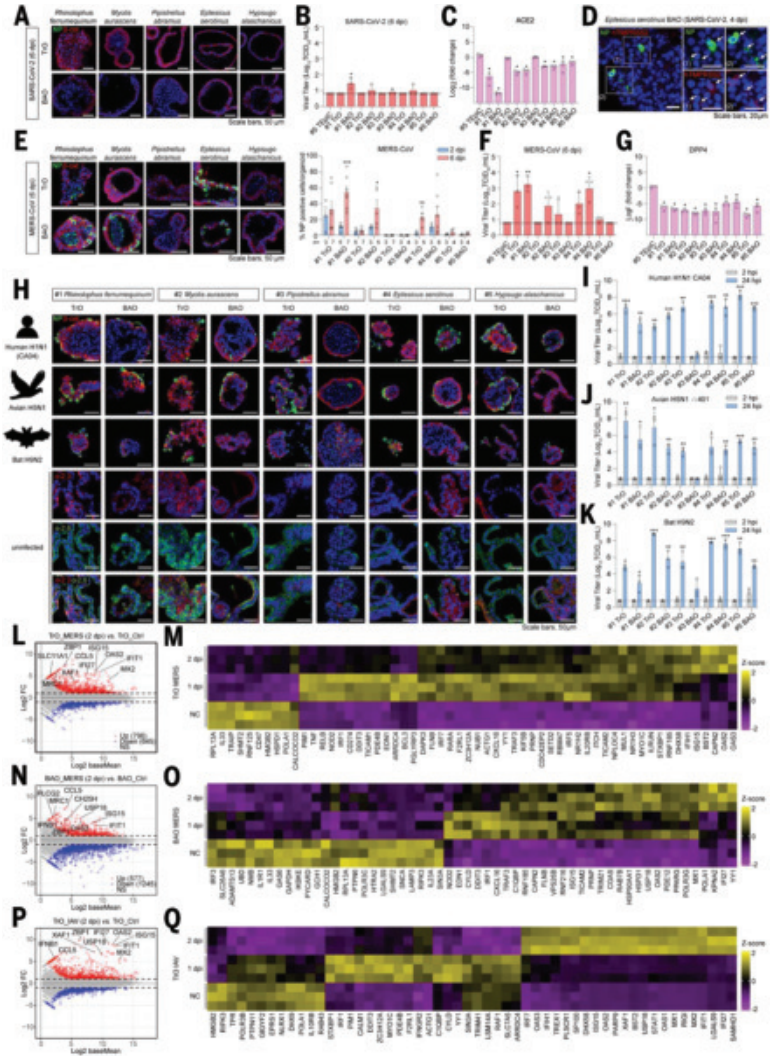

Fig. 2. Multispecies bat respiratory organoids differentially support replications of zoonotic viruses. (**A**) Whole-mount immunofluorescence imaging of multispecies bat respiratory tracheal (TrO) and bronchoalveolar organoids (BAO) for viral nucleocapsid protein (NP) after SARS-CoV-2 infection for 6 days at a multiplicity of infection (MOI) of 1. Scale bars, 50 μm. (**B**) Viral titers measured by 50% tissue culture infectious dose ($TCID_{50}$) after 6 days of SARS-CoV-2 infection. The dashed line indicates the limit of detection (0.8 $TCID_{50}$/mL). Error bars are ± SEM ($n = 3$). One-sided *t*-test [versus #5 tracheal epithelial cells (TEpiC)]: $^{*}P < 0.05$. (**C**) GAPDH-normalized RNA expression levels of ACE2 from multispecies bat respiratory organoids. *Hypsugo alachanicus* (#5) TEpiC cells were used as a control. Error bars are ± SEM ($n = 3$). One-sided *t*-test (versus #5 TEpiC): $^{*}P < 0.05$. (**D**) Whole-mount immunofluorescence imaging of *E. serotinus* bronchoalveolar organoids ectopically overexpressing human TMPRSS2. Arrows indicate co-staining of human TMPRSS2 (red) and SARS-CoV-2 NP (green), after lentivirally overexpressing hTMPRSS2 and infection with SARS-CoV-2 for 4 days. Scale bars, 20 μm. (**E**) Whole-mount immunofluorescence imaging of multispecies bat respiratory organoids for MERS-CoV NP proteins 6 days after infection (1 MOI). Proportions of MERS-CoV–positive (NP-positive) cells at 2 dpi and 6 dpi per organoid were counted and plotted (right). Error bars are ± SEM. Scale bars, 50 μm. One-sided *t*-test (versus 2 dpi): $^{***}P < 0.001$, $^{**}P < 0.01$, $^{*}P < 0.05$. (**F**) $TCID_{50}$ viral titers were measured at 6 days post MERS-CoV infection using Vero E6 cells. Dashed line indicates the limit of detection (0.8 $TCID_{50}$/mL). Error bars are ± SEM ($n = 3$). One-sided *t*-test (versus #5 TEpiC): $^{**}P < 0.01$, $^{*}P < 0.05$. (**G**) Normalized RNA levels of DPP4 in multispecies TrO and BAO. *H. alachanicus* (#5) TEpiC cells were used as a control. Error bars are ± SEM ($n = 3$). One-sided *t*-test (versus #5 TEpiC): $^{*}P < 0.05$. (**H**) Whole-mount immunostaining of influenza NP protein after infections of multispecies bat respiratory organoids (TrO and BAO) with human H1N1, avian H5N1, or bat H9N2 for 2 days. Also, α-2,3 and α-2,6 sialic acids were stained in uninfected multispecies bat respiratory organoids. β-Catenin was used as an epithelial cell marker and DAPI was used for nucleus staining. Scale bars, 50 μm. Schematic images of the bird and bat were created with BioRender.com. (**I** to **K**) $TCID_{50}$ was measured from supernatants of the multispecies bat respiratory organoids infected with human H1N1 (I), avian H5N1 (J), or bat H9N2 (K). The dashed line indicates the limit of detection (0.8 $TCID_{50}$/mL). Error bars are ± SEM ($n = 3$). One-sided *t*-test (versus 2 hpi): $^{***}P < 0.001$, $^{**}P < 0.01$, $^{*}P < 0.05$. (**L**) DEGs from mRNA-seq data of *R. ferrumequinum* tracheal organoids infected with MERS-CoV for 2 days versus uninfected control were plotted as an MA plot (an application of a Bland–Altman plot) ($n = 3$ per group). The ISGS with the largest log2 fold change (log2FC) values were annotated. The adjusted *P*-value threshold was set to <0.05. (**M**) Heatmap plot of representative ISGs after MERS-CoV infection (for 0, 1, and 2 days) in *R. ferrumequinum* tracheal organoids, based on the z-score of transcripts per million (TPM). Three independent replicates are shown. (**N**) DEGs from mRNA-seq data of *R. ferrumequinum* bronchoalveolar organoids infected with MERS-CoV for 2 days versus uninfected control were plotted as an MA plot ($n = 3$ per group). The top ISGs with the largest log2FC values were annotated. The adjusted *P*-value threshold was set to <0.05. (**O**) Heatmap plot of representative ISGs after MERS-CoV infection (for 0, 1, and 2 days) in *R. ferrumequinum* bronchoalveolar organoids, based on the z-score of TPM. Three independent replicates are shown. (**P**) DEGs from mRNA-seq data of *R. ferrumequinum* tracheal organoids infected with human IAV CA04 for 2 days versus uninfected control were plotted as an MA plot ($n = 3$ per group). The top ISGs with the largest log2FC values were annotated. The adjusted *P*-value threshold was set to less than 0.05. (**Q**) Heatmap plot of representative ISGs after IAV infection (for 0, 1, and 2 days) in *R. ferrumequinum* tracheal organoids, based on the z-score of TPM. Three independent replicates were shown. #1: *R. ferrumequinum*, #2: *M. aurascens*, #3: *P. abramus*, #4: *E. serotinus*, #5: *H. alaschanicus*.

E. serotinus and *H. alaschanicus* showed that SEOV replicated most effectively in kidney organoids (Fig. 3, H and I, and fig. S18, C and D), as expected from the clinical manifestations of Hemorrhagic Fever with Renal Syndrome (*40*).

Isolation and characterization of bat-borne mammalian orthoreovirus and paramyxovirus

We explored the possibilities of using the organoid platform to isolate hitherto unknown bat viruses from fecal matter collected from the originating bat sampling sites (figs. S1F and S19A). For initial detection of bat mammalian orthoreovirus (MRV), the supernatant of cleared bat fecal samples was first applied to kidney epithelial cells of *H. alaschanicus* for three sequential blind passages. The collected supernatant from cells exhibiting cytopathic effects was then used for total RNA extraction and analyzed by degenerate PCR and sequencing to confirm MRV identity. The enriched MRV isolates were inoculated into congenic organoids. The tracheal, kidney, and intestinal organoids all supported bat MRV growth (Fig. 4A and fig. S19, B to F). Functional virions were produced from tracheal organoids (Fig. 4A), as evidenced by the detection of viral RNA in the supernatant (fig. S19, D and E) and plaque-forming activity (Fig. 4B). The MRV virions reinfected bat organoids more effectively than human organoids [$P = 0.000033$ at 5 days post infection (dpi)] (fig. S19G), indicating species-specificity. TEM analysis showed that the virus had an icosahedral morphology, characteristic of most MRV strains (fig. S19H). Total RNA sequencing indicated possible reassortment from four different MRV strains (Fig. 4C and fig. S19I).

All tracheal organoids from various bat species supported MRV replication (Fig. 4, D and E and fig. S19, J to L). Moreover, bat-isolated

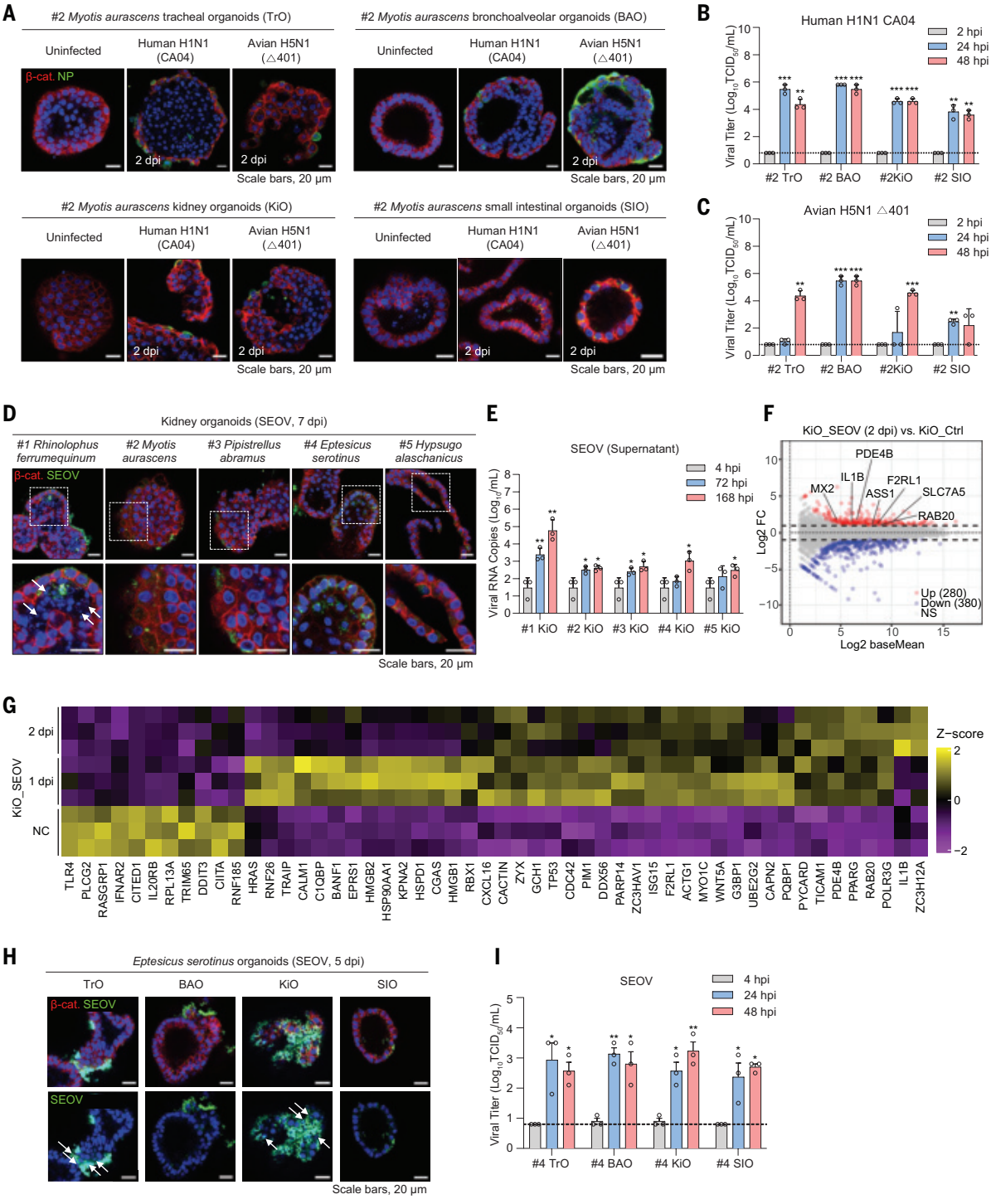

Fig. 3. Multiorgan bat organoids show organ-specific infection dynamics. (**A**) Multiorgan bat organoids of *M. aurascens*—including TrO, BAO, kidney organoids (KiO), and small intestinal organoids (SIO)—were infected with the human H1N1 or avian H5N1 influenza virus. Whole-mount viral NP staining was performed at 2 dpi. Scale bars, 20 μm. (**B** to **C**) Viral titers were measured after infection of multiorgan organoids of *M. aurascens* with human H1N1 (B) or avian H5N1 (C) by TCID50 assay. The dashed line indicates the limit of detection (0.8 $TCID_{50}$/mL). Error bars are ± SEM ($n = 3$). (**D**) Whole-mount immunofluorescence analysis of SEOV from infected multispecies bat kidney organoids. β-Catenin was counterstained as an epithelial cell marker. White arrows indicate fragmented nuclei. Scale bars, 20 μm. (**E**) SEOV RNA copies were measured from virions in infected multispecies KiO supernatants; 4 hpi values were from *E. serotinus* KiO. Error bars are ± SEM ($n = 3$). (**F**) DEGs from mRNA-seq data of *R. ferrumequinum* kidney organoids infected with SEOV for 2 days versus uninfected control were plotted as an MA plot ($n = 3$ per group). The ISGS with the largest log2 fold change (log2FC) values were annotated. The adjusted *P*-value threshold was set to <0.05. (**G**) Heatmap plot of representative ISGs after SEOV infection (for 0, 1, and 2 days) in *R. ferrumequinum* kidney organoids, based on the z-score of TPM. Three independent replicates were shown. (**H**) Whole-mount immunofluorescence imaging of SEOV in multiorgan organoids of *E. serotinus*. Arrows indicate massive SEOV virion staining with fragmented nuclei. Scale bars, 20 μm. (**I**) Viral titers were measured after infection of multiorgan organoids of *E. serotinus* with SEOV by TCID50 assay. Dashed line indicates the limit of detection (0.8 $TCID_{50}$/mL). Error bars are ± SEM ($n = 3$). One-sided *t*-test (versus 2 hpi or 4 hpi): ***$P < 0.001$, **$P < 0.01$, *$P < 0.05$. #1: *R. ferrumequinum*, #2: *M. aurascens*, #3: *P. abramus*, #4: *E. serotinus*, #5: *H. alaschanicus*.

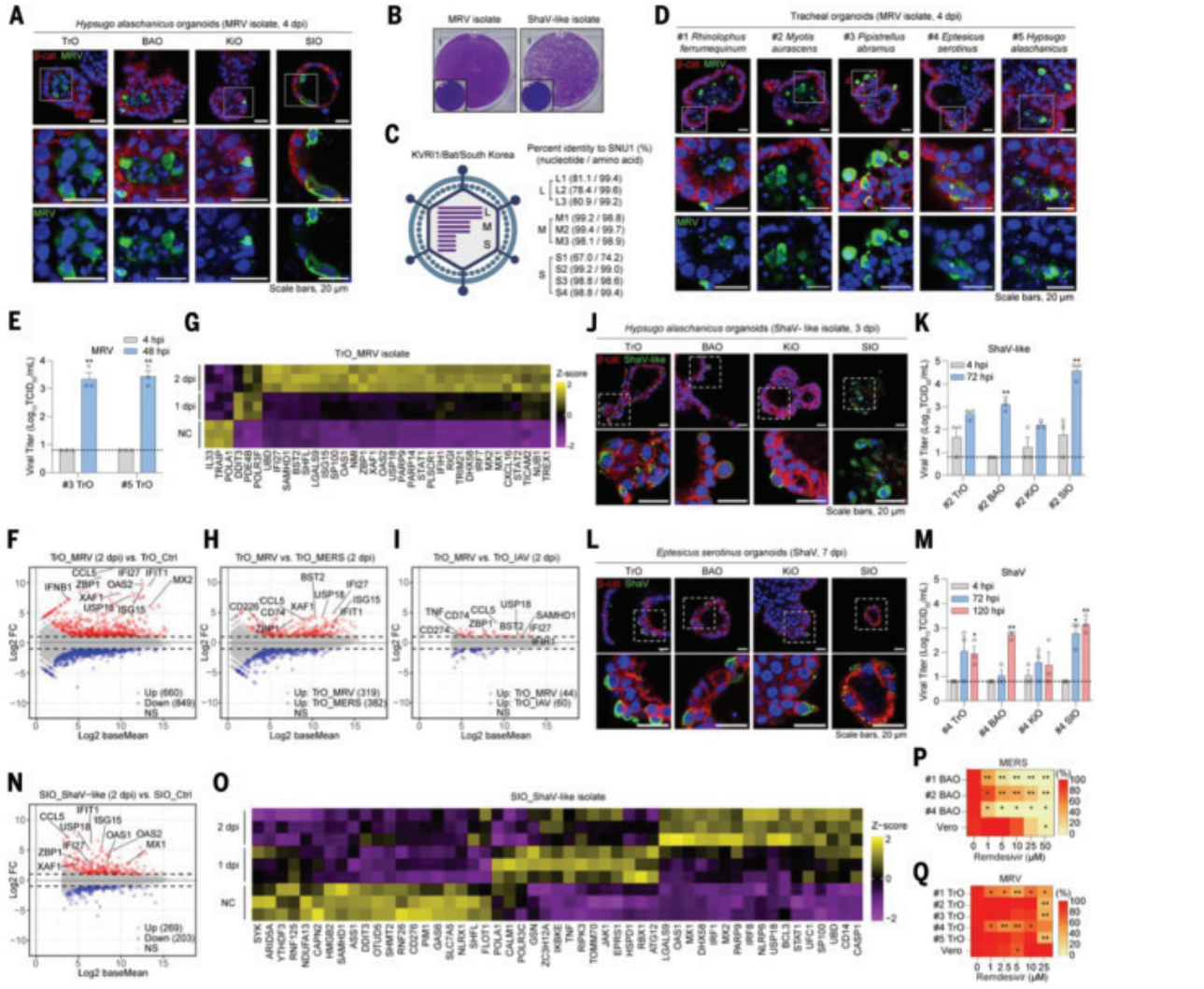

Fig. 4. Isolation and characterization of novel bat-borne *mammalian orthoreovirus* and a paramyxovirus using multispecies and multiorgan bat organoid platform. (**A**) Whole-mount immunofluorescence of bat-originated MRV in multiorgan organoids of *H. alaschanicus*. β-Catenin was stained as an epithelial cell marker. Areas in the dashed rectangles are enlarged in the second and third rows. Scale bars, 20 μm. (**B**) Plaque assays for bat-derived MRV and Shaan-like virus (ShaV-like). Diluted samples were inoculated (10^{-1} or 10^{-6}) in a six-well plate. (**C**) Homology analysis of genomic segments of the newly isolated MRV strain (KVRI1/Bat/South Korea) compared with its closest bat MRV strain SNU1 (SNU1/Bat/South Korea). Percent identities of nucleotide and amino acid sequences between the two strains were calculated for each of the 10 genomic segments, labeled as L1, L2, L3, M1, M2, M3, S1, S2, S3, and S4. Schematic virion shape was created with BioRender.com. (**D**) Whole-mount immunofluorescence of bat MRV in multispecies bat tracheal organoids. Areas in the dashed rectangles are enlarged in the second and third rows. Scale bars, 20 μm. (**E**) MRV viral titers were measured by $TCID_{50}$ in the supernatants from tracheal organoids of *P. abramus* (#3) and *H. alaschanicus* (#5). Error bars are ± SEM ($n = 3$). One-sided *t*-test (versus 4 hpi): $^{**}P < 0.01$. (**F**) DEGs from mRNA-seq data of *R. ferrumequinum* tracheal organoids infected with bat MRV isolate for 2 days versus uninfected control were plotted as an MA plot ($n = 3$ per group). The top ISGs with the largest log2 foldchange (log2FC) values were annotated. The adjusted *P*-value threshold was set to <0.05. (**G**) Heatmap plot of representative ISGs after bat MRV isolate infection (for 0, 1, and 2 days) in *R. ferrumequinum* tracheal organoids, based on the z-score of TPM. Three independent replicates are shown. (**H**) Comparative DEG analysis between MERS-CoV infected tracheal organoids (2 dpi) (see Fig. 2L) and bat MRV isolate infected tracheal organoids (2 dpi) ($n = 3$ per group). Selected ISGs are marked. (**I**) Comparative DEG analysis between IAV-infected tracheal organoids (2 dpi) (see Fig. 2P) and bat MRV isolate–infected tracheal organoids (2 dpi) ($n = 3$ per group). Selected ISGs are marked. (**J**) Whole-mount immunofluorescence imaging of multiorgan organoids of *H. alaschanicus* infected with *Shaanvirus*-like isolates using anti-*Shaanvirus* (B16-40) antibody. β-Catenin was counterstained for epithelial adherence junction. Areas enclosed by the dashed rectangles were enlarged below. Scale bars, 20 μm. (**K**) ShaV-like viral titers were measured by $TCID_{50}$ in the supernatants of *M. aurascens* multiorgan organoids. Error bars are ± SEM ($n = 3$). One-sided *t*-test (versus 4 hpi): $^{**}P < 0.01$. (**L**) Whole-mount immunofluorescence analysis of multiorgan organoids of *E. serotinus* for *Shaanvirus* (ShaV) B16-40 7 days after infection. β-Catenin was counterstained as an epithelial cell marker. Areas in the dashed rectangles were enlarged below. Scale bars, 20 μm. (**M**) Viral titers were measured after infection of multiorgan organoids of *E. serotinus* with ShaV by TCID50 assay. The dashed line indicates the limit of detection (0.8 $TCID_{50}$/mL). Error bars are ± SEM ($n = 3$). One-sided *t*-test (versus 4 hpi): $^{**}P < 0.01$, $^{*}P < 0.05$. (**N**) DEGs from mRNA-seq data of *R. ferrumequinum* small intestinal organoids infected with ShaV-like isolate for 2 days versus uninfected control were plotted as MA plot ($n = 3$ per group). The ISGs with the largest log2 fold change (log2FC) values were annotated. The adjusted *P*-value threshold was set to <0.05. (**O**) Heatmap plot of representative ISGs after ShaV-like isolate infection (for 0, 1, and 2 days) in *R. ferrumequinum* small intestinal organoids, based on the z-score of TPM. Three independent replicates are shown. (**P** to **Q**) Heatmap plot of antiviral activity test of Remdesivir against MERS-CoV in multispecies bat bronchoalveolar organoids (BAO) (P) or bat MRV isolate in multispecies tracheal organoids (TrO) (Q) along with control cell line Vero E6. Color gradient indicates relative viral infection compared with the control, based on the fluorescence imaging of the viral protein. See figs. S22 to S25 for imaging and IC50 calculation results. One-sided *t*-test (versus 0 μM): $^{**}P < 0.001$, $^{*}P < 0.01$. #1: *R. ferrumequinum*, #2: *M. aurascens*, #3: *P. abramus*, #4: *E. serotinus*, #5: *H. alaschanicus*.

MRV successfully induced ISGs in the tracheal organoids of *R. ferrumequinum* and *E. serotinus* (Fig. 4, F and G and fig. S20, A and B). ISGs induced by MRV were distinct, characterized by higher expressions of XAF1, IFI27, USP18, BST2, OAS1, MX1, and ISG15 compared with MERS-CoV infection, and SIGLEC1, IL1RL1, and CD74 compared with IAV infection (Fig. 4, H and I, and fig. S20, C to H). Hence, dsRNA viruses, such as MRV, appeared to induce a different range of ISGs to those induced by ssRNA viruses, such as MERS-CoV and IAV.

We also detected a paramyxovirus in our degenerate PCR screening (fig. S19A) (*41*). Total RNA sequencing revealed that the isolated paramyxovirus is the closest relative of Shaan virus B16-40 (ShaV) (fig. S21A). However, although ShaV readily replicated in the MARC-145 cell line, we were only able to recover the paramyxovirus from bat primary cells and organoids and not from MARC-145 cells. Therefore, we referred to our isolate as a ShaV-like paramyxovirus and used our organoid platform for further characterization. In our experience, the ShaV-like paramyxovirus replicated most efficiently in the tracheal and small intestinal bat organoids, consistent with the tropism for enteric and respiratory epithelia of ShaV (Fig. 4, J to M, and fig. S21, B to E). The ShaV-like paramyxovirus induced a subset of type I and II ISGs, characterized by IFIT1, IFI27, ISG15, OAS1, OAS2, MX1, ZBP1, XAF1, USP18, and CCL5 in the small intestinal organoids of *R. ferrumequinum* (Fig. 4, N and O).

Bat organoids for antiviral efficacy testing

To evaluate the bat organoid platform for rapid testing for antiviral therapeutics, we adapted 3D bat organoids to a 2D format by plating them onto matrigel-coated 96-well plates, as previously described (*11*). The 2D system effectively recapitulated species-specific MERS-CoV replication seen in 3D organoids (Fig. 2, E and F, and figs. S22 and S23A), and outperformed Vero E6 cells in evaluating the antiviral effects of Remdesivir, Molnupiravir, and/or Ribavirin (Fig. 4P and figs. S22 and S23, B and C). Moreover, Remdesivir efficiently suppressed replication of the bat MRV isolate in bat tracheal organoids, but not in Vero E6 cells (Fig. 4Q, figs. S24 and S25, A to C).

Conclusions

We have successfully developed and tested a multispecies and multiorgan organoid platform from nontropical, insectivorous bats of the Vespertilionidae and Rhinolophidae families. This platform enables investigation of the behavior of zoonotic viruses that pose serious threats to human health. Our organoids support the growth of several zoonotic viruses, and we have successfully isolated and characterized bat-borne mammalian orthoreovirus and paramyxovirus from bat fecal samples, highlighting organoid utility in studying virus-host interactions across multiple organ systems. The organoid platform also allows simultaneous surveillance and rapid drug efficacy testing for a range of bat-borne viruses.

Our study advances the field but has notable limitations. The lack of reference genomes for Vespertilionidae species limits in-depth genetic analysis of our organoids. Developing these genomes could enhance genetic studies and understanding of bat biology. Additionally, although our organoids model viral infection dynamics, they do not replicate complex biological systems such as immune-epithelial interactions. Future research should integrate immune cells into organoid cultures to better mimic these systems.

REFERENCES AND NOTES

1. World Health Organization, "Zoonoses" (WHO, 2020); https://www.who.int/news-room/fact-sheets/detail/zoonoses.
2. S. Sampath *et al.*, *Cureus* **13**, e18136 (2021).
3. L. H. Taylor, S. M. Latham, M. E. Woolhouse, *Philos. Trans. R. Soc. B.* **356**, 983–989 (2001).
4. K. Van Brussel, E. C. Holmes, *Curr. Opin. Virol.* **52**, 192–202 (2022).
5. B. He *et al.*, *Proc. Natl. Acad. Sci. U.S.A.* **121**, e2313789121 (2024).
6. K. J. Olival *et al.*, *Nature* **546**, 646–650 (2017).
7. M. Ruiz-Aravena *et al.*, *Nat. Rev. Microbiol.* **20**, 299–314 (2022).
8. P. Eby *et al.*, *Nature* **613**, 340–344 (2023).
9. A. Su *et al.*, *Microbiol. Spectr.* **11**, e0309822 (2023).
10. L. L. Y. Chan *et al.*, *Emerg. Microbes Infect.* **12**, e2148561 (2023).
11. M. J. Kellner *et al.*, Reconstructing bat antiviral immunity using epithelial organoids. bioRxiv 2024.04.05.588241 [Preprint] (2024); https://doi.org/10.1101/2024.04.05.588241.
12. M. Elbadawy *et al.*, *Int. J. Mol. Sci.* **22**, 10763 (2021).
13. J. Zhou *et al.*, *Nat. Med.* **26**, 1077–1083 (2020).
14. M. Hashimi *et al.*, *Nat. Commun.* **14**, 6882 (2023).
15. G. F. Gunnell, R. Smith, T. Smith, *PLOS ONE* **12**, e0172621 (2017).
16. S. Alkhovsky *et al.*, *Viruses* **14**, 113 (2022).
17. F. Schutgens *et al.*, *Nat. Biotechnol.* **37**, 303–313 (2019).
18. N. Sachs *et al.*, *EMBO J.* **38**, e100300 (2019).
19. B. K. Koo *et al.*, *Nature* **488**, 665–669 (2012).
20. T. Sato *et al.*, *Nature* **459**, 262–265 (2009).
21. J. D. Davis, T. P. Wypych, *Mucosal Immunol.* **14**, 978–990 (2021).
22. H. Kim *et al.*, *Dev. Cell* **56**, 1118–1130.e6 (2021).
23. D. Park *et al.*, *J. Med. Virol.* **96**, e29600 (2024).
24. A. A. Salahudeen *et al.*, *Nature* **588**, 670 (2020). (2020).
25. X. Tian *et al.*, *J. Biomed. Biotechnol.* **2011**, 567305 (2011).
26. Y. Yamamoto *et al.*, *Nat Methods* **14**, 1097–1106 (2017).
27. D. Delaune *et al.*, *Nat. Commun.* **12**, 6563 (2021).
28. S. Temmam *et al.*, *Nature* **604**, 330–336 (2022).
29. H. A. Mohd, J. A. Al-Tawfiq, Z. A. Memish, *Virol. J.* **13**, 87 (2016).
30. S. Murakami *et al.*, *Transbound. Emerg. Dis.* **69**, 3388–3396 (2022).
31. X. Liu *et al.*, *Signal Transduct. Target. Ther.* **7**, 392 (2022).
32. S. Tong *et al.*, *Proc. Natl. Acad. Sci. U.S.A.* **109**, 4269–4274 (2012).
33. S. Tong *et al.*, *PLOS Pathog.* **9**, e1003657 (2013).
34. A. Kandeil *et al.*, *J. Virol.* **93**, e01059–e01018 (2019).
35. R. El-Shesheny *et al.*, *Nat. Commun.* **15**, 3449 (2024).
36. H. Zhang *et al.*, *J. Integr. Agric.* (2024).
37. W. Tang *et al.*, *Acta Virol.* **63**, 121–125 (2019).
38. C. Cilloniz, C. M. Luna, J. C. Hurtado, M. A. Marcos, A. Torres, *Eur. Respir. Rev.* **31**, 220051 (2022).
39. Y. S. Kim *et al.*, *Nephron J.* **71**, 419–427 (1995).
40. C. Kang *et al.*, *PLOS Negl. Trop. Dis.* **15**, e0009168 (2021).
41. J. Y. Noh *et al.*, *Sci. Rep.* **8**, 12533 (2018).
42. "TreeBASE" (2025); https://treebase.org/treebase-web/home.html.

ACKNOWLEDGMENTS

We thank C.-W. Jung for providing wild-caught bats and bat specimens; J. Shin and J. Kim for providing coding sequences of some bat genes; and M.A. Casel and Y.-s. Lee for critical reading of the manuscript. BioRender.com was used to create part of the images in Figs. 1B, 2H, 4C, and figs. S1H, S4D, S15A, and S19A. We acknowledge the use of ChatGPT for text editing to improve grammatical accuracy. **Funding:** This work was supported by the Institute for Basic Science (IBS-R021-D1 to B.-K.K.), by the Institute for Basic Science (IBS-R801-D1 to Y.K.C.), and the National Research Foundation (NRF) funded by the Korean government (MSIT) (RS-2024-00400771 to Y.K.C.). **Author contributions:** Conceptualization: H.K., B.-K.K., and Y.K.C. Methodology: H.K., S.-Y.H., Y.-I.K., D.P., H.J., J.H., B.-K.K., and Y.K.C. Investigation: H.K., S.-Y.H., Y.-I.K., D.P., M.P.A.N., S.H., Y.L., H.J., J.-W.A., J.H., S.P., H.Y.J., S.K., I.C., W.K., J.K., K.K., J.G., B.J., J.C.D.L., R.R., and J.H.C. Resources: Y.-I.K., J.K., E.H.-K., S.-G.J., H.K.K., B.-Y.J., G.K., and R.J.W. Writing-original draft: H.K. Writing-review & editing: H.K., B.-K.K., and Y.K.C. with input from all authors. Visualization: H.K., S.-Y.H., Y.-I.K., D.P., M.P.A.N., S.H., Y.L., H.J., and J.-W.A. Supervision: B.-K.K. and Y.K.C. Project administration: Y.K.C. Funding acquisition: B.-K.K. and Y.K.C. **Competing interests:** Authors declare that they have no competing interests. **Data and materials availability:** Genome sequences and annotation information for the two virus isolates, BatMRV2/KVRI1/KOREA/2024 (bat MRV) and Bat-ParaV/KVRI1 (ShaV-like, partial) were deposited to the GenBank database in NCBI, using the accession numbers PV005835-PV005844 and PV019437-PV019445, respectively. Genome sequences of Bat-ParaV/B16-40 (ShaV, full) (PV005834) and MERS-CoV/KOR/2016-001 (PV000776) were deposited to the GenBank. The processed and associated raw data on scRNA-seq and bulk mRNA-seq can be accessed through the Gene Expression Omnibus (GEO) and the Sequence Read Archive (SRA) databases, using the accession numbers PRJNA1211818/GSE287598 and PRJNA1214407/GSE287878, respectively. Phylogenetic data have been deposited in TreeBASE (*42*). Protein docking data are in the supplementary data file. The cell lines and organoids generated for this study are available from Y.K.C. under a material transfer agreement with the Institute for Basic Science. All other data needed to evaluate the conclusions in the paper are present in the main text or the supplementary materials. **License information:** Copyright © 2025 the authors, some rights reserved; exclusive licensee American Association for the Advancement of Science. No claim to original US government works. https://www.science.org/about/science-licenses-journal-article-reuse

SUPPLEMENTARY MATERIALS

science.org/doi/10.1126/science.adt1438
Materials and Methods; Figs. S1 to S25; Tables S1 to S7; References (*43*–*67*); Movies S1 to S5; Data S1

Submitted 13 September 2024; resubmitted 22 January 2025; accepted 19 March 2025

10.1126/science.adt1438

NEUROPHYSIOLOGY

GPCR signaling gates astrocyte responsiveness to neurotransmitters and control of neuronal activity

Kevin A. Guttenplan[1]*, Isa Maxwell[1], Erin Santos[1], Luke A. Borchardt[1], Ernesto Manzo[1], Leire Abalde-Atristain[1], Rachel D. Kim[2], Marc R. Freeman[1]*

How astrocytes regulate neuronal circuits is a fundamental question in neurobiology. Specifically, how astrocytes respond to different neurotransmitters in vivo and how they affect downstream circuit modulation are questions that remain to be fully elucidated. Here, we report a mechanism in *Drosophila* by which G protein–coupled adrenergic signaling in astrocytes can control—or "gate"—their ability to respond to other neurotransmitters. Further, we show that manipulating this pathway potently regulates neuronal circuit activity and animal behavior. This gating mechanism is conserved in cultured primary mammalian astrocytes, suggesting that it might be an ancient feature of astrocyte circuit function. Our work establishes a mechanism by which astrocytes dynamically respond to and modulate neuronal activity in different brain regions and in different behavioral states.

Astrocytes causally regulate neuronal circuits (*1*). Not only do astrocytes display complex calcium transients in response to neuronal activity, but astrocyte calcium influx is necessary and sufficient to regulate the firing of specific circuits with reliable behavioral consequences (*2*, *3*). Understanding how astrocytes modulate neuronal circuit activity is critical for deciphering how the brain encodes information. However, little is known about precisely what signals astrocytes respond to in vivo, the kinds of computations they perform, the mechanisms by which they regulate neuronal activity, and how these features may vary across brain regions or behavioral states (*4*).

Complicating this understanding, astrocyte intracellular signaling pathways behave in fundamentally different ways than those of neurons. For instance, neurons typically increase calcium activity in response to $G_{\alpha q}$ signaling and decrease it in response to $G_{\alpha i}$ signaling (*5*). By contrast, astrocytes increase calcium activity in response to both (*6*–*9*). Further, whereas most calcium activity in neurons can be understood to represent action potential generation and the calcium-dependent release of neurotransmitters, distinct methods of increasing calcium activity in astrocytes lead to vastly different effects on the activity of downstream neuronal circuits (*6*–*8*). Finally, astrocytes exhibit highly varied responses to the same neurotransmitters across brain regions, times, and behavioral states of animals (*10*–*17*). Some studies have observed that a single neurotransmitter release event can simultaneously increase and decrease cytoplasmic calcium concentrations in neighboring astrocytes within the same organism (*13*). Together, these studies emphasize that to understand the role that astrocytes play in neuronal circuits and behavior, we must gain a better understanding of the mechanisms that govern their responses to neurotransmission.

[1]Vollum Institute, Oregon Health and Sciences University, Portland, OR, USA. [2]Neuroscience Institute, NYU Grossman School of Medicine, New York, NY, USA. ***Corresponding author. Email: freemmar@ohsu.edu (M.R.F.); guttenpl@ohsu.edu (K.A.G.)**

Results

Tyramine gates the response of astrocytes to other neurotransmitters

To understand the molecular mechanisms that determine how astrocytes respond to different neurotransmitters, we used astrocytes of the larval *Drosophila* ventral nerve cord (VNC), the equivalent of the mammalian spinal cord. *Drosophila* VNC astrocytes have been shown to share most known functions of mammalian astrocytes (*18*) and have been used to identify specific molecules that astrocytes use to causally regulate intrinsic calcium signaling and downstream neuronal activity (*2*), a mechanism subsequently validated in vertebrates (*3*). Using an established method to image astrocytes in intact larval brains ex vivo, we bath applied neurotransmitters in the presence of the sodium channel blocker tetrodotoxin (TTX) to block neuronal activity and assessed direct astrocyte responses (Fig. 1A). In this context, astrocytes labeled using the *alrm-Gal4* driver reliably responded to octopamine and tyramine, the functional homologs of epinephrine and norepinephrine (NE), with an increase in calcium across the entire VNC, but were unresponsive to all other neurotransmitters tested (Fig. 1, B to D, and fig. S1, A and B) (*2*). Previous reports have suggested that animal behavior state and adrenergic signaling can change astrocyte calcium activity in response to local circuit activity (*19*, *20*). On the basis of these observations, we next investigated whether pre-exposure of astrocytes to tyramine could change their response to other neurotransmitters. Approximately 3 minutes after exposure to tyramine (with or without tyramine washout), astrocytes started to exhibit robust responses to dopamine, glutamate, acetylcholine, and γ-aminobutyric acid (GABA) (Fig. 1, E and F, and fig. S1, C to E), as shown by increased calcium influx. This indicates that pre-exposure to tyramine can control the response of astrocytes to other neurotransmitters in the larval VNC, which we refer to as "gating." This response was specific to tyraminergic signaling; glutamate and acetylcholine could not elicit a response (i.e., did not affect calcium signaling) after dopamine administration, suggesting that some aspect of the tyramine signaling cascade was necessary for gating (Fig. 1F).

We previously found that whole-cell astrocyte calcium responses to tyramine depend on a single G protein–coupled receptor (GPCR), the octopamine-tyramine receptor (Oct-TyrR) (Fig. 1G, blue field) (*2*). Knocking down *Oct-TyrR* specifically in astrocytes abolished both the tyramine response and the gating response to all neurotransmitters tested, suggesting that the gating mechanism is dependent on signaling downstream of Oct-TyrR (Fig. 1H). Octopamine, which can also stimulate Oct-TyrR, could also elicit gating (fig. S1F). One hypothesis for how tyramine stimulation could gate a secondary response is through the calcium influx that it induces in astrocytes, which might fill the calcium reserves necessary for a secondary response or mediate a calcium-dependent intracellular signal that allows gating (Fig. 1G, orange field). To test this hypothesis, we expressed *transient receptor potential cation channel A1* (*TrpA1*) in astrocytes because this channel passes calcium in response to the exogenous ligand allyl-isothiocyanate (AITC) and has been shown to functionally replace endogenous Oct-TyrR–dependent calcium signaling in the astrocytic regulation of neuronal circuits (*2*). Stimulating calcium influx through TrpA1 did not facilitate gating of any neurotransmitters despite inducing a similar calcium response magnitude as tyramine (Fig. 1, H and I). Thus, although TRP channel–mediated calcium entry itself drives astrocyte-mediated changes in neural circuit activity and animal behavior (*2*), it is not sufficient to mediate gating of astrocyte responses to glutamate, acetylcholine, or dopamine.

To better understand how tyramine might be gating other neurotransmitter responses, we added tyramine simultaneously with dopamine, glutamate, or acetylcholine. Simultaneous addition of tyramine and dopamine did not lead to a response larger than that triggered by tyramine alone, but both glutamate and acetylcholine led to larger combined responses (Fig. 1J). This shows that whereas all gated responses required Oct-TyrR, the kinetics of dopamine versus glutamate and/or acetylcholine gating appear to differ. In the case of dopamine, the lack of a simultaneous enhancement from tyramine and dopamine together

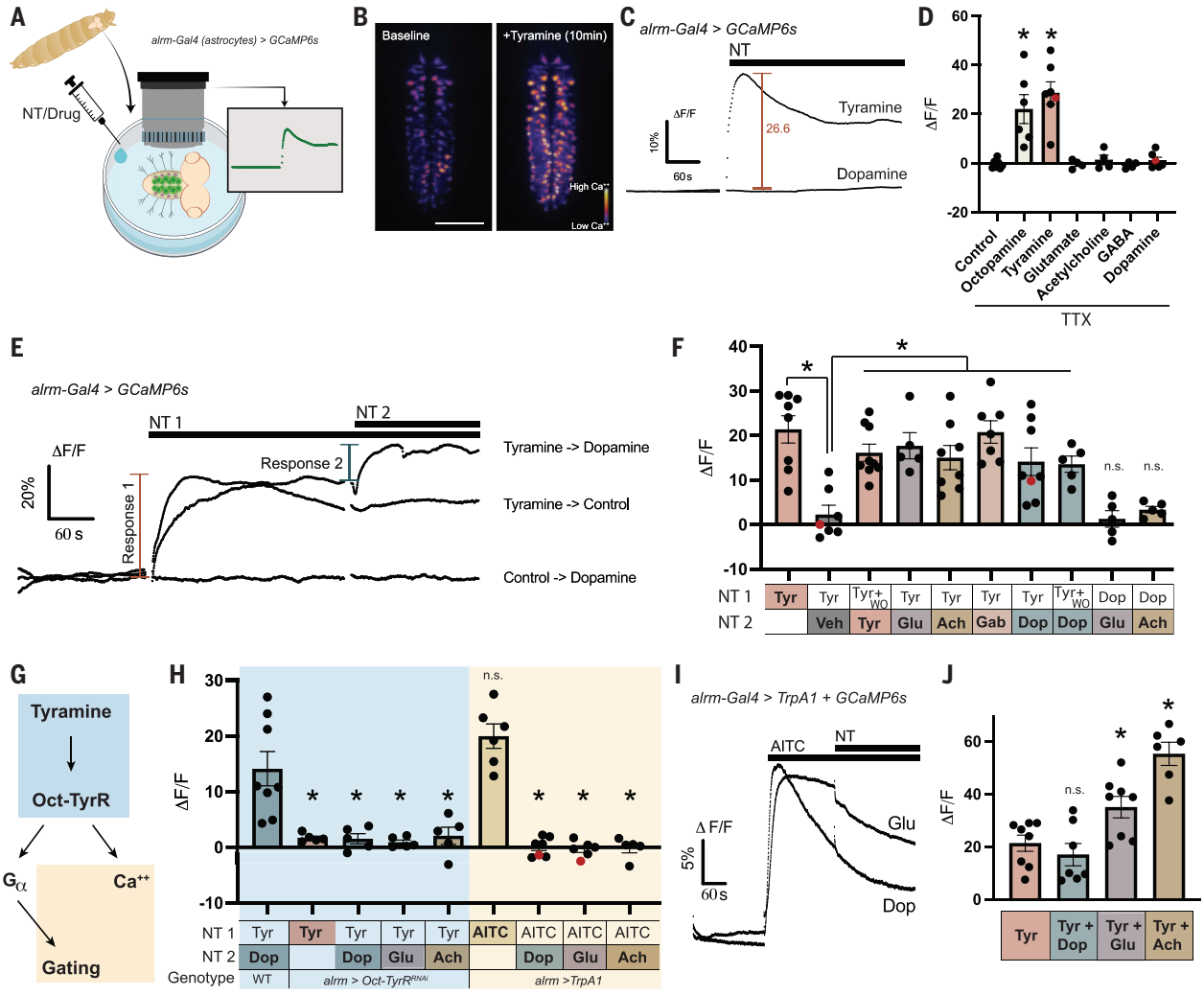

Fig. 1. Tyramine gates the response to other neurotransmitters through Oct-TyrR. (**A**) Schematic demonstrating the ex vivo preparation used to image larval VNC astrocytes in an intact nervous system. (**B**) VNC astrocytes before and after exposure to tyramine with GCaMP6s fluorescence pseudocolored to demonstrate calcium influx. Scale bar, 100 μm. (**C**) Example trace of GCaMP6s fluorescence for a field of VNC astrocytes after tyramine or dopamine addition and a demonstration of the quantification method for the tyramine response. (**D**) Quantification of astrocyte calcium response to various neurotransmitters (NTs). (**E**) Example traces of astrocyte calcium when exposed to tyramine followed by a second NT or vehicle control. (**F**) Quantification of astrocyte calcium responses to various combinations of NT exposures. Veh, vehicle control; WO, washout; Ach, acetylcholine; Glu, glutamate; Tyr, tyramine; Gab, GABA. (**G**) Schematic demonstrating the initial pathway of gating. (**H**) Quantification of astrocyte calcium responses in *Oct-TyrR* knockdown and *TrpA1*-expressing flies. (**I**) Example traces of calcium activity of *TrpA1*-expressing astrocytes responding to AITC followed by subsequent glutamate or dopamine. (**J**) Quantification of astrocyte calcium responses to simultaneous addition of NT combinations. *$P < 0.05$. Details of statistical comparisons and exact *P* values are provided in table S1. All error bars represent SEM. Red dots in bar graphs correspond to traces chosen as examples.

suggests that astrocytes undergo some form of intracellular signaling to facilitate dopamine responsiveness, a finding supported by a more in-depth analysis of the time course of dopamine gating (fig. S1G).

Dopamine gating is dependent on $G_{\alpha i}$ GPCR regulation of dopamine 2–like receptor internalization

We next investigated whether the GPCR signaling downstream of Oct-TyrR could be responsible for gating (Fig. 2A). Expressing a cyclic adenosine monophosphate (cAMP) indicator in astrocytes, we found that tyramine exposure led to a decrease in cAMP, which aligns with previous reports in cell lines showing that Oct-TyrR functions as a $G_{\alpha i}$-coupled GPCR (Fig. 2B) (*21*). To validate that $G_{\alpha i}$ signaling itself is necessary for gating, we overexpressed the *pertussis toxin α subunit* (*PTXa*), which inhibits $G_{\alpha i}$ signaling, and separately knocked down the $G_{\alpha i}$ protein in astrocytes. In both instances, disrupting $G_{\alpha i}$ signaling prevented gating of dopamine, glutamate, and acetylcholine, confirming that G protein signaling downstream of Oct-TyrR is required for the gating effect (Fig. 2C). Because $G_{\alpha i}$ signaling leads to a decrease in cAMP, we next tested whether modulating cAMP without Oct-TyrR stimulation could trigger the astrocyte gating response. Indeed, pretreatment of astrocytes with the adenylyl cyclase inhibitor SQ22536, but not the adenylyl cyclase–activating drug forskolin, was sufficient to gate the astrocyte response to dopamine (Fig. 2, C and D). The data also show that cAMP modulation was not sufficient to gate the responses to glutamate or acetylcholine (Fig. 2C). Thus, consistent with the different kinetics of dopamine versus glutamate and acetylcholine gating (Fig. 1J), the mechanisms of gating of neurotransmitters diverge in terms of cAMP regulation.

What receptor could be mediating the response of astrocytes to dopamine? Four metabotropic dopamine receptors are present in the fly genome. After knocking down each receptor selectively in astrocytes, we found

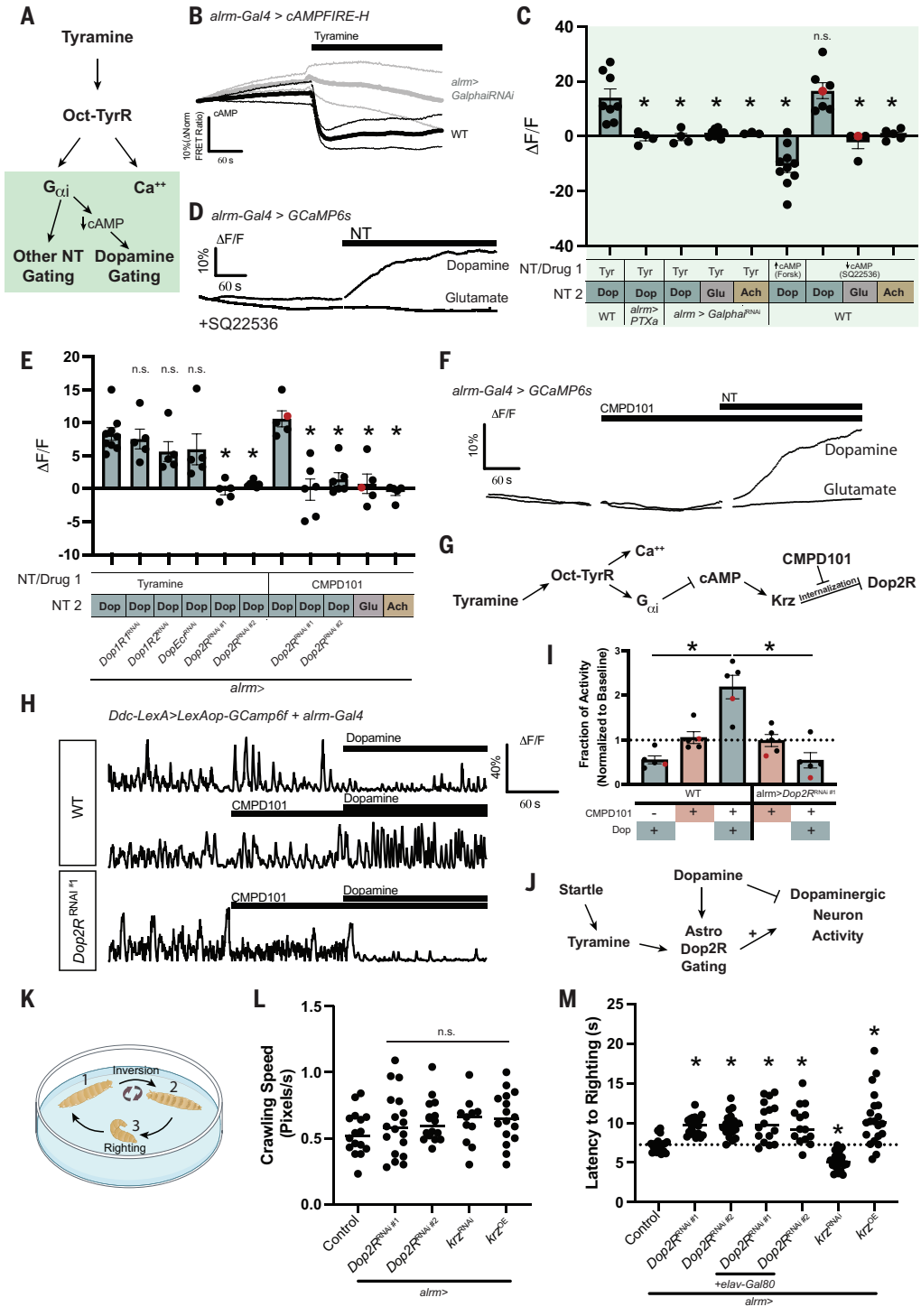

Fig. 2. Dopamine gating is dependent on $G_{\alpha i}$ signaling. (**A**) Schematic showing the mechanism of gating for different classes of NTs. (**B**) Mean trace (thick line) and 95% confidence interval (thin lines) of cAMP amounts as measured by the fluorescence resonance energy transfer (FRET) ratio of the cAMP indicator cAMPFIRE-H in astrocytes ($n = 5$). (**C**) Quantification of astrocyte calcium responses while targeting $G_{\alpha i}$ signaling and modulating cAMP. (**D**) Example traces of astrocytes treated with the adenylyl cyclase inhibitor SQ22536 followed by exposure to dopamine or glutamate. (**E**) Quantification of astrocyte calcium responses to NTs in wild-type (WT) versus astrocyte-specific dopamine receptor knockdown flies after either tyramine or CMPD101 exposure. (**F**) Example traces of astrocytes exposed to CMPD101 followed by exposure to dopamine or glutamate. (**G**) Schematic showing the mechanism that links tyramine exposure to dopamine response gating. (**H**) Traces (without TTX) of *Ddc*$^{+}$ dopamine neuron activity in response to dopamine or CMPD101 followed by dopamine in WT and astrocyte-specific *Dop2r* knockdown flies. (**I**) Quantification of neuronal activity from experiments outlined in (H). (**J**) Schematic showing role of astrocyte gating of Dop2R on the response of dopaminergic neurons to bath application of dopamine. (**K**) Diagram of the larval-righting assay. (**L**) Larval crawling speed analysis of WT larvae or larvae with *Dop2R* knockdown, *Krz* knockdown, or *Krz* overexpression in astrocytes. (**M**) Quantification of latency to right of larvae turned to their posterior side (righting) in WT larvae or larvae with *Dop2R* knockdown, *Krz* knockdown, or *Krz* overexpression in astrocytes. *$P < 0.05$. Details of statistical comparisons and exact *P* values are provided in table S1. All error bars represent SEM. Red dots in bar graphs correspond to traces chosen as examples.

that *dopamine 2-like receptor* (*Dop2R*) knockdown completely prevented the response to dopamine after tyramine, whereas other dopamine receptor knockdowns had no effect (Fig. 2E). Therefore, the cAMP-mediated regulation of dopamine responses in astrocytes occurs through Dop2R.

One known mechanism by which cAMP can regulate the activity of GPCRs is through the activation of kinases that initiate internalization of receptors, which in *Drosophila* occurs through the arrestin homolog Kurtz (Krz). We speculated that the gating of calcium responses to dopamine could occur through the inhibition of Dop2R internalization in astrocytes, permitting more receptors to remain on the surface and enhancing receptor signaling. CMPD101 is an inhibitor of kinases required for receptor internalization, and we sought to determine whether it could functionally replace adenylyl cyclase inhibition in preventing receptor internalization and gating responsiveness to dopamine (Fig. 2G). Indeed, we found that CMPD101 treatment successfully gated dopamine responses through Dop2R but did not affect glutamate or acetylcholine responses (Fig. 2, E and F). Thus, gating of dopamine responses in astrocytes downstream of tyramine stimulation appears to occur through the cAMP-mediated modulation of Dop2R internalization (Fig. 2G). Given its lack of effect on glutamate or acetylcholine responses, our data further suggest that gating of astrocyte responsiveness to other neurotransmitters occurs through different mechanisms. Protein internalization has also been proposed to underlie the astrocytic regulation of GABA in mammals (*22*), suggesting that surface exposure might be an evolutionarily conserved mechanism to tune astrocyte sensitivity to neurotransmission.

To better understand how neurotransmitter response gating could affect information processing in the brain, we sought to identify an in vivo circuit specifically modulated by Dop2R signaling in astrocytes. Larval VNC astrocytes have been shown to mediate the inhibition of dopamine neurons by the arousal cue tyramine (*2*), raising the possibility that astrocyte Dop2R responses could affect state-dependent changes in dopamine circuit regulation. We expressed *GCaMP6f* in dopaminergic neurons and found that the addition of dopamine in the VNC led to a reduction of dopaminergic neuron activity (Fig. 2, H and I). Pretreating the preparation with CMPD101, which gates the astrocyte dopamine response, inverted this effect and caused a marked increase in dopaminergic neuron activity in response to dopamine application (Fig. 2, H and I). This reversal was abolished when *Dop2R* was selectively eliminated from astrocytes, demonstrating that it was mediated by astrocyte Dop2R (Fig. 2, H and I). Our data therefore unexpectedly reveal that Dop2R-mediated responses gated by arousal-associated tyraminergic cues in astrocytes can drive enhanced dopaminergic activity (Fig. 2J).

We next investigated whether the tyramine-gated dopamine response in astrocytes could influence whole-animal behavior. When a larva is rolled onto its dorsal side, this induces a startle response that requires coordinated, dopamine-modulated motor activity for it to right itself (Fig. 2K) (*23*). Given the intersection of a startle response and dopamine circuit activity and the ability of astrocytes, which tile much of the brain, to detect dopamine input from a large array of sources, we wondered if the gating of dopamine responses in astrocytes could regulate this behavior. Knocking down *Dop2R* in astrocytes using two distinct RNA interference constructs did not affect baseline larval locomotion but did delay larval righting (Fig. 2, L and M). This aligns with our calcium imaging of dopaminergic neurons, suggesting that the gated astrocyte dopamine response enhances dopamine circuit activity (Fig. 2G). To further confirm that the effect of *Dop2R* knockdown was neuron independent, we combined astrocyte *Dop2R* knockdown with a transgene that prevents any *Dop2R* knockdown in neurons (*elav-Gal80*) and observed a similar delay in larval righting (Fig. 2M).

If the observed changes are caused by arousal-mediated changes in Dop2R trafficking in astrocytes, as our imaging experiments suggest, then we would predict that modulation of Krz activity would also modulate larval righting. Indeed, we found that overexpressing *krz*, which should drive excess internalization of Dop2R, phenocopied *Dop2R* knockdown and slowed larval righting (Fig. 2M). Reciprocally, knocking down *krz* to retain Dop2R at the surface enhanced righting behavior (Fig. 2M). Thus, increased or decreased Krz activity can bidirectionally modulate larval-righting efficiency.

Together with our results from imaging dopamine neuron activity, these findings suggest that dynamic trafficking of Dop2R downstream of arousal signaling to astrocytes can powerfully modulate neuronal circuit activity, ultimately affecting animal behavior.

Astrocyte response gating by adrenergic signaling is conserved in mammals

Astrocytes can change neural circuit activity downstream of adrenergic-like signaling in many species (*2*, *3*, *14*, *19*), suggesting that the fundamental mechanisms of astrocyte circuit modulation are highly conserved. To determine whether adrenergic signaling drives dopamine gating in mammalian astrocytes, we performed calcium-imaging experiments in primary rat astrocytes loaded with the calcium indicator Fluo-4 (Fig. 3, A and B). For each primary preparation, we first determined the highest dose of dopamine that would not induce a calcium response in primary astrocytes. Working at that concentration of dopamine, we found that bath application of NE was sufficient to gate the response of astrocytes to the previously subthreshold dopamine exposure (Fig. 3, B to D). Thus, exposure of mammalian astrocytes to NE can also promote astrocyte responsiveness to dopamine.

Unlike *Drosophila* astrocytes, in which calcium responses to noradrenergic homologs occur downstream of a single $G_{\alpha i}$ GPCR (*2*), mammalian astrocytes express a host of adrenergic receptors, including the high-affinity $\alpha 1$ $G_{\alpha q}$–coupled and $\alpha 2$ $G_{\alpha i}$–coupled receptors (Fig. 3C and fig. S2). To determine whether gating is mediated by $G_{\alpha i}$ signaling, we stimulated astrocytes with the $\alpha 1$ agonist phenylephrine (PE) or the $\alpha 2$ agonist UK14304, followed by a subthreshold dose of dopamine. Although PE induced a robust calcium response, it was unable to gate the dopamine response (Fig. 3, C to E). By contrast, although a high concentration of UK14304 could induce a calcium response, a subthreshold UK14304 stimulation was sufficient to gate dopamine (Fig. 3, C to E). Thus, $\alpha 2$ $G_{\alpha i}$ signaling in the absence of initial calcium influx is sufficient to enhance the astrocytic response to dopamine in mammalian astrocytes.

Modulation of cAMP and inhibition of receptor internalization were both sufficient to modulate dopamine responses in fly astrocytes. To test whether these mechanisms are conserved in mammals, we modulated cAMP using either forskolin (to increase cAMP) or SQ22536 (to decrease cAMP). Inhibition, but not activation, of adenylyl cyclase was sufficient to gate the dopamine response in the absence of NE or $\alpha 2$ agonist exposure (Fig. 3, E to G). Similarly, CMPD101-mediated inhibition of receptor internalization was also able to induce responses to dopamine (Fig. 3E). Thus, the mechanism of dopamine gating through $G_{\alpha i}$ GPCR activation, inhibition of adenylyl cyclase, and inhibition of receptor internalization appears to be conserved from flies to mammals. Gating was also observed for glutamate after NE exposure (Fig. 3E).

Although caution should be taken in comparing the observed gating responses in *Drosophila* astrocytes in an intact brain with mammalian astrocytes in vitro, our observations may suggest that the gating response is less binary in mammalian astrocytes. Further, it is important to note that our in vitro culture method used 24- to 48-hour exposure to serum before switching cells to a defined, serum-free medium, which may lead to prolonged reactivity (*24*). Given the differences in neurotransmitter response behavior that have been observed between different primary culture methods (*25*), future studies exploring how these responses occur in vivo and across brain regions will be crucial.

Finally, to more directly test whether our manipulations of dopamine response gating were caused by changes in receptor localization, we treated astrocytes with UK14304, forskolin, SQ22536, and CMPD101 (Fig. 3E) and stained them using an antibody against the extracellular domain of DRD2 (Fig. 3H). We quantified the amount of cell surface DRD2 exposure by staining without permeabilization. Consistent with

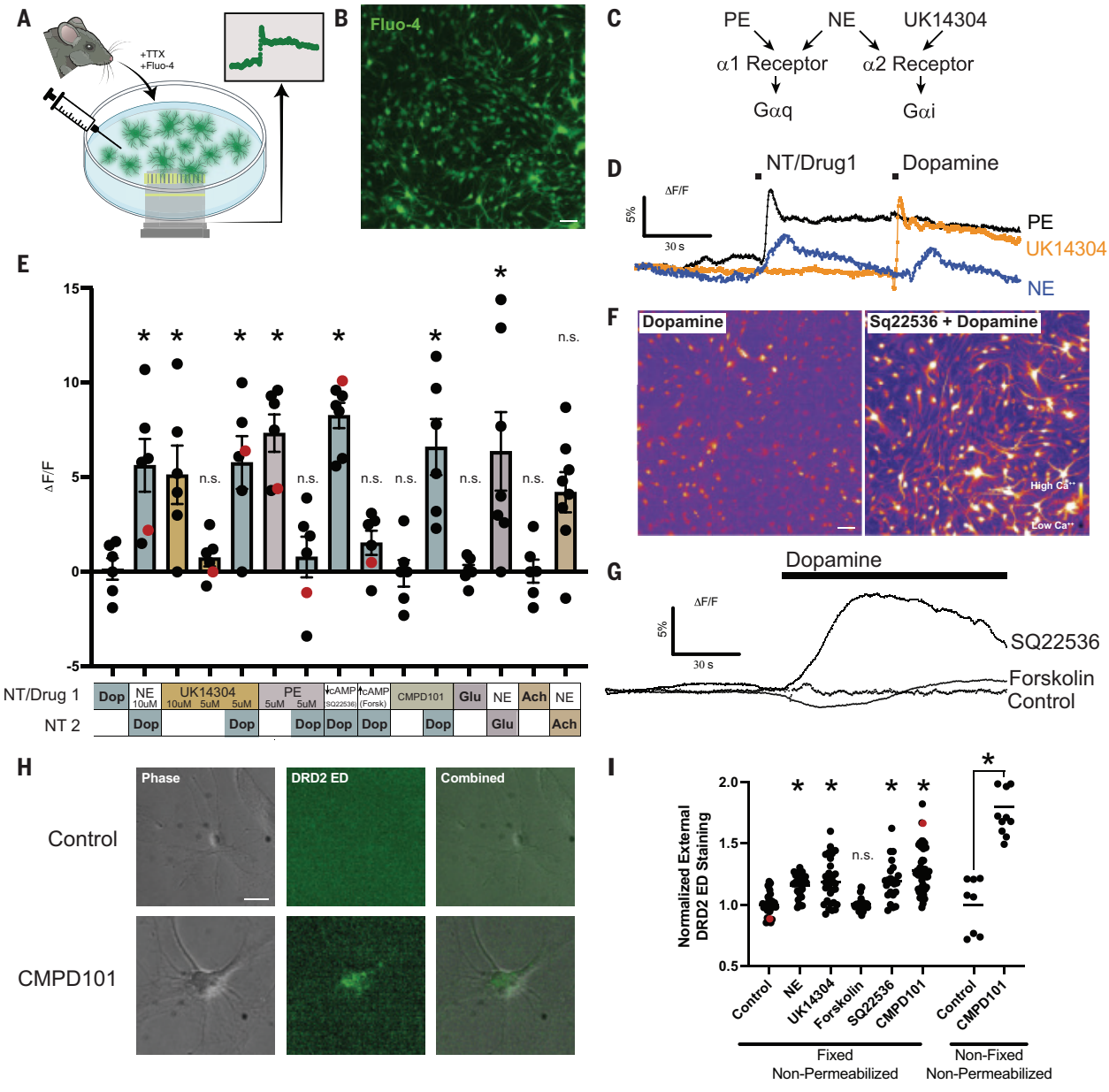

Fig. 3. Gating of dopamine is conserved in mammals. (**A**) Schematic showing the method of calcium imaging in primary rat astrocytes. (**B**) Example image of primary rat astrocytes loaded with the calcium indicator Fluo-4. Scale bar, 20 μm. (**C**) Schematic of NE and drug selectivity for α1 versus α2 adrenergic receptors. (**D**) Example traces of rat astrocyte calcium responses to NE, PE, and UK14304 followed by dopamine. (**E**) Quantification of astrocyte calcium responses to various combinations of drugs and NTs. (**F**) Example astrocyte calcium responses after dopamine versus SQ22536 followed by dopamine as shown by pseudocolored Fluo-4 fluorescence. Scale bar, 20 μm. (**G**) Example trace of rat astrocyte calcium response to dopamine on its own or after either SQ22536-mediated inhibition of adenylyl cyclase or forskolin-mediated activation of adenylyl cyclase. (**H**) Example images of astrocytes (phase) with or without treatment with CMPD101 for 30 min and then stained with an antibody against the extracellular domain of DRD2 (DRD2 ED; green). Scale bar, 10 μm. The brightness of the DRD2 ED staining is enhanced in the example control image to demonstrate that astrocyte staining is at or near background expression. (**I**) Quantification of primary rat astrocytes stained for the extracellular domain of DRD2. *$P < 0.05$. Details of statistical comparisons and exact P values are provided in table S1. All error bars represent SEM. Red dots in bar graphs correspond to traces chosen as examples.

our hypothesized mechanism, exposure to NE, UK14304, SQ22536, and CMPD101, all of which can gate dopamine responsiveness, led to an increase in DRD2 extracellular staining, whereas forskolin, which does not lead to enhanced dopamine responsiveness, did not enhance cell surface staining (Fig. 3, H and I).

Discussion

To determine how astrocytes regulate neurons, it is essential to understand the mechanisms that link astrocytic neurotransmitter exposure to intracellular calcium signaling and downstream circuit modulation. Our data suggest that astrocytes dynamically alter their response to neurotransmitters based on cell state, such as whether the cell has recently received an arousal cue including tyramine or NE. The modulation of neurotransmitter responses downstream of NE and/or GPCR signaling is also conserved in mammals, leading us to hypothesize that it is an ancient and fundamental feature of complex nervous systems. An important question for the future will be whether the observed response enhancement during gating of mammalian astrocytes is truly

an on-or-off mechanism, as appears to be the case in flies, or if it acts as more of a priming effect to increase or decrease the gain of astrocyte responses. Further, although we focused on adrenergic signaling in this study, our observations that modulating GPCR signaling components is sufficient to mediate or prevent gating suggest that other GPCR-mediated signals may similarly gate neurotransmitter responses in astrocytes. This may be especially true in mammals, in which Gαi-coupled adrenergic receptors are heterogeneously expressed in astrocytes (fig. S2) and other Gαi receptors may be involved.

We also discovered that astrocyte responsiveness to different neurotransmitters is regulated differently downstream of initial GPCR signaling: Dopamine is gated over long time periods by changes in cAMP and broad manipulation of receptor surface exposure, whereas acetylcholine and glutamate responsiveness is modulated simultaneously with tyramine exposure and appears to not require cAMP modulation. A long-standing mystery in neuroscience has been how a single astrocyte could specifically "listen" to the thousands of synapses from disparate neuronal subtypes that are contained within its territory. Local gating of each neurotransmitter response, through the signaling events that we describe here, might serve as a flexible mechanism to allow astrocytes to turn their sensitivity to the various circuits within their domain on and off or, if used more broadly, to drive state-dependent changes in neuronal activity (*2*, *3*, *6*, *26*).

The observation that one neurotransmitter can alter an astrocyte's response to others suggests that differences in cell state might underpin regional and temporal variations in astrocyte responses and thus the discrepant reports of astrocyte responsiveness to neurotransmitters. For instance, the ability of glutamate to induce astrocytic calcium activity appears to vary based on brain region and age (*10*–*17*). We speculate that gating might potentially contribute to such differences in astrocyte responses over time and space. Recent studies have also suggested that neurotransmitter responses within one astrocyte can modulate the responsiveness of gap junction–coupled astrocytes nearby, potentially adding variability to what different experimenters might witness in response to the same manipulation (*10*). Because gap junctions are thought to be large enough to pass cAMP, an intriguing hypothesis is that local changes in cAMP might travel between cells and mediate gating responses across the larger astrocyte syncytium.

Although neuromodulation is often thought about in terms of how far a given neuromodulator could potentially diffuse, serial electron micrograph reconstructions of the brain have highlighted the dense nature of the brain parenchyma, which likely limits the long-range diffusion of neuromodulators in the extracellular space (*27*). Given the dense infiltration of astrocyte processes in the brain, the numerous ways that astrocytes can respond to neuromodulators, and the different mechanisms by which they can regulate neuronal activity, astrocytes increasingly appear as likely candidates for the long-range transmission of neuromodulatory cues through receipt and rebroadcasting of neuronal signals. Thus, astrocytic regulation of downstream neuronal activity should be considered when examining both local and broad aspects of neural circuit function, particularly in the context of slower-acting neuromodulatory events.

How does gating affect specific neuronal circuits? Our results reveal that dopamine neuron activity can be potently regulated by astrocyte Dop2R signaling. They further show that CMPD101-mediated inhibition of receptor internalization leads to a twofold increase in dopamine neuron activity through astrocytic Dop2R in *Drosophila* larvae. This powerful bidirectional modulation of dopamine circuitry is mirrored by a bidirectional control of larval behavior; knocking out Dop2R in astrocytes regulates the speed of larval righting, a behavior that sits at the intersection of a tyramine-induced arousal signal and downstream dopamine-regulated motor actions. How astrocytes can regulate dopaminergic neuron signaling so profoundly is a crucial next question.

Our results also imply that astrocyte modulation of dopaminergic activity is complex and context dependent. Whereas previous studies demonstrated that calcium influx downstream of octopamine and/or tyramine stimulation leads to silencing of dopaminergic neurons, likely through adenosine signaling (*2*, *3*), our present data indicate that Dop2R signaling in astrocytes leads to an increase in dopamine neuron activity. We propose three alternative models to explain this diversity of signaling mechanisms: (i) the source of calcium influx (such as extracellular entry versus release from internal stores) or strength of calcium response can co-opt different downstream signaling mechanisms and drive disparate outputs, (ii) the localization of calcium influx in the cell can dictate different outputs, or (iii) second messengers other than calcium that accompany metabotropic signaling are responsible for some neuromodulatory signals in astrocytes. Consistent with these alternative possibilities, cAMP amounts can be modulated by calmodulin activity downstream of calcium influx, highlighting the complex interactions between these secondary signaling cascades. Only by continuing to decipher the mechanistic links between these various astrocyte intracellular signals (including calcium influx and GPCR signaling) and downstream neuromodulation will we be able to decipher how astrocytes regulate information processing in the brain.

REFERENCES AND NOTES

1. J. Nagai *et al.*, *Neuron* **109**, 576–596 (2021).
2. Z. Ma, T. Stork, D. E. Bergles, M. R. Freeman, *Nature* **539**, 428–432 (2016).
3. Y. Mu *et al.*, *Cell* **178**, 27–43.e19 (2019).
4. C. Murphy-Royal, S. Ching, T. Papouin, *Nat. Neurosci.* **26**, 1848–1856 (2023).
5. B. L. Roth, *Neuron* **89**, 683–694 (2016).
6. T. V. Vaidyanathan, M. Collard, S. Yokoyama, M. E. Reitman, K. E. Poskanzer, *eLife* **10**, e63329 (2021).
7. A. Adamsky *et al.*, *Cell* **174**, 59–71.e14 (2018).
8. A. Kol *et al.*, *Nat. Neurosci.* **23**, 1229–1239 (2020).
9. S. H. Lee, A. Mak, M. H. G. Verheijen, *Front. Cell. Neurosci.* **17**, 1159756 (2023).
10. M. K. Cahill *et al.*, *Nature* **629**, 146–153 (2024).
11. N. Kuga, T. Sasaki, Y. Takahara, N. Matsuki, Y. Ikegaya, *J. Neurosci.* **31**, 2607–2614 (2011).
12. V. Kellner *et al.*, *Neuron* **109**, 2545–2555.e7 (2021).
13. A. Park *et al.*, *Curr. Biol.* **32**, 3952–3970.e8 (2022).
14. F. Ding *et al.*, *Cell Calcium* **54**, 387–394 (2013).
15. W. Sun *et al.*, *Science* **339**, 197–200 (2013).
16. Z. U. Khan, P. Koulen, M. Rubinstein, D. K. Grandy, P. S. Goldman-Rakic, *Proc. Natl. Acad. Sci. U.S.A.* **98**, 1964–1969 (2001).
17. A. Jennings *et al.*, *Glia* **65**, 447–459 (2017).
18. T. Stork, A. Sheehan, O. E. Tasdemir-Yilmaz, M. R. Freeman, *Neuron* **83**, 388–403 (2014).
19. M. Paukert *et al.*, *Neuron* **82**, 1263–1270 (2014).
20. S. Pittolo *et al.*, *Cell Rep.* **40**, 111426 (2022).
21. S. Robb *et al.*, *EMBO J.* **13**, 1325–1330 (1994).
22. J. Nagai *et al.*, *Neuron* **109**, 2256–2274.e9 (2021).
23. K. D. Bodily, C. M. Morrison, R. B. Renden, K. Broadie, *J. Neurosci.* **21**, 3113–3125 (2001).
24. K. A. Guttenplan, S. A. Liddelow, *J. Exp. Med.* **216**, 71–83 (2019).
25. L. C. Foo *et al.*, *Neuron* **71**, 799–811 (2011).
26. I. D. Blum *et al.*, *Curr. Biol.* **31**, 150–162.e7 (2021).
27. A. Shapson-Coe *et al.*, *Science* **384**, eadk4858 (2024).

ACKNOWLEDGMENTS

We thank all members of the Freeman lab for thoughtful discussions and suggestions throughout this project, the fly community for generous sharing of reagents, and the OHSU Advanced Light Microscopy Core (RRID:SCR_009961) for expert technical assistance. **Funding:** This work was supported by the Helen Hay Whitney Foundation (K.A.G.) and the National Institutes of Health (grant 5F32NS119352 to E.M.; grant 5T32NS007466-25 to I.M., E.S., and L.A.B.; and grants 5R01NS053538 and 5R01NS124146 to M.R.F.). **Author contributions:** Conceptualization: K.A.G., M.R.F.; Investigation: K.A.G., I.M., E.S., L.A.B., E.M., L.A.-A., R.D.K.; Visualization: K.A.G., M.R.F.; Writing – original draft: K.A.G., E.S., L.A.B., E.M., L.A.-A., M.R.F.; Writing – review & editing: K.A.G., E.S., L.A.B., E.M., L.A.-A., M.R.F. **Competing interests:** The authors declare no competing interests. **Data and materials availability:** All data are available in the main text or in the supplementary materials. **License information:** Copyright © 2025 the authors, some rights reserved; exclusive licensee American Association for the Advancement of Science. No claim to original US government works. https://www.science.org/about/science-licenses-journal-article-reuse

SUPPLEMENTARY MATERIALS

science.org/doi/10.1126/science.adq5729
Materials and Methods; Figs. S1 and S2; Table S1; References (*28*–*32*); MDAR Reproducibility Checklist

Submitted 20 May 2024; accepted 21 November 2024

10.1126/science.adq5729

NEUROPHYSIOLOGY

Norepinephrine changes behavioral state through astroglial purinergic signaling

Alex B. Chen[1,2,3]*, Marc Duque[2,3], Altyn Rymbek[4], Mahalakshmi Dhanasekar[5], Vickie M. Wang[2,3], Xuelong Mi[6], Loeva Tocquer[5], Sujatha Narayan[1]†, Emmanuel Marquez Legorreta[1], Mark Eddison[1], Guoqiang Yu[7], Claire Wyart[5], David A. Prober[4], Florian Engert[2], Misha B. Ahrens[1]*

Both neurons and glia communicate through diffusible neuromodulators; however, how neuron-glial interactions in such neuromodulatory networks influence circuit computation and behavior is unclear. During futility-induced behavioral transitions in the larval zebrafish, the neuromodulator norepinephrine (NE) drives fast excitation and delayed inhibition of behavior and circuit activity. We found that astroglial purinergic signaling implements the inhibitory arm of this motif. In larval zebrafish, NE triggers astroglial release of adenosine triphosphate (ATP), extracellular conversion of ATP into adenosine, and behavioral suppression through activation of hindbrain neuronal adenosine receptors. Our results suggest a computational and behavioral role for an evolutionarily conserved astroglial purinergic signaling axis in NE-mediated behavioral and brain state transitions and position astroglia as important effectors in neuromodulatory signaling.

Neural circuits perform fast computations through precise patterns of synaptic connectivity and direct electrical coupling through gap junctions (*1*, *2*), but they can also be rapidly modulated by diffusible chemical messengers, including monoamines [such as norepinephrine (NE), dopamine, and serotonin] and neuropeptides (*3*–*5*). Such signaling accounts for a large portion of neural activity patterns that cannot be explained by synaptic connectivity alone (*6*–*8*) and has long been known to reconfigure synaptic networks to orchestrate behavioral states (*9*–*13*). Recent discoveries have shown that astroglia communicate bidirectionally with neurons through neuromodulatory signaling, suggesting that non-neuronal cells could play more important roles as neuromodulatory actuators than previously thought (*14*). Astrocytes and neurons have substantially different physiologies. Astrocytes are electrically inexcitable, exhibit local and global intracellular calcium transients, and have complex arbors of processes that form nonoverlapping territories and interact with thousands of individual neuronal synapses (*15*, *16*). However, how the specific physiology of astrocytes contributes to their role as active modulatory elements in neural circuits is still unresolved.

Our work focuses on three major neuromodulators, NE, adenosine triphosphate (ATP), and adenosine, and their role in mediating behavioral state changes. Since its discovery in the 1940s (*17*), NE has been known to profoundly influence neurophysiology, neural circuit dynamics, and behavior (*17*–*25*). Although the dominant assumption over the past eight decades has been that NE acts primarily through activation of adrenergic receptors on neurons, recent discoveries that NE also activates non-neuronal cells, particularly astroglia, challenge this assumption. In astroglia, NE triggers large intracellular calcium events caused by α1-adrenergic receptor (α1-AR) activation (*26*–*30*), but the specific roles played by astroglia in noradrenergic modulation remain unclear, as do the pathways linking NE-mediated astroglial calcium elevation to modulation of circuit activity.

As with NE, the purinergic signaling molecules ATP and adenosine are ubiquitous and critical neuromodulators. They play important roles in sleep-wake cycles (*31*–*33*), synaptic plasticity (*34*), and motor pattern generation (*35*), among other functions (*36*–*38*). Although astroglia have been argued to be a source of extracellular adenosine through ATP secretion (*34*, *36*) and extracellular ATP-to-adenosine metabolism (*39*), the behavioral relevance of such release remains, in many cases, controversial (*40*, *41*). Furthermore, whereas astroglial calcium elevation appears to trigger ATP secretion, the behavioral contexts that recruit astroglial purinergic signaling remain poorly understood because of the reliance on exogenous activation and/or ex vivo conditions in existing studies (*42*–*44*).

Leveraging the larval zebrafish, in which NE, ATP, and astroglial calcium can be imaged in conjunction with neural activity during behavior, we found that, during rapid behavioral state transitions, the noradrenergic and purinergic systems can be conceptualized as, respectively, fast excitatory and delayed inhibitory arms of a feedforward motif with astroglia as a coordinating intermediary. Therefore, beyond slow modulation of state, NE also acts through astroglial purinergic signaling to rapidly reconfigure circuit dynamics and enact behavioral state transitions.

NE neurons drive a biphasic futility response

Larval zebrafish have an innate tendency to stabilize their position by swimming in the direction of coherent visual flow (*45*, *46*). We have previously shown that when swims no longer move the fish forward, futility drives firing in hindbrain NE neurons, and NE signals through radial astroglia, a glial cell type similar to mammalian astrocytes (*47*, *48*), to suppress futile swims (*49*). Here, we made use of our previously published behavioral assay for futility-induced passivity in larval zebrafish (*49*, *50*). Fish were immobilized in agarose and their tails freed. The animals' tail positions were then automatically tracked, and detected swims were used to deliver realistic online visual feedback through projection of drifting grating stimuli to the floor of the chamber (Fig. 1A and materials and methods). To encourage robust swimming behavior, we delivered a steady, constant-velocity forward drifting grating (*45*) (Fig. 1B). Simultaneously, we manipulated the efficacy of the fish's swims by cycling between two stimulus conditions: closed loop and open loop. During closed loop, the fish's swim attempts resulted in visual feedback (backward drift of the visual stimuli) to signal successful forward swimming (Fig. 1B, left). In open loop, swim attempts resulted in no change to the visual stimulus (Fig. 1B, right) and were thus futile. Futility is encoded by a population of NE neurons in the medulla oblongata known as NE-MO neurons [putatively homologous to mammalian cluster A2 (*51*)], and NE-MO activation drives astroglial calcium elevation to drive motor-inhibitory GABAergic neurons in the lateral medulla oblongata (L-MO) (Fig. 1C) (*49*).

Consistent with previous work (*26*, *49*), we found that behavioral futility signaled by a lack of visual feedback caused fish to enter, with a delay, a passive state, in which swimming ceases for tens of seconds (Fig. 1, D and E; fig. S1; and movie S1). Before passivity, fish exhibited an increase in swim vigor and were more likely to perform high-amplitude, struggle-like swims (Fig. 1, D and E, and fig. S1). Although NE-MO activation was previously shown to cause passivity (*49*), the contribution of NE neurons in the transient up-regulation of swim vigor at futility onset has not been thoroughly investigated. Given NE's well-documented ability to

[1]Janelia Research Campus, Howard Hughes Medical Institute, Ashburn, VA, USA. [2]Department of Molecular and Cellular Biology, Harvard University, Cambridge, MA, USA. [3]Graduate Program in Neuroscience, Harvard Medical School, Boston, MA, USA. [4]Tianqiao and Chrissy Chen Institute for Neuroscience, Division of Biology and Biological Engineering, California Institute of Technology, Pasadena, CA, USA. [5]Sorbonne Université, Paris Brain Institute (Institut du Cerveau, ICM), Institut National de la Santé et de la Recherche Médicale U1127, Centre National de la Recherche Scientifique Unité Mixte de Recherche 7225, Assistance Publique–Hôpitaux de Paris, Campus Hospitalier Pitié-Salpêtrière, Paris, France. [6]Bradley Department of Electrical and Computer Engineering, Virginia Polytechnic Institute and State University, Arlington, VA, USA. [7]Department of Automation, Tsinghua University, Beijing, P.R. China. †Present address: Allen Institute for Brain Science, Seattle, WA, USA. ***Corresponding author. Email: abchen@g.harvard.edu (A.B.C.); ahrensm@janelia.hhmi.org (M.B.A.)**

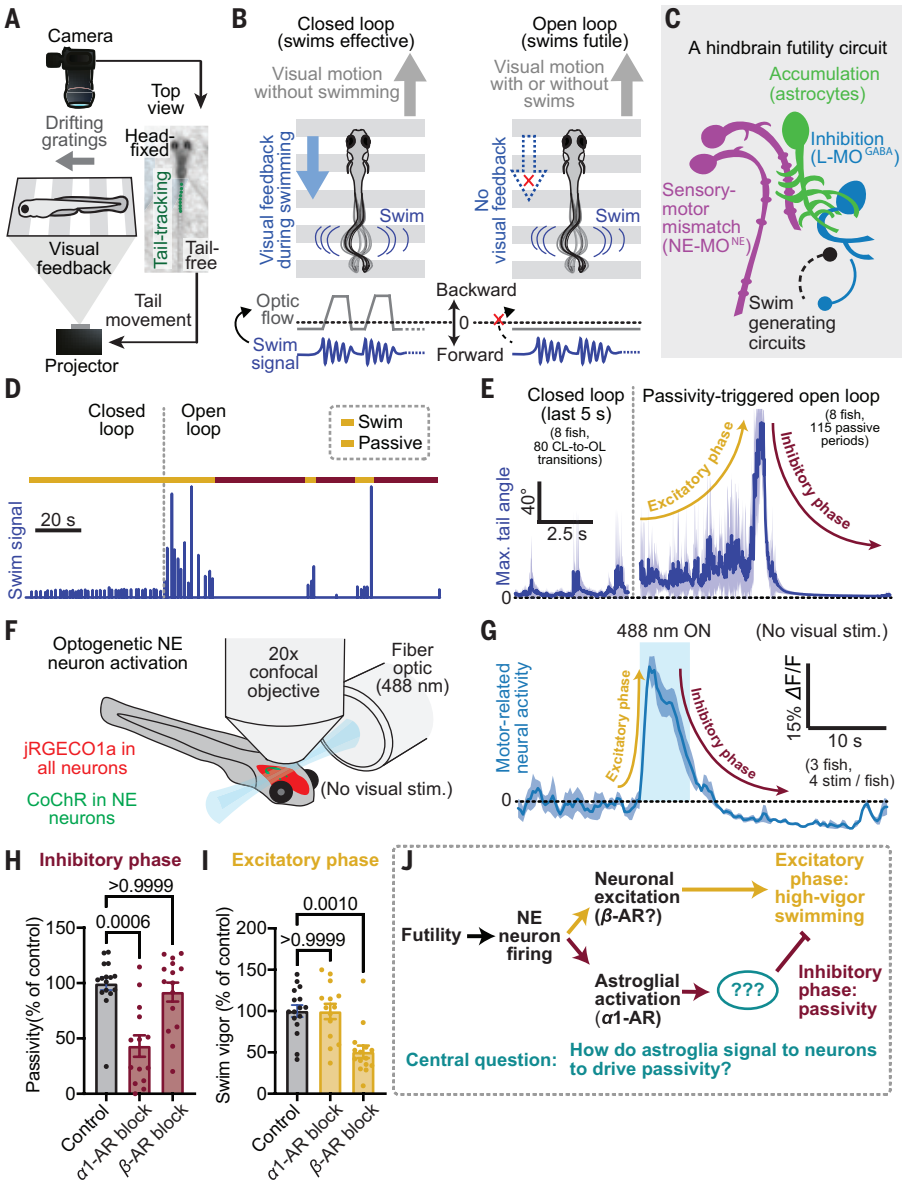

Fig. 1. Futility triggers a biphasic behavioral and neural response through NE neuron activation. (**A**) Schematic of virtual reality behavioral experiments with real-time swim detection and visual feedback. (**B**) Diagram illustrating the difference between closed-loop (visual feedback in response to swims) and open-loop (no visual feedback) conditions. (**C**) Schematic of the known cell types involved in futility-induced passivity. (**D**) Swim trace of an example trial demonstrating closed-loop and open-loop swim behavior. (**E**) Average closed-loop and passivity-triggered open-loop tail angle demonstrating an initial increase in swim amplitude (excitatory phase) followed by inhibition of swimming (inhibitory phase) in open loop. (**F**) Neural activity imaged with a confocal microscope while NE neurons were optogenetically activated using a fiber-optic cable. (**G**) Optogenetic stimulation–triggered average of neural activity in motor areas demonstrating fast excitation and delayed inhibition, similar to the behavioral futility response. (**H** and **I**) Effect of blocking α1-ARs (with 100 μM prazosin) or β-ARs (with 100 μM propranolol) on open-loop passivity (H) and open-loop swim vigor (I). For (H) and (I), $n = 16$ control, $n = 14$ α1-AR block, and $n = 15$ β-AR block fish. For (H), $P > 0.9999$ for control versus β-AR block fish and $P = 0.0006$ for control versus α1-AR block fish. For (I), $P = 0.001$ for control versus β-AR block fish and $P > 0.9999$ for control versus α1-AR block fish by Kruskal-Wallis test. (**J**) Model of parallel noradrenergic channels that contribute to the excitatory and inhibitory phases of the futility response and central problem statement. All error bars and shaded error regions represent SEM.

enhance arousal and effort (*21*, *52*), we tested whether NE neuron firing immediately promotes the rapid enhancement of vigor, in addition to driving temporally delayed swim inhibition (Fig. 1F and fig. S2). We found that optogenetic stimulation of NE neurons drove fast excitation and persistent but delayed inhibition of hindbrain motor circuits (Fig. 1G and fig. S2, A to C). We further observed that persistent inhibition of motor circuits coincided with sustained activity in L-MO (*49*) (fig. S2D). Therefore, in larval zebrafish, behavioral futility promotes a biphasic response in both behavior and neural dynamics, which can be defined as an excitatory phase consisting of increased behavioral vigor, followed by an inhibitory phase involving behavioral suppression (Fig. 1, E and G). Both phases are driven by NE neuron firing.

NE neurons act on downstream targets through activation of α-ARs and β-ARs by NE, as well as through fast synaptic excitation through co-released glutamate. Astroglial calcium elevation through α1-AR activation has been shown to be both necessary and sufficient for the inhibitory phase of the futility response in larval zebrafish (*49*), but its relationship to the excitatory phase of the futility response is less understood. Our findings suggest that astroglial calcium signaling is not involved in the excitatory phase. First, optogenetic stimulation of NE neurons elevated astroglial calcium with a temporal delay likely too long to account for the more rapid increase in motor activity (fig. S3A). Second, inhibition of α1-AR signaling with prazosin, which completely abolishes NE-evoked astroglial calcium responses (*49*), had no effect on futility-induced vigor enhancement but did suppress futility-induced passivity (Fig. 1, H and I). Thus, α1-AR signaling and astroglial calcium elevation are likely dispensable for the excitatory phase.

The activation of α1-ARs and downstream astroglial calcium elevation seem to act in a feedforward inhibitory–like manner. Feedforward inhibition in synaptic networks serves to sharpen the window of excitatory drive (*53*, *54*). Similarly, elevating astroglial calcium activation through optogenetic stimulation in *Tg(gfap:CoChR-eGFP)* fish or inhibiting calcium using prazosin shortened or lengthened the window of higher-vigor open loop swimming, respectively (fig. S3, B and C). Furthermore, longer-duration NE-MO stimulation reliably triggered swim cessation within a few seconds (fig. S3D) despite NE likely remaining elevated for much longer (*50*). This is consistent with feedforward inhibition, rather than feedback inhibition, of noradrenergic drive.

Conversely, blockade of β-ARs strongly attenuated the excitatory phase (Fig. 1, H and I), suggesting that different adrenergic receptor subtypes may implement different aspects of the futility response. Blocking β-ARs also reduced passivity in some fish, potentially because inhibiting the excitatory phase reduces higher-vigor struggles, leading to less NE release (*26*, *49*) and lowering subsequent passivity. Alternatively, β-ARs could mediate feedback inhibition of the excitatory phase. In any case, specific astroglial involvement in the inhibitory phase raises a fundamental question that is central to this work (Fig. 1J): Because neurons ultimately control motor output, how do astroglia signal to downstream neurons to drive the inhibitory phase by suppressing swimming?

Futility-induced, NE-dependent astroglial ATP release

We reasoned that astroglia likely communicate with downstream neurons by secreting a neuroactive substance. In particular, we hypothesized that futility drives calcium-dependent astroglial release of ATP, because glial-derived ATP can modulate neural activity in other contexts (*43*, *44*, *55*, *56*). To investigate whether futility-induced astroglial calcium elevation leads to release of ATP, we generated a fish line (*Tg(gfap:GRAB$_{ATP}$;gfap:jRGECO1a)*) expressing GRAB$_{ATP}$, an extracellular green fluorescent ATP sensor (*57*), as well as the intracellular red fluorescent calcium sensor jREGCO1, in astroglia (see the materials and methods). First, we validated the specificity of GRAB$_{ATP}$ for ATP over adenosine in fish (fig. S4A). We then performed simultaneous brain-wide functional imaging of both glial calcium and secreted ATP while immobilized animals behaved in virtual reality (see the materials and methods) (Fig. 2A). We found that during open-loop swimming, both astroglial intracellular calcium and extracellular ATP around astroglia exhibited a rapid elevation throughout the hindbrain, followed by a slower return to baseline over tens of seconds (Fig. 2, B to D).

These data suggest that astroglia, and not neurons, release ATP during futile swimming. However, because the ATP sensor used is extracellular, it cannot distinguish between astroglial-secreted ATP and ATP released by neurons near astroglial processes. However, five additional lines of evidence support an astroglial origin for the released ATP. First, ATP elevation lags behind intracellular astroglial calcium elevation (fig. S4, B to D), consistent with astroglial calcium elevation causing ATP release. Second, simultaneous imaging of neuronal calcium activity and extracellular ATP revealed that neuronal calcium elevation failed to reliably predict ATP release, whereas glial calcium events were always accompanied by ATP elevation (fig. S4, E to G). Third, inhibition of astroglial calcium with pharmacological blockade of α1-ARs strongly attenuated both futility-triggered ATP elevation (Fig. 2E) and astroglial calcium (fig. S4H), but had no effect on closed-loop ATP or astroglial calcium dynamics (fig. S4H). Because this pharmacological manipulation is not cell-type specific we also generated a fish expressing the calcium extruder hPMCA2 specifically in astroglia (*Tg(gfap:hPMCA2-mCherry)*). Astroglial-specific hPMCA2 expression

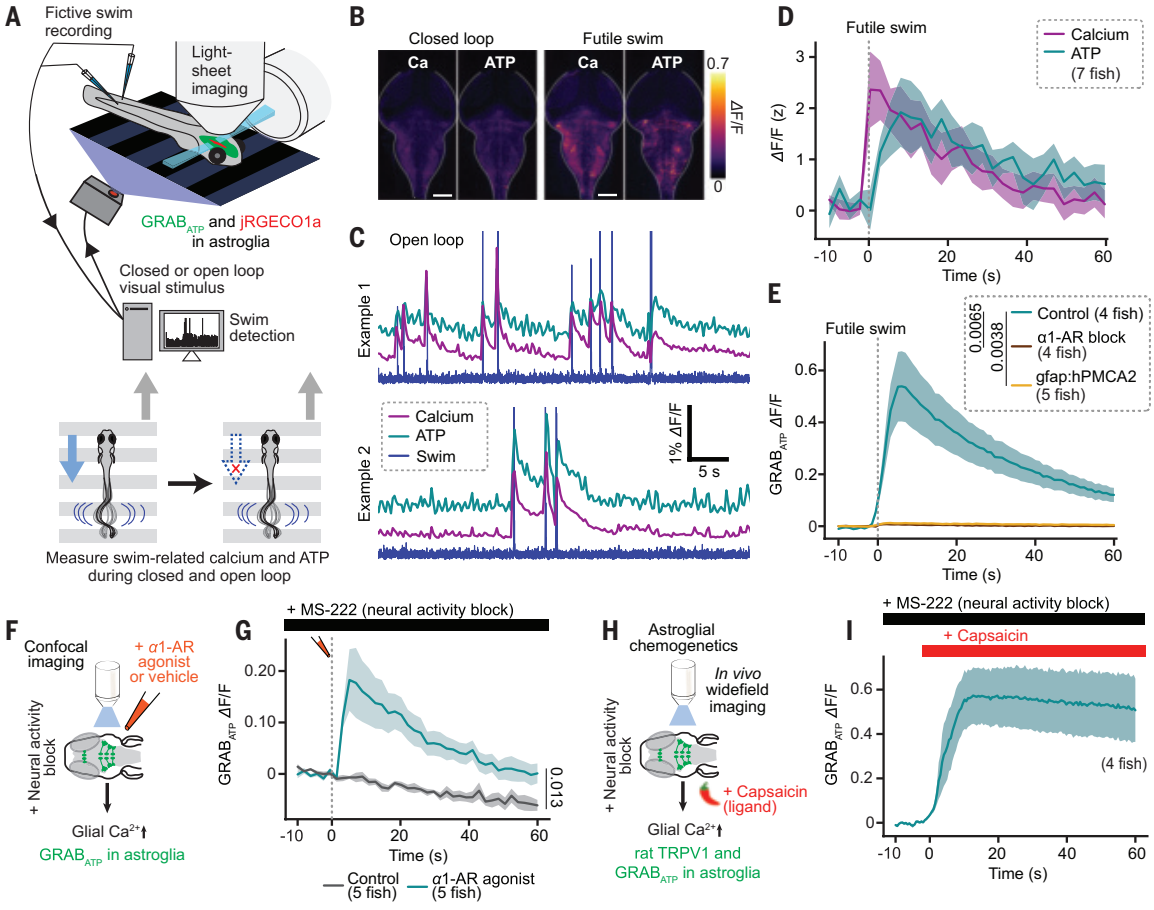

Fig. 2. Futility drives astroglial release of ATP. (**A**) Experimental schematic: two-color light-sheet imaging of extracellular ATP and astroglial calcium in *Tg(gfap:GRAB$_{ATP}$;gfap:jRGECO1a)* fish along with fictive behavioral recording. (**B**) Fluorescence micrographs of simultaneously collected GRAB$_{ATP}$ and jRGECO1a signals in a fish in baseline condition or during a futile swim. (**C**) Two examples of motor nerve electrical activity, GRAB$_{ATP}$ and jRGECO1a, signals during open-loop periods. Swim, calcium, and ATP traces are manually offset along the vertical axis to allow for better visualization. (**D**) Futile swim–triggered astroglial calcium and extracellular ATP signals averaged across fish ($n = 7$). (**E**) Futile swim–triggered GRAB$_{ATP}$ signal in fish treated with an α1-AR blocker (100 μM prazosin) or vehicle and in fish expressing hPMCA2 in astroglia ($n = 4$ control, $n = 5$ α1-AR block, and $n = 5$ hPMCA2). $P = 0.0065$ for control versus α1-AR block fish and $P = 0.0038$ for control versus hPMCA2 fish. Kruskal-Wallis test on area under the curve (AUC) from 0 to 60 s was used. (**F**) Experimental schematic: ex vivo confocal imaging during puffing of an α1-AR agonist (10 μM methoxamine) or vehicle in the presence of a neural activity blocker (160 mg/liter MS-222, a sodium channel inhibitor) in *Tg(gfap:GRAB$_{ATP}$)* fish. (**G**) GRAB$_{ATP}$ signal in fish in experiments described in (F) triggered on puff and futility onset aligned ($n = 5$ for both conditions). $P = 0.013$, Mann-Whitney on AUC from 0 to 60 s. (**H**) Experimental schematic: in vivo wide-field imaging during chemogenetic activation of *Tg(gfap:rTRPV1-eGFP)* fish with 200 nM capsaicin in the presence of a neural activity blocker (170 mg/L MS-222). (**I**) GRAB$_{ATP}$ signal in fish treated with capsaicin as described in (F) triggered capsaicin administration and futility onset aligned. All error bars and shaded error regions represent SEM.

inhibited astroglial calcium elevation during futile swims (fig. S5A) and, accordingly, decreased the duration of passivity in open loop (fig. S5, B to E). This effect was not caused by a decrease in general health of the animal or in the health of astroglia, because animals expressing hPMCA2 in astroglia behaved similarly to their wild-type siblings during normal swimming (fig. S5, F to H) and had astroglia that still exhibited microdomain calcium events (fig. S5, I to K). Inhibiting glial calcium elevation with hPMCA2 also suppressed futile swim–evoked ATP elevation (Fig. 2E). Fourth, pharmacological activation of α1-ARs was sufficient to cause ATP elevation even when neural activity was inhibited with a sodium channel blocker (Fig. 2, F and G). Finally, direct chemogenetic activation of astroglia also elevated ATP when neural activity was inhibited (Fig. 2, H and I). Neither pharmacological nor chemogenetic astroglial activation affected neuronal activity under conditions of sodium channel block (fig. S6, A and B). These converging lines of evidence implicate NE-mediated astroglial, and not neuronal, calcium signaling as being critical for extracellular ATP elevation during behavioral futility.

ATP promotes passivity through extracellular metabolism into adenosine

We investigated whether ATP elevation promotes passivity by treating fish with NPE-caged ATP, a P(3)-[1-(2-nitrophenyl)]ethyl ester of ATP that is pharmacologically inert until exposed to ultraviolet (UV) light (Fig. 3A). Freely swimming fish treated with caged ATP or vehicle were exposed to UV light, and passivity duration was recorded. UV light constitutes an inescapable aversive stimulus, conceptually similar to the open-loop conditions described in Fig. 1. As a result, fish exposed to UV light eventually exhibited futility-induced passivity after a period of high-vigor swimming (Fig. 3B and fig. S7A). However, fish treated with caged ATP exhibited increased passivity compared with vehicle controls (Fig. 3, B and C) while exhibiting no difference in struggle onset or time to peak swimming (fig. S7B). Therefore, ATP elevation drives the inhibitory, but not the excitatory, phase of futility-induced passivity.

Having established that ATP is an astroglia-to-neuron signal that induces passivity, we next sought to determine the mechanism through which ATP release suppresses swimming. ATP directly binds to two families of purinergic (P2) receptors, ionotropic P2X receptors and metabotropic P2Y receptors. Broad P2 receptor inhibition with suramin (100 μM bath administration) did not inhibit futility-induced passivity (Fig. 3D). This result suggests that although ATP elevation drives passivity, P2 purinergic receptors do not mediate futility-induced swimming suppression.

Because direct action of ATP does not seem to play an important role in futility-induced passivity, we considered an alternative hypothesis in which the ATP metabolite adenosine acts directly on neurons and suppresses swimming. Once secreted into the extracellular space, ATP is rapidly metabolized into adenosine through the action of two membrane-localized, extracellular-facing enzymes: Cd39 (or Entpd), which converts ATP into AMP by hydrolyzing the γ- and β-phosphate residues of ATP, and Cd73 (or Nt5e), which catabolizes AMP into adenosine (*39*) (Fig. 3E). In the spinal cord, such extracellular ATP-to-adenosine conversion is thought to contribute to locomotor rhythms (*35*). We performed two experiments to test the involvement of both components of this extracellular, biochemical pathway in futility-induced passivity. First, we blocked Cd73 with AMPCP and found that futility-induced passivity was inhibited (Fig. 3, E and F). Additionally, we treated fish with ARL 67156, a nonhydrolyzable ATP analog and competitive Cd39 inhibitor (Fig. 3E), and used optogenetics to directly activate astroglia (fig. S7C). Consistent with our previous work (*49*), optogenetic stimulation of astroglia caused passivity in untreated fish, mimicking the effect of astroglial calcium increases during natural futility-induced passivity. However, pretreatment with ARL 67156 delayed passivity in response to optogenetic astroglial stimulation (Fig. 3G). Although optogenetic stimulation of astroglia has been shown in some cases to elicit nonphysiological calcium responses (*58*–*60*), the stimulation here elicited behavioral output similar to open-loop visual stimuli. These results indicate that the passivity-stimulating action of extracellular ATP is mediated by extracellular biochemical pathways that metabolize it into adenosine.

To directly visualize extracellular adenosine dynamics during futility-induced passivity, we generated a fish line expressing the extracellular green fluorescent adenosine sensor $GRAB_{Ado1.0}$ (*32*) in neurons and found that, as predicted by our behavioral experiments (Fig. 3, E to G), extracellular adenosine increased during futile swims (Fig. 3, H and I). Preventing astroglial activation, and therefore ATP release, by blocking α1-ARs with prazosin abolished futility-induced adenosine elevation (Fig. 3I, blue). Further, inhibiting metabolism of astroglial-secreted ATP into adenosine with ARL 67156 attenuated adenosine buildup during futility (Fig. 3I, red). Finally, inhibiting ATP-to-adenosine metabolism prevented $GRAB_{Ado1.0}$ elevation to exogenously applied ATP (fig. S8, A and B). These experiments indicate that adenosine elevation, downstream of astroglial ATP release, is a component of the futility-induced astroglial noradrenergic-to-purinergic pathway.

Adenosine acts as a signaling molecule in the central nervous system primarily by binding G protein–coupled adenosine receptors. To assess the involvement of adenosine receptors in the futility response, we performed pharmacological experiments to either drive or inhibit adenosine receptor signaling. We found that the adenosine receptor agonist 2-chloroadenosine increased passivity and decreased the swim rate in both closed loop and open loop (fig. S8, C to E), demonstrating that adenosine receptor activation is sufficient to trigger passivity. Nonspecific inhibition of adenosine receptor signaling with caffeine, an adenosine receptor antagonist, suppressed open-loop passivity (Fig. 3J, left) but had no effect on open-loop struggle probability (Fig. 3J, right). The suppression of passivity did not result from effects upstream of astroglial calcium, because caffeine did not decrease astroglial calcium elevation or ATP secretion in response to NE (if anything, both seemed to increase after caffeine treatment, but the effect was variable) (fig. S8, F and G). Caffeine has off-target effects unrelated to its inhibition of adenosine receptors. However, we found that directly buffering adenosine with the high-affinity sensor $GRAB_{Ado1.0}$ also resulted in a small but significant reduction in futility-induced passivity compared with their wild-type siblings (fig. S8H, $P = 0.0355$). Finally, more specific blockade of A2B adenosine receptors (A2BRs), but not A1Rs or A2ARs, inhibited futility-induced passivity (Fig. 3, K and L). Therefore, the astroglial noradrenergic-to-purinergic pathway recruited by futility implements the inhibitory, but not excitatory, phase of the futility response primarily through A2Rs on downstream neurons.

Adenosine drives swim-suppressing neurons in the lateral medulla

Neurons are the cells that ultimately control swimming. Therefore, we reasoned that futility-induced astroglial adenosine release acts on neural targets to drive passivity. Because our pharmacological evidence supported a role for the A2BR (Fig. 3L), we performed in situ hybridization with probes targeting *adora2b* (mRNA for A2BR) transcripts and found, consistent with previous reports (*61*), *adora2b* expression in the midbrain and hindbrain, near the midline and in the subventricular zone (SVZ), as well as in bilaterally symmetrical hindbrain neuronal populations (fig. S9). Neuronal expression of *adora2b* appeared anatomically proximal to L-MO, a population that is activated by futility and suppresses swimming (Fig. 4, A and B, and fig. S10) (*49*). Imaging L-MO activity during behavior in *Tg(elavl3:jRGECO1a)* fish revealed that inhibition of adenosine receptors with caffeine reduced the magnitude and duration of persistent L-MO activation triggered by high-amplitude futile swims (Fig. 4C). This reduction was also reflected in a decrease in average futility-triggered passivity duration (Fig. 4D). Possible interpretations of the remaining struggle-induced L-MO activation is an incomplete block by caffeine or occurring through mechanisms independent of adenosine receptor activation. Furthermore, chemogenetic activation of astroglia using *Tg(gfap:TRPV1-eGFP;elavl3:jRGECO1a)* fish increased the rate of L-MO activation events, and the adenosine receptor

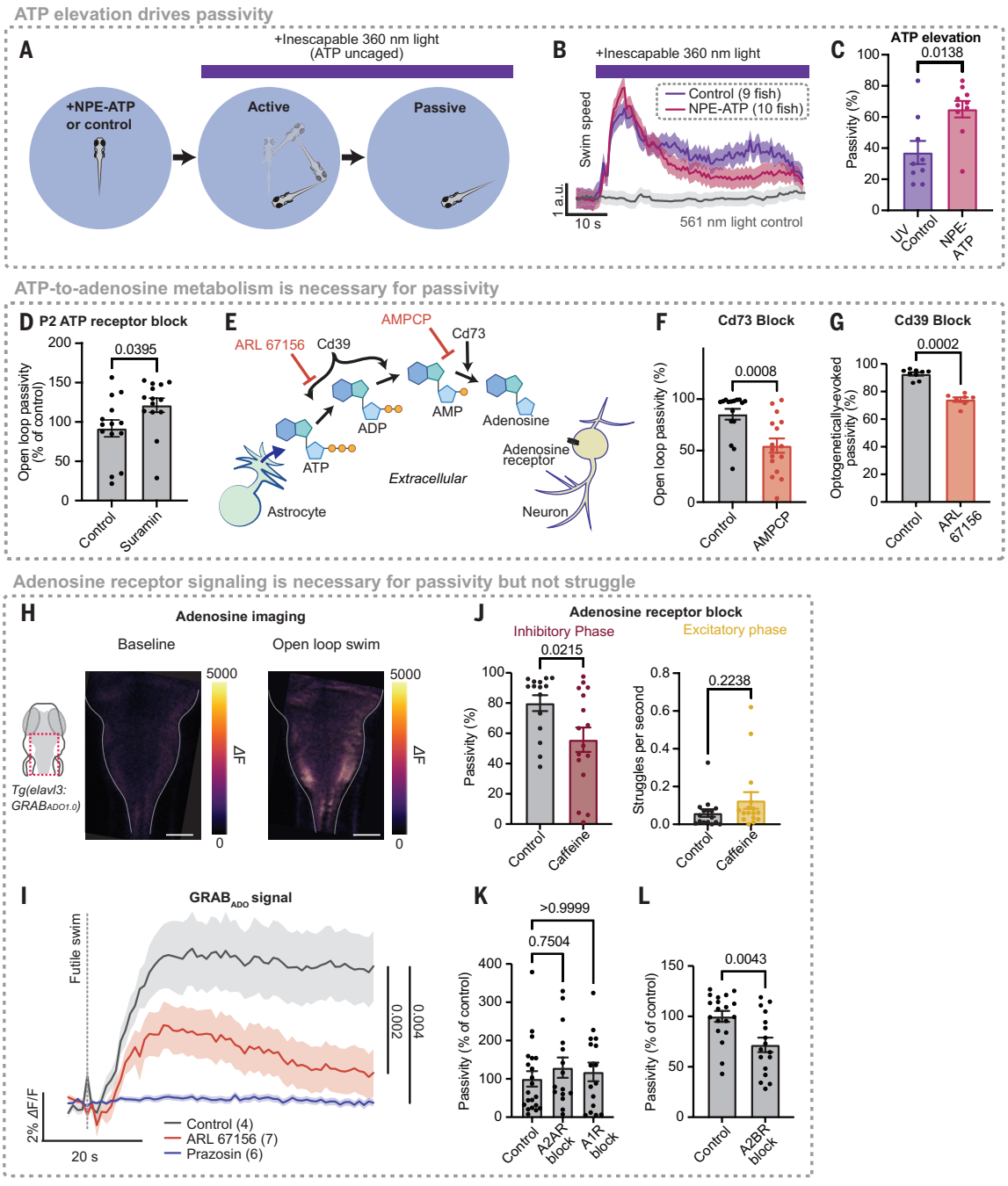

Fig. 3. ATP promotes passivity through extracellular metabolism into adenosine. (**A**) Experimental schematic: behavioral recording of freely swimming fish treated with 100 μM NPE-ATP or vehicle and then subjected to inescapable UV (360 nm) light, which uncages ATP. (**B**) Light onset–triggered swim speed of fish treated with NPE-ATP or vehicle. (**C**) Percentage of light ON period spent passive for vehicle control and NPE-ATP–treated fish ($n = 9$ control and $n = 10$ NPE-ATP fish). $P = 0.0138$, Mann-Whitney test. (**D**) Effect of a P2 receptor blocker (100 μM suramin) or vehicle on open-loop passivity in head-fixed behavior ($n = 14$ control and $n = 14$ suramin-treated fish). $P = 0.0395$, Mann-Whitney test. (**E**) Diagram illustrating the extracellular biochemical ATP-to-adenosine pathway through the enzymes Cd39 and Cd73 and pathway inhibition by the competitive Cd39 inhibitor ARL 67156 and the Cd73 inhibitor AMPCP. (**F**) Effect of Cd73 block (100 μM AMPCP) on open-loop passivity in head-fixed behavior ($n = 16$ control and $n = 16$ AMPCP fish). $P = 0.0008$, Mann-Whitney test. (**G**) Percentage passivity after the onset of optogenetic stimulation for fish treated with ARL 67156 or vehicle ($n = 9$ control and $n = 7$ ARL 67156 fish). $P = 0.0002$, Mann-Whitney test. (**H**) Extracellular adenosine ($GRAB_{ADO1.0}$) signal of a fish in baseline (left) and during a futile swim (right). (**I**) Futile swim–triggered average of $GRAB_{ADO1.0}$ signal in fish treated with vehicle, an α1-AR blocker (100 μM prazosin), or a Cd39 inhibitor (1 mM ARL 67156) ($n = 4$ control, $n = 7$ ARL 67156, and $n = 6$ prazosin fish). $P = 0.002$ for control versus ARL and $P = 0.004$ for control versus prazosin, Kruskal-Wallis on AUC from 0 to 60 s after futile swim. (**J**) Effect of vehicle or adenosine receptor blocker (100 μM caffeine) on the proportion of open loop spent passive (left) and open-loop struggle rate (right) ($n = 15$ control and $n = 16$ caffeine). $P = 0.0215$ for proportion passivity and $P = 0.2238$ for struggle rate, Mann-Whitney test. (**K** and **L**) Effect of an A1R blocker (DPCPX) and an A2AR blocker (SCH-58261) (K) or an A2BR blocker (MRS 1754) (L) on proportion of open loop spent passive. For (K), $n = 21$ control, $n = 15$ DPCPX and $n = 16$ SCH-58261. For (L), $n = 19$ control and $n = 17$ MRS 1754. All error bars and shaded error regions represent SEM.

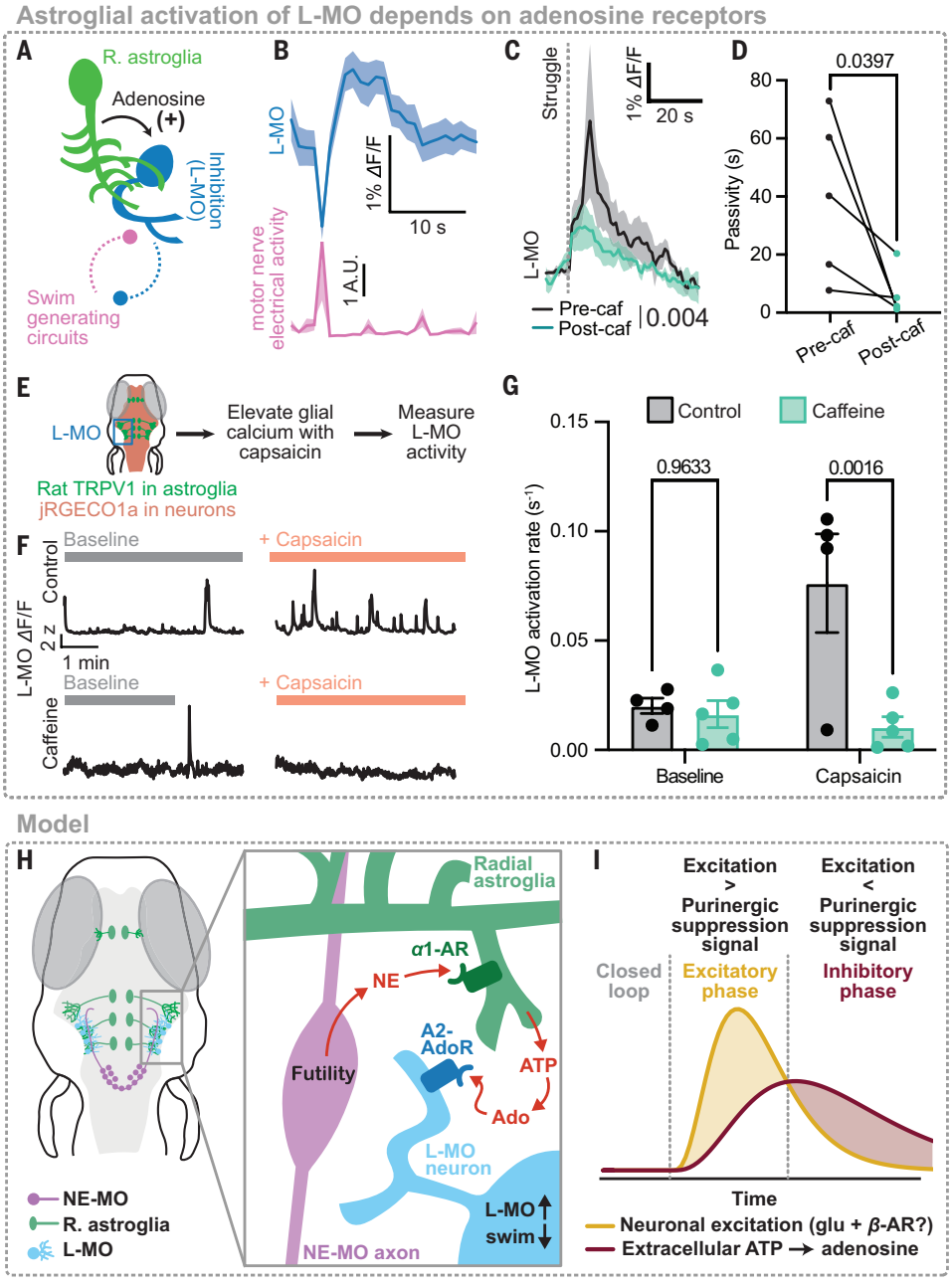

Fig. 4. Adenosine persistently activates the swim-suppressing region L-MO. (**A**) Schematic: astroglial communication with L-MO and mutual inhibition between L-MO and motor regions. (**B**) Example of L-MO neuronal activity anticorrelation to swim vigor in one fish. (**C**) Struggle-evoked L-MO activity before and after caffeine (100 μM). Shown is the mean across five fish ($n = 5$). $P = 0.004$, Mann-Whitney on AUC from 0 to 60 s after struggle. (**D**) Mean of futility swim–triggered passivity durations before and after caffeine treatment ($n = 5$). $P = 0.0397$, paired t test. (**E**) Schematic: activating astroglia in *Tg(gfap:TRPV1-eGFP;elavl3:JRGECO1a)* fish while imaging L-MO activity using light-sheet microscopy. (**F**) L-MO activity in four example fish treated with either vehicle control (top row) or 100 μM caffeine (an adenosine receptor blocker, bottom row) or vehicle control, either in baseline untreated condition (left) or with capsaicin (right). (**G**) Summary of rate of L-MO activation across all fish and conditions ($n = 4$ control and $n = 5$ caffeine). $P = 0.9633$ for baseline control versus caffeine and $P = 0.0016$ for capsaicin control versus caffeine, two-way ANOVA with Šídák's multiple-comparisons test. (**H**) Model: futility-triggered NE release drives astroglial ATP release. ATP is metabolized extracellularly into adenosine, and adenosine activates A2 adenosine receptors in L-MO to increase L-MO activity and suppress swimming. (**I**) Model: futility-related NE-MO firing drives fast excitation (yellow). NE mediates delayed inhibition (red) through astroglial activation, ATP release, and ATP-to-adenosine metabolism. Eventually, inhibition overcomes fast excitation to drive the inhibitory phase of passivity. Thus, an astroglial noradrenergic-to-purinergic pathway mediates feedforward inhibition of the passivity response. All error bars and shaded error regions represent SEM.

antagonist caffeine inhibited this increase but had no effect on baseline L-MO activity (Fig. 4, E to G). A caveat of this experiment is that our chemogenetic activation of astroglia causes astroglial calcium elevation across large areas of the brain; therefore, in this experiment we cannot rule out involvement of regions beyond L-MO in suppressing swimming. However, we previously demonstrated that L-MO is likely the primary driver of futility-induced passivity (*49*). Altogether, these data provide evidence that the purinergic signal released by astroglia exerts feedforward inhibition on motor circuits through the activation of inhibitory neurons in L-MO through A2BRs (Fig. 4, H and I).

Discussion

Our work shows that the rapid state transition orchestrated by NE proceeds through astroglia using purinergic neuromodulation. We identified a functional logic connecting these two critical neuromodulatory systems: Noradrenergic neurons drive fast excitation but also recruit purinergic signaling through astroglia to implement delayed, feedforward inhibition. Thus, astroglia play a central role in coordinating across different neuromodulatory systems.

The NE-astroglia-purinergic pathway is recruited when actions become futile and a behavioral state change is necessary, analogous to NE-mediated transitions under the "global model failure" conceptualization of NE function (*18*–*20*, *62*). The components of this pathway, monoamine-triggered astroglial calcium signaling, astroglial ATP release, extracellular ATP-to-adenosine conversion, and adenosinergic suppression of neural activity, are ubiquitous across brain regions and species, which suggests that this conserved NE-astroglia-purinergic (NAP) signaling motif could be a fundamental computational unit implementing feedforward inhibition over neuromodulatory timescales (*63*–*65*). Indeed, a companion paper by Lefton *et al.* (*65*) demonstrates that NE's well-known depressive effect on excitatory synapses in mice proceeds entirely through this same NE-astroglia-ATP/adenosine pathway, and several additional emerging lines of evidence support the behavioral importance of this pathway in mammals (*66*, *67*). Our results, along with those of Lefton *et al.* (*66*), argue that the neuromodulatory effects of NE, and perhaps other neuromodulators, must be reconsidered under the lens of astroglial modulation of neurophysiology and circuit dynamics.

Feedforward inhibition is widespread in synaptically coupled circuits (*53*, *54*, *69*, *70*). Synaptic feedforward inhibition serves many functions, such as improving the spatial and

temporal precision of neural coding (*53*, *54*), gain control (*69*), and improving sensory acuity (*70*). Here, we show that feedforward inhibition can also be implemented through molecular circuits to play similar computational roles on much longer timescales (tens of seconds) that are complementary to the millisecond timescales of neuronal feedforward inhibition. Although astroglial activation by NE is widespread and quite synchronized, output diversification may occur at each step, from ATP release to ATP-to-adenosine metabolism and finally to adenosine receptor activation. For example, adenosine receptor expression could be altered in different brain regions, the sensitivity of astroglia to NE could be modulated by local neuronal activity, or the activity of the extracellular enzymes that transform ATP into adenosine could be tuned to modulate this extrasynaptic circuit motif in a context-dependent manner. Astroglia-mediated feedforward inhibition may therefore be similarly flexible and ubiquitous but operate on slower timescales.

Over the past few decades, several lines of work have raised the possibility of an evolutionarily conserved role for the NAP motif in feedforward inhibition. Classic work has shown that an ATP-to-adenosine pathway acts in the spinal cord to inhibit locomotion in tadpoles (*35*), and more recent work suggests that astroglia contribute to spinal cord ATP release and locomotion suppression in rodents (*71*). Astroglia have also been shown to drive the inhibitory phases of a variety of episodic behaviors such as sleep (*72*) and sensory-evoked arousal (*30*, *73*). We speculate that the seemingly conserved role for astroglia in feedforward inhibition after rapid excitation may reflect—and may have arisen from—a fundamental astroglial function to regulate neuronal network excitability. Indeed, both astroglia and purinergic signaling play central roles in controlling excitability (*64*, *74*), and astroglial and purinergic dysfunction is implicated in epileptic seizure generation (*75*). Because astroglia have multiple molecular pathways for modulating neuronal excitation, such as those involved in potassium buffering, purinergic release, and glutamate metabolism (*75*, *76*), an ancestral astroglial role in excitability regulation may have been appropriated to modulate circuit activity in many different behaviorally relevant contexts to modulate neuronal excitability.

REFERENCES AND NOTES

1. M. V. Bennett, Y. Nakajima, G. D. Pappas, *J. Neurophysiol.* **30**, 161–179 (1967).
2. A. Bhattacharya, U. Aghayeva, E. G. Berghoff, O. Hobert, *Cell* **176**, 1174–1189.e16 (2019).
3. S. J. Smith *et al.*, *eLife* **8**, e47889 (2019).
4. M. Lovett-Barron *et al.*, *Cell* **171**, 1411–1423.e17 (2017).
5. J. C. Marques, M. Li, D. Schaak, D. N. Robson, J. M. Li, *Nature* **577**, 239–243 (2020).
6. C. I. Bargmann, E. Marder, *Nat. Methods* **10**, 483–490 (2013).
7. F. Randi, A. K. Sharma, S. Dvali, A. M. Leifer, *Nature* **623**, 406–414 (2023).
8. L. Ripoll-Sánchez *et al.*, *Neuron* **111**, 3570–3589.e5 (2023).
9. S. L. Hooper, E. Marder, *Brain Res.* **305**, 186–191 (1984).
10. S. R. Yeh, R. A. Fricke, D. H. Edwards, *Science* **271**, 366–369 (1996).
11. P. S. Katz, P. A. Getting, W. N. Frost, *Nature* **367**, 729–731 (1994).
12. J. S. Coggan *et al.*, *Science* **309**, 446–451 (2005).
13. G. Mountoufaris *et al.*, *Cell* **187**, 5998–6015.e18 (2024).
14. J. Nagai *et al.*, *Neuron* **109**, 576–596 (2021).
15. E. A. Bushong, M. E. Martone, Y. Z. Jones, M. H. Ellisman, *J. Neurosci.* **22**, 183–192 (2002).
16. G. Perea, M. Navarrete, A. Araque, *Trends Neurosci.* **32**, 421–431 (2009).
17. U. S. V. Euler, *Nature* **156**, 18–19 (1945).
18. R. Jordan, *Trends Neurosci.* **47**, 92–105 (2024).
19. R. Jordan, G. B. Keller, *eLife* **12**, RP85111 (2023).
20. D. G. R. Tervo *et al.*, *Cell* **159**, 21–32 (2014).
21. S. J. Sara, S. Bouret, *Neuron* **76**, 130–141 (2012).
22. G. Aston-Jones, J. D. Cohen, *Annu. Rev. Neurosci.* **28**, 403–450 (2005).
23. M. E. Hasselmo, C. Linster, M. Patil, D. Ma, M. Cekic, *J. Neurophysiol.* **77**, 3326–3339 (1997).
24. V. Zerbi *et al.*, *Neuron* **103**, 702–718.e5 (2019).
25. E. Bülbring, J. H. Burn, *J. Physiol.* **101**, 289–303 (1942).
26. A. Uribe-Arias *et al.*, *Neuron* **111**, 4040–4057.e6 (2023).
27. L. K. Bekar, W. He, M. Nedergaard, *Cereb. Cortex* **18**, 2789–2795 (2008).
28. F. Ding *et al.*, *Cell Calcium* **54**, 387–394 (2013).
29. Z. Ma, T. Stork, D. E. Bergles, M. R. Freeman, *Nature* **539**, 428–432 (2016).
30. M. E. Reitman *et al.*, *Nat. Neurosci.* **26**, 579–593 (2023).
31. T. Porkka-Heiskanen *et al.*, *Science* **276**, 1265–1268 (1997).
32. W. Peng *et al.*, *Science* **369**, eabb0556 (2020).
33. A. Suppermpool, D. G. Lyons, E. Broom, J. Rihel, *Nature* **629**, 639–645 (2024).
34. O. Pascual *et al.*, *Science* **310**, 113–116 (2005).
35. N. Dale, D. Gilday, *Nature* **383**, 259–263 (1996).
36. M. Wall, N. Dale, *Curr. Neuropharmacol.* **6**, 329–337 (2008).
37. D. van Calker, K. Biber, K. Domschke, T. Serchov, *J. Neurochem.* **151**, 11–27 (2019).
38. L. Weltha, J. Reemmer, D. Boison, *Brain Res. Bull.* **151**, 46–54 (2019).
39. T. V. Dunwiddie, L. Diao, W. R. Proctor, *J. Neurosci.* **17**, 7673–7682 (1997).
40. R. de Ceglia *et al.*, *Nature* **622**, 120–129 (2023).
41. D. Lovatt *et al.*, *Proc. Natl. Acad. Sci. U.S.A.* **109**, 6265–6270 (2012).
42. L. Yang, Y. Qi, Y. Yang, *Cell Rep.* **11**, 798–807 (2015).
43. M. J. Broadhead, G. B. Miles, *Front. Cell. Neurosci.* **14**, 30 (2020).
44. G. R. J. Gordon *et al.*, *Nat. Neurosci.* **8**, 1078–1086 (2005).
45. M. B. Orger, M. C. Smear, S. M. Anstis, H. Baier, *Nat. Neurosci.* **3**, 1128–1133 (2000).
46. E. Yang *et al.*, *Cell* **185**, 5011–5027.e20 (2022).
47. N. Jurisch-Yaksi, E. Yaksi, C. Kizil, *Glia* **68**, 2451–2470 (2020).
48. J. Chen, K. E. Poskanzer, M. R. Freeman, K. R. Monk, *Nat. Neurosci.* **23**, 1297–1306 (2020).
49. Y. Mu *et al.*, *Cell* **178**, 27–43.e19 (2019).
50. M. Duque *et al.*, *Neuron* **113**, 426–443.e5 (2025).
51. L. Rinaman, *Am. J. Physiol. Regul. Integr. Comp. Physiol.* **300**, R222–R235 (2011).
52. G. Moruzzi, H. W. Magoun, *Electroencephalogr. Clin. Neurophysiol.* **1**, 455–473 (1949).
53. F. Pouille, M. Scanziani, *Science* **293**, 1159–1163 (2001).
54. W. Mittmann, U. Koch, M. Häusser, *J. Physiol.* **563**, 369–378 (2005).
55. A. V. Gourine *et al.*, *Science* **329**, 571–575 (2010).
56. T. A. Babola *et al.*, *J. Neurosci.* **41**, 594–612 (2021).
57. Z. Wu *et al.*, *Neuron* **110**, 770–782.e5 (2022).
58. W.-H. Cho, E. Barcelon, S. J. Lee, *Exp. Neurobiol.* **25**, 197–204 (2016).
59. E. Gerasimov *et al.*, *Int. J. Mol. Sci.* **22**, 9613 (2021).
60. S. A. Sloan, B. A. Barres, *Neuron* **84**, 1112–1115 (2014).
61. W. Boehmler *et al.*, *Gene Expr. Patterns* **9**, 144–151 (2009).
62. C. Li *et al.*, *Neuron* **111**, 2727–2741.e7 (2023).
63. M. Corkrum *et al.*, *Neuron* **105**, 1036–1047.e5 (2020).
64. S. Pittolo *et al.*, *Cell Rep.* **40**, 111426 (2022).
65. T. Deemyad, J. Lüthi, N. Spruston, *Nat. Commun.* **9**, 4336 (2018).
66. K. B. Lefton *et al.*, *Science* **388**, 776 (2025).
67. Q. Xin *et al.*, *Cell* 10.1016/j.cell.2025.04.010 (2025).
68. G. T. Drummond *et al.*, Cortical norepinephrine-astrocyte signaling critically mediates learned behavior. bioRxiv 620009 [Preprint] (2024); https://doi.org/10.1101/2024.10.24.620009
69. S. R. Olsen, R. I. Wilson, *Nature* **452**, 956–960 (2008).
70. M. Wehr, A. M. Zador, *Neuron* **47**, 437–445 (2005).
71. D. Acton, G. B. Miles, *PLOS ONE* **10**, e0134488 (2015).
72. M. M. Halassa *et al.*, *Neuron* **61**, 213–219 (2009).
73. J. Lines, E. D. Martin, P. Kofuji, J. Aguilar, A. Araque, *Nat. Commun.* **11**, 3689 (2020).
74. A. Badimon *et al.*, *Nature* **586**, 417–423 (2020).
75. C. Diaz Verdugo *et al.*, *Nat. Commun.* **10**, 3830 (2019).
76. T. Miyashita *et al.*, *Science* **382**, eadf7429 (2023).
77. Data and analysis code for: A. B. Chen *et al.*, Norepinephrine changes behavioral state through astroglial purinergic signaling, Zenodo (2025); https://doi.org/10.5281/zenodo.14278354

ACKNOWLEDGMENTS

We thank M. Ellisman, D. Bergles, Y. Mu, and L. Looger, as well as members of the Engert and Ahrens labs, for discussions and feedback. **Funding:** This work was supported by Boehringer Ingelheim Fonds (Graduate Fellowship to M.Du. and A.R.), the European Research Council (ERC Consolidator grant ERC-CoG-101002870 to C.W.), the European Union (Horizon 2020 Research and Innovation program Marie Skłodowska-Curie grant 813457 to C.W.), Fondation Bettencourt Schueller (grant FBS-don-0031 to C.W.), the Howard Hughes Medical Institute (A.B.C., M.Du., S.N., M.B.A.); the National Institutes of Health (grant R35NS122172 to D.A.P., grants U19NS104653 and 1R01NS124017 to F.E., and grants U19NS123719 and R01MH110504 to G.Y.), the National Science Foundation (grant IIS-1912293 to F.E. and grant GRFP DGE1745303 to A.B.C.), and the Simons Foundation (grant SCGB 542943SPI to F.E. and M.B.A.). **Author contributions:** Conceptualization: A.B.C., M.B.A.; Funding acquisition: G.Y., C.W., D.A.P., F.E., M.B.A.; Investigation: A.B.C., M.Du.; Methodology: A.B.C., M.Du., A.R., M.Dh., V.M.W., X.M., A.R., E.M.L., M.E., S.N., D.A.P., G.Y.; Project administration: A.B.C., F.E., M.B.A.; Supervision: G.Y., C.W., D.A.P., F.E., M.B.A.; Visualization: A.B.C., M.Du., X.M.; Writing – original draft: A.B.C., M.B.A.; Writing – review & editing: all authors. **Competing interests:** The authors declare no competing interests. **Data and materials availability:** Data and analysis code are available at Zenodo (*77*).

License information: Copyright © 2025 the authors, some rights reserved; exclusive licensee American Association for the Advancement of Science. No claim to original US government works. https://www.science.org/about/science-licenses-journal-article-reuse

SUPPLEMENTARY MATERIALS

science.org/doi/10.1126/science.adq5233
Materials and Methods; Figs. S1 to S10; Table S1; References (*78*–*92*); MDAR Reproducibility Checklist; Movie S1

Submitted 20 May 2024; accepted 6 December 2024

10.1126/science.adq5233

NEUROPHYSIOLOGY

Norepinephrine signals through astrocytes to modulate synapses

Katheryn B. Lefton[1], Yifan Wu[1], Yanchao Dai[1], Takao Okuda[3], Yufen Zhang[3], Allen Yen[2], Gareth M. Rurak[1], Sarah Walsh[1], Rachel Manno[1]†, Bat-Erdene Myagmar[4], Joseph D. Dougherty[2], Vijay K. Samineni[3], Paul C. Simpson[4], Thomas Papouin[1]*

Locus ceruleus (LC)–derived norepinephrine (NE) drives network and behavioral adaptations to environmental saliencies by reconfiguring circuit functional connectivity, but the underlying synapse-level mechanisms are elusive. Here, we show that NE remodeling of synaptic function is completely independent from its binding on neuronal receptors. Instead, astrocytic adrenergic receptors and calcium dynamics fully gate the effect of NE on synapses. Additionally, we found that NE suppression of synaptic strength results from an adenosine 5′-triphosphate (ATP)–derived and A1 adenosine receptor–mediated control of presynaptic efficacy. These findings suggest that astrocytes are a core component of neuromodulatory systems and the circuit effector through which NE produces network and behavioral adaptations.

Neuromodulators exert global control over brain function and behavior by reshaping brain activity and functional connectivity. A canonical example, norepinephrine (NE), is produced by locus ceruleus (LC) neurons that extend NE-releasing projections throughout the brain (*1*). The activity of the LC-NE system is broadly associated with network adaptations in response to environmental contingencies, making it instrumental to brain state transitions, processing of sensory saliencies, as well as cognitive functions including goal-directed decision-making, learning, and cognitive flexibility (*2*, *3*). The functional relevance of LC-derived NE signaling relates to its ability to reconfigure neural circuits by altering the strength of synaptic connections within and across networks, with original evidence dating back eight decades (*4*–*6*). This is central to mesoscale theories that bridge the behavioral and cellular effects of the LC-NE system, such as the "adaptive gain" (*7*), "network reset" (*8*), and "global model failure" theories (*9*). However, in contrast to their broad applicability, these models conceal a surprisingly limited understanding of how NE controls synaptic function.

A broadly accepted view is that NE remodels synaptic connectivity by acting on cognate receptors on neurons (*1*, *2*), but this is now at odds with a growing appreciation for the multicellular nature of the brain and evidence that NE also signals onto non-neuronal cells such as astrocytes (*10*–*12*). Astrocytes are ubiquitous circuit components of the central nervous systems (CNS) of vertebrates and other bilaterians. They each form an extensive meshwork of ultrafine processes known to infiltrate and control the microenvironment of 10^5 synapses and other functional units, and they are increasingly recognized as state-dependent orchestrators of neural circuit function (*13*–*15*). Astrocytes express various noradrenergic receptors (*16*) and respond to NE occurrence with cell-wide elevations of intracellular free calcium (Ca^{2+}), a phenomenon observed across phylogenetically distant species (*12*, *13*, *16*–*19*). Ca^{2+}-dependent intracellular cascades, in turn, mobilize various forms of astrocyte activities and outputs that are potent regulators of synaptic and neuronal function (*17*–*20*). However, whether astrocytes actively contribute to the circuit effects of neuromodulators such as NE remains an open question.

LC-derived NE reduces synaptic efficacy

The ability of NE to reshape synaptic connectivity has been documented in diverse species, preparations, and regions of the CNS (*2*, *21*–*28*). To investigate the underlying mechanisms in a tractable system, we performed extracellular recordings of AMPAR-mediated field excitatory postsynaptic potentials (fEPSPs) in the stratum radiatum of acute hippocampal slices taken from adult mice (Fig. 1A, materials and methods, and fig. S1A). After a baseline period of 20 min, NE was bath applied continuously to mimic past studies. Consistent with previous work, this produced a marked and concentration-dependent decrease in synaptic strength (fEPSP slope; Fig. 1, B and C, and fig. S1B; for statistical analyses, see table S1). This rapid remodeling was distinct from the *N*-methyl-D-aspartate receptor (NMDAR)–mediated, activity-dependent long-term depression caused by NE (*26*, *29*) because it persisted in the presence of the NMDAR blocker D-AP5 and was still observed when synaptic stimulations were paused at the onset of NE application (fig. S1, D and E). The magnitude of NE-induced inhibition did not depend on initial synaptic properties (fig. S1F), which, together with the presence of γ-aminobutyric acid A receptor ($GABA_A$-R) blocker in the bath, ruled out the possibility of an inhibitory feedback mechanism. Changes in presynaptic properties were simultaneously assessed with a classic paradigm consisting of pairs of stimulations delivered 200 ms apart. This yielded a paired-pulse facilitation index (PPF) (see the materials and methods), which varies inversely with the probability of neurotransmitter release at presynaptic terminals. Concomitant to its effect on synaptic strength, NE elicited an increase in PPF, indicative of a reduction in release probability (Fig. 1, B and C). The increase in PPF and decline in fEPSP closely coincided in their temporal profiles (Fig. 1B), and their magnitude strongly correlated (Fig. 1D), pointing at a presynaptic effect of NE. A coefficient of variation ($1/CV^2$) analysis (fig. S1C) was also consistent with a presynaptic mechanism of action (*30*). To directly test this, we performed minimal-stimulation experiments in whole-cell patch-clamp recordings, which allow monitoring unitary excitatory postsynaptic currents (EPSCs) occurring at single synapses (Fig. 1, A and E, and materials and methods) (*31*). Under these conditions, an increased rate of presynaptic failures became apparent within minutes of NE application [decreased (pre)synaptic efficacy; Fig. 1, E to G], with no change in the amplitude of successful EPSCs [(post)synaptic potency], strongly suggesting that NE inhibits synapse strength (total EPSC amplitude) through a presynaptic mechanism.

Because single NE release events from individual LC-NE varicosities only increase volume-averaged NE to ~0.2 μM over a 50-μm-wide area, with local maxima of ~1 to 2 μM (*32*), we next used optogenetics to verify that these observations were not limited to the bath application of exogenous NE. To drive the specific expression of channel-rhodopsin (ChR2) in LC-NE neurons, we microinjected AAV5-*EF1α*::DIO-hChR2(H134R)-EYFP into the LC of *Dbh*^{Cre} knock-in mice expressing Cre recombinase from the endogenous dopamine beta-hydroxylase locus (*33*) (Fig. 1, H and I). Abundant expression of EYFP in LC-NE fibers that densely innervate the hippocampal CA1 became evident 10 weeks later and plateaued at 12 weeks (*34*) (Fig. 1I and fig. S1G). Acute hippocampal slices were obtained 12 weeks after injection (see the materials and methods), and fEPSPs and PPFs were recorded as above. Although they are often experimentally stimulated with paradigms as strong as 25 Hz, LC-NE fibers fire tonically at 1 to 3 Hz in vivo, with bouts of 10-Hz phasic activity (*35*). Accordingly, we found that an optical stimulation as weak as 1 Hz (450 nm, 15 mW, 10 min; Fig. 1J) caused

[1]Department of Neuroscience, Washington University in St. Louis, St. Louis, MO, USA. [2]Department of Genetics, Washington University in St. Louis, St. Louis, MO, USA. [3]Department of Anesthesiology, Washington University in St. Louis, St. Louis, MO, USA. [4]Deparment of Medicine and Research Service, San Francisco Veterans Affairs Medical Center and Cardiovascular Research Institute, University of California San Francisco, San Francisco, CA, USA.
***Corresponding author. Email: thomas.papouin@wustl.edu** †Present address: Department of Pediatrics, Washington University in St. Louis, St. Louis, MO, USA.

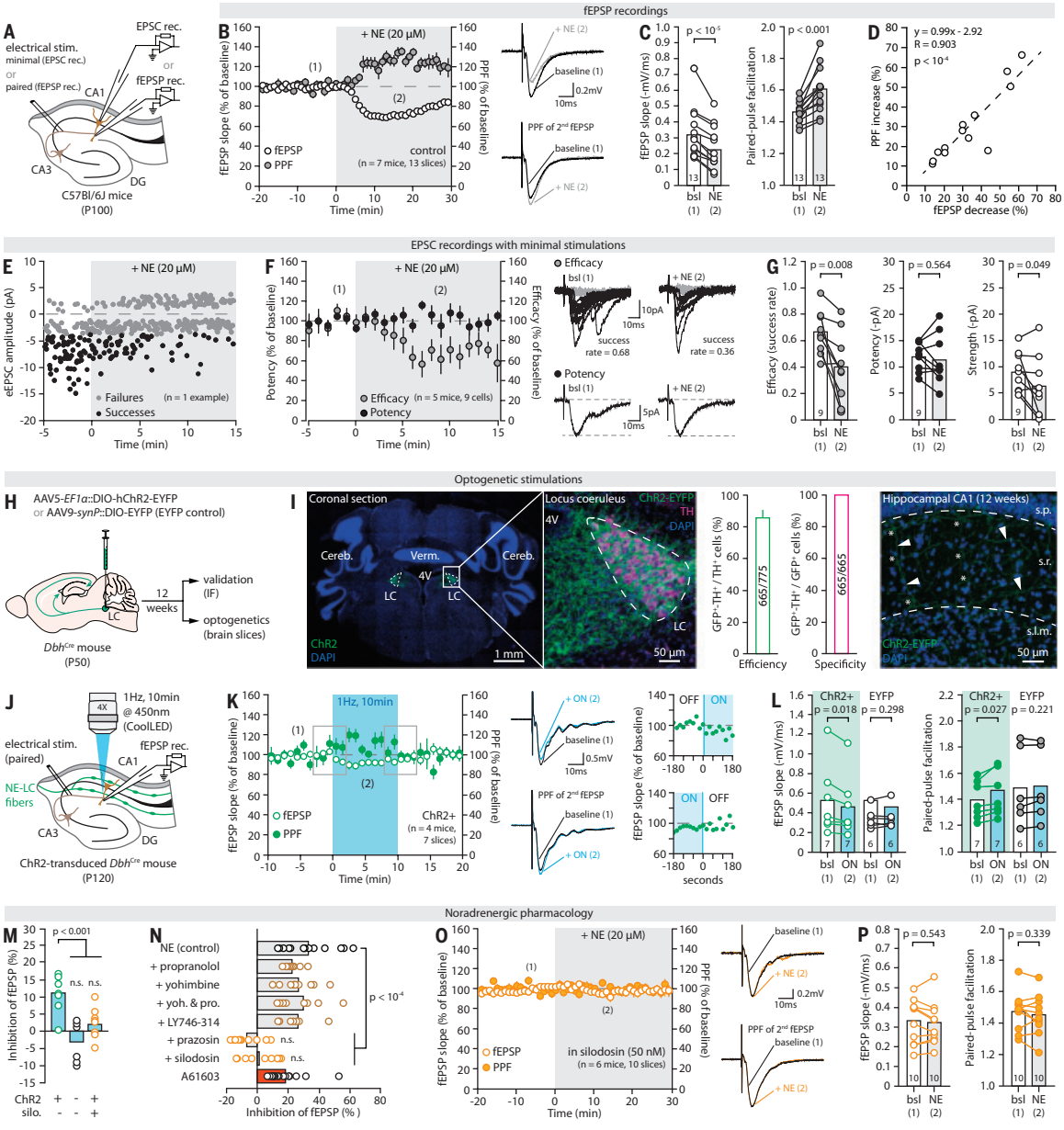

Fig. 1. NE and LC-NE activity inhibit presynaptic efficacy. (**A**) Schematic of the recording conditions. (**B**) Left: time course of the effect of 20 µM NE applied at time $t = 0$ (gray area) on fEPSP slope and PPF. Each circle is the average of three data points per minute. (1) and (2) indicate the approximate epochs at which sample traces were obtained and quantifications performed for the baseline and NE conditions, respectively. Right: representative traces showing the effect of NE on the slope of the first fEPSP (top) and on the PPF of the second fEPSP (bottom) from the same recording. Stimulation artifacts were cropped for clarity. (**C**) Pairwise quantification of the effect of NE on fEPSP slope and PPF for the experiments shown in (B). (**D**) Correlation between NE-induced fEPSP decrease and PPF increase in experiments shown in (B) and (C). (**E**) Representative recording of EPSC amplitude in response to minimal stimulations, showing failures (gray) and successes (black). (**F**) Left: averaged time course (per minute) of minimal-stimulation experiments showing the effect of 20 µM NE on synaptic efficacy (gray) and potency (black). Right: representative traces illustrating the effect of NE on efficacy (gray traces, failures; black traces, successes) and potency (average of successes) over 1-min epochs. (**G**) Quantification and pairwise comparison of the effect of NE on synaptic efficacy, potency, and strength for individual experiments shown in (F). (**H**) Schematic illustration of the procedure for expressing ChR2 in LC-NE fibers. (**I**) Immunohistochemistry (IHC) images of ChR2-EYFP expression in the LC (left) and hippocampal CA1 (right) at 12 weeks, and quantification of efficiency and specificity of ChR2-EYFP expression in the LC (center). Tyrosine hydroxylase (TH) was used as a marker of NE-producing neurons $n = 22$ sections from 4 animals. Cereb., cerebellum; 4V, fourth ventricle; Verm., vermis; s.p., stratum pyramidale; s.r., stratum radiatum; s.l.m., stratum lacunosum moleculare. Arrowheads indicate ChR2-EYFP-expressing LC-NE projections with major bifurcation points (asterisks). (**J**) Schematic of the recording and optogenetic stimulation conditions. (**K**) Time course of the effect of the optical stimulation of LC-NE fibers on fEPSPs and PPFs and representative traces. Insets show the detailed time course (20-s bins) at the onset and offset of light (SEM is omitted for clarity). (**L**) Pairwise quantification of the effect of light (1 Hz, 10 min) on fEPSP slope and PPF for the experiments shown in (K) and in EYFP-control slices. (**M**) Plot summarizing the effect of light in ChR2-positive slices, EYFP-control slices, and ChR2-positive slices in the presence of silodosin (silo.) (50 nM). (**N**) Plot summarizing the effect of NE on synaptic strength in the presence of blockers of α2-AR (yohimbine, 500 nM), β-AR (propranolol, 1 µM), α1B-AR (LY746-314, 1 µM), α1-AR (prazosin, 1 µM), α1A-AR (silodosin, 50 nM), or the α1A-AR agonist A61603 (70 nM). $n = 5$ to 10 mice. (**O** and **P**) Time course of the effect of 20 µM NE on fEPSP and PPF in the presence of silodosin (50 nM), representative traces, and pairwise quantification. Data were analyzed with paired Student's t test, Pearson's correlation, ANOVA multiple comparisons, and Tukey's post hoc tests and are shown as means ± SEM.

a modest but reproducible and sustained decline in fEPSP slope accompanied by an equivalent increase in PPF (Fig. 1, K and L), neither of which was observed in EYFP control slices taken from AAV9-*SynP*::DIO-EYFP injected *Dbh*^{Cre} mice (Fig. 1, L and M; fig. S1H; and table S1). These effects appeared within 20 s of light onset, remained constant for the duration of the stimulation, and subsided within 2 min of light cessation (Fig. 1K). Taken together, these results support the notion that exogenous and endogenous NE inhibits transmission at excitatory synapses by hindering (pre)synaptic efficacy.

LC-derived NE alters synapses through α1-ARs

NE has been shown to bind at least three classes of G protein–coupled receptors (GPCRs): α1 adrenergic receptors (α1-ARs), α2-ARs, and β-ARs. Consistent with prior work, we found that the α1-AR antagonist prazosin blocked the effect of NE both at commonly used doses (10 μM; fig. S1K) and at concentrations no greater than ~100 times its inhibition constant (K_i) for α1-ARs (1 μM; Fig. 1N and fig. S1L) (*36*). Conversely, the α2-AR and β-AR antagonists yohimbine and propranolol, respectively, alone or in combination, failed to block the effect of NE, even at higher doses (Fig. 1N and fig. S1, M to P). Additionally, we found that NE applications (Fig. 1, N to P) and optogenetic stimulations of LC-NE fibers (Fig. 1M and fig. S1, I and J) were ineffective in the presence of the α1A-AR–specific antagonist silodosin (50 nM) but were unaffected by LY746-314, an α1B-AR–specific antagonist (1 μM; Fig. 1N and fig. S1Q). Furthermore, the α1A-AR agonist A61603 mimicked the effect of NE (70 nM; Fig. 1N and fig. S1, R and S). Therefore, in our conditions, the action of NE on synapses depended on the α1A-AR subtype alone.

Although it is consistent with existing literature (*25*, *26*), the fact that NE suppresses presynaptic release probability through α1A-ARs is surprising in two ways. First, α1A-ARs are the G_q type of GPCRs, such that their activation should enhance Ca^{2+} influx in presynaptic boutons and facilitate synaptic transmission (*37*). Consistently, using a chemogenetic approach, we found that the stimulation of the Gq-GPCR hM3d(Gq) expressed presynaptically enhanced synaptic transmission by facilitating synaptic efficacy (fig. S2). Second, the median inhibitory concentration (IC_{50}) of the observed effect of NE on synapses (3.5 μM; fig. S1B) was 12 times greater than its binding affinity on the α1A-AR [~0.28 μM (*38*)]. Overall, these considerations are hard to reconcile with a direct action of NE on presynaptic α1A-ARs implied by our observations and suggest instead that NE alters synaptic function through a more intricate mechanism than commonly assumed.

Astrocyte Ca^{2+} dynamics gate NE effectiveness

A recent paradigm shift in neuroscience has been the realization that synaptic connectivity is the result of a subtle multicellular interplay between fast neuronal activity and instructive or permissive signals from non-neuronal cells, including astrocytes (*39*). To capture the effect of NE on astrocytes, we transduced C57BL/6J adult mice (P70) with an AAV5-*gfaABC1D*::lck-GCaMP6f in the CA1 region of the hippocampus [fig. S3A (*40*)], yielding robust expression of the Ca^{2+} indicator lck-GCaMP6f in glial fibrillary acidic protein (GFAP)–positive cells (astrocytes) of the stratum radiatum (fig. S3B). We then performed two-photon laser scanning microscopy (2-PLSM) imaging in acute slices 20 to 30 days later (fig. S3, C and D, and materials and methods). Consistent with previous reports (*12*, *16*–*19*), NE applications elicited large, cell-wide and dose-dependent Ca^{2+} responses in nearly all astrocytes in the field of view (fig. S3, E and F). The α1A-AR–specific antagonist silodosin (50 nM), which obliterated the effect of NE on synapses (Fig. 1, N to P), markedly hampered this response (fig. S3F). In addition, silodosin alone reduced the amplitude and frequency of astrocyte spontaneous Ca^{2+} transients (fig. S3, G and H) while increasing fEPSP slope and reducing PPF (fig. S1T), suggesting that a tonic α1A-AR–mediated activation of astrocytes coincided with a tonic α1A-AR–mediated inhibition of synapses. Combined, these observations suggest the existence of a causal link between astrocyte Ca^{2+} dynamics and synaptic changes caused by NE.

To test this idea, we used iβARK, a Gαq sequestrator that prevents Ca^{2+} elevations secondary to the activation of G_q-GPCRs in astrocytes (*41*). The transduction of AAV5-*gfaABC1D*::iβARK-mCherry in the CA1 of wild-type mice (Fig. 2A) yielded a robust, cell-specific expression in 92% of hippocampal astrocytes (Fig. 2B). Evoked fEPSP amplitude and PPF under basal conditions were normal in slices obtained from iβARK-transduced animals relative to AAV5-*gfaABC1D*::mCherry-transduced slices [red fluorescent protein (RFP) control; Fig. 2C]. As expected, spontaneous Ca^{2+} dynamics were reduced in frequency and amplitude in iβARK astrocytes (Fig. 2, D and E) (*41*), and NE-evoked Ca^{2+} responses were blunted by 75% relative to RFP controls (Fig. 2, F and G), consistent with their reliance on G_q-coupled α1A-ARs (fig. S3). NE yielded the expected effect on synapses in RFP control slices (Fig. 2H), but it was ineffective on fEPSP slope and PPF in iβARK slices (Fig. 2, I and J). Although greatly reduced (Fig. 2K), the impact of NE remained evident in some iβARK slices. It averaged 4.8% across experiments, equivalent to 16% of the inhibition achieved in RFP-controls (Fig. 2K), reminiscent of the proportion of NE-induced Ca^{2+} response that persisted in iβARK astrocytes (Fig. 2G). It remains unclear whether Ca^{2+} input-output coding in astrocytes follows a threshold-based all-or-nothing logic, correlates linearly with the magnitude of Ca^{2+} events, or follows other nonlinear rules, muddying the rigorous interpretation of these data. However, we obtained identical results with other proven methods of astrocyte Ca^{2+} silencing, such as CalEx (calcium extrusion; Fig. 2L and fig. S4) (*42*) and thapsigargin (Fig. 2L and fig. S5) (*43*). Because these approaches are mechanistically distinct, we interpret the apparent residual effect on synaptic strength in all three conditions as the consequence of the incomplete blockade of NE-induced astrocyte Ca^{2+} elevations achieved by each of them, and we conclude that silencing astrocytes occludes NE neuromodulation of synapses. An alternative interpretation, however, is that astrocytes contribute most (~80 to 85%), but not all, of the inhibitory effect of NE, with the rest (15 to 20%) being attributable to a direct action on neurons.

Neuronal α1-ARs are not required for NE neuromodulation

To determine how direct signaling of NE onto neurons and indirect signaling through astrocytes contribute to the functional remodeling of synapses, we sought to delete α1A-ARs from presynaptic, postsynaptic, and inhibitory neurons by microinjecting AAV5-*hSyn*::Cre-GFP in *Adra1a*$^{fl/fl}$ mice, in which the first coding exon for α1A-AR is floxed (Fig. 3A). Immunofluorescent examinations confirmed the strong expression of Cre-GFP in 88 and 89% of CA3 and CA1 NeuN-positive cells (neurons), respectively, with high neuronal specificity (Fig. 3B). Effective genetic recombination was verified at the genomic DNA (gDNA) level and confirmed a 43% decrease in unmodified *Adra1a* gDNA in Cre-transduced *Adra1a*$^{fl/fl}$ hippocampi compared with Cre-transduced *Adra1a*$^{+/+}$ controls (Fig. 3C). Furthermore, native *Adra1a* gDNA was reduced by 54% in fluorescence-sorted green fluorescent protein (GFP)–positive cells (neurons) from *Adra1a*$^{fl/fl}$ hippocampi compared with *Adra1a*$^{+/+}$ (Fig. 3D, fig. S6A, and materials and methods), but not in GFP-negative cells, and this was accompanied by a 94% decline in *Adra1a* mRNA in GFP-positive cells only (fig. S6, A and B), demonstrating that genetic recombination was effective and restricted to neurons. Low or transient expression of Cre can be missed with such readouts, however, and lead to recombination in a subset of GFP-negative cells. To rule out this possibility, we repeated immunofluorescence evaluations in Cre-injected Rosa-CAG::LSL-tdTomato mice (Ai14; fig. S6D), in which any recombination-capable Cre activity results in the permanent expression of the tdTomato reporter (*44*). We found that 78% of CA3 neurons and 69% of CA1 neurons were tdTomato-positive, whereas <0.1% of astrocytes, Iba-1–positive cells

(microglia), or Olig-2–positive cells (oligodendrocytes) expressed td-Tomato (fig. S6, E and F), further confirming the specific recombination of *Adra1a* from CA3 and CA1 neurons in Cre-transduced *Adra1a*$^{fl/fl}$ mice (neuron-specific *Adra1a* knockout, N-Adra1a^{KO}). Finally, we sought to ascertain the absence of functional α1A-ARs on hippocampal neurons of N-Adra1a^{KO} mice. Because NE facilitates neuronal excitability (*28*, *45*), in particular through an α1A-AR–mediated reduction in K^+ conductance that causes a sustained membrane depolarization (*46*), we used whole-cell patch-clamp recordings to determine the effect of NE on intrinsic membrane properties. Consistent with past literature, we found that NE elicited a rapid (<5 min) and marked inward current in the presence of tetrodotoxin (TTX) (fig. S6, H and I), which was blocked by the α1A-AR antagonist silodosin (fig. S6H,I). This effect was also completely absent in GFP-positive neurons from

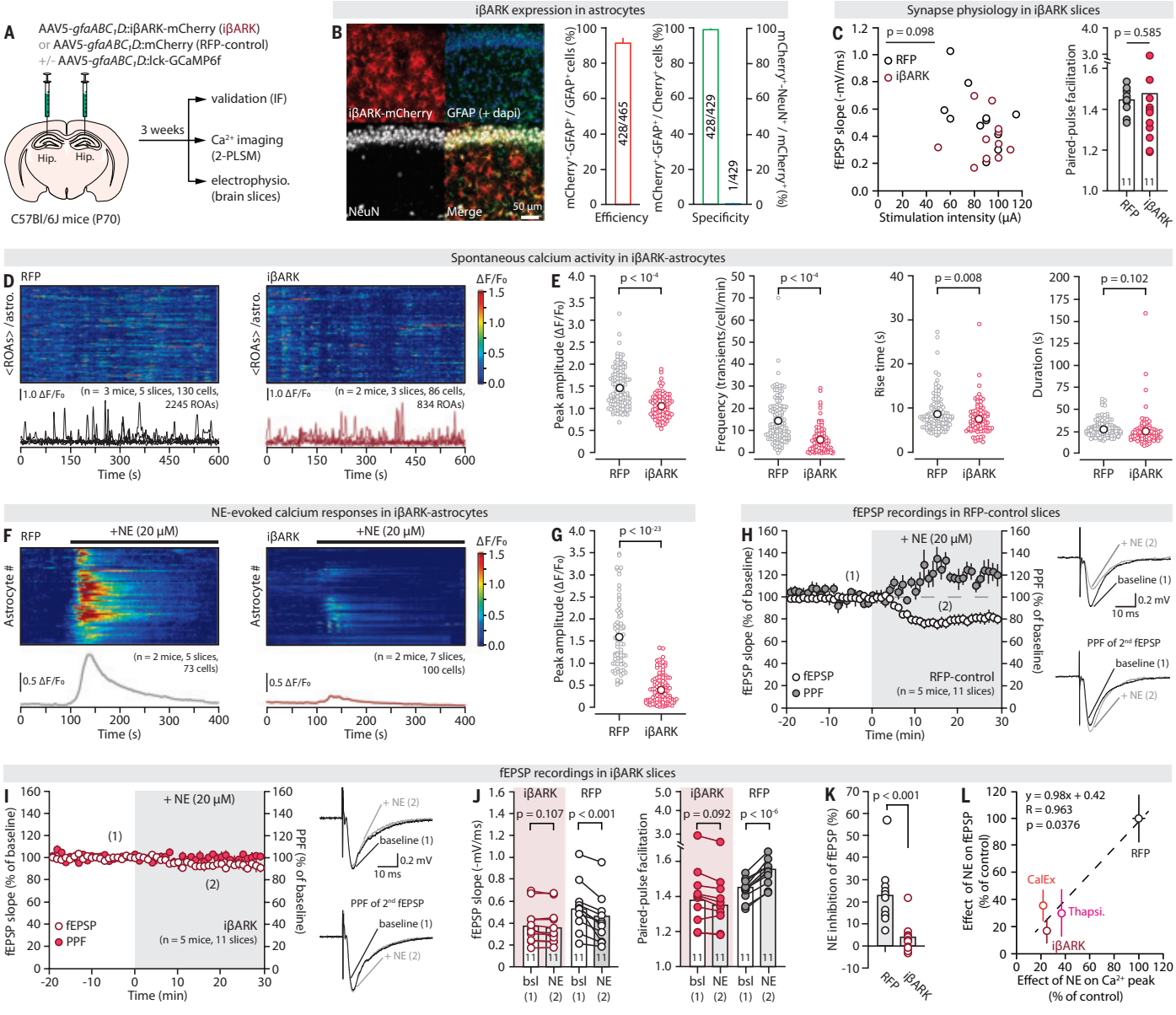

Fig. 2. Astrocyte Ca^{2+} dynamics gate the effect of NE on synapses. (**A**) Approach for astrocyte Ca^{2+} silencing with iβARK. (**B**) Representative IHC images of iβARK-mCherry expression in the hippocampal CA1, along with quantification of efficiency and specificity ($n = 5$ sections). (**C**) Plot of the stimulation intensity/fEPSP slope relationship (left, unpaired Student's *t* test on slope/stimulation ratio) and summary bar graphs of PPF values (right) in RFP-control and iβARK slices at baseline. (**D**) Kymograph, in which each row shows the average fluorescence across regions of activity (ROAs) of an individual astrocyte, and five representative $\Delta F/F_0$ traces (from individual ROAs) of spontaneous Ca^{2+} transients in RFP-control and iβARK slices. Horizontal time axis applies to the kymograph and representative traces. (**E**) Plots of the peak amplitude, frequency, and kinetics of spontaneous Ca^{2+} transients in RFP-control and iβARK slices. Each data point shows the mean fluorescence across ROAs for an individual astrocyte. (**F**) Kymographs, in which each row shows the whole-cell fluorescence of an individual astrocyte, and average $\Delta F/F_0$ traces (±SEM) across all astrocytes in response to 20 µM NE application in RFP-control and iβARK slices. (**G**) Plot of the peak $\Delta F/F_0$ response in RFP-control and iβARK conditions for experiments shown in (F). (**H** and **I**) Time courses of the effect of 20 µM NE on fEPSP slope and PPF and representative traces in RFP-control and iβARK slices. (**J**) Pairwise quantifications of the effect of NE on fEPSP slope and PPF for the experiments shown in (H) and (I). (**K**) Plots summarizing the effect of NE on fEPSP slope in RFP-control and iβARK slices. (**L**) Correlation between the effect of 20 µM NE on astrocyte peak Ca^{2+} responses and fEPSP slope across three methods of astrocyte silencing and RFP controls (figs. S4 and S5 and table S1). Data were analyzed with paired Student's *t* test, Pearson's correlation, ANOVA multiple comparisons, Tukey's post hoc, and permutation tests and are shown as means ± SEM.

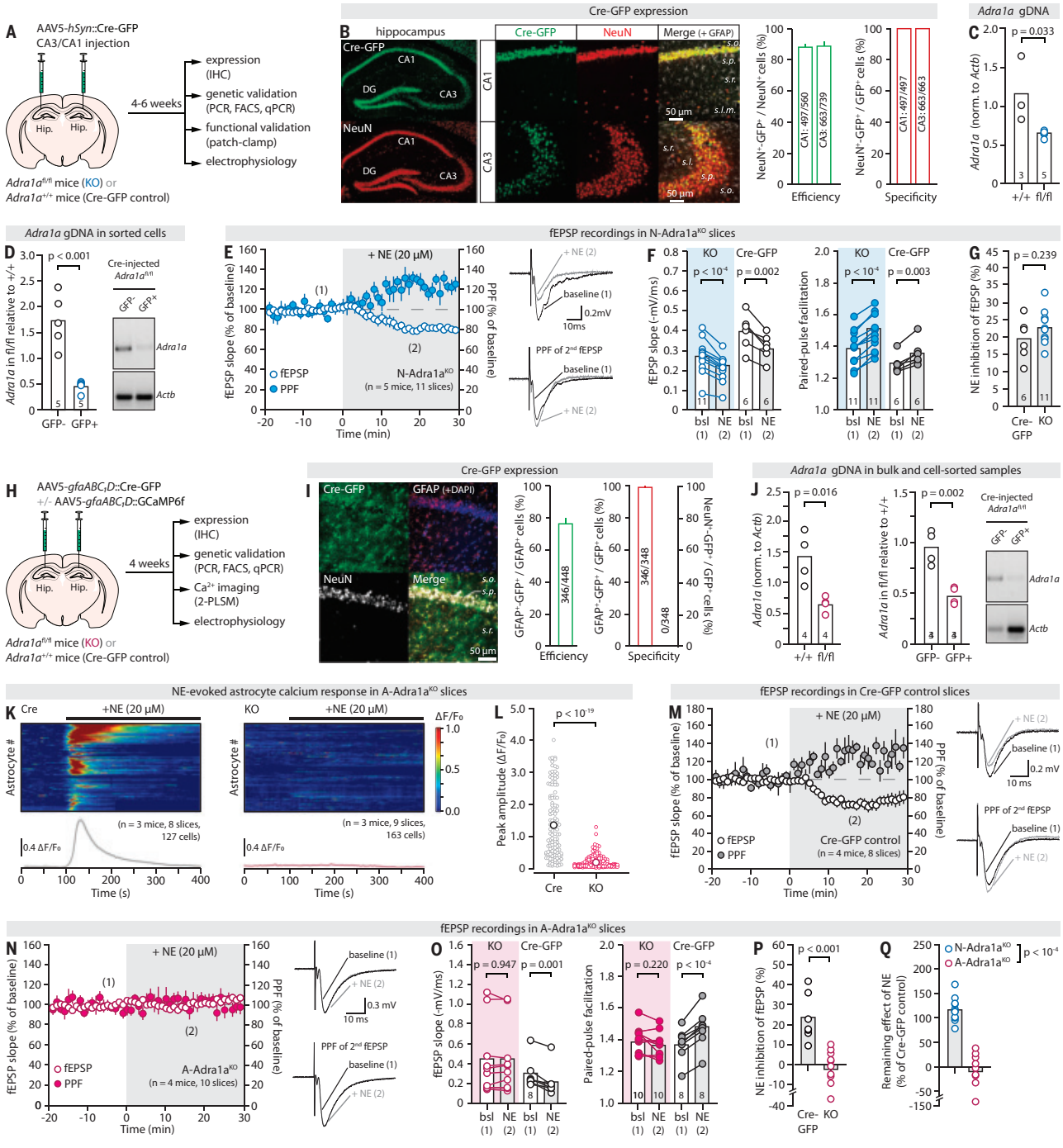

Fig. 3. Astrocytic, but not neuronal, α1A-ARs are required for NE to affect synapses. (**A**) Approach for the neuronal deletion of *Adra1a*. (**B**) Representative IHC images of Cre-GFP expression in hippocampal CA1 and CA3 neurons, along with quantification of efficiency and specificity ($n = 4$ sections from 2 mice). (**C**) Quantification of bulk *Adra1a* gDNA polymerase chain reaction (PCR) band intensity, normalized to *Atcb* (β-actin), in Cre-injected *Adra1a*$^{+/+}$ and *Adra1a*$^{fl/fl}$ mice. (**D**) Quantification of *Adra1a* gDNA, normalized to *Atcb* (β-actin), in GFP-positive and GFP-negative cells from Cre-injected *Adra1a*$^{fl/fl}$ mice ($n = 5$) relative to *Adra1a*$^{+/+}$ mice ($n = 5$) (left), and representative PCR gels (right). (**E**) Time course of the effect of 20 µM NE on fEPSPs and PPFs in N-Adra1a^{KO} slices and representative traces. (**F** and **G**) Pairwise quantification of the effect of NE on fEPSP slope and PPF in N-Adra1a^{KO} and N-Adra1a$^{Cre\text{-}GFP}$ control slices and summary plot of the effect of NE on fEPSPs in both conditions. (**H**) Approach for the astrocytic deletion of *Adra1a*. (**I**) Representative IHC images of Cre-GFP expression in hippocampal CA1 astrocytes, along with quantification of efficiency and specificity ($n = 6$ sections from 2 mice). (**J**) Quantification of bulk *Adra1a* gDNA levels, normalized to *Actb* (β-actin), in Cre-injected *Adra1a*$^{fl/fl}$ mice and Cre-injected *Adra1a*$^{+/+}$ controls (left) and quantification of *Adra1a* gDNA, normalized to *Atcb* (β-actin), in GFP-positive and GFP-negative cells from Cre-injected *Adra1a*$^{fl/fl}$ mice ($n = 4$) relative to *Adra1a*$^{+/+}$ mice ($n = 3$) (right). Representative PCR gels are shown. (**K** and **L**) Kymographs, in which each row shows the whole-cell fluorescence of an individual astrocyte; average $\Delta F/F_0$ traces (± SEM) across all astrocytes; and quantification of the peak Ca^{2+} signal in response to 20 µM NE application in A-Adra1a$^{Cre\text{-}GFP}$ and A-Adra1a^{KO} slices. (**M** to **P**) Time courses of the effect of NE on fEPSPs and PPFs and representative traces in A-Adra1a^{control} (M) and A-Adra1a^{KO} slices (N), pairwise quantification of the effect of NE on fEPSP slope and PPF (O), and summary plot of the effect of NE in both conditions (P). (**Q**) Summary plot of the inhibitory effect of NE on fEPSPs in A-Adra1a^{KO} and N-Adra1a^{KO} slices relative to their respective controls. Data were analyzed by paired and unpaired Student's *t* test and permutation tests and are shown as means ± SEM.

N-Adra1a^{KO} mice (fig. S6H,I), confirming the lack of functional α1A-AR. Combined, this series of experiments ascertains the neuron-specific loss of α1A-ARs in N-Adra1a^{KO} mice. The inhibitory action of NE on synaptic function was next assessed in N-Adra1a^{KO} slices 4 to 6 weeks after microinjections, using Cre-GFP–injected *Adra1a*$^{+/+}$ animals as controls (N-Adra1a$^{Cre\text{-}GFP}$; Fig. 3A). We found that NE yielded a sharp decline in fEPSPs and an increase in PPFs in N-Adra1a$^{Cre\text{-}GFP}$ and N-Adra1a^{KO} slices (Fig. 3, E and F, and fig. S6K). Both conditions were statistically indistinguishable from one another and from other control conditions (Fig. 3G and table S1). Additionally, α1A-AR deletion, on its own, did not alter synaptic strength or presynaptic release probability (fig. S6J). In total, the deletion of α1A-AR from neurons was thus without effect on basal synaptic properties and NE-induced remodeling of synaptic function.

Astrocytic α1-AR deletion renders NE inoperant

The above results suggest that astrocytes mediate the modulatory action of NE on synapses. To directly test this, α1A-ARs were deleted from astrocytes by transducing AAV5-*gfaABC1D*::Cre-GFP (*10*) in the CA1 of *Adra1a*$^{fl/fl}$ mice (Fig. 3H). Robust expression of Cre-GFP was apparent in 76% of stratum radiatum astrocytes with 99% specificity 4 weeks later (Fig. 3I), accompanied by a 52% reduction in native *Adra1a* gDNA in Cre-transduced *Adra1a*$^{fl/fl}$ hippocampi (astrocyte-specific *Adra1a* knockouts, A-Adra1a^{KO}) compared with Cre-transduced *Adra1a*$^{+/+}$ controls (A-*Adra1a*$^{Cre\text{-}GFP}$; Fig. 3J). Unmodified *Adra1a* gDNA was intact in fluorescence-sorted GFP-negative cells of A-Adra1a^{KO} hippocampi but reduced by 52% in fluorescence-sorted GFP-positive cells (astrocytes) relative to A-Adra1a$^{Cre\text{-}GFP}$ (Fig. 3J and fig. S6A). This coincided with a 67% decline in *Adra1a* mRNA in GFP-positive cells but not in GFP-negative cells (fig. S6C). Additionally, AAV5-*gfaABC1D*::Cre-GFP microinjections in Ai14 mice (fig. S6D) resulted in tdTomato expression in 96% of astrocytes but only 8.9% of neurons, 2% of microglia, and 19% of oligodendrocytes (fig. S6, E and F). We next evaluated astrocyte responsiveness to NE using 2-PLSM and found that NE-induced Ca^{2+} elevations were still observed in A-Adra1a$^{Cre\text{-}GFP}$ slices but completely missing in A-Adra1a^{KO} slices (Fig. 3, K and L), corroborating the functional ablation of α1A-ARs from astrocytes and confirming that NE-induced astrocyte Ca^{2+} responses result from the direct activation of α1A-ARs on astrocytes (fig. S3) (*10*). The effect of NE on fEPSPs and PPFs, preserved in A-Adra1a$^{Cre\text{-}GFP}$ control slices (Fig. 3M), was also totally absent in slices taken from A-Adra1a^{KO} (Fig. 3, N to P). This was not associated with any noticeable changes in basic synaptic properties or astrocyte spontaneous activity (fig. S6, L to N), ruling out the possibility that the ineffectiveness of NE resulted from adverse disruptions in synaptic or astrocytic function. Collectively, these results strongly indicate that NE remodels synaptic activity, not by signaling directly onto neurons, but by recruiting astrocytes (Fig. 3Q).

NE acts by mobilizing ATP-adenosine signaling

A corollary of the above conclusion is that the observed inhibitory effect of NE on synapses is likely to be the result of an astrocyte output mobilized in response to NE. A variety of NE-driven astrocyte activities have been documented across brain regions, organisms, and preparations that are consequential to synaptic connectivity over second to minute timescales (*20*). Among them is the regulation of extracellular K^+ (*47*), the supply of lactate, and the secretion of signaling molecules such as D-serine (*48*) and ATP (*18*, *19*). The latter is of particular importance because in the hippocampus, ATP is readily hydrolyzed into adenosine to act on A1 receptors (A1Rs) (Fig. 4A), a G_i-coupled subtype of purinergic GPCR selective for adenosine. At CA3-CA1 synapses, A1Rs are predominantly presynaptic and their activation decreases transmitter release probability (*49*). Accordingly, direct applications of adenosine in hippocampal slices triggered an inhibitory effect on synaptic strength and presynaptic efficacy, the magnitude and timing of which resembled that of NE (fig. S7, A to C). We found that blocking A1Rs with specific antagonists, CPT (200 nM) or DPCPX (100 nM), was sufficient to completely abolish the ability of NE to modulate synaptic transmission in slices from wild-type animals (Fig. 4, A to C, and fig. S7D). By contrast, inhibiting other purinergic receptors, including P_2X and P_2Y receptors, as well as A2ARs and A2BRs did not have any effects, pointing at a major role of adenosine rather than ATP and indicative of an A1R-specific mechanism (Fig. 4A and fig. S7E). To ascertain the presynaptic locus of A1Rs involved, *Adora1*$^{fl/fl}$ mice were transduced with an AAV5-*hSyn*::Cre-GFP viral vector in the CA3 of the dorsal hippocampus (Fig. 4D), which yielded robust GFP expression in 72% of CA3 neurons (presynaptic) and minimal expression in CA1 (6%; Fig. 4E). Mice transduced with the same virus in the CA1 (postsynaptic neurons) were used as controls (Fig. 4D) and showed a mirroring pattern of GFP expression (Fig. 4E). In slices obtained 5 weeks later from CA3-injected mice, adenosine had a markedly reduced effect on fEPSPs and PPFs compared with CA1-injected controls (Fig. 4, F and G), confirming the loss of ~50% of presynaptic A1R signaling at CA3-CA1 synapses in these mice (CA3-specific *Adora1* knockdown, CA3-Ado1^{KD}). Whereas NE achieved a nominal inhibition of fEPSPs and an accompanying PPF increase in slices from CA1-Ado1^{KD} mice, its effect was diminished by 59% in CA3-Ado1^{KD} slices (Fig. 4, H to J). Therefore, the knockdown of A1Rs in CA3 (presynaptic) neurons reduced the effect of adenosine on synapses by 50% and the effect of NE by a similar 59%, whereas A1R deletion in CA1 neurons had no effects on either, consistent with an instrumental role of presynaptic A1Rs in NE neuromodulation of synapses. The partial blockade observed in these experiments was likely caused by the incomplete targeting of CA3 neurons necessary to achieve regional specificity (Fig. 4E). Indeed, repeating these experiments in mice that received four bilateral Cre injections in the CA3 (two per side; see the materials and methods) yielded a complete loss of the effect of adenosine and NE (fig. S7, F and G), confirming that NE requires presynaptic A1R signaling to functionally remodel synapses. By contrast, inhibiting metabotropic glutamate receptors, another modulator of presynaptic efficacy targeted by astrocytes, had no impact on the outcome of NE applications (Fig. 4A and fig. S7H).

To interfere with adenosine directly rather than A1Rs, we bathed brain slices in adenosine deaminase (ADA, 1 U/ml, 15 min before and throughout the experiment), an enzyme that hydrolyzes extracellular adenosine into inosine, which is a by-product inoperant on A1R and A2A or A2BR at physiological concentrations (*50*). ADA completely prevented the effect of NE on synapses (Fig. 4A and fig. S7I), confirming that adenosine is the effector that remodels synaptic function rather than NE itself. Seeking a pharmacology-free confirmation, we reasoned that NE should be ineffective in slices obtained from *NT5e*^{KO} mice lacking CD73, an ecto-5′-nucleotidase that catalyzes the conversion of interstitial AMP into adenosine, the last step in the enzymatic production of adenosine from extracellular ATP (Fig. 4A). Indeed, NE caused no changes in fEPSPs or PPFs in *NT5e*^{KO} slices (Fig. 4, K and L). This was not caused by the absence or down-regulation of presynaptic A1Rs in these mice or any overt compensations that would disrupt the basic synaptic machinery, because direct applications of adenosine elicited a normal fEPSP inhibition, accompanied by an increase in PPF, in the same slices (Fig. 4, M and N, and fig. S7, J and K). This was also true for other conditions described above, including iβARK (fig. S7, L to N), CalEx (fig. S4, H, I, and L), thapsigargin (fig. S5, E, F, and I), A-Adra1a^{KO} slices (fig. S6, O to Q), and N-Adra1a^{KO} slices (fig. S6R). In total, these results demonstrate that the ability of NE to remodel synaptic function relies on an ATP-adenosine-A1R–dependent control of presynaptic efficacy.

Discussion

Our findings reveal that NE functionally remodels synapses by signaling through astrocytes. Although presynaptic in nature, as documented in the past (*19*, *21*, *24*), the canonical effect of NE on synaptic function

is unaffected by the deletion of its target receptor, α1A-AR, on neurons, but is abolished by silencing astrocytes, by suppressing astrocyte sensitivity to NE, and by genetic, enzymatic, or pharmacological interference at any level of an ATP-adenosine-A_1R pathway. Collectively, this supports a model in which NE engages astrocyte Ca^{2+} dynamics, ATP-adenosine signaling, and the activation of presynaptic purinergic receptors to update synaptic weights in a non-Hebbian mechanism and reshape neuronal connectivity, consistent with past evidence (*18*, *19*). Using continuous bath applications of 20 μM NE, our primary goal was to replicate the approach and findings from past studies. This conservative approach, however, also allows the conclusion that even under continuous perfusion of 20 μM NE, synaptic remodeling happens independently of neuronal adrenergic receptors, thus unequivocally putting astrocytes at the center of NE-induced functional synaptic adaptations. As demonstrated in an accompanying paper by Chen *et al.* (*51*), an analogous astrocytic purinergic pathway recruited by NE is instrumental to behavioral state transition in the larval zebrafish, portraying astrocyte-based purinergic signaling as a general mechanism

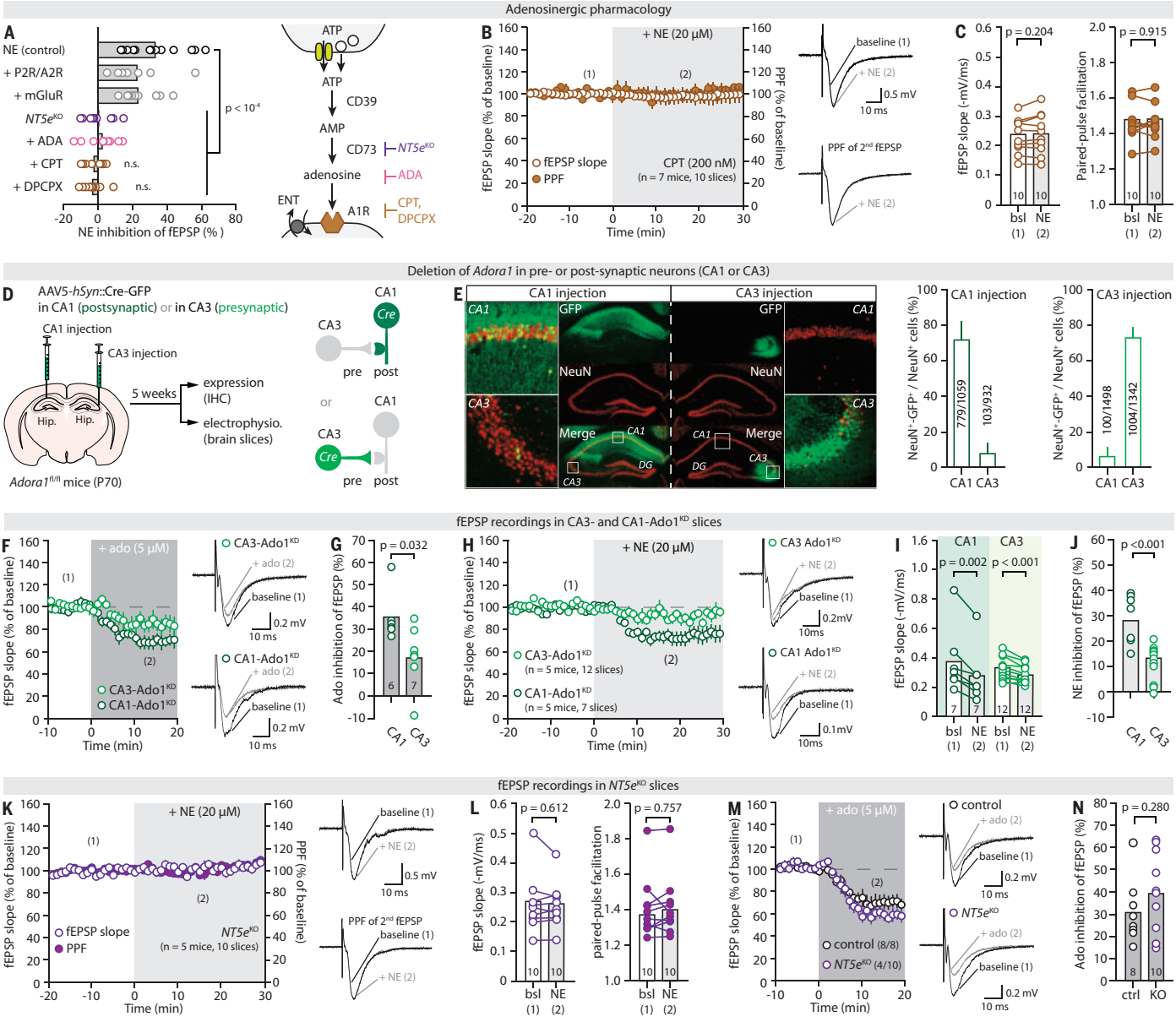

Fig. 4. NE leverages ATP-adenosine-A1R signaling to modulate synaptic efficacy. (**A**) Left: plot summarizing the effect of 20 μM NE in the presence of A1R antagonists (CPT, 200 nM, or DPCPX, 100 nM), an adenosine scavenger (ADA, 1U/ml), a cocktail of P2X/P2Y (PPADS, 10 μM), A2A (ZM241385, 50 nM) and A2B (PSB603 50 nM) receptor antagonists, a cocktail of mGluR inhibitors (CPPG, 5 μM; MPEP, 3.6 μM; YM298198, 2 μM), or in slices from *NT5e*^{KO} mice ($n = 4$ to 9 mice). Right: schematic of the ATP-adenosine-A1R pathways showing different points of genetic or pharmacological intervention. (**B**) Time course of the effect of NE on fEPSPs and PPFs in the presence of the A1R antagonist CPT and representative traces. (**C**) Pairwise quantification for the experiments shown in (B). (**D**) Approach for the deletion of *Adora1* in CA3 or CA1 neurons. (**E**) Representative IHC images of Cre-GFP expression in CA1- and CA3-injected animals, along with quantification of regional specificity ($n = 4$ sections from 2 mice). (**F** and **G**) Time course, representative traces, and quantification of the effect of 5 μM adenosine on fEPSPs in CA1-Ado1^{KD} and CA3-Ado1^{KD} slices. (**H** to **J**) Time course, representative traces, pairwise quantification, and summary plot of the effect of 20 μM NE on fEPSPs in CA1-Ado1^{KD} and CA3-Ado1^{KD} slices. (**K** and **L**) Time course, representative traces, and summary plot of the effect of 20 μM NE on fEPSPs and PPFs in *NT5e*^{KO} slices. (**M** and **N**) Time course, representative traces, and quantification of the effect of adenosine on fEPSPs in *NT5e*^{KO} and control slices. Data were analyzed with paired and unpaired Student's *t* test, ANOVA multiple comparisons, and Tukey's post hoc tests and are shown as means ± SEM.

by which LC-NE activity remaps neural circuits. Consistently, work in the fly larvae described astrocyte responsiveness to octopamine (Oct) and tyrosine (Tyr) through the Oct and Tyr receptors, which are invertebrate analogs of NE and α1-AR, respectively, and showed that it inhibits chemotaxis-regulating dopamine neurons through adenosine receptors (*18*). That astrocytes across three phylogenetically distant organisms share the same response to an evolutionarily conserved neuromodulator (NE-Oct-Tyr) indicates that they have evolved as an integral mechanism for monoaminergic systems to dynamically remodel synaptic connectivity and brain circuits, adding to mounting evidence that the role of astrocytes in brain function has been severely underestimated.

Past functional studies of the effect NE at the synaptic and cellular level were conducted at a time when cell-specific and genetic approaches were unavailable or uncommon, and electron microscopy confirmations were scant or lacked systematic quantification (*4*–*7*). Alternative interpretations involving non-neuronal cells were also given little credit because these cells were conceptualized as "inactive" at the time (*13*, *39*). Therefore, observations that NE elicited a presynaptic modulation sensitive to adrenergic pharmacology prompted the conclusion that it acted directly on presynaptic receptors. In view of recent studies that paint a diverse picture of adrenergic receptor expression and responsiveness across cell types, our findings call for a systematic reexamination of the effects of NE signaling at various scales. The multiplex nature of astrocytes, and their circuit-specific input-output rules (*13*), could shed light on the spatial and temporal heterogeneity of NE neuromodulation that has been traditionally attributed to the expression of receptor subtypes at various subcellular locations. Furthermore, the existence of an astrocyte relay, in which NE signaling is transduced into ATP signaling at synapses, may enable specific processing rules for NE inputs within the synaptic microenvironment, distinct from those at play in neighboring compartments (such as the neuronal soma). In that sense, a central role of astrocytes in NE neuromodulation emphasizes the importance of interstitial space compartments, their specialization, their area of influence, and their regulation to brain signaling. NE, like other volume-transmitted neuromodulators, diffuses away from its release sites and into the extracellular space, where the spatiotemporal characteristics of NE signaling are not homogeneous (*32*, *52*). Conceptualizing the extracellular space as an ensemble of well-defined functional units that influence the behavior of cellular elements contiguous to them (*13*) could refine our understanding of how NE neuromodulation shapes brain function and the role of astrocytes in this multifaceted process.

More generally, our work brings a new perspective to our understanding of the cellular and molecular underpinnings of neuromodulation at large. The responsiveness of astrocytes to neuromodulators is not limited to NE but encompasses all canonical monoamines, as well as acetylcholine and oxytocin (*13*), which raises the question of the transferability of our findings. Thus, the molecular rules by which all neuromodulators achieve their circuit and mesoscale effects might benefit from being reevaluated with a more holistic view, because the mechanism we describe here might be generalizable to other neuromodulatory systems.

REFERENCES AND NOTES

1. D. J. Chandler *et al.*, *J. Neurosci.* **39**, 8239–8249 (2019).
2. C. W. Berridge, B. D. Waterhouse, *Brain Res. Brain Res. Rev.* **42**, 33–84 (2003).
3. V. Breton-Provencher, G. T. Drummond, J. Feng, Y. Li, M. Sur, *Nature* **606**, 732–738 (2022).
4. R. J. Matthews Jr., *J. Pharmacol. Exp. Ther.* **116**, 433–443 (1956).
5. E. Bülbring, J. H. Burn, *J. Physiol.* **101**, 289–303 (1942).
6. A. S. Marrazzi, *Science* **90**, 251–252 (1939).
7. G. Aston-Jones, J. D. Cohen, *Annu. Rev. Neurosci.* **28**, 403–450 (2005).
8. S. Bouret, S. J. Sara, *Trends Neurosci.* **28**, 574–582 (2005).
9. R. Jordan, *Trends Neurosci.* **47**, 92–105 (2024).
10. M. E. Reitman *et al.*, *Nat. Neurosci.* **26**, 579–593 (2023).
11. M. Paukert *et al.*, *Neuron* **82**, 1263–1270 (2014).
12. F. Ding *et al.*, *Cell Calcium* **54**, 387–394 (2013).
13. C. Murphy-Royal, S. Ching, T. Papouin, *Nat. Neurosci.* **26**, 1848–1856 (2023).
14. R. N. Rasmussen, A. Asiminas, E. M. M. Carlsen, C. Kjaerby, N. A. Smith, *Trends Neurosci.* **46**, 418–425 (2023).
15. K. T. Baldwin, K. K. Murai, B. S. Khakh, *Trends Cell Biol.* (2023).
16. L. K. Bekar, W. He, M. Nedergaard, *Cereb. Cortex* **18**, 2789–2795 (2008).
17. Y. Mu *et al.*, *Cell* **178**, 27–43.e19 (2019).
18. Z. Ma, T. Stork, D. E. Bergles, M. R. Freeman, *Nature* **539**, 428–432 (2016).
19. G. R. Gordon *et al.*, *Nat. Neurosci.* **8**, 1078–1086 (2005).
20. J. Wahis, M. G. Holt, *Front. Cell. Neurosci.* **15**, 645691 (2021).
21. M. Scanziani, B. H. Gähwiler, S. M. Thompson, *J. Neurosci.* **13**, 5393–5401 (1993).
22. D. Dahl, J. M. Sarvey, *Proc. Natl. Acad. Sci. U.S.A.* **86**, 4776–4780 (1989).
23. M. E. Hasselmo, C. Linster, M. Patil, D. Ma, M. Cekic, *J. Neurophysiol.* **77**, 3326–3339 (1997).
24. A. Kirkwood, C. Rozas, J. Kirkwood, F. Perez, M. F. Bear, *J. Neurosci.* **19**, 1599–1609 (1999).
25. D. Law-Tho, F. Crepel, J. C. Hirsch, *Eur. J. Neurosci.* **5**, 1494–1500 (1993).
26. C. L. Scheiderer, L. E. Dobrunz, L. L. McMahon, *J. Neurophysiol.* **91**, 1071–1077 (2004).
27. V. Zerbi *et al.*, *Neuron* **103**, 702–718.e5 (2019).
28. T. J. Bacon, A. E. Pickering, J. R. Mellor, *Cereb. Cortex* **30**, 6135–6151 (2020).
29. E. C. Burgard, G. Decker, J. M. Sarvey, *Brain Res.* **482**, 351–355 (1989).
30. J. A. Brock, A. Thomazeau, A. Watanabe, S. S. Y. Li, P. J. Sjöström, *Front. Synaptic Neurosci.* **12**, 11 (2020).
31. M. Raastad, *Eur. J. Neurosci.* **7**, 1882–1888 (1995).
32. J. Feng *et al.*, *Neuron* **102**, 745–761.e8 (2019).
33. E. Y. Levin, B. Levenberg, S. Kaufman, *J. Biol. Chem.* **235**, 2080–2086 (1960).
34. L. A. Schwarz *et al.*, *Nature* **524**, 88–92 (2015).
35. M. E. Carter *et al.*, *Nat. Neurosci.* **13**, 1526–1533 (2010).
36. H. Tsuchihashi, T. Nagatomo, *J. Pharmacobiodyn.* **12**, 170–174 (1989).
37. M. J. Berridge, *Nature* **361**, 315–325 (1993).
38. M. D. Meyer *et al.*, *J. Med. Chem.* **39**, 4116–4119 (1996).
39. T. Papouin, J. Dunphy, M. Tolman, J. C. Foley, P. G. Haydon, *Philos. Trans. R. Soc. Lond. B Biol. Sci.* **372**, 12 (2017).
40. E. Shigetomi, S. Kracun, M. V. Sofroniew, B. S. Khakh, *Nat. Neurosci.* **13**, 759–766 (2010).
41. J. Nagai *et al.*, *Neuron* **109**, 2256–2274.e9 (2021).
42. X. Yu *et al.*, *Neuron* **99**, 1170–1187.e9 (2018).
43. O. Thastrup, P. J. Cullen, B. K. Drøbak, M. R. Hanley, A. P. Dawson, *Proc. Natl. Acad. Sci. U.S.A.* **87**, 2466–2470 (1990).
44. L. Madisen *et al.*, *Nat. Neurosci.* **13**, 133–140 (2010).
45. D. E. Bergles, V. A. Doze, D. V. Madison, S. J. Smith, *J. Neurosci.* **16**, 572–585 (1996).
46. Z. Wang, D. A. McCormick, *J. Neurosci.* **13**, 2199–2216 (1993).
47. F. Wang *et al.*, *Sci. Signal.* **5**, ra26 (2012).
48. Y. Kohro *et al.*, *Nat. Neurosci.* **23**, 1376–1387 (2020).
49. N. Rebola, P. C. Pinheiro, C. R. Oliveira, J. O. Malva, R. A. Cunha, *Brain Res.* **987**, 49–58 (2003).
50. A. A. Welihinda, M. Kaur, K. Greene, Y. Zhai, E. P. Amento, *Cell. Signal.* **28**, 552–560 (2016).
51. A. B. Chen *et al.*, *Science* **388**, 769 (2025).
52. Ö. D. Özçete, A. Banerjee, P. S. Kaeser, *Mol. Psychiatry* **29**, 3680–3693 (2024).
53. Data for: K. B. Lefton *et al.*, Norepinephrine signals through astrocytes to modulate synapses, Dryad (2025); https://doi.org/10.5061/dryad.18931zd7t
54. Y. Wu, Y. Dai, K. B. Lefton, T. E. Holy, T. Papouin, *STAR Protoc.* **5**, 103305 (2024).

ACKNOWLEDGMENTS

We thank P. Simpson (UCSF) for his generous gift of *Adra1a*$^{fl/fl}$ mice, R. W. Greene (UT Southwestern) for his gift of the *Adora1*$^{fl/fl}$ mice, P. Bayguinov (Washington University Center for Cellular Imaging) and M. Li (Washington University Hope Center Viral Vectors Core) for their technical assistance. *Adra1a*$^{fl/fl}$ mice were obtained as part of materials transfer agreement A2022-1511 (UCSF), and *Adora1*$^{fl/fl}$ mice were obtained through materials transfer agreement A2023-0094. **Funding:** This work was supported by the National Institutes of Health (grant R01MH127163-01 to T.P., grant R01DK128475 TO V.K.S., grant R01NS102272 to J.D.D., grant R01HL31113-30 to P.C.S.); the Department of Defense (grant W911NF-21-1-0312 to T.P.); the Brain & Behavior Research Foundation (NARSAD Young Investigator Award 28616 to T.P.), the Whitehall Foundation (grant 2020-08-35 to T.P.); and the McDonnell Center for Cellular and Molecular Neurobiology (grant 22-3930-26275U to T.P.). **Author contributions:** Conceptualization: K.B.L., Y.W., Y.D., T.P.; Funding acquisition: P.C.S., J.D.D., V.K.S., T.P.; Methodology: K.B.L., Y.W., Y.D., A.Y., T.O., Y.Z., G.M.R., B.E.M., S.W., R.M., P.C.S.; Investigation: K.B.L., Y.W., Y.D., A.Y., T.O., Y.Z., S.W., R.M., P.C.S.; Project administration: S.W., R.M., T.P.; Supervision: T.P.; Visualization: T.P.; Writing – original draft: K.B.L., T.P.; Writing – review & editing: K.B.L., Y.W., Y.D., S.W., J.D.D., V.K.S., P.C.S., T.P. **Competing interests:** T.P. is a scientific adviser for Surveyor Biosciences Inc. The remaining authors declare no competing interests. **Data and materials availability:** All data are available in the main text or the supplementary materials and from Dryad (*53*). All codes and methods for the STARDUST pipeline are available from (*54*) and can also be downloaded from https://github.com/papouinlab.

License information: Copyright © 2025 the authors, some rights reserved; exclusive licensee American Association for the Advancement of Science. No claim to original US government works. https://www.science.org/about/science-licenses-journal-article-reuse

SUPPLEMENTARY MATERIALS

science.org/doi/10.1126/science.adq5480
Materials and Methods; Figs. S1 to S7; Tables S1 to S4; References (*55*–*57*); MDAR Reproducibility Checklist

Submitted 20 May 2024; accepted 19 March 2025

10.1126/science.adq5480

GENETICS

Distribution of haploid chromosomes into separate nuclei in two pathogenic fungi

Yan Xu[1,2]†, Lei Tian[2,3]†, Jinyi Tan[2,3]†, Weijie Huang[2], Josh Li[2], Nigel O'Neil[2], Martin Hirst[2], Phil Hieter[2], Yuelin Zhang[1,3]*, Xin Li[2,3]*

Nuclei define eukaryotes, enabling macromolecular compartmentalization and cellular regulation. Each nucleus is believed to contain one or more haploid sets of chromosomes (1N). However, we discovered that haploid cells of the pathogenic fungi *Sclerotinia sclerotiorum* and *Botrytis cinerea* distribute their chromosomes such that each of their nuclei contains only a subset of the haploid chromosomes (≤½N). The unusual chromosomal distribution was confirmed by cellular and molecular methods including chromosome counting, fluorescence in situ hybridization, flow cytometry–based DNA measurements, and single-nucleus polymerase chain reaction experiments. This phenomenon challenges fundamental assumptions about nuclear organization and opens fresh avenues in chromosome biology.

Sclerotinia sclerotiorum (Lib.) de Bary (*S. sclerotiorum*) is a soilborne fungal pathogen that poses serious threats to agriculture. This ascomycete can infect more than 600 plant species (*1*), causing severe yield and quality loss in many economically important crops including soybean, sunflower, and canola (*2*, *3*). During its life cycle, *S. sclerotiorum* produces durable, black structures termed sclerotia, which can survive in the soil for years (*4*, *5*). Under the right conditions, sclerotia can either grow into filamentous mycelia or form a reproductive cup-shaped fruiting body called apothecium, releasing sexual ascospores into the air to infect adjacent plants (*3*). A closely related pathogen, *Botrytis cinerea* (*B. cinerea*), is a major threat to both field and greenhouse crops. It spreads quickly by releasing large numbers of airborne asexual conidia spores. It can also form sclerotia to survive harsh conditions (*6*). Despite their impact on agriculture, the mechanisms underlying how these fungi develop and cause disease are still not fully understood. Studying either fungus is challenging because the mycelial cells of these fungi are multinucleated, hindering efficient genetic dissection (*7*).

Previous studies using pulsed-field gel electrophoresis–based karyotyping and de novo genome assembly revealed that *S. sclerotiorum* has 16 chromosomes in its haploid genome (1N = 16) (*8*, *9*). As each ascospore has two nuclei, likely produced by two mitotic divisions following meiosis (*10*), we expected each nucleus to have a full set of 16 chromosomes. This would make the ascospore functionally similar to a diploid cell. As part of our study investigating the process of sclerotia formation, we conducted a forward genetic screen to identify ascospore mutants of *S. sclerotiorum* unable to form sclerotia (*11*). Upon ultraviolet (UV)–induced random mutagenesis, we expected that any induced mutation should affect only one of the two ascospore nuclei, resulting in a fungal colony of cells with both wild-type and mutant genotypes. However, examination of more than 100 mutants that failed to form sclerotia revealed that they all contained only mutant cells; no sectors that form sclerotia were observed. This unexpected result suggested that the ascospores might actually be haploid, with the full set of 16 chromosomes divided between the two nuclei. Because this prediction challenges established principles of chromosome biology, we conducted a closer examination of the ascospores' nuclei and chromosomes.

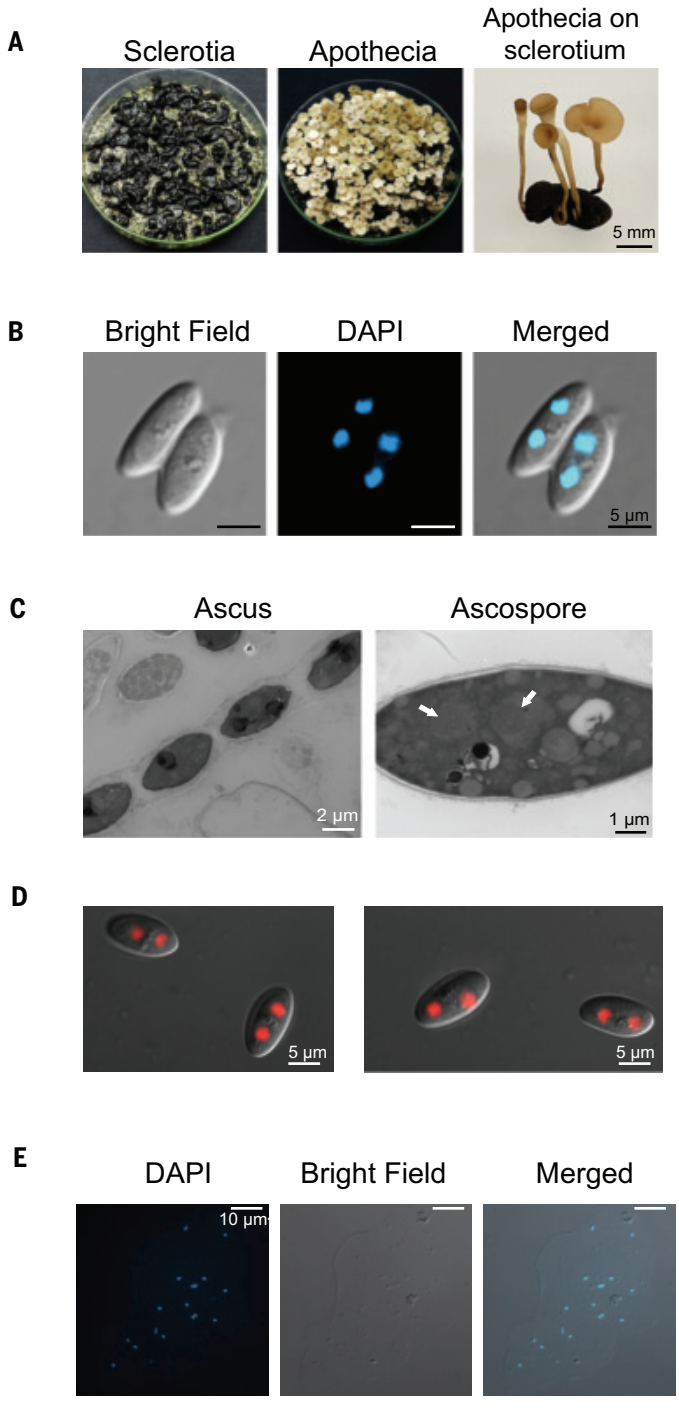

Fig. 1. A haploid *S. sclerotiorum* ascospore contains 16 chromosomes distributed across two nuclei. (**A**) Formation of apothecia from sclerotia. Scale bar, 5 mm. (**B**) DAPI staining of ascospores. Scale bar, 5 μm. (**C**) TEM images of an ascus and ascospores. White arrows indicate nucleoli inside the nuclei. Left: Scale bar, 2 μm; right: scale bar, 1 μm. (**D**) Fluorescence microscopy images of ascospores from the *S. sclerotiorum* SsH4-mCherry strain. Scale bar, 5 μm. (**E**) DAPI staining of chromosomes inside a representative protoplast of a *S. sclerotiorum* ascospore. Scale bar, 10 μm.

[1]Key Laboratory of Bio-resource and Eco-environment of Ministry of Education, College of Life Sciences, Sichuan University, Chengdu, Sichuan, China. [2]Michael Smith Laboratories, University of British Columbia, Vancouver BC, Canada. [3]Department of Botany, University of British Columbia, Vancouver BC, Canada. ***Corresponding author. Email: yuelin.zhang@scu.edu.ca (Y.Z.); xinli@msl.ubc.ca (X.L.)** †These authors contributed equally to this work.

A

Probe	No. of ascospores without probe signal	No. of ascospores with probe signal in one nucleus	No. of ascospores with probe signal in two nuclei	Total number of ascospores examined
18S-rDNA probe	105	236	0	341
Chr4-specific probe	79	243	0	322
18S-rDNA and Chr4-specific probes	13	207	76	296
Telomere probe	16	30	126	172

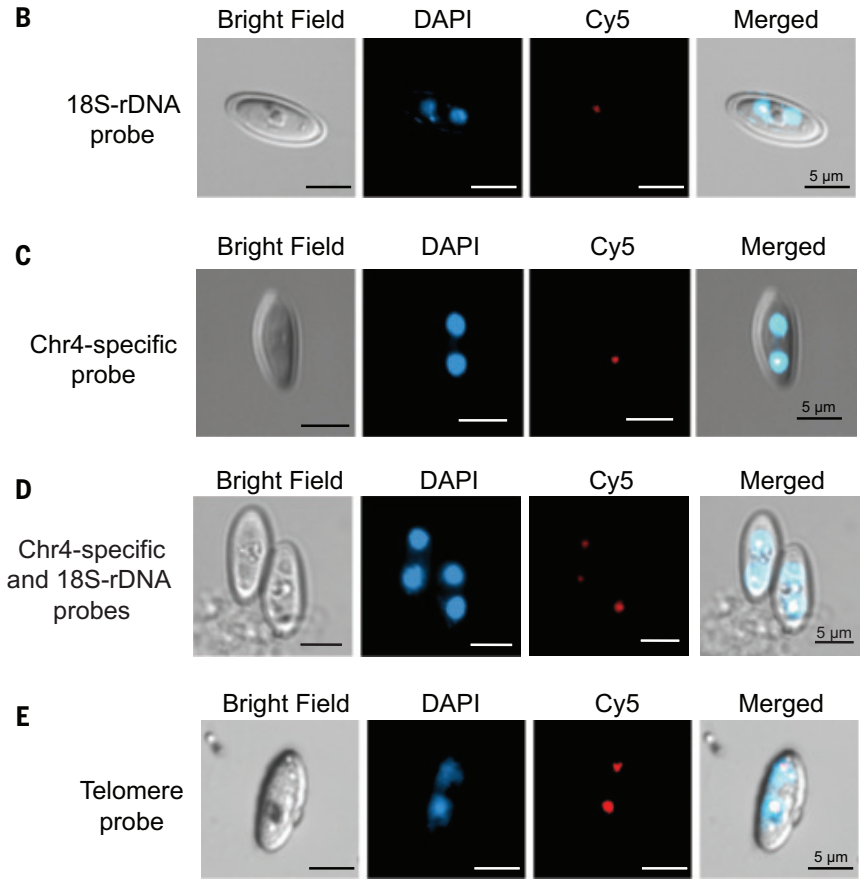

Fig. 2. The chromosomes in the two nuclei of an *S. sclerotiorum* ascospore are distinct. (**A**) Summary of FISH signals for 18*S*-rDNA (Chr 7), Chr4-specific, 18*S*-rDNA + Chr4-specific, or telomere probes in one or both nuclei of examined ascospores. (**B** to **E**) FISH signals of 18*S*-rDNA (B), Chr4-specific (C), Chr4-specific + 18*S*-rDNA (D), and telomere (E) probes in representative ascospores. Blue and red signals are from DAPI-stained nuclei and hybridized probes, respectively. Scale bars, 5 μm.

Each ascospore of *S. sclerotiorum* contains two nuclei with a total of 16 chromosomes

To generate ascospores, apothecia of wild-type *S. sclerotiorum* strain 1980 were induced from sclerotia (Fig. 1A). The nuclei were visualized by staining 1606 ascospores with DAPI (4′,6-diamidino-2-phenylindole), a fluorescent dye that binds to DNA. Under a fluorescence microscope, each ascospore consistently displayed two bright signals (Fig. 1B and fig. S1A), suggesting the presence of two nuclei per spore. To confirm that these DAPI signals indeed represented two separate nuclei, transmission electron microscopy (TEM) was carried out. On the basis of previously described criteria (*12*), each ascospore contained two well-defined nuclei, each with a visible nucleolus (Fig. 1C).

To examine the nuclei in live cells, we created *S. sclerotiorum* lines expressing histone 4 (SsH4) fused to mCherry or enhanced green fluorescence protein (eGFP). Under the fluorescence microscope, the SsH4-mCherry ascospores showed two separate signals (Fig. 1D), corroborating the presence of two nuclei per ascospore.

Treatment of the SsH4-mCherry ascospores with UV light did not result in a loss of nuclei, as the surviving ascospores continued to divide while maintaining paired nuclei fluorescence (fig. S1, B and C). Notably, we did not observe any incidence of odd-numbered nuclei, indicating that all recovered fungal colonies originated from ascospores containing two nuclei rather than a single one. In addition, live-cell imaging of the first and second mitotic divisions of SsH4-mCherry and SsH4-eGFP ascospores (movies S1 and S2) and in SsH4-mCherry mycelial cells (movie S3) revealed no observable connection between the paired nuclei. Finally, after refining a method to fix and analyze ascospore protoplasts, we counted their chromosomes. Each ascospore consistently contained 16 chromosomes, rather than 32, supporting our hypothesis that each ascospore, not each nucleus, holds a complete haploid genome of about 16 chromosomes (Fig. 1E and fig. S2).

Molecular evidence for irregular assortment of the 16 chromosomes into two nuclei in *S. sclerotiorum* ascospore

To examine the distribution of the chromosomes between the two ascospore nuclei, we carried out fluorescence in situ hybridization (FISH) experiments using an 18*S*-rDNA (ribosomal DNA) probe targeting chromosome 7 and a chromosome 4 (Chr4)–specific probe (fig. S3, A and B). When these probes were applied individually, hybridization signals were exclusively observed in one nucleus per ascospore (Fig. 2, A to C, and fig. S4, A and B). Notably, we never observed either the 18*S*-rDNA signal or the Chr4-specific signal in both nuclei of an ascospore, suggesting that the two nuclei harbor distinct sets of chromosomes. To rule out the possibility that the probe entered only one nucleus, we used a control probe targeting telomeres, which should hybridize to nearly all chromosomes (fig. S3C). Telomere probe signals were detected in both nuclei (Fig. 2, A and E, and fig. S4D), confirming that the fluorescent probes could freely access both nuclei. When the FISH assay was performed using both the 18*S*-rDNA and Chr4-specific probes together, among 296 ascospores examined, 207 showed signals in only one nucleus, whereas 76 displayed signals in both nuclei (Fig. 2, A and D, and fig. S4C), suggesting that chromosome distribution in the two paired nuclei is not the same among ascospores. Similar patterns were observed in germinating ascospores

with four nuclei and in older mycelial cells (fig. S5), suggesting that the full haploid chromosome set splits into two nuclei throughout its life cycle. Taken together, these data indicate that the chromosomes of the two nuclei in *S. sclerotiorum* ascospore are distinct. Each nucleus carries about half (8) of the total 16 chromosomes.

To further test our hypothesis, we used flow cytometry with fluorescence-activated cell sorting (FACS) to measure the DNA content of purified nuclei from *S. sclerotiorum* ascospores. Haploid and diploid *Saccharomyces cerevisiae* (baker's yeast) strains BY4741 and BY4743 were used as controls (fig. S6A). On the basis of the relative fluorescence intensity (RFI) of nuclei, we estimated the DNA content per nucleus for each fungal species (Fig. 3A and fig. S6B). The results showed that each *S. sclerotiorum* ascospore nucleus contained, on average, only about half of

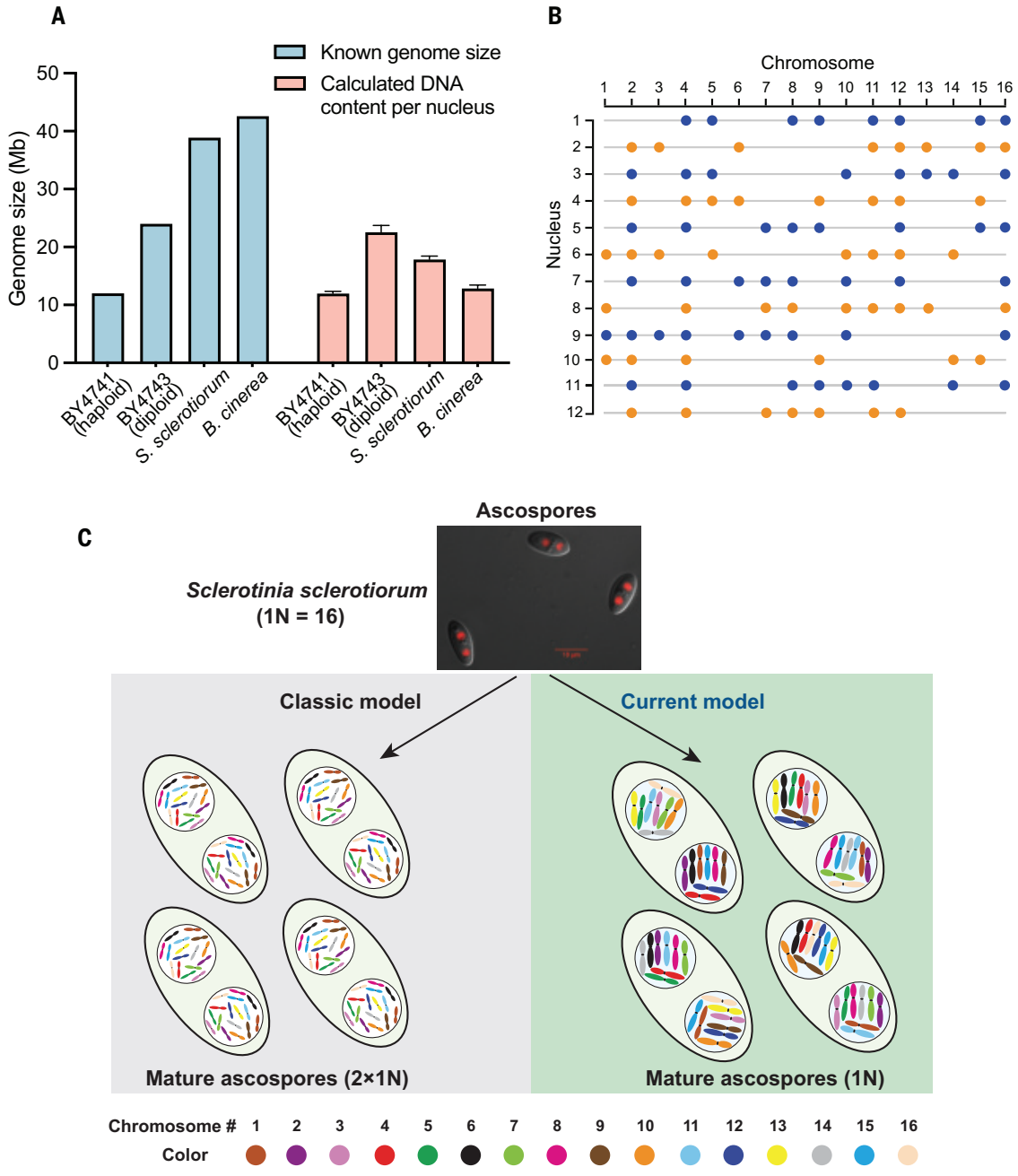

Fig. 3. *S. sclerotiorum* distributes its 16 haploid chromosomes into two nuclei in an irregular manner. (**A**) Calculated DNA content per nucleus in *Saccharomyces cerevisiae* BY4741 (haploid yeast), BY4743 (diploid yeast), germinating ascospores of *S. sclerotiorum*, and germinating conidia of *B. cinerea*. The known genome sizes of these strains are 12, 24, 38.9, and 42.6 Mb, respectively. The DNA content in each nucleus was calculated by multiplying the genome size of the haploid yeast strain BY4741 by the fold-change values derived from data in fig. S6B. Error bars indicate the standard deviation ($n = 15$). (**B**) Summary of single-nucleus PCR results using chromosome-specific primers. DNA from individually sorted nuclei prepared from young mycelia that originated from sclerotia was subjected to whole-genome amplification. The amplified genomic DNA served as a template for PCR using chromosome-specific primers (see fig. S8). Blue and orange dots indicate the presence of the corresponding chromosomes in each nucleus. (**C**) A model depicting chromosome distribution in *S. sclerotiorum* nuclei. In the classic model, both nuclei in an ascospore contain identical sets of 16 haploid chromosomes (1N = 16). In the new model, the 16 chromosomes are distributed into two nuclei in an irregular manner. The fluorescence microscopy image shows nuclei in ascospores of the *S. sclerotiorum* SsH4-mCherry strain. Scale bar, 10 μm.

the total genome, supporting our hypothesis that the full set of chromosomes is split between the two nuclei.

To determine the exact chromosomal composition of each nucleus, we performed polymerase chain reaction (PCR) analysis on individually sorted nuclei isolated from young mycelia grown from sclerotia. After sucrose gradient centrifugation and fractionation (fig. S7), the purified nuclei were singly sorted into 96-well plates. After whole-genome DNA amplification, the amplified DNA from each nucleus was subjected to PCR using chromosome-specific primers. Each nucleus contained ~8 chromosomes (Fig. 3B and fig. S8). Similar patterns were observed in nuclei purified from germinating ascospores or older mycelial cells derived from single ascospores (fig. S9). These results align with our chromosome counting, FISH, and flow cytometry data, confirming that each nucleus in

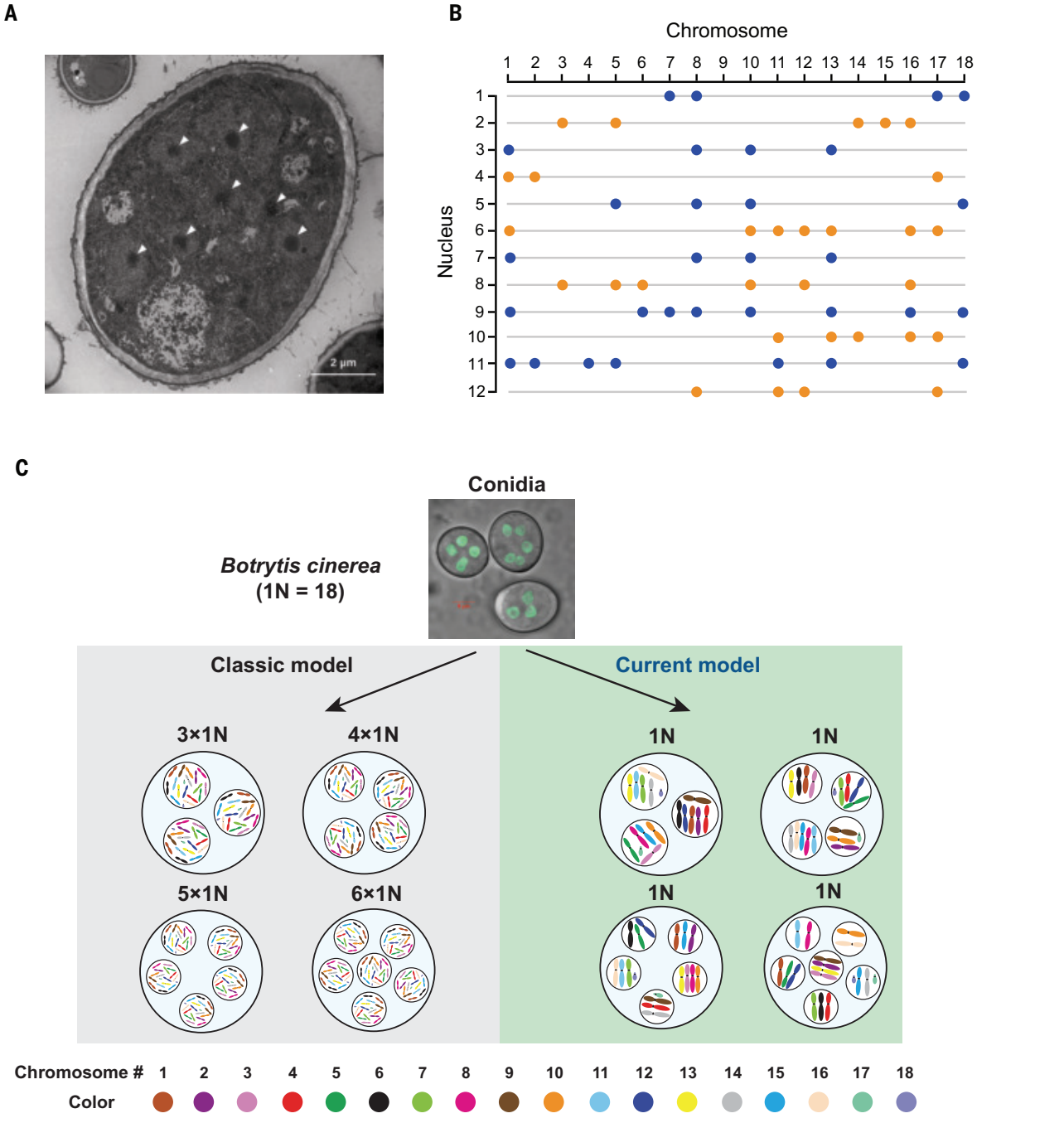

Fig. 4. *B. cinerea* distributes its haploid chromosomes into different nuclei in an irregular manner. (**A**) A TEM image of a *B. cinerea* conidium, with white arrows indicating nucleoli inside the nuclei. Scale bar, 2 μm. (**B**) Summary of single-nucleus PCR results with chromosome-specific primers. DNA from individually sorted nuclei underwent whole-genome amplification, and the amplified genomic DNA served as a template for PCR with chromosome-specific primers (see fig. S11). Blue and orange dots indicate the presence of the corresponding chromosomes in each nucleus. (**C**) A model illustrating chromosome distribution in *B. cinerea* nuclei. In the classic model, each nucleus in a conidium contains a full complement of 18 haploid chromosomes (1N = 18). In the new model, the 18 chromosomes are distributed into different nuclei inside each conidium in an irregular manner. The fluorescence microscopy image shows the nuclei in conidia of the *B. cinerea* histone H1-eGFP strain (*21*). Scale bar = 5 μm.

ascospores, and in young and older mycelial cells, contains ~8 chromosomes. Consistent with our FISH observations using Chr4- and Chr7- specific probes, the chromosomal composition varied among nuclei (Fig. 3B and figs. S8 and S9), indicating an irregular assortment of the 16 chromosomes into different nuclei in *S. sclerotiorum* (Fig. 3C).

Irregular assortment of the 18 haploid chromosomes into multiple nuclei in *B. cinerea*

After observing the irregular chromosome distribution in *S. sclerotiorum*, in which 16 chromosomes were divided between two nuclei, we wondered whether this phenomenon also occurs in other fungi. In *B. cinerea*, each conidium is also multinucleated, typically containing four or five nuclei per cell (Fig. 4) (*13*). The haploid genome of *B. cinerea* is composed of 18 chromosomes (1N = 18) on the basis of de novo genome sequencing and assembly (*14*).

When we analyzed the DNA content of conidial nuclei using flow cytometry, we found that each nucleus contained, on average, less than 30% of the total haploid genome (Fig. 3A and fig. S6). This suggests that, like *S. sclerotiorum*, *B. cinerea* spores are haploid but divide their chromosomes among multiple nuclei. In addition, using the single-nucleus purification approach (fig. S10A), we isolated single nuclei from *B. cinerea* conidia and sorted them into 96-well plates (fig. S10B). Chromosome-specific single-nucleus PCR was used to assess the presence of individual chromosomes. Each nucleus contained between three and eight chromosomes, distributed in an irregular manner (Fig. 4B and fig. S11). Thus, similar to *S. sclerotiorum*, *B. cinerea* does not assign its full set of haploid chromosomes to each nucleus. Rather it allocates them across nuclei in the conidium (Fig. 4C). This likely explains why pure knockout or transgenic fungal colonies can be easily obtained from *B. cinerea* germinating conidia without the need for additional purification (*15*).

Discussion

Our analysis using chromosome counting, FISH, flow cytometry, and single-nucleus PCR demonstrates that in both *S. sclerotiorum* ascospores and *B. cinerea* conidia, each set of haploid chromosomes is divided among separate nuclei. However, the mechanism by which these chromosomes are allocated while preserving genetic integrity during cell division remains unclear. Although not observed yet, it is possible that the two paired nuclei are connected with filaments or membrane structures, maintaining genome fidelity during synchronized mitosis and meiosis. Although stable nuclear fusion of *S. sclerotiorum* was not detected, paired nuclei often came into close proximity and even collided with each other before chromosome condensation and nuclear division (movies S1 and S2), suggesting that the full set of chromosomes may come together transiently before redistributing into separate nuclei (fig. S12). Further investigation using advanced cell biology tools is needed to clarify these processes.

The advantage of this chromosome distribution pattern remains uncertain. One possibility is that it enables fungi to respond and adapt more effectively to local environmental stresses within their extensive mycelial networks. Nuclear shuffling may facilitate the rapid generation of new genotypes, enhancing adaptability to changing environments. This feature may contribute to the ecological success of *S. sclerotiorum* and *B. cinerea*, particularly the latter, which is known for its rapid adaptation to fungicides in greenhouses and fields (*16*).

Binucleate or multinucleate spores have also been observed in other *Sclerotinia* species and some basidiomycetes (*17*–*20*), suggesting that the chromosome assortment pattern that we identified may be widespread among fungi. Investigating this phenomenon in other fungal species and eukaryotes could provide broader insights into chromosome biology. Future studies focused on genes and mechanisms involved in chromosome sorting and regulation could have implications for synthetic biology and genetic engineering.

This study presents an alternative model for how multinucleated cells manage their chromosomal content. Mycelial cells of many fungi may contain hundreds of nuclei with partial chromosome sets, providing positional diversity to enable rapid local response to environmental cues. Our findings have important implications for forward and reverse genetic analyses in fungi with multinucleate spores. Historically, forward genetic screens have rarely been attempted in species such as *S. sclerotiorum* or *B. cinerea* owing to the multinucleate nature of their spores. However, our discovery that each conidium contains a complete haploid chromosome set suggests that forward genetic screens can also be conducted in *B. cinerea* through random mutagenesis of conidia. Additionally, knockout experiments can be simplified by using ascospores or conidia.

REFERENCES AND NOTES

1. X. Liang, J. A. Rollins, *Phytopathology* **108**, 1128–1140 (2018).
2. D. D. Hegedus, S. R. Rimmer, *FEMS Microbiol. Lett.* **251**, 177–184 (2005).
3. M. D. Bolton, B. P. Thomma, B. D. Nelson, *Mol. Plant Pathol.* **7**, 1–16 (2006).
4. P. B. Adams, W. A. Ayers, *Phytopathology* **69**, 896–899 (1979).
5. H. J. Willetts, J. A. L. Wong, *Bot. Rev.* **46**, 101–165 (1980).
6. S. Petrasch, S. J. Knapp, J. A. L. van Kan, B. Blanco-Ulate, *Mol. Plant Pathol.* **20**, 877–892 (2019).
7. E. J. Ford, R. V. Miller, H. Gray, J. E. Sherwood, *Mycol. Res.* **99**, 241–247 (1995).
8. L. Fraissinet-Tachet, P. Reymond-Cotton, M. Fèvre, *Curr. Genet.* **29**, 496–501 (1996).
9. J. Amselem *et al.*, *PLOS Genet.* **7**, e1002230 (2011).
10. M. Ekins, Genetic diversity in *Sclerotinia* species, thesis, The University of Queensland (1999).
11. Y. Xu *et al.*, *Mol. Plant Microbe Interact.* **35**, 244–256 (2022).
12. T. Takagi, M. Osumi, A. Shinohara, *Commun. Biol.* **4**, 1009 (2021).
13. N. Shirane, M. Masuko, Y. Hayashi, *Phytopathology* **78**, 1627–1630 (1988).
14. J. A. Van Kan *et al.*, *Mol. Plant Pathol.* **18**, 75–89 (2017).
15. H. Reis, S. Pfiffi, M. Hahn, *Mol. Plant Pathol.* **6**, 257–267 (2005).
16. Z. Wu *et al.*, *mBio* **15**, e0223723 (2024).
17. W. G. Kim, W. D. Cho, *Mycobiology* **30**, 41–46 (2002).
18. F. C. Chen, F.-C. Chen, N. Shimomura, T. Yamaguchi, T. Aimi, *Mycoscience* **62**, 341–344 (2021).
19. R. Rebecca *et al.*, *MicrobiologyOpen* **10**, e1233 (2021).
20. X. H. Du *et al.*, *Front. Microbiol.* **14**, 1286501 (2023).
21. N. Shlezinger *et al.*, *PLOS Pathog.* **7**, e1002185 (2011).

ACKNOWLEDGMENTS

The authors thank J. Rollins (University of Florida) for providing the *S. sclerotiorum* strain 1980 and for valuable insights and discussions on various aspects of *Sclerotinia* biology. We extend our gratitude to A. Sharon (Tel Aviv University) and M. Hahn (University of Kaiserslautern) for the *B. cinerea* B05.10 and histone H1-eGFP strains, and to A. Nebenführ and D. Jiang for vectors used for making the SsH4-mCherry strain. J. Kronstad and G. Haughn from the University of British Columbia are thanked for their careful reading of the manuscript. Our appreciation goes to J. Wong and A. Johnson from the UBC Flow Cytometry facility, J. Shi from Chengdu Zhijing Technology Co., and H. Kang and Y. Yi from Sichuan University for assistance in single-nucleus sorting and flow cytometry analysis. Additionally, we thank K. Ao for help in designing the FISH probe, as well as J. Lu, T. Weerasinghe, Y. Gong, and S. Liu for providing apothecia and assisting with various experiments. **Funding:** This study was financially supported by grants awarded to X.L. and Y.Z. from the Canadian Natural Sciences and Engineering Research Council (NSERC) Discovery program, NSERC-CREATE-PRoTECT, Canada Research Chair (CRC), the Canadian Foundation for Innovation (CFI), and the Fundamental Research Funds for the Central Universities (YJ202255). Y.X. and L.T. were supported by scholarships from the Chinese Scholarship Council, and J.T. was supported by the University of British Columbia Four-year fellowship program. **Author contributions:** Conceptualization: X.L., Y.Z. Methodology: All authors. Investigation: Y.X., L.T., J.T., J.L., W.H. Visualization: Y.X., L.T., J.T., J.L., W.H. Funding acquisition: X.L., Y.Z. Project administration: X.L., Y.Z. Supervision: X.L., Y.Z. Writing – original draft: Y.X., L.T., X.L. Writing – review and editing: All authors. **Competing interests:** The authors declare that they have no competing interests. **Data and materials availability:** All data are available in the main text or the supplementary materials. Y.Z. and X.L. are responsible for distribution of materials integral to the findings presented in this paper.

License information: Copyright © 2025 the authors, some rights reserved; exclusive licensee American Association for the Advancement of Science. No claim to original US government works. https://www.sciencemag.org/about/science-licenses-journal-article-reuse

SUPPLEMENTARY MATERIALS

science.org/doi/10.1126/science.abn7811
Materials and Methods; Figs. S1 to S12; Tables S1 to S3; References (*22*–*29*); MDAR Reproducibility Checklist; Movies S1 to S3

Submitted 5 October 2023; resubmitted 5 July 2024; accepted 22 March 2025

10.1126/science.abn7811

ScienceCareers.org
Science Careers

myIDP ScienceCareers
INDIVIDUAL DEVELOPMENT PLAN

Features in myIDP include:

- Exercises to help you examine your skills, interests, and values.
- 20 career paths with a prediction of which ones best fit your skills and interests.
- A tool for setting strategic goals with optional reminders to keep you on track.
- Articles and resources to guide you through the process.
- Options to save materials online and print them for further review and discussion.
- A certificate of completion for users that finish myIDP.

Start planning your future today!
myIDP.sciencecareers.org

In partnership with:

FASEB Federation of American Societies for Experimental Biology
UMASS University of Massachusetts Medical School
UCSF University of California San Francisco
UIC
BURROUGHS WELLCOME FUND

The cost of health

Lara de Macedo Monteiro

I stepped out of the car, travel backpack in hand, returning from winter break rested and rejuvenated by seeing friends. I was feeling optimistic about my health, too. A recent appointment with an ear specialist had offered some hope that doctors would be able to diagnose the cause of the dizziness that had plagued me since nearly the beginning of my Ph.D. and finally treat it effectively. But what I found in my mailbox made my heart race: a stack of medical bills, the latest additions to the pile of unpaid invoices already sitting on my dresser.

When I first arrived in the United States from Brazil to pursue my Ph.D., I felt nothing could stand in my way. But a few months into my studies, a persistent dizziness crept in. Walking to campus, reading papers, and even grocery shopping left me unsteady. I rushed to the university clinic, where the doctor said I had vertigo and recommended rehab. But I had heard countless stories of graduate students paying thousands of dollars out of pocket for treatment of various ailments, and I was hesitant to rack up bills that would certainly outpace my meager stipend. Instead, I turned to YouTube, where I found at-home exercises. For weeks, every night before bed, I moved my head from side to side, then up and down. Eventually, the symptoms disappeared. I thought I was in the clear.

Two years later, the dizziness returned. This time, the exercises failed, and over-the-counter medications offered little relief. With my worsening symptoms making it difficult to keep up with my Ph.D. work, I didn't see any alternative but to seek medical treatment despite my worries about the cost. I went back to the doctor, who referred me to an ear specialist. I called to book an appointment, only to be told the wait was 4 months. Far from my family, with no clear treatment plan, I felt helpless and frustrated.

Shortly afterward, I traveled out of state for winter break in a larger city, where I secured a last-minute appointment with an ear specialist. After being referred to one medical center, then another, I was given a steroid shot and orders for a brain MRI and more ear tests. No final diagnosis yet, but a clear message: The dizziness would likely return until I found the cause. Still, the steroids brought my first moment of relief in months.

Back home, after collecting the pile of medical bills from my mailbox, I contacted the university's health insurance office for a cost estimate for the recommended tests. Even with my student insurance, the out-of-pocket amount was far beyond what I could afford. Then came another blow: The referrals from the out-of-state doctors weren't valid locally. I would still need to wait for the in-state ear specialist appointment. There I was, facing the imminent return of my symptoms, medical bills piling up, and unable to schedule or afford the tests I needed. My stress levels soared.

In the weeks that followed, I began to experience heart palpitations, shortness of breath, and insomnia. After I wore a doctor-ordered heart monitor for 2 days, the diagnosis came back as sinus tachycardia—in other words, stress-induced anxiety. My body was sounding an alarm I could no longer ignore: This situation was unsustainable.

That was 3 months ago. Since then, I finally had my in-state appointment; with it came new referrals and, of course, more bills. This time, however, I have found a stopgap solution: I travel to Brazil yearly to conduct fieldwork, and during those trips I also attend medical checkups. This year, with multiple U.S. medical referrals in hand, I was able to schedule tests that will finally get me closer to a diagnosis. It's unbelievable to think that, even with travel costs, care can be so much cheaper or even free through Brazil's public and universal health care system. I know I'm lucky to have this option. Many other students face similar challenges without it.

Medical expenses can be overwhelming, especially for international students whose visas often restrict us from earning income beyond our stipends. No student should have to choose between financial survival and medical care. No student should lose valuable time and mental energy over something as fundamental as health care. Universities must step up and provide more comprehensive health coverage for their students so we can focus on our work. □

Lara de Macedo Monteiro is a Ph.D. candidate at the University of Vermont.

ILLUSTRATION: ROBERT NEUBECKER

CALL FOR PAPERS

SPJ
SCIENCE PARTNER JOURNALS

Journal of Remote Sensing

The *Journal of Remote Sensing* is an online-only Open Access Science Partner Journal published in affiliation with **Aerospace Information Research Institute, Chinese Academy of Sciences (AIR-CAS)** and distributed by the **American Association for the Advancement of Science (AAAS)**. Like all partners participating in the Science Partner Journal program, the *Journal of Remote Sensing* is editorially independent from the *Science* family of journals and AIR-CAS is responsible for all content published in the journal. This journal covers multiple research areas that include theory, science, technology of remote sensing, and interdisciplinary research with earth science and information science. Particular topics of interest within the journal include radiative transfer modeling, biogeosciences remote sensing, remote sensing of energy, and more.

Submit your research to the *Journal of Remote Sensing* today!

Learn more at **spj.science.org/remotesensing**

The Science Partner Journal (SPJ) program was established by the American Association for the Advancement of Science (AAAS), the nonprofit publisher of the *Science* family of journals. The SPJ program features high-quality, online-only, Open Access publications produced in collaboration with international research institutions, foundations, funders and societies. Through these collaborations, AAAS furthers its mission to communicate science broadly and for the benefit of all people by providing top-tier international research organizations with the technology, visibility, and publishing expertise that AAAS is uniquely positioned to offer as the world's largest general science membership society.

Visit us at **spj.science.org**

@SPJournals @SPJournals @SPJournals

OPEN ACCESS

ARTICLE PROCESSING CHARGES WAIVED UNTIL JULY 2025

AAAS | Science

CONGRATULATIONS TO THE WINNERS OF THE

MANI L. BHAUMIK
BREAKTHROUGH OF THE YEAR AWARD

FOR THEIR INTEGRAL ROLE IN DEVELOPING THE

2024 *Science* Breakthrough of the Year: lenacapavir

A long-lasting HIV drug, based on a novel mechanism

YVETTE RAPHAEL
ADVOCACY FOR PREVENTION OF HIV IN AFRICA

GILEAD SCIENCES *WITH SPECIAL RECOGNITION OF* MOUPALI DAS

WESLEY I. SUNDQUIST
UNIVERSITY OF UTAH

The full story and more information can be found at engage.aaas.org/4387hDH

PHOTO CREDITS (LEFT TO RIGHT): ERIK ESPERA, A SHOT IN THE ARM MEDIA | MOUPALI DAS | RACHEL MERRILL / UNIVERSITY OF UTAH HEALTH